Unraveling Molecular Mechanisms of Gecko Adhesion: Multi-Scale Molecular Dynamics

Entschlüsselung der molekularen Mechanismen der Gecko-Adhäsion: Mehrskalen-Molekulardynamik

Vom Fachbereich Chemie der Technischen Universität Darmstadt zur Erlangung des Grades
Doctor rerum naturalium (Dr. rer. nat.)

Genehmigte Dissertation von Tobias Materzok, M.Sc. aus Frankfurt am Main, Deutschland
Tag der Einreichung: 9. März 2023, Tag der Prüfung: 20. April 2023

Erstgutachter: Prof. Dr. Florian Müller-Plathe
Zweitgutachter: Prof. Dr. Stanislav N. Gorb
Drittgutachter: Prof. Dr. Paola Carbone
Darmstadt, Technische Universität Darmstadt

TECHNISCHE
UNIVERSITÄT
DARMSTADT

Fachbereich Chemie

Eduard-Zintl-Institut für
Anorganische und
Physikalische Chemie

Prof. Dr. Florian
Müller-Plathe

Unraveling Molecular Mechanisms of Gecko Adhesion: Multi-Scale Molecular Dynamics
Entschlüsselung der molekularen Mechanismen der Gecko-Adhäsion: Mehrskalen-Molekulardynamik

Genehmigte Dissertation von Tobias Materzok, M.Sc.

Tag der Einreichung: 9. März 2023
Tag der Prüfung: 20. April 2023

Darmstadt, Technische Universität Darmstadt

Bitte zitieren Sie dieses Dokument als:
URN: urn:nbn:de:tuda-tuprints-232973
URL: http://tuprints.ulb.tu-darmstadt.de/23297

Veröffentlicht im Jahr 2023 auf TUprints,
E-Publishing-Service der TU Darmstadt
http://tuprints.ulb.tu-darmstadt.de
tuprints@ulb.tu-darmstadt.de

Erklärungen laut Promotionsordnung

§ 8 Abs. 1 lit. c PromO

Ich versichere hiermit, dass die elektronische Version meiner Dissertation mit der schriftlichen Version übereinstimmt.

§ 8 Abs. 1 lit. d PromO

Ich versichere hiermit, dass zu einem vorherigen Zeitpunkt noch keine Promotion versucht wurde. In diesem Fall sind nähere Angaben über Zeitpunkt, Hochschule, Dissertationsthema und Ergebnis dieses Versuchs mitzuteilen.

§ 9 Abs. 1 PromO

Ich versichere hiermit, dass die vorliegende Dissertation selbstständig und nur unter Verwendung der angegebenen Quellen verfasst wurde.

§ 9 Abs. 2 PromO

Die Arbeit hat bisher noch nicht zu Prüfungszwecken gedient.

Darmstadt, 9. März 2023

T. Materzok

Die vorliegende Dissertation wurde unter der Leitung von Herrn Prof. Dr. Florian Müller-Plathe in der Zeit vom 01. Februar 2019 bis zum 24. April 2022 im Fachbereich Chemie der Technischen Universität Darmstadt durchgeführt.

Teile dieser Arbeit sind bereits veröffentlicht:

- T. Materzok, S. N. Gorb, F. Müller-Plathe, *Gecko adhesion: a molecular-simulation perspective on the effect of humidity*, Soft Matter, **18**, 1247-1263, DOI: 10.1039/D1SM01232K (2022)
- T. Materzok, A. Canestraight, S. N. Gorb, F. Müller-Plathe, *How Does Gecko Keratin Stick to Hydrophilic and Hydrophobic Surfaces in the Presence and Absence of Water? An Atomistic Molecular Dynamics Investigation*, ACS Nano, **16**, 19261–19270, DOI: 10.1021/acsnano.2c08627 (2022)
- T. Materzok, D. de Boer, S. N. Gorb, F. Müller-Plathe, *Gecko Adhesion on Flat and Rough Surfaces: Simulations with a Multi-Scale Molecular Model*, Small, **18**, 2201674, DOI: 10.1002/smll.202201674 (2022)
- T. Materzok, H. Eslami, S. N. Gorb, F. Müller-Plathe, *Understanding Humidity-Enhanced Adhesion of Geckos: Deep Neural Network-Assisted Multi-Scale Molecular Modeling*, Small, DOI: 10.1002/smll.202206085 (2023)

In dieser Dissertation nicht enthalten, aber im gleichen Zeitraum und Kontext entstanden sind:

- M. Khani, T. Materzok, H. Eslami, S. N. Gorb, F. Müller-Plathe, *Water uptake by gecko β-keratin and the influence of relative humidity on its mechanical and volumetric properties*, J. R. Soc. Interface, **19**, 20220372, DOI: 10.1098/rsif.2022.0372 (2022)
- H. Eslami T. Materzok, F. Müller-Plathe, *Molecular Structure and Dynamics in Wet Gecko β-Keratin*, ACS Biomater. Sci. Eng., **9**, 257-268, DOI: 10.1021/acsbiomaterials.2c01022 (2022)

Acknowledgements

First and foremost, I would like to express my deepest gratitude to my thesis advisor, Prof. Dr. Florian Müller-Plathe, for his exceptional guidance, support, and mentorship throughout my Ph.D. journey. From the outset, Florian has consistently struck a perfect balance between providing strategic directions and granting me the freedom to determine the tactical approach. His scientific expertise and wit are genuinely unique, and I have learned so much from him both in and out of the subject matter. In addition to his mentorship, I equally appreciate his efforts to foster a close-knit and supportive working environment within the group, especially during these recent times of social distancing.

I want to express my gratitude to Prof. Dr. Nico van der Vegt for examining my thesis and his helpful suggestions and support during our group seminar. I am particularly grateful to Nico for sparking my deep interest in theoretical chemistry and for his role in guiding me toward this field of study. I would also like to express my sincere gratitude to one of my co-authors and evaluation committee member, Prof. Dr. Stanislav N. Gorb, for his valuable insights, support, and collaboration throughout my doctoral journey. I am grateful for the opportunity to have worked with him and learned from his expertise in the field.

I am grateful to Dana Voss for her efforts to create a social and supportive environment within the group and for her professionalism in handling administrative tasks. I also want to express my gratitude to Marvin and Viktor from the group of Nico van der Vegt for their contributions to the administration of our computer clusters and to Hans-Jürgen Bär for his support with these efforts as well as for designing challenging and insightful math and physical chemistry exercises throughout my studies.

I am incredibly grateful for the relationships I have formed with my colleagues and friends in the Müller-Plathe group. From the very beginning, I have felt welcomed and supported by the members of this community, who have always been willing to share their knowledge with me. Over the years, I have had the privilege of working with and learning from some truly brilliant and passionate scientists. I am grateful for the opportunities I have had to collaborate with them on exciting research projects.

But beyond the scientific discussions and collaborations, I am incredibly thankful for the personal connections I have made within the group. The cultural exchange and discussions about world politics, science, technology, culture and everything in between have been some of the most enriching and meaningful parts of my Ph.D. journey. I will sincerely miss the camaraderie and sense of community we had, and I am grateful to have had such supportive and understanding friends and colleagues throughout my studies. Thanks go out to Dr. Angelina Folberth, Annabelle Canestraight, Danna De Boer, Prof. Dr. Donatas Surblys, Dr. Eunsang Lee, Dr. Gustavo Rondina, Prof. Dr. Hari Kishna Chilukoti, Prof. Dr. Hossein Eslami, Dr. Jeffrey M. Young, Dr. Jurek Schneider, Dr. Marvin Bernhard, Melissa Meinel, Saeed Norouzi, Dr. Saientan Bag, Dr. Saurav Prasad, Dr. Shubhadip Das, Simon Alberti, Dr. Tianhang Zhou, Yash Jain, and Dr. Zhenghao Wu.

Finally, I want to express my deep appreciation to my family, friends, and loved ones for their unwavering support and encouragement throughout life and my Ph.D. Thank you all for everything.

Zusammenfassung

Diese Arbeit präsentiert einen Multi-Skalen-Simulationsansatz, um die Mechanismen der Geckohaftung in Längenskalen von atomar bis mesoskalig zu untersuchen. Wir haben unsere Modelle und Verfahren gegen Experimente validiert und liefern neue molekulare Erkenntnisse zur Geckohaftung. Wir untersuchen den Effekt von Feuchtigkeit, die Rolle elektrostatischer Wechselwirkungen und den Einfluss der Oberflächenrauheit auf die Geckohaftung. Ein bedeutender Durchbruch ist unsere Lösung einer fast zwei Jahrzente alten wissenschaftlichen Debatte über den primären Mechanismus der Geckohaftung unter Bedingungen hoher Luftfeuchtigkeit. Wir können zeigen, dass der von uns gefundene wasservermittelte Effekt die Hauptrolle in der Feuchtigkeitsverstärkten Haftung spielt.

Ein besonders signifikanter Aspekt dieser Arbeit ist deshalb die Untersuchung der Rolle von Wasser bei der Feuchtigkeitsverstärkten Haftung. Frühere Hypothesen deuteten darauf hin, dass kapillare Kräfte oder Materialaufweichung als Haupttreiber fungieren. Allerdings zeigen unsere Simulationen, dass Wasser-Moleküle die Lücken zwischen Gecko Keratin und der Oberfläche ausfüllen und die Anzahl und Stärke der Anziehungskräfte zwischen diesen erhöhen. Zudem glättet das Füllen der molekularen Lücken die Spatula-Oberflächen-Grenzfläche und vergrößert dadurch die Kontaktfläche. Wir zeigen in dieser Arbeit, dass dieser wasservermittelte Effekt für die beobachtete Zunahme der Klebrigkeit bei höheren Luftfeuchtigkeit verantwortlich ist.

Ein weiterer signifikanter Beitrag dieser Arbeit ist die Entwicklung eines Mesoskalen Modells der Gecko-Spatula, welches experimentelle Spatula-Abzugskräfte reproduzieren kann. Das Modell wurde durch die Kombination eines Bottom-up-Top-down-Ansatzes und der Berücksichtigung des Spatula-Abziehens anstelle der vertikalen Abtrennung entwickelt. Es stellt das erste uns bekannte Modell dar, welches in der Lage ist, experimentelle Gecko Abzugskräfte präzise wiederzugeben.

Wir untersuchen auch die Rolle elektrostatischer Wechselwirkungen bei der Geckohaftung und finden heraus, dass sie für hydrophile Oberflächen relevant sind. Außerdem zeigen wir zum ersten Mal, dass intrakeratin-elektrostatische Wechselwirkungen während des Ablöseprozesses elastische Energie speichern, die erst nach der Abtrennung freigesetzt wird. Diese elastischen Beiträge sind unabhängig vom Wassergehalt und der Oberflächenhydrophilie und haben dieselbe Größenordnung wie van-der-Waals-Beiträge und sind auch bei der Haftung auf trockenen hydrophoben Oberflächen wichtig.

Insgesamt liefert diese Arbeit neue Erkenntnisse zu den molekularen Mechanismen der Geckohaftung und könnte dazu beitragen Gecko-inspirierte Klebstoffe zu Entwickeln, die unter einer Vielzahl von Feuchtigkeitsbedingungen effektiv funktionieren sollen. Unsere Studie betont die

Bedeutung der Berücksichtigung von molekularen Wechselwirkungen und Mechanismen und der Rolle von Wasser bei der Haftung und legt neue Richtungen für zukünftige Forschungen in diesem Bereich nahe.

Abstract

Gecko adhesion has attracted considerable scientific and public attention over the past two decades. Much effort is going into developing mimetics and gecko-inspired adhesives to replicate the gecko's adhesive mechanisms. Although much research has focused on the hierarchical micrometer and submicrometer structures of the gecko foot leading to the extraordinary gecko adhesion, the molecular-level mechanisms have remained largely unexplored. This work presents a novel multiscale simulation approach that allows us to study gecko adhesion at multiple length scales, from the atomistic to the mesoscale. We investigate the effect of humidity, the role of electrostatic interactions, and the impact of surface roughness on gecko adhesion. Finally, we reconcile a long-standing scientific debate regarding the primary mechanism of gecko adhesion under humid conditions, providing clarity and confirming the significant role of a previously undiscovered molecular mechanism in enhancing adhesion.

Our simulations go beyond previous computational and theoretical studies of gecko adhesion, which treated the spatula and surface as continuum bodies and modeled their interaction using the Hamaker theory. Instead, we bridge the gap in our understanding of gecko adhesion by using molecular dynamics simulations to investigate the molecular mechanism, uncovering a previously unknown effect called "water-mediation". This mechanism involves small numbers of water molecules filling the gaps between keratin and the surface and increasing the number of keratin-surface contacts by partially absorbing into the keratin at the interface, thereby increasing the local density and the effective surface energy of the spatula.

Parallel to the endeavor of designing synthetic gecko-inspired adhesives, the remarkable impact of relative humidity (or the presence of water) on the stickiness of gecko spatulae and setae has been discovered. Through single-spatula atomic force microscopy experiments, it was found that the pull-off forces required to separate two surfaces increased with the relative humidity and decreased with the water contact angle of the surface. Despite years of investigation into the adhesion phenomena, the molecular mechanisms behind humidity-enhanced adhesion had remained elusive due to limitations in resolution and length scale. This work addresses this gap by combining molecular dynamics simulations, a true multiscale protocol, with experimental literature, providing a deeper understanding of the molecular mechanisms in gecko adhesion and its response to relative humidity.

The present work extends the understanding of attachment to rough surfaces. It shows that the stickiness decreases as the size of the surface features falls below the spatula contact area. We demonstrate that spatula-softening, the process by which the stiffness of the spatula decreases due to the presence of water, only assists adhesion at near saturation, meaning that the ambient

relative humidity is close to 100%. While previous studies have suggested capillary forces as an alternative mechanism to spatula-softening, superhydrophobic surfaces lack attractive capillary forces. Nevertheless, we still observe increased adhesion under humid conditions compared to dry conditions on superhydrophobic surfaces. We conclude that water-mediation determines humidity-enhanced adhesion on hydrophobic flat and rough surfaces and that spatula-softening assists adhesion when the surface is rough and the ambient relative humidity is well above 80%.

Unlike on hydrophobic surfaces, keratin shows a remarkable difference on hydrophilic surfaces. The folding of polar and charged amino acids towards the hydrophilic surface maximizes electrostatic and van-der-Waals interactions, leading to a stronger attachment, even in dry conditions. The keratin attaches closer to flat hydrophilic surfaces than hydrophobic surfaces, even in dry conditions. These observations suggest that the keratin exhibits a functional-polymer-like ability to selectively change its tertiary structure upon contacting a hydrophilic surface. Moreover, we find that the presence of water enhances adhesion to hydrophilic surfaces due to water-mediated interactions between the keratin and the surface.

Overall, this work provides new insights into the molecular mechanisms of gecko adhesion and may be useful in finding new directions for developing gecko-inspired adhesives that can function effectively under a wide range of humidity conditions, by optimizing for water-mediated adhesion. Our work highlights the importance of considering the molecular-level interactions and the role of water in adhesion and provides a new direction for future research in this field.

Contents

1 Introduction

1.1 Theoretical Background of Gecko Adhesion Research and State of the Art

Geckos have long been a source of fascination for scientists and researchers, thanks to their unique ability to walk and run vertically up walls[1] and cling to ceilings. As the gecko walks over a surface, it uses its feet to stick to the substrate, and while a typical gecko weighs only around 10 to 100 grams, it can overcome around 10 N of force (Figure 1.1). They owe this remarkable stickiness to the hierarchical gecko foot structure. The structure gives geckos the ability to attach their spatulae to various surfaces, making them an ideal subject of study for understanding the mechanisms of dry adhesion.

The multilevel hierarchical structure begins at the millimeter scale, where millions of setae (length ~ 100 µm) are organized on lamellae located on the gecko's toe pads. Fibrils within the setae containing beta-keratin filaments[2, 3] yield hundreds to thousands of spatulae (length ~ 0.1 - 0.5 µm) at their ends.[4, 5] The separation of the setae into smaller contact regions increases the total surface area of contact between the gecko's foot and the substrate, which in turn increases the adhesive forces and enables the gecko to cling to a variety of surfaces, and is known as contact splitting. Immunolocalization by Alibardi[2] found that the Ge-cprp-9 protein, one of the cysteine-rich gecko keratin proteins, is located at the spatula-air interface. The beta-sheet regions of Ge-cprp-9 proteins polymerize into nanofibrils[6] and associate further into fibrils.[3, 5, 7] These macroscopic fibrils are embedded into a matrix and make up the gecko setae.[5] Essentially, around 100 to 1000 fibrils with flattened tips (spatulae) are embedded into a matrix, of yet unknown composition. However, only the fibrils, not the matrix, contact the surface.[8] This nano- to millimeter-scale structure gives geckos the ability to attach their spatulae to various surfaces.[9, 10] The mechanisms underlying geckos' adhesive ability have been investigated for decades[11].

Autumn et al. first inferred in 2000 that spatulae can make close molecular contact with surfaces and that this direct molecular contact is responsible for the strong adhesion.[12, 13] The authors further inferred that van-der-Waals forces drive adhesion. Previous hypotheses were, among others, that frictional forces lead to the ability of geckos to stick.[4]

The gold dust day gecko (*Phelsuma laticauda*) is native to the lush rain forests of northern Madagascar and it is often seen maneuvering its way across leaves (as shown in Figure 1.2 (A,

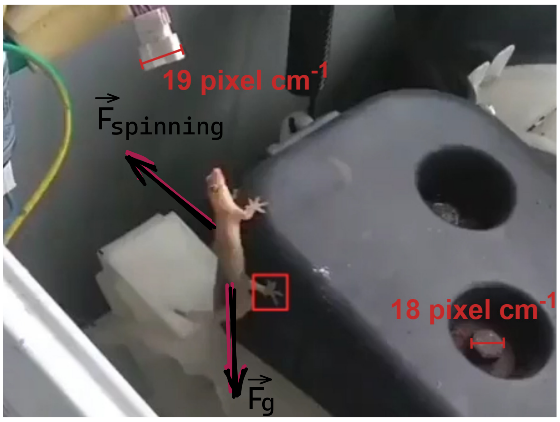

$$\begin{aligned}
x &= A\cos(\omega t)\\
v &= -A\omega\sin(\omega t)\\
a_{\text{spinning}} &= -A\omega^2\cos(\omega t)\\
F_{spinning} &= ma_{\text{spinning}}\\
F_{spinning} &= 0,04\ \text{kg}\cdot 196,25\ \text{m}\,\text{s}^{-2}\\
F_{spinning} &= 7,85\ \text{N}\\
F_g &= 0,39\ \text{N}
\end{aligned}$$

Figure 1.1: A gecko sticking to a tumbling washing machine. (Source of the video: https://www.reddit.com/r/donthelpjustfilm/comments/dpatj4/he_shakin/). We track the position of one of its feet over time. We take estimates of typical lengths of different structures seen in the video. We then fit the tracked position as a function of time with a harmonic oscillator $x = Acos(\omega t + \phi)$. From the tracked position, the amplitude A can be directly extracted. Since the interior looks close to a Siemens-type IQ washing machine, we can reasonably expect that the frequency ω only falls into the range of spin speeds accessible to these machines. The only unknown is then the phase shift ϕ. Thus, by fitting the tracked data using fixed $A = 1.06$ cm and definite spin speeds of 600, 700, ..., and 1600 revolutions per minute (RPM) as initial parameter guesses, we can calculate the errors in both angular frequency and phase shift. The minimum error is found at 1100 RPM. The resulting maximum force the gecko needs to overcome as the surface is pulled away is, thus, between 7 and 8 N. This value is much larger than the gravitational force this type of gecko encounters ($F_g = 0.39$ N). Hence, this gecko will run with ease along ceilings.

B)). Hydrophobic epicuticular wax coats plant leaves. But, geckos adaptability extends beyond just rainforest habitats, as they are also capable of traversing a variety of surfaces, including hydrophilic rocks and boulders, which are commonly found in arid environments. The rock gecko, a member of the genus *Afroedura* within the Gekkonidae family, bears a unique camouflage pattern that exemplifies its ability to move effortlessly on these hydrophilic surfaces, as depicted in Figure 1.2 (C, D)). Since rocks commonly comprise oxides[14, 15] and oxide surfaces are polar, the surface is hydrophilic, which results in small water contact angles. Thus, the most prominent hypothesis about what physical force is responsible for gecko adhesion may depend on **surface chemistry in a balance between van-der-Waals interactions and electrostatics**. Currently, it is thought that electrostatics are not essential[2, 12, 16, 17] or only have minor effects[18].

Furthermore, experimental[17, 19–21] and computational[8, 22, 23] works demonstrate that relative humidity has a significant impact on spatula stickiness, known as **humidity-enhanced adhesion**, which can increase stickiness by up to 300% compared to dry conditions.[8, 19, 21, 22] Experimental work uses atomic force microscopy (AFM) of whole spatulae or setae glued to an AFM cantilever, which is then pulled away from the substrate. The force necessary to detach the adhesive material (the pull-off force) is measured. Past work used AFM to investigate humidity-enhanced adhesion. However, the nature of this experimental method only allows a microscopic investigation and conclusions can only be inferred by clever experimental setups. As a result, the humidity effect is still being debated.[19, 24–26] The most prominent hypothesis[21, 24, 25, 27] states that the change in Young's modulus of gecko keratin upon swelling with water, the so-called **material softening effect**, is responsible for the increased adhesion, as the softer gecko keratin would lead to an increase in the interfacial contact area. Another explanation is the presence of capillary forces between the spatula and the surface.[17, 19] Only very recently, Mitchell et al.[21] inferred that the two hypotheses are not mutually exclusive but coincide depending on the water contact angle of the substrate. The authors[21] believe that capillary forces increase adhesion at hydrophilic surfaces, whereas, at hydrophobic surfaces, material softening is responsible for humidity-enhanced adhesion.

We have so far discussed the adhesion of gecko keratin on flat surfaces; however, in geckos' natural habitat, surfaces are rough. The **influence of surface roughness** on gecko adhesion was first systematically investigated theoretically by Persson and Gorb[28] and later by Huber et al. on the single-spatula level using AFM and macroscale observations in behavioral experiments with freely moving geckos.[10] In experiments, it can be shown that the adhesion force on rough surfaces experiences a minimum in the root mean square roughness (RMS) from 100 to 300 nm[10]. RMS is a measure of the roughness of a surface and is calculated by taking the square root of the average of the squares of the heights of the surface deviations from the mean height. In the context of gecko adhesion, this minimum implies that geckos tend to adhere best to surfaces that are either flat or have an RMS value higher than the characteristic dimension of the spatula pad. This suggests that a combination of spatulae being small enough to follow macroscopic surface asperities and the spatula pad being flexible enough to follow the surface topography are the important factors at rough surfaces.[28, 29]

Besides the theoretical work of Persson and Gorb, a finite element analysis of gecko spatulae on rough surfaces was performed by Sauer et al. in 2011.[30] The finite element method (FEM) uses a meshed representation of a continuum medium. The mesh follows constitutive laws that define the material properties. Consequently, the scope of all behavior is predefined top-down by the investigator. These authors confirmed the previous hypothesis of the spatula being able to follow the surface topography. They showed that spatulae could bend around the asperities for surfaces with a maximum peak to valley distance of 8 nm. However, the material properties of the FEM spatulae did not match experimental realities, particularly the Poisson ratio had no physical basis but was guessed. Its value is 50% of the value derived by our group[3, 8]. Furthermore, the FEM model did not account for anisotropic spatula-internal fibrils.

1.2 Objectives and Structure of this Work

This thesis aims to further our understanding of gecko adhesion and support the field of gecko-inspired synthetic adhesive research through the use of molecular simulations, which have not yet been utilized in the study of gecko adhesion. Prior to this work, the scope of computational studies was restricted to FEM and theoretical work and did not include an explicit molecular treatment. This thesis is the first work to investigate gecko adhesion on a molecular level by means of molecular dynamics (MD) (Section 2.1).

The mechanisms underlying humidity-enhanced adhesion are still debated. The primary objective of this thesis is to elucidate the molecular mechanisms governing the increase in stickiness due to humidity. First, a coarse-grained (CG) model of gecko beta keratin (Section 3.4), previously developed in our group, was extended and adapted to model gecko adhesion on a hydrophobic octadecyl trichlorosilane self-assembled monolayer (OTS-SAM) in both the presence and absence of water. This foundational work shows that neither the change in elasticity nor capillary forces can exclusively explain the increase in pull-off forces at higher relative humidity. Instead, we established the first molecular picture of gecko adhesion, in which a mediator effect of water enhances pull-off forces.[22] Specifically, water molecules fill molecular gaps (≈ 2 nm) between the spatula and the surface and, thus, smooths the spatula-surface interface while increasing the interfacial contact area. This closing of the spatula-surface gaps by water results in an increased number of amino acids near the interface and more van-der-Waals spatula-surface interactions. Additionally, as water accumulates at the surface, it leads to an increase in the total number of interactions.

The coarse-grained gecko keratin model mentioned earlier only considered dispersion attraction (van-der-Waals interactions) and did not account for electrostatics because it was based on the MARTINI force field[35–37]. The model simplifies the amino acid sequence significantly by assuming that all amino acids are equivalent. The model uses an „average amino acid“ interaction site (or bead) for all surface interacting amino acids. Thus, chemical detail is lacking. However, we must confirm how critical the water-mediating effect that we discovered with the CG model is.

Further, the second goal of this thesis is to study the molecular mechanism of gecko adhesion at hydrophobic and hydrophilic surfaces, including the impact of electrostatic interactions. While the CG model did not consider electrostatics, the united-atom gecko keratin model we developed

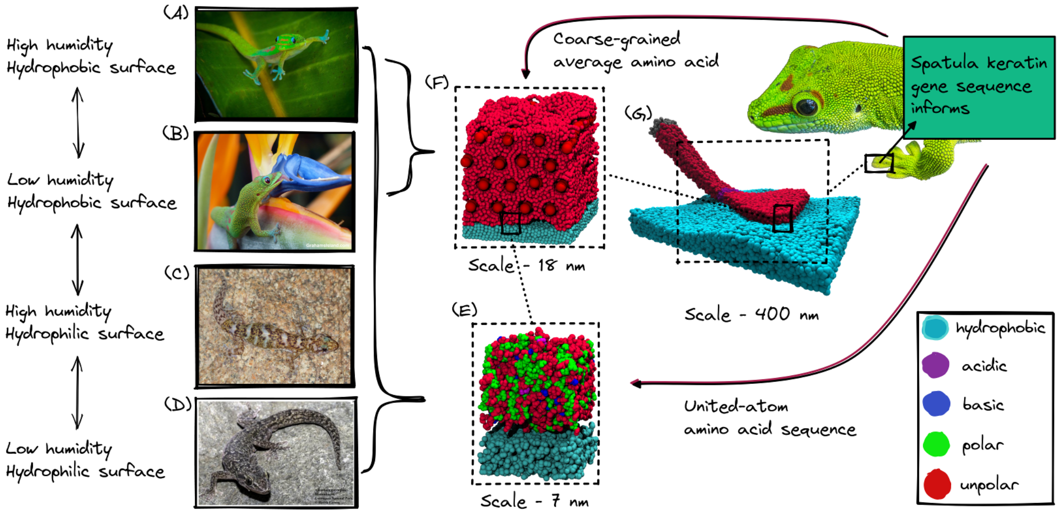

Figure 1.2: Overview of the current work and the relationship of different molecular systems to the multi-scale hierarchical adhesion system and geckos in different environments. The photographs[31–34] on the left show geckos in humid (A, B) and arid (C, D) environments on hydrophobic and hydrophilic surfaces. These habitats are modeled using a united-atom force field **(E)**, as we will discuss later in this thesis: „**How does Gecko Keratin Stick to Hydrophilic and Hydrophobic Surfaces in the Presence and Absence of Water? An Atomistic Molecular Dynamics Investigation**“. The coarse-grained gecko keratin **(F)** models a larger part of the gecko spatula (18x18 nm area). It includes the fibrils located inside the spatula, illustrated in the figure by larger beads. During this work, we first encountered an apparent mechanism of water molecules mediating between surface and spatula. More details can be found in „**Gecko adhesion: a molecular-simulation perspective on the effect of humidity**“. We then modeled the fibrils only intrinsically inside the 400 nm long mesoscale spatula model **(G)** we derived. By matching the stickiness of the dry united-atom keratin model on a hydrophobic surface, we obtained a mesoscale nonbonded field with which experimental pull-off forces are reproducible. Details about spatula stickiness on rough surfaces can be found in „**Gecko Adhesion on Flat and Rough Surfaces: Simulations with a Multi-scale Molecular Model**“. To isolate the softening effect of water from capillary forces and the water-mediating effect, we adapted the mesoscale spatula model to mimic water content implicitly. In „**Understanding Humidity-Enhanced Adhesion of Geckos: Deep Neural Network-Assisted Multi-Scale Molecular Modeling**“, we could prove that keratin softening cannot solely explain the humidity-enhanced adhesion on hydrophobic surfaces. The coarse-grained gecko keratin model is apolar. Chemical details were only introduced with the united-atom gecko keratin model that was used to coarse-grain the mesoscale model. In summary, this thesis developed and utilized multiple molecular models to investigate the hierarchical structure of gecko keratin and its adhesive properties on various surfaces in different environments. The findings suggest that water content, surface chemistry, and surface roughness play critical roles in gecko adhesion.

includes atomic partial charges. Thus, we can examine polar amino acids at the hydrophobic and hydrophilic surface and analyze how water bounds to keratin or the surface.

By developing a more precise model of gecko keratin in a united-atom representation (Section 3.2), we were are able to confirm the water-mediating effect at the hydrophilic and hydrophobic surface. The water contact angles of the two surfaces correspond to those used in AFM experiments.[19] In agreement with these experiments, we found the stickiness (Section 2.3) of the united-atom gecko keratin model to be inversely related to the water contact angle and proportional to the water content. We decomposed energetic contributions during the pull-off process of keratin from both surfaces. Interestingly, electrostatic interactions dominate the process through long-range elastic contributions even at the hydrophobic surface.

Although the trend of stickiness as a function of relative humidity or water contact angle and their relative increase agrees with the experiment, the absolute values show a large discrepancy. In our simulations, a keratin sample is pulled vertically-flat off a surface. By normalizing the force required to detach a periodic keratin sample by its area and extrapolating the resulting pull-off pressure to an actual spatula size, the force was overestimated by two to three orders of magnitude. In reality, the spatula pad is peeled off successively from the surface and not all at once. However, a peel-off geometry is impossible with periodic boundary conditions (Section 2.2). We hypothesized that this discrepancy in geometry is responsible for overestimating the adhesion force and, therefore, we developed a mesoscale spatula model to test our hypothesis.

The mesoscale model (Section 3.3) resembles an actual spatula shape and reproduces the pull-off pressure of the UA keratin model. Young's modulus and Poisson's ratio of the UA and CG keratin models are likewise reproduced. Utilizing this mesoscale geometry, we show that our hypothesis was correct and that the peel-off geometry reproduces AFM experimental pull-off forces (approximately 10 nN per spatula). Since the mechanical properties of the mesoscale model are easily adapted, we implicitly model the effect of water content (or relative humidity) on the spatula softness to study the two remaining objectives: the influence of surface roughness and the material softening effect.

This thesis is constructed as follows: Chapter 1 provides an overview of gecko adhesion research and outlines the motivation for this work. In chapter 2, the most relevant concepts and methods are introduced. My (peer-reviewed) journal articles are presented in chapter 3. They are ordered, beginning with the work that pulls all individual projects together (Section 3.1, Figure 1.2 (G)) and corroborated by results of the united-atom gecko keratin study (Section 3.2, Figure 1.2 (E)), the development of the mesoscale model (Section 3.3, Figure 1.2 (G)) and backed up by the fundamental findings of the coarse-grained investigation (Section 3.4, Figure 1.2 (F)). The results of the coarse-grained investigation (Section 3.4) are largely reproduced in the united-atom gecko keratin study (Section 3.2).

2 Methods

2.1 Molecular Dynamics Simulations

Molecular dynamics (MD) is a method to simulate a system of N-particles at the molecular scale. The approach MD takes is to solve Newton's equation of motion (EOM) to compute the time evolution of a system of particles, the trajectory. In MD, the EOMs are solved iteratively at predetermined time steps.[38] For atom i, the EOM is

$$\frac{\mathrm{d}^2 \vec{r}_\mathrm{i}}{\mathrm{d}t^2} = \frac{\vec{F}_\mathrm{i}}{m_\mathrm{i}} \tag{2.1}$$

where $\vec{r}_\mathrm{i}$ is the position of the particle i, m_i is the mass of the particle i and $\vec{F}_\mathrm{i}$ is the force acting onto the particle due to interactions with the surrounding particles or an external field. Since the Born-Oppenheimer approximation allows us to treat the motion of electrons and atomic nuclei separately and the degrees of freedom of individual electrons are neglected, atoms can be modeled by point masses, and one-dimensional interaction potentials are used. Interactions are separated into bonded and nonbonded interactions.[39] Bonded interactions model covalently connected atoms within one molecule, like the 4-body dihedral, the 3-body angle and the 2-body bond, via a potential function. A harmonic potential often describes covalent bonds between atoms in the form of

$$U_\mathrm{bond}(r_\mathrm{ij}) = \frac{1}{2} k_\mathrm{ij} \left(r_\mathrm{ij} - b_\mathrm{ij}\right)^2 \tag{2.2}$$

where $U_\mathrm{bond}(r_\mathrm{ij})$ is the one-dimensional interaction potential of two covalently bonded atoms i and j. The force constant k_ij describes the strength of interaction between these two specific atoms, and b_ij is the constant equilibrium bond length. Finally, r_ij is the distance between both atoms.

In contrast to bonded interactions, nonbonded interactions are assumed to be pairwise additive and, hence, only describe 2-body interactions. While the parameterization of many-body nonbonded interaction potentials is difficult, the time spent to compute 2-body nonbonded interactions is already the primary reason why MD simulations are restricted to 10^6 to 10^8 steps, making the use of many-body nonbonded potentials also computationally impractical. The omission of interactions described by more than two bodies has its most notable effect in neglecting polarizability, which in turn leads to a false screening of electrostatic interactions. In MD, the Coulomb potential describes electrostatics. The well-known van-der-Waals (dispersion) interactions are described by a Lennard-Jones potentials, i.e,

$$U_{\mathrm{vdW}}(r_{\mathrm{ij}}) = 4\epsilon \left[\left(\frac{\sigma}{r_{\mathrm{ij}}} \right)^{12} - \left(\frac{\sigma}{r_{\mathrm{ij}}} \right)^{6} \right] \tag{2.3}$$

where ϵ is the dispersion energy and σ the excluded volume radius. Essentially, all MD interactions use parameters to calculate energies and forces, and the set of these parameters is called a force field.

2.2 Periodic Boundary Conditions

A periodic boundary is an essential method in molecular dynamics simulations. Periodic boundary conditions (PBC) are, in this work, primarily required to remove surface effects any finite-sized sample has. Surface effects dominate the internal structure of small volumes (surface tension of a small drop of water leads to a spherical shape). The usage of PBC in molecular dynamics simulations consisting of only a few atoms can mimic infinite volumes; thus, bulk properties are accessible.

Figure 2.1 illustrates the idea of two-dimensional periodic boundary conditions using the coarse-grained gecko keratin model. Here, only the red-colored keratin sample is the system we consider - the simulation box. The surrounding gray-colored boxes are copies of the simulation box where all particle positions are copied over the periodic boundary. Thus, if one of the nanofibril segments moves, all copies of this segment move likewise.

Every time a particle leaves the simulation box and crosses the periodic boundary, it is replaced with its image particle entering from the opposite side of the simulation box with the same velocity. The number of atoms in the cell is therefore conserved.

Since, according to these boundary conditions, particles are duplicated an infinite number of times, interactions between particles may be double-counted. To circumvent double-counting, the minimum-image convention remarks that an interaction cutoff cannot be greater than half the shortest simulation box length. Therefore, particles only interact with the closest image.

Two-dimensional PBC are used in this work to make the keratin periodic parallel to the surface (Figure 2.2) and model a larger keratin volume. Thus, only a keratin-surface and keratin-vacuum interface exists. The consequence of a periodic semi-infinite keratin sample on top of a surface is that during pull-off, the keratin is pulled flat-on-flat off the surface. This flat-on-flat pull-off greatly increases pull-off force[30] and makes a comparison to experimental pull-off forces difficult. The mesoscale spatula is of actual real spatula size and shape and does not need PBC to model a larger volume. Hence, pull-off forces are not overestimated by an artificial flat-on-flat pulling geometry and can be compared directly to AFM experiments.

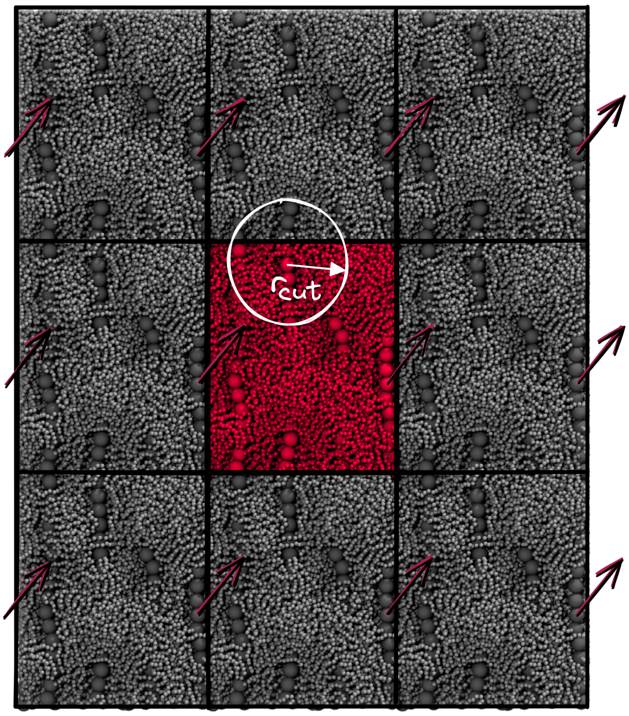

Figure 2.1: Illustration of the two-dimensional periodic boundary conditions of the coarse-grained gecko keratin. The box with the simulated keratin sample (red) is surrounded by mirror images (grey). An interaction cutoff is illustrated for one of the nanofibril segments (white). The arrows indicate an illustrated movement of a particle across the periodic boundary enforced by its topology.

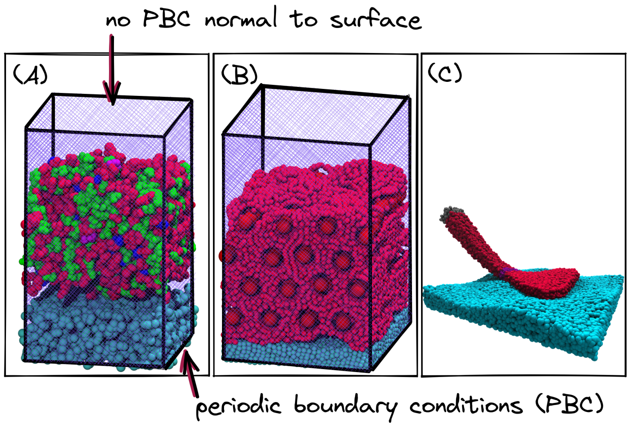

Figure 2.2: Periodic boundary conditions (PBC) are parallel to the surface (A) in the united-atom gecko keratin model and (B) the coarse-grained gecko keratin model. The systems are not periodic in the dimension normal to the surface. In essence, periodic boundary conditions are only used in the x and y dimension. (C) The mesoscale spatula model does not utilize PBC.

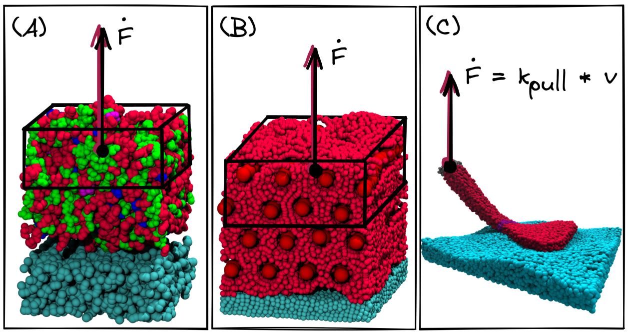

Figure 2.3: During pull-off simulations, a harmonic potential links the center of mass of a part of the keratin to a virtual cantilever that moves vertically away from the space-fixed surface. (A) The united-atom gecko keratin model is shown on a hydrophobic surface (cyan). (B) The coarse-grained gecko keratin model is shown, with its nanofibers exposed, attached to a hydrophobic surface. (C) The mesoscale spatula model is depicted on a hydrophobic rough surface.

2.3 From Non-Equilibrium Pulling to Adhesion: Force Probe Molecular Dynamics with Gecko Keratin

To measure the stickiness, or pull-off force of gecko keratin, we used force probe molecular dynamics (FPMD). We computed the force necessary to detach gecko keratin from a space-fixed hard surface.

In resemblance to atomic force microscopy (AFM) experiments of gecko setae and spatulae[40], the keratin is first preloaded against the surface. While experimental work needs to then shear the spatula over the surface to make molecular contact between the spatulae and the surface, we can directly place the keratin close enough to the surface that a short preload is sufficient for direct contact. The keratin is preloaded until the distance to the surface converges. In AFM experiments, the external force is removed, and the spatula is pulled off the surface. We simulate this switch by removing the preload force and running our simulations until the keratin-surface distance converges. We assume the time spent during an experiment to switch between the preload and the subsequent pull-off is large enough to yield equilibrium.

In the subsequent pull-off simulation, the attached keratin is pulled away from the surfaces by linking either the center of mass (COM) of the top half of the keratin (Figure 2.3 (A, B)) or the spatula shaft haft COM (C) to a virtual cantilever. AFM cantilever bending is modeled by a harmonic potential with a force constant (k_{pull}). The cantilever is moved away from the surface at a constant pulling velocity, normal to the surface. The spring constant and the pulling velocity result in a theoretical[41] loading rate $\dot{F}$. As the virtual cantilever is moved away from the surface, the force steadily increases until a maximum in the force-displacement (or force-time) curve occurs, the so-called pull-off force (Figure 2.4). The pull-off force is the negative of the adhesion force and describes the maximum force with which the keratin can stick to the surface.

Moving the virtual cantilever away from the surface at constant velocity, as the keratin sticks to the surface, leads to a linear increase in force $F_{\text{cant}} = k_{\text{pull}}(vt)$, with v being the pulling velocity

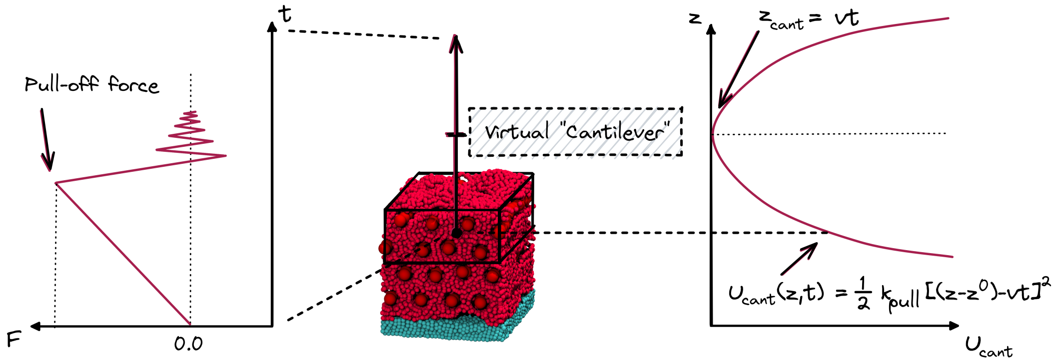

Figure 2.4: The schematic representation illustrates the pull-off simulation, where the keratin is connected to a virtual cantilever and pulled away from the surface at a constant velocity. The simulation results in a steadily increasing force on the keratin sample until the maximum force (pull-off force) is reached. The potential due to the cantilever (U_{cant}) is shown on the right side. The cantilever bending is modeled by a harmonic potential with force constant k_{pull}. The center of mass of the top keratin layer is subjected to a potential energy given by $U_{\text{cant}}(z,t) = \frac{1}{2}k_{\text{pull}} \cdot [(z - z^0) - vt]^2$, where z is the center of mass of the top keratin layer, z^0 is the center of mass position at the start of the simulation, v is the pulling velocity (the velocity with which the virtual cantilever moves away from the surface), and t is the time. The resulting force experienced by the keratin sample increases linearly with time until the keratin detaches.

and t the time. The force experienced by the keratin is $F = k_{\text{pull}}(z(t) - vt)$, where $z(t)$ denotes the position of the linked center of mass in the dimension of pulling (normal to the surface) and is measured relative to the position of the linked center of mass at the start of the simulation, denoted as z^0 in Figure 2.4. Fluctuations in the raw force profile F are a result of the resonance frequency of the harmonic spring[41] and due to thermal fluctuations of the atoms. These fluctuations are artifacts that are smoothed with a Gaussian filter by convolution of the signal with a Gaussian function with a kernel width respective of 0.1 nm, inspired by Sheridan et al.[42]

FPMD is a non-equilibrium MD method that is most commonly used to elucidate unfolding pathways[42] or receptor-ligand unbinding[43] processes. In contrast, we use FPMD simulations to study the stickiness of gecko keratin. Since we were not interested in the details of the underlying average free energy landscape, we save resources by using fewer simulations.

3 Results

3.1 Understanding Humidity-Enhanced Adhesion of Geckos: Deep Neural Network-Assisted Multi-Scale Molecular Modeling

Reproduced with permission from Materzok et al. [Small 2023] Copyright 2023 Wiley.

RESEARCH ARTICLE

NANO · MICRO small

www.small-journal.com

Understanding Humidity-Enhanced Adhesion of Geckos: Deep Neural Network-Assisted Multi-Scale Molecular Modeling

Tobias Materzok, Hossein Eslami, Stanislav N. Gorb, and Florian Müller-Plathe*

A higher relative humidity leads to an increased sticking power of gecko feet to surfaces. The molecular mechanism responsible for this increase, however, is not clear. Capillary forces, water mediating keratin-surface contacts and water-induced softening of the keratin are proposed as candidates. In previous work, strong evidence for water mediation is found but indirect effects via increased flexibility are not completely ruled out. This article studies the latter hypothesis by a bottom-up coarse-grained mesoscale model of an entire gecko spatula designed without explicit water particles, so that capillary action and water-mediation are excluded. The elasticity of this model is adjusted with a deep neural network to atomistic elastic constants, including water at different concentrations. Our results show clearly that on nanoscopic flat surfaces, the softening of keratin by water uptake cannot nearly account for the experimentally observed increase in gecko sticking power. Here, the dominant mechanism is the mediation of keratin-surface contacts by intervening water molecules. This mechanism remains important on nanostructured surfaces. Here, however, a water-induced increase of the keratin flexibility may enable the spatula to follow surface features smaller than itself and thereby increase the number of contacts with the surface. This leads to an appreciable but not dominant contribution to the humidity-increased adhesion. Recently, by atomistic grand-canonical molecular dynamics simulation, the room-temperature isotherm is obtained for the sorption of water into gecko keratin, to the authors' knowledge, the first such relation for any beta-keratin. In this work, it relates the equilibrium water content of the keratin to the ambient relative humidity.

1. Introduction

Geckos can climb vertically[1] and even upside down on flat[2–4] and rough[5,6] hydrophobic and hydrophilic surfaces. Hundreds of sticky spatulae at the end of billions of setae on their toes form direct contact with surfaces.[2] This direct molecular contact with the surface leads to van der Waals interactions on hydrophobic surfaces resulting in excellent adhesion.[2] Furthermore, experimental[3,7–9] and computational[10,11] works show a link between relative humidity and increased adhesion. Compared to dry spatulae, humidity can enhance the stickiness by up to 300%.[10] In experiments, the spatulae have been attached to surfaces and pulled off using atomic force microscopy (AFM), allowing only investigations of micrometer resolution. As a consequence, the humidity effect is still intensively debated.[3,4,12,13] Some authors[9,12–15] believe that the change in the Young modulus of gecko keratin upon swelling, so-called material softening, is responsible for the humidity-enhanced adhesion. Capillary forces induced by absorbed water on the surface are another explanation for the enhanced adhesion.[3,7] Mitchell et al.[9] recently inferred that the two mechanisms are not mutually exclusive: while capillary forces increase adhesion on hydrophilic surfaces, material softening increases stickiness on hydrophobic surfaces.

Recently, we have put forward a different explanation for humidity-enhanced adhesion: water fills gaps between the spatula and the surface and smoothes the spatula-surface interface.[10] It locally increases the number density of keratin at the surface and facilitates more van der

T. Materzok, H. Eslami, F. Müller-Plathe
Eduard-Zintl-Institut für Anorganische und Physikalische Chemie
and Profile Area Thermofluids and Interfaces
Technische Universität Darmstadt
Alarich-Weiss-Str. 8, D-64287 Darmstadt, Germany
E-mail: t.materzok@theo.chemie.tu-darmstadt.de

The ORCID identification number(s) for the author(s) of this article can be found under https://doi.org/10.1002/smll.202206085.

DOI: 10.1002/smll.202206085

H. Eslami
Department of Chemistry
Colleges of Sciences
Persian Gulf University
Boushehr 75168, Iran

S. N. Gorb
Zoological Institute Functional Morphology and Biomechanics
Kiel University
Am Botanischen Garten 1-9, D-24118 Kiel, Germany

Waals interactions with the hydrophobic surface.[11] We call this the water mediating effect.[10,11] Water mediating is distinctly different from capillary forces as it does not refer to a water volume but water molecules that form bridges between surface and spatula. Water molecules stick to the hydrophilic keratin protein and fill surface-spatula gaps, making the interface smoother. Water mediation is present even at low humidities and its effect on adhesion may follow a sigmoidal function, as we will discuss later. Furthermore, as the water mediation does not require an entire layer of adsorbed water as the capillary hypothesis does[3,7,16] but on individual water molecules, this effect can explain humidity-increased adhesion even at very hydrophobic surfaces.

Complementary to experiments, molecular dynamics (MD) simulations provide detailed atomistic-level information about the system. This allows us to elucidate underlying processes during spatula pull-off. To this end, we have done coarse-grained[10] (CG) and united-atom[11] (UA) simulations to confirm the water mediating effect. Furthermore,[17] we have developed a mesoscale model of a whole spatula, which reproduces pull-off pressure, Young's modulus, and Poisson's ratio of the UA keratin model. The mesoscale spatula model comprises particles (beads randomly distributed) in an actual spatula shape, acquired by scanning electron microscopy imaging of Xu et al.[18] In the mesoscale model, each bead maps five whole keratin molecules into a single interaction site. We tuned the anisotropic bonded force field that harmonically connects each bead with at least 30 neighboring beads to yield the material properties of the dry UA keratin. We then parameterized the spatula-surface Lennard–Jones interaction to replicate the UA keratin pull-off pressure (at a specific loading rate). We have shown before that the mesoscale spatula model reproduces AFM single-spatula experimental pull-off forces[3,5,7] (≈10 nN) when extrapolated to loading rates typically used in these experiments.[17] The validation of the mesoscale spatula model is a significant new result, as no other prior work exist that reproduced experimental spatula pull-off forces in a bottom-up manner.

In the simulations explained above, the presence of water molecules may lead to material softening, capillary forces, and the water mediating effect. In the present work, we isolate the effect of water-induced material softening on the pull-off force from capillary forces and the water mediating effect. We explicitly do not simulate water molecules to investigate the effect of spatula softness without water molecules being present but set the elasticity of the keratin to the same values it would have if it contained water. In this way, we can separate the two possible mechanisms by which water leads to enhanced adhesion: 1) through mediation by water molecules (explicitly excluded here) and 2) through a water-induced flexibility increase in the keratin (included here).

Since the relationship between water content (solubility) in spatula gecko keratin and the ambient relative humidity is experimentally not known, we previously[19] computed it using our united-atom keratin model. Subsequently, we tune the mesoscale anisotropic force field to reproduce, without water molecules present, the reduced Young modulus, which is normally due to water-induced softening.[12] The value of Young's modulus of water-loaded keratin, we have previously obtained in the united-atom reference model.[11] Therefore, any change in stickiness upon adding water to keratin can be attributed to the material softening effect but not to the capillary forces and/or the water mediator effect.

We extend the mesoscale model with four additional, deep neural network-derived, bonded force fields, which implicitly model different water contents. The spatulae are linked to a virtual cantilever and pulled away from surfaces with constant velocity to mimic the AFM experiments. The mesoscale surface model was developed previously[17] to simulate hydrophobic crystalline surfaces of tuneable roughness. We establish the first link between relative humidity, the water content in the keratin, the change in elasticity and material softening-induced adhesion.

2. Methods and Models

2.1. United-Atom Gecko Keratin Model

Our previously developed united-atom (UA) gecko keratin model is based on the GROMOS 54A7 force field.[20–23] It is made up of an amorphous gecko beta-keratin protein (Ge-cprp-9), where only the intrinsically disordered parts of the protein are considered. It was assumed that only intrinsically disordered protein regions (IDRs) directly contact the surface and are responsible for the adhesive energetic interaction between spatula and surface.[11] The water model is SPC/E.[24] Section S2 (Supporting Information) summarizes some simulation details, which are discussed in more detail elsewhere.[11]

Previously, we computed Young's modulus, E, and Poisson's ratio, ν, for the dry UA gecko keratin system (0 wt.% of water) and a system of wet keratin containing 10 wt.% water.[11] Here, we simulate two additional wet keratin systems containing: 5 and 20 wt.% water, and we compute E and ν for both new water contents. **Table 1** summarizes all UA-derived E and ν.

Experimentally reported Young's moduli range from 1.2 GPa in nanoindentation tests to 7.3 ± 1.0 GPa during in situ tensile

Table 1. The calculated Young' moduli and Poisson' ratios of keratin-water mixtures at different water contents. The subscripts ”UA” and ”meso” refer to calculations using united-atom and mesoscale models, respectively. The water contents are connected to relative humidity (RHs) according to the results presented in **Figure 1**. Computations are performed as described in the united-atom gecko keratin work[11] and the mesoscale work.[17]

wt.%	RH [%]	E_{UA} [GPa]	ν_{UA}	E_{meso} [GPa]	ν_{meso}
0	0	4.53	0.409	4.529 ± 0.033	0.409 ± 0.002
5	52	4.03	0.437	4.038 ± 0.045	0.435 ± 0.002
10	86	3.84	0.423	3.838 ± 0.040	0.422 ± 0.002
20	100	2.28	0.475	2.247 ± 0.025	0.496 ± 0.004

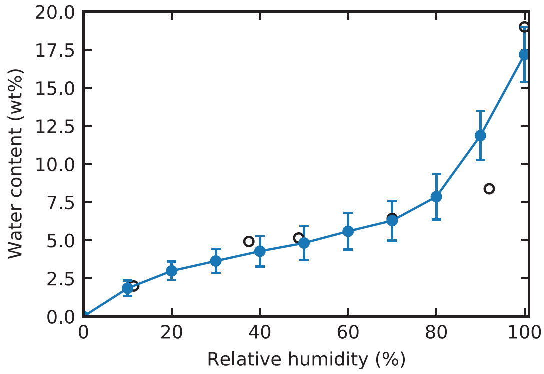

Figure 1. Water content of gecko keratin, as a function of relative humidity, calculated using our united-atom gecko keratin model.[11] The filled (blue) and open (black) markers are the results of the grand canonical ensemble simulations[19] and experimental data for the dorsal and ventral scales of the snake *Naja nigricollis*, respectively, and the curve connects the calculated points. Error bars are the root-mean-square deviation of concentration of water in keratin from the average value.

tests.[14] Humidity affects the elasticity of setal keratin, as 30% relative humidity yields $E = 3.2 \pm 0.2$ GPa and with increased humidity of 80% Young's modulus decreases to 2.2 ± 0.2 GPa.[12] In a computational model, previously developed in our group, dry seta keratin was found to be rather stiff with $E = 9.2$ GPa.[25] The Young moduli of the UA dry and wet spatulae are, therefore, within the range of experimental values.

2.2. Water Solubility in Gecko Keratin

The details of the calculation of water solubility in gecko keratin, as a function of RH, are reported elsewhere.[19] Here, we only report a summary, which is needed to understand the essential elements of the method. We performed MD simulations in the grand canonical ensemble (GCE) to find the phase coexistence point (vapor pressure of water and equilibrium density of water in the keratin phase) at 300 K. In the GCE simulation method,[26] the system (keratin plus water) couples to an ideal gas reservoir of water molecules through a coupling parameter. A fractional molecule, whose potential energy of interaction with the rest of the system is scaled with the coupling parameter, is added to the system, and the equation of motion for the coupling parameter is solved. The coupling parameter varies dynamically between 0 and 1; when it reaches 0, a water molecule is removed from the system. When it reaches 1, the fractional water molecule becomes a fully coupled molecule. In equilibrium, the number of water molecules in the keratin phase fluctuates around an average value, consistent with the imposed conditions (fixed chemical potential, temperature, and volume). Because adhesion and gecko keratin softening by water uptake depends on the water content inside keratin and its relation with the RH, we reproduce our calculated sorption isotherm of water in gecko keratin[19] in Figure 1. We have also shown in Figure 1 our experimental data on the water uptake of dorsal and ventral scales of the snake *Naja nigricollis* and the claw tips of the Tokay gecko (*Gekko Gecko*) toes (≈30 g water/100 g sample at 100% RH) at 297 K and 100% RH. The calculated sorption isotherm has a general sigmoidal shape, consistent with that for water sorption in α-keratin.[27,28]

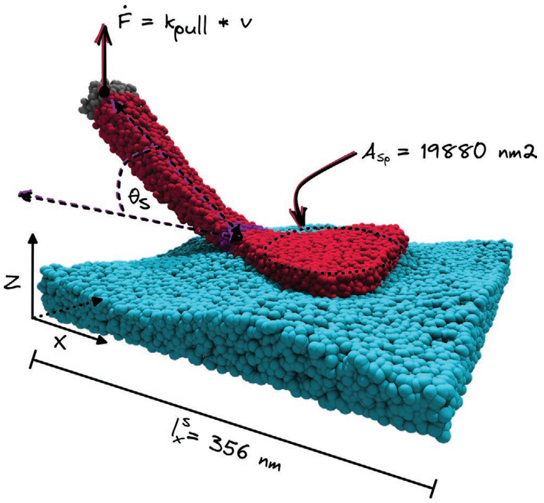

Figure 2. Snapshot of the mesoscale spatula (red) on a rough hydrophobic surface (cyan). During pull-off simulations, a virtual cantilever is linked to the shaft haft and pulled vertically with loading rate $\dot{F}$, to mimic atomic force microscopy experiments, as we discuss in Section 2.6.

2.3. Mesoscale Spatula Model

The spatula model (**Figure 2**) uses the previously derived mesoscale keratin force field[17] that was validated against experimental single-spatula AFM experiments with typical pull-off forces in the range of 8–20 nN[3,5,7] when used with an actual spatula shape. The experimental setup used in AFM studies to investigate single-spatula pull-off forces is shown in Figure S1 (Supporting Information). The elastic and structural properties of the spatula are modeled with a simple bead spring model with directional force constants to mimic the fibrillar structure present in gecko spatulae.[10,11,17,25,29–31]

The beta-sheet region (Core-box region[30,31]) of the Ge-cprp-9 peptide (which, in the united-atom simulation of keratin, was omitted, see Section 2.1) forms dimers. The dimers polymerize into nanofibrils,[32] which associate to mesoscale fibrils.[25,29,30] These fibrils are visible in scanning electron microscopy (SEM) cross sections of gecko setae, and the spatula is possibly made up of almost pure fibrils.[29] The fibrils significantly contribute to the mechanical properties of gecko spatulae. Consequently, the model must describe the anisotropic elasticity arising from fibrils inside the spatula. Since the spatula model consists of randomly distributed, highly coarse-grained beads that each incorporate the mass of about five keratin proteins, we have to model the fibrils implicitly.[17] The bead-bead harmonic bond potential is expressed as $V(r) = K/2 \cdot (r - b_0)^2$, b_0 and K being the equilibrium bond length and the force constant, respectively. For each bond, these parameters are unique. Once assigned, all K and b_0 stay unchanged. The value of K increases, as the initial direction of a bond aligns with the direction of the "virtual" fibril:

$$K = k + k_b \cdot |\cos\theta| \tag{1}$$

where k and k_b are the isotropic part of the force constant and the force constant in the fibril direction, respectively, and θ is the angle between the bond vector and the "virtual" fibril direction. Hence, the spatula model implicitly accounts for fibrils due to the anisotropy of the bonded potential. The potential is adjusted such that in equilibrium, the spatula shaft is bent by $\theta_S = 45$ degrees with respect to the surface (Figure 2). The effect of pre-bent spatulae on the adhesion is discussed elsewhere.[17]

A Lennard–Jones (12–6) potential models the adhesive interactions with the surface, as is discussed in more detail in the previous work.[17] The spatula-surface interaction was parameterized against the pull-off pressure (pull-off force normalized by the area) of the dry UA gecko keratin model.[11]

The mesoscale keratin model was optimized against the material properties of the dry UA gecko keratin model in our previous work.[17] We here extend the mesoscale spatula model and optimize k and k_b against properties of wet keratin at different implicit relative humidities using a deep neural network (see Section 2.5). We do not change the spatula-surface interaction, and the mesoscale model does not include water particles. As a result, any changes in stickiness are uniquely due to the changed elastic material properties. This allows us to isolate the effect of keratin softening from capillary forces and the water mediating effect.[10,11]

2.4. Mesoscale Surface Models

The mesoscale spatula is attached to and detached from hydrophobic surfaces (water contact angle $\theta_c \approx 110°$) of varying roughnesses which are modeled by a particle model of similar beads size.[11,17] The surface follows a two-dimensional sinusoidal topography and has the same density as the spatula material. The minimum thickness z_m of the slab representing the surface is always 24 nm. The 3D landscape is defined by $z_m = 24\,nm + 8\,nm \cdot \sin(x \cdot \pi n_p / l_x^s + \pi X_x) \cdot \sin(y \cdot \pi n_p / l_y^s + \pi X_y)$, where 8 nm is the peak height, n_p is the number of peaks in the x- and y-direction, and l_x^s and l_y^s are the lengths of the surface in the x- and y-directions, respectively.

To simulate random placements of the spatula on top of a surface (see **Figure 3**), we apply a random phase shift using a uniformly distributed random number $X \sim U([0, 2])$ in the x and y directions. We generate eight surfaces with peak densities ρ_p ranging from $\rho_p = 0$ to 394.12 µm^{-2}. The surface has an area of 356 nm × 356 nm.

We expect a surface describing an oxide mineral (e.g., the amorphous silica substrate of Huber et al. used in the UA model) not to be deformable. Such a surface is orders of magnitude stiffer than gecko keratin. Thus, we choose to make our surface entirely rigid. Therefore, surface beads are frozen and only interact with the keratin. As a result, the surface acts as a space-fixed attractive 3D external potential.

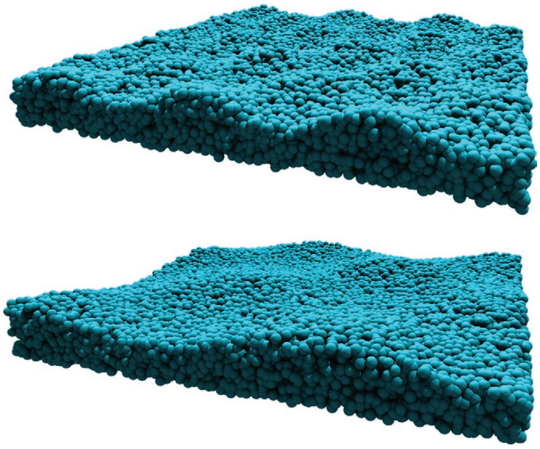

Figure 3. Two surfaces with different peak densities (top $\rho_p = 141.88$ µm^{-2} and bottom $\rho_p = 39.41$ µm^{-2}). The center of the surface (where the spatula attaches), can present anything between a valley and a peak, depending on phase shift. The height between the peak and valley (amplitude) is 16 nm for all surfaces, resulting in a root-mean-squared roughness of 4 nm.

2.5. Parameterizing the Mesoscale Spatula Model with Implicit Water Contents

The "wet" mesoscale spatula model should explicitly only reproduce the change in material properties due to water-induced material softening. We, thus, optimize only the isotropic part, k, and the anisotropic part, k_b, of the bond force constant K (Section 2.3) against the elastic properties of wet keratin as determined from united-atom simulations (Section 2.1). We create four bonded force fields that reproduce Young's modulus and Poisson's ratio at 0, 5, 10, and 20 wt.% water contents.

We use existing parameter-exploration simulations of the previous work[17] to train a deep neural network (DNN). Grid search-based hyperparameter tuning yields a network architecture that does not overfit. The DNN feeds the input vector (of the two scalars) k and k_b to a fully connected layer (6x64) and subsequently an output layer (1×2). The output layer maps to Young's modulus E and Poisson's ratio ν of the mesoscale keratin. The DNN generalizes the regression between the inputs and the outputs well and performs better in the prediction of E than a bilinear fit of E against the scalars k and k_b. In Section S1 (Supporting Information), a detailed description of the DNN can be found (source code and DNN weights are available at github.com/TobiasMaterzok/DNN-Gecko-Implicit-Water).

We use the DNN to predict the force constant coefficients k and k_b corresponding to the material properties of wet keratin (computed using the united-atom keratin model, Section 2.1) to model the water content in the mesoscale spatula implicitly. **Figure 4** shows the DNN-interpolated solution landscape. Black dots represent actual simulations performed during the previously discussed parameter exploration.

The DNN derived anisotropic force constant coefficients (summarized in Table S1, Supporting Information) are validated by stress-strain simulations (details in Section S2, Supporting Information). Strains of 0%, 1%, and 2% are applied in the

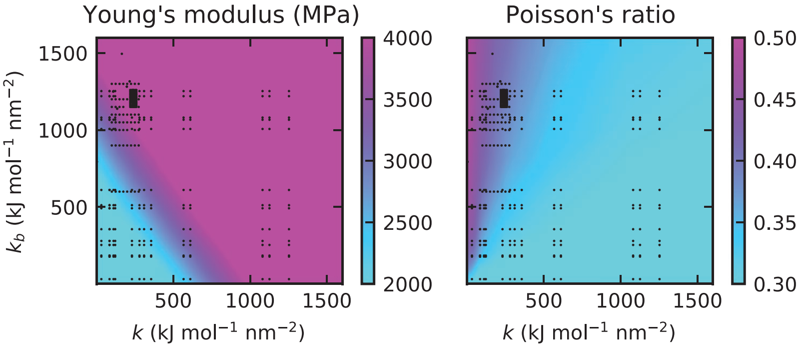

Figure 4. Result of the deep neural network prediction of Young's modulus E and Poisson's ratio ν from the force constant coefficients k and k_b. Black dots are actual simulations done previously,[17] during our parameterization of the dry spatula model. The black dots are denser in the upper left corner as we have tuned the search space to find the values corresponding to $E = 4.5$ GPa and $\nu = 0.4$ of corresponding to dry gecko keratin.

(virtual) fibril direction for ten independently created keratin systems for each coefficient combination (4×10 simulations in total) to compute E and ν. The method is described in our previous work.[17]

As a result, we can relate Young's modulus and Poisson's ratio of the UA keratin (Section 2.1) and mesoscale spatula model (this section) to the water content (and relative humidity) (Section 2.2), as summarized in Table 1.

2.6. Spatula Detachment Simulations

Gecko spatulae attached to surfaces can be inclined (inclination angle θ_S, Figure 2), and in experimental imaging, a whole range of possible inclinations have been observed.[33,34] In previous work,[17] we tested $\theta_S = 45°$ to $\theta_S = 75°$ and found a direct relationship between the pull-off force and θ_S. The smallest pull-off force was found for $\theta_S = 45°$, and it also had the smallest standard deviation.

We use the bent equilibrium configurations of spatulae of the previous work (with an inclination of $\theta_S = 45°$) to perform non-equilibrium pulling simulations.[17]

A preload is applied for 600 ns to initially attach the spatula to the surface. In this preload step, an external pressure of 0.4 pN nm^{-2} presses the spatula pad against the surface, as was done in the experiment by Xu et al.[18] After the preload, the system is allowed to relax for 500 ns without any external force. These simulation times are sufficient to converge the distance between spatulae and surfaces.

In the pull-off simulations, the attached spatulae are pulled away from the surfaces by linking the center of mass of the spatula shaft haft (Figure 2) to a virtual cantilever. The link is modeled by a harmonic potential with a force constant of $k_{\text{pull}} = 1000$ kJ mol^{-1} nm^{-2}. The virtual cantilever is moved at a constant pulling velocity vertically away from the surface. The harmonic potential of the linker and the pulling velocity results in a theoretical[35] loading rate of 1.66×10^{12} pN s^{-1}. At the pull-off force, which is the maximum in the force-displacement (or force-time) curve, the spatula detaches from the surface.

A vacuum surrounds the surface and the spatula. All spatula detachment simulations are performed in the NVT ensemble with a thermostat keeping the temperature of the spatula constant at 300 K. The preload step uses a stochastic dynamics (SD) thermostat[36] with $\tau_T = 1$ ps; the relaxation step uses SD with $\tau_T = 10$ ps; and all other steps use a velocity rescaling thermostat[37] with $\tau_T = 1$ ps, following our established protocol.[17]

3. Results and Discussion

3.1. High Relative Humidity (100%) Allows Spatulae to Stick to a Wider Range of Surface Roughness

The pull-off force (also called critical force or rupture force) is the force needed to detach the spatula from the surface and can be interpreted as the stickiness of the spatula. A detailed explanation of the spatula peel-off, including force-displacement curves, can be found in our previous work using the mesoscale spatula.[17] Here, we are only interested in how stickiness or pull-off force depends on water-induced material softening.

The spatula area is $A_{\text{Sp}} = 19880$ nm^2. For illustrative purposes, the spatula pad can be viewed as an isosceles triangle of area $A_t = 19880$ nm^2 corresponding roughly to $A_t \approx 1/2 \times (185 \pm 10\,\text{nm}) \times (215 \pm 10\,\text{nm})$. Furthermore, we call the inverse of the peak density the peak area or valley area $A_{\text{P}} = A_{\text{valley}} = 1/\rho_{\text{p}}$. We use the ratio $A_{\text{valley}}/A_{\text{Sp}}$ to express if the sinusoidal surface wavelength $(\pi n_p / l_\gamma^s)$ is smaller than the pad dimensions. Thus, at $A_{\text{valley}}/A_{\text{Sp}} = 1$, a valley of the sinusoidal surface topography has the same area as the spatula pad. Recall that the surface amplitude is 16 nm (Section 3.1). Figure 3 (bottom) corresponds to a ratio of $A_{\text{valley}}/A_{\text{Sp}} = 1.28$ and (bottom) $A_{\text{valley}}/A_{\text{Sp}} = 0.35$.

We computed the average pull-off force from detachment simulations of 10 independently generated spatulae and surfaces as a function of surface roughness. **Figure 5**A shows the pull-off force against the ratio $A_{\text{valley}}/A_{\text{Sp}}$. Figure S3 (Supporting Information) shows four examples of force-displacement curves; only the maximum force (the pull-off force) is used in this investigation. Finally, **Figure 6** illustrates the ratio.

In agreement with our previous findings,[17] the stickiness of the spatula as a function of the ratio $A_{\text{valley}}/A_{\text{Sp}}$ is well described by a sigmoidal (Richards[38]) curve (solid lines in Figure 5A) at all implicit water contents (relative humidities).

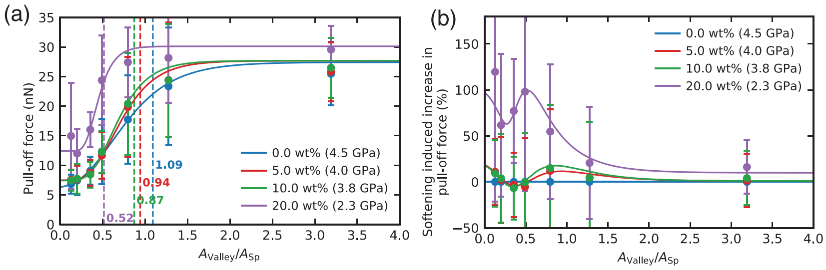

Figure 5. A) Pull-off force as a function of keratin water content and $A_{\mathrm{valley}}/A_{\mathrm{Sp}}$. The water content and corresponding Young's modulus are denoted in the legend. The average pull-off forces follow a sigmoidal (Richards[38]) curve (solid lines). Vertical dashed lines denote a threshold of 80% pull-off force relative to the maximum on a flat surface. The average is computed from $n = 10$ independent samples, and the standard deviation of the mean is used as the error. B) The relative increase in pull-off force due to the implicit water content, compared to the dry spatula (blue line at 100%). The solid lines are used to guide the eye. The error is calculated as the Gaussian error propagation of the standard deviations of the mean of (A).

When $A_{\mathrm{valley}}/A_{\mathrm{Sp}}$ falls below a certain threshold, the spatula loses its ability to follow the surface contour, i.e., the stickiness decreases significantly. We have indicated the ratio where the stickiness falls below 80% of that of a flat surface with vertical dashed lines in Figure 5. For dry spatulae, this threshold already occurs at $A_{\mathrm{valley}}/A_{\mathrm{Sp}} = 1.09$. Thus, when the spatula pad area is on the same length scale as the area of surface asperities, its stickiness is 20 % lower than on an ideally flat surface.

With increasing relative humidity (higher water content, softer keratin, cf. Table 1), this threshold is only reached at smaller surface-feature sizes A_{valley}; gecko spatulae in high relative humidity can adapt to finer surface topographies. The threshold decreases linearly with both water content and Young's modulus from 1.09 to 0.52 (Figure 5A bottom).

3.2. Non-Linear Increase in Stickiness Due to Material Softening

We also study the increase in stickiness due to humidity in percent over the dry keratin (Figure 5B). It is shown as a function of the ratio $A_{\mathrm{valley}}/A_{\mathrm{Sp}}$.

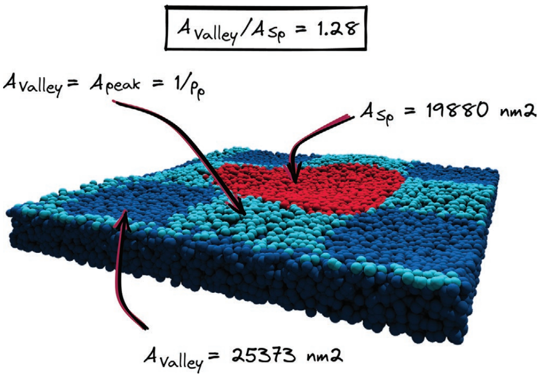

Figure 6. An illustration of the ratio of valley area against spatula pad area for the example of $A_{\mathrm{valley}}/A_{\mathrm{Sp}} = 1.28$. The surface peaks are cyan, and the surface valleys are blue. We color all surface beads within the cutoff length of the spatula red as an approximation to the spatula pad area. Thus, the actual spatula pad is smaller than illustrated.

On flat surfaces, there is essentially no increase of stickiness due to (implicit) humidity. This holds at all humidities (**Figure** 7B blue). Experimental work shows that between 1.5% and 45% relative humidity,[3] the pull-off force increases by 60% on a flat hydrophobic surface and between 55% and 80% relative humidity,[9] the shear adhesion increases by 158 ± 40%. In contrast, our softened spatula sticks just 10% better at maximum humidity. Thus, given that the humidity-enhanced adhesion increase on flat surfaces is ≈ 200–300%[3,9–11] in total, it follows that the material softening hypothesis can be ruled out for flat hydrophobic surfaces, as we previously conjectured from CG[10] simulations of gecko keratin.

We, therefore, have to conclude that other mechanisms than keratin-softening are responsible for the larger stickiness at higher humidities. Based on united-atom and coarse-grained molecular dynamics, we have previously suggested that water molecules mediate the attraction between keratin and surface.[11] The molecular-level simulations have shown that water fills the spatula-surface gaps and increases the number of interacting sites and the magnitude of interactions between surface and spatula. Since the availability of water molecules in the keratin increases sigmoidally with relative humidity (Figure 1), we expect the water mediating effect to scale similarly.

The situation is different for nanostructured surfaces. Here, the effect of material softening becomes more pronounced. Figure 7 shows a marked increase in relative stickiness at a material softness corresponding to a high (>86%) humidity or 20% water content. However, at a relative humidity below 86%, the material softening effect does not strongly influence the humidity-enhanced adhesion, even on rough surfaces. The better adhesion of wet keratin to rough surfaces is, in part, brought about by its increased flexibility and its better ability to follow small surface features (see Figures S4 and S5, Supporting Information). The effect is small at 5%, and 10% water content and only takes off at 20% water content. This is simply a consequence of the fact that the elastic modulus only becomes markedly smaller at the highest water load (Figure 7C, Table 1). However, even on rough surfaces, the moisture-induced keratin softness can only explain some fraction of the observed increase in stickiness (it is 1/3–1/2 even when compared to experimental work using single spatulae on flat surfaces[3,9]).

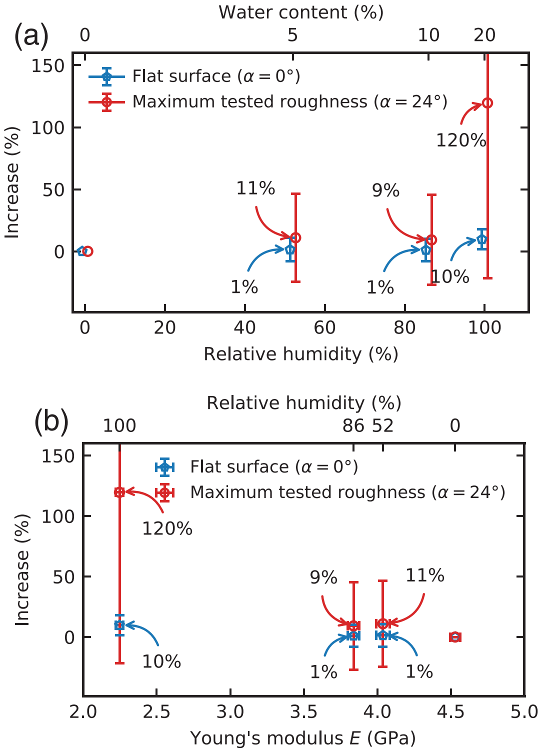

Figure 7. A) The percentage increase in the pull-off force (stickiness) of gecko spatulae due to material softening on flat and rough surfaces, compared to dry spatulae $[F(\mathrm{RH}) - F(\mathrm{RH} = 0\%)]/F(\mathrm{RH} = 0\%)$. The increased pull-off force depends non-linear on implicit water content (relative humidity). The error is calculated as the Gaussian error propagation of the standard deviations from $n = 10$ independent samples. The values are offset by 0.7% relative humidity against each other to clearly show the error bars. B) The percentage increase in the pull-off force (stickiness) of gecko spatulae due to material softening on flat and rough surfaces, compared to dry spatulae. The increased pull-off force is shown as a function of Young's modulus. The error is calculated as the Gaussian error propagation of the standard deviations from $n = 10$ independent samples.

4. Conclusion

It is known that a humidity increase in the environment enhances the sticking power of geckos. Several mechanisms have been put forward to explain this feature. Most prominent are i) capillary forces, ii) water molecules mediating between surface and keratin and iii) water uptake leading to a softening of keratin (lower elastic modulus) and, consequently, stronger adhesion. We have previously reproduced the positive effect of humidity on stickiness by united-atom (UA) and coarse-grained (CG) molecular simulations. We collected strong arguments for water mediation (ii) in our simulations.[10,11] Since we used explicit water molecules in those simulations, however, we could not rule out the indirect action of water via keratin softening (iii), which is still a very popular hypothesis in gecko biophysics.[9,12–14] In order to separate the different mechanisms, we adapted a mesoscale model[17] for entire spatulae to reproduce the elasticity of water-swollen keratin without containing explicit water molecules. Thus, capillary force (i) and water-mediation (ii) are excluded from the model. The elastic constants of water-swollen keratin, in turn, were determined by atomistic simulations, and the equilibrium water content at a given relative humidity was calculated previously[19] by atomistic grand-canonical molecular dynamics. We, thus, pursue a true multi-scale simulation protocol.

We trained a deep neural network to predict the mechanical properties, Young's modulus and Poisson's ratio, from bonded force field parameters of our previously published mesoscale spatula model reusing existing data.[17] The trained DNN (Section 2.5) allowed us to directly infer bonded force field parameters (Section 2.3) that produce the exact target material properties instead of relying on lengthy and costly classical parameter optimization. We computed material properties for four different water contents using our united-atom (UA) gecko keratin model[11] (Section 2.1). The DNN prediction was then used to find the necessary force field parameters of the mesoscale model to reproduce the elastic constants from the UA simulations of the water-swollen keratin. This adaptation of the mesoscale force field parameters only affects the elasticity of the keratin, not its interaction with the surface. Thus, capillary forces (i) and water-mediation (ii) cannot operate through effective interactions either. In the absence of water molecules, capillary forces and the water mediating effect can be rigorously ruled out in any observations we made.

Our results disprove the hypothesis of material softening being responsible for humidity-enhanced adhesion of spatulae on flat hydrophobic surfaces.[3,7,9] On flat surfaces, an implicitly fully "water-soaked" keratin sticks better to a surface than complete water-free keratin by a mere 10% (Figure 7). In comparison, experimental[3,9] and computational[10,11] reports show that the adhesion increase due to humidity is ≈200–300%. As a result, we rule out softening as a mechanism dominating the humidity-enhanced adhesion of whole spatulae on flat surfaces. The primary mechanism underlying humidity-enhanced adhesion is the mediation of keratin-surface interactions by water. Our previous findings for wet UA gecko keratin[11] showed that elastic interactions are one of the smaller contributions controlling the pull-off force from the flat hydrophobic surface. As an interesting side note, elasticity significantly contributes to the pull-off of dry keratin from a hydrophobic surface. However, as keratin gets wet, water mediation (ii) becomes dominant.

While material softening does not determine spatula stickiness at ideal flat surfaces, it is one critical factor at nanoscopic rough surfaces. Here, the mesoscale spatula model showed a material softening-induced increase in adhesion of up to 120% compared to dry keratin. The higher flexibility of keratin (which only becomes appreciable at water contents at or near saturation) enables the spatula to follow surface structures smaller than itself. Thus, the spatula can keep the full adhesion potential when surfaces get rougher (Section 3.1) and surface structures are smaller than the spatula.

Of the mechanisms underlying humidity, the water mediating effect dominates in all circumstances at the very hydrophobic surface except in extremely humid environments (relative humidity >86%). Here, if the surface is rough and surface features are smaller than the spatula, the material softening effect may be responsible for 1/3–1/2 of the increased stickiness compared to the dry keratin. In short, the water-induced increase in flexibility allows spatulae to follow surface features smaller than themselves, thereby increasing contact area with the surface and, thus, contributing to humidity-enhanced adhesion. In contrast, in laboratory experiments using very hydrophobic nanoscopic flat surfaces, the humidity-enhanced adhesion is determined by the water mediating effect we proposed.[10,11] Capillary forces depend on a water volume absorbed to the surface. Capillary bridges are either completely absent on very hydrophobic surfaces at relative humidities smaller than the supersaturation limit or of convex geometry.[10] The latter case could even lead to capillary forces that are repulsive.[39,40]

Finally, let us discuss the generality of our findings. Here, we investigated material softening in terms of the more common single-spatula experiments; however, how does this transfer to whole setae adhesion? For the per-spatula level, we have shown the effect of material softening in this work. However, setae break up large contact areas into multiple smaller sub-areas (spatulae). This strategy is called contact splitting.[33,41,42] Consequently, the characteristic adhesive feature length increases from the spatula's contact area to the setae's theoretical contact area. Water-softened setae, therefore, likely exhibit increased stickiness even if surface features are larger than the spatula, as long as the surface features are in the order of the theoretical seta contact area. The quantitative impact of material softening on seta-level adhesion is up for future investigation. While neither rough surfaces nor seta adhesion investigations are currently common or even well enough defined, systematic fine-grained classification of surfaces in geckos' habitats are completely absent from the literature, and seta investigations do not report the number of spatulae of the investigated setae—it will be nonetheless important to fully understand the complete adhesion strategy employed by geckos in their natural habit. Furthermore, what happens on surfaces other than the one we investigated? We have only explored a hydrophobic surface in this work. On a hydrophilic surface, water mediation is enhanced,[11] and capillary action may become relevant at very high humidity as water can pool up. Finally, and most interesting to synthetic gecko adhesive research,[43–49] can the results be generalized to other materials? Both this work and our first coarse-grained work[10] use molecular models that are more generic than our more precise united-atom model.[11] Therefore, results are generalizable to other materials with similar properties. Synthetic adhesives can create better contact if they are flexible enough to follow nanostructured surfaces. A water mediation-like effect may also be constructed with small diffusive molecules instead of water (i.e., tackifiers[50–53]).

In this simulation study, we "deactivated" the effects of water mediation (ii) and capillary forces (i) to only investigate spatula softness (iii). In reality, spatulae are softened by water molecules, which also operate as mediators for water-surface interactions. Possible non-additive effects between the three mechanisms should be the subject of further investigation.

Supporting Information

Supporting Information is available from the Wiley Online Library or from the author.

Acknowledgements

Open access funding enabled and organized by Projekt DEAL.

Conflict of Interest

The authors declare no conflict of interest.

Data Availability Statement

The data that support the findings of this study are available from the corresponding author upon reasonable request.

Keywords

deep neural networks, gecko adhesion, humidity, molecular dynamics, multiscale molecular model, pull-off, spatula

Received: October 4, 2022
Revised: December 6, 2022

---

[1] Q. Jiang, Z. Wang, J. Zhou, W. Chen, Z. Dai, *J. Bionic Eng.* **2019**, *16*, 115.
[2] K. Autumn, Y. A. Liang, S. T. Hsieh, W. Zesch, W. P. Chan, T. W. Kenny, R. Fearing, R. J. Full, *Nature* **2000**, *405*, 681.
[3] G. Huber, H. Mantz, R. Spolenak, K. Mecke, K. Jacobs, S. N. Gorb, E. Arzt, *Proc. Natl. Acad. Sci. U.S.A.* **2005**, *102*, 16293.
[4] A. Y. Stark, S. Subarajan, D. Jain, P. H. Niewiarowski, A. Dhinojwala, *Philos. Trans. Royal Soc.* **2016**, *374*, 20160184.
[5] G. Huber, S. N. Gorb, N. Hosoda, R. Spolenak, E. Arzt, *Acta Biomater.* **2007**, *3*, 607.
[6] T. W. Kim, B. Bhushan, *Ultramicroscopy* **2007**, *107*, 902.
[7] W. Sun, P. Neuzil, T. S. Kustandi, S. Oh, V. D. Samper, *Biophys. J.* **2005**, *89*, L14.
[8] A. Y. Stark, M. R. Klittich, M. Sitti, P. H. Niewiarowski, A. Dhinojwala, *Sci. Rep.* **2016**, *6*, 30936.
[9] C. T. Mitchell, C. B. Dayan, D.-M. Drotlef, M. Sitti, A. Y. Stark, *Sci. Rep.* **2020**, *10*, 19748.
[10] T. Materzok, S. N. Gorb, F. Müller-Plathe, *Soft Matter* **2022**, *18*, 1247.
[11] T. Materzok, A. Canestraight, S. N. Gorb, F. Müller-Plathe, *ACS Nano* **2022**, *16*, 19261.
[12] M. Prowse, M. Wilkinson, J. Puthoff, G. Mayer, K. Autumn, *Acta Biomater.* **2010**, *7*, 733.
[13] J. B. Puthoff, M. S. Prowse, M. Wilkinson, K. Autumn, *J. Exp. Biol.* **2010**, *213*, 3699.
[14] G. Huber, S. Orso, R. Spolenak, U. G. K. Wegst, S. Enders, S. N. Gorb, E. Arzt, *Mater. Res.* **2008**, *99*, 1113.
[15] D. Tan, A. Luo, X. Wang, Z. Shi, Y. Lei, M. Steinhart, A. Kovalev, S. N. Gorb, K. T. Turner, L. Xue, *ACS Appl. Nano Mater.* **2020**, *3*, 3596.
[16] J. O. Wolff, S. N. Gorb, *Proc. Biol. Sci.* **2012**, *279*, 139.
[17] T. Materzok, D. De Boer, S. N. Gorb, F. Müller-Plathe, *Small* **2022**, *18*, 2201674.
[18] Q. Xu, Y. Wan, T. S. Hu, T. X. Liu, D. Tao, P. H. Niewiarowski, Y. Tian, Y. Liu, L. Dai, Y. Yang, Z. Xia, *Nat. Commun.* **2015**, *6*, 8949.
[19] M. Khani, T. Materzok, H. Eslami, S. Gorb, F. Müller-Plathe, *J. R. Soc. Interface* **2022**, *19*, 20220372.
[20] L. D. Schuler, X. Daura, W. F. v. Gunsteren, *J. Comput. Chem.* **2001**, *22*, 1205.

[21] C. Oostenbrink, A. Villa, A. E. Mark, W. F. V. Gunsteren, *J. Comput. Chem.* **2004**, *25*, 1656.
[22] N. Schmid, A. P. Eichenberger, A. Choutko, S. Riniker, M. Winger, A. E. Mark, W. F. van Gunsteren, *Eur. Biophys. J.* **2011**, *40*, 843.
[23] W. Huang, Z. Lin, W. F. van Gunsteren, *J. Chem. Theory Comput.* **2011**, *7*, 1237.
[24] H. J. C. Berendsen, J. R. Grigera, T. P. Straatsma, *J. Phys. Chem.* **1987**, *91*, 6269.
[25] K. S. Endoh, T. Kawakatsu, F. Müller-Plathe, *J. Phys. Chem. B* **2018**, *122*, 2203.
[26] H. Eslami, F. Müller-Plathe, *J. Comput. Chem.* **2007**, *28*, 1763.
[27] S. Rosenbaum, *J. Polym. Sci.* **1970**, *31*, 45.
[28] J. D. Leeder, I. C. Watt, *J. Phys. Chem.* **1965**, *69*, 3280.
[29] N. W. Rizzo, K. H. Gardner, D. J. Walls, N. M. Keiper-Hrynko, T. S. Ganzke, D. L. Hallahan, *J. R. Soc. Interface* **2006**, *3*, 441.
[30] D. L. Hallahan, N. M. Keiper-Hrynko, T. Q. Shang, T. S. Ganzke, M. Toni, L. D. Valle, L. Alibardi, *J. Exp. Zool. B: Mol. Dev. Evol.* **2009**, *312B*, 58.
[31] L. Alibardi, *Tissue Cell* **2013**, *45*, 231.
[32] M. Calvaresi, L. Eckhart, L. Alibardi, *J. Struct. Biol.* **2016**, *194*, 282.
[33] E. Arzt, S. Gorb, R. Spolenak, *Proc. Natl. Acad. Sci. U.S.A.* **2003**, *100*, 10603.
[34] G. Huber, S. N. Gorb, R. Spolenak, E. Arzt, *Biol. Lett.* **2005**, *1*, 2.
[35] H. Grubmüller, *Methods Mol. Biol.* **2005**, *305*, 493.
[36] N. Goga, A. J. Rzepiela, A. H. de Vries, S. J. Marrink, H. J. C. Berendsen, *J. Chem. Theory Comput.* **2012**, *8*, 3637.
[37] G. Bussi, D. Donadio, M. Parrinello, *J. Chem. Phys.* **2007**, *126*, 014101.
[38] F. J. Richards, *J. Exp. Bot.* **1959**, *10*, 290.
[39] M. Dörmann, H.-J. Schmid, *Procedia Eng.* **2015**, *102*, 14.
[40] P. A. Kralchevsky, K. Nagayama, in *Particles at Fluids Interfaces and Membranes*, 1st ed., (Eds.: P. A. Kralchevsky, K. Nagayama), Elsevier Science, Oxford **2001**, pp. 469–502.
[41] M. Varenberg, B. Murarash, Y. Kligerman, S. N. Gorb, *Appl. Phys. A* **2011**, *103*, 933.
[42] M. Kamperman, E. Kroner, A. del Campo, R. M. McMeeking, E. Arzt, *Adv. Eng. Mater.* **2010**, *12*, 335.
[43] H. Lee, B. P. Lee, P. B. Messersmith, *Nature* **2007**, *448*, 338.
[44] L. Wang, Y. Hui, C. Fu, Z. Wang, M. Zhang, T. Zhang, *J. Adhes. Sci. Technol.* **2020**, *34*, 2275.
[45] W. Ruotolo, D. Brouwer, M. R. Cutkosky, *Sci. Robot.* **2021**, *6*, eabi9773.
[46] X. Li, D. Tao, H. Lu, P. Bai, Z. Liu, L. Ma, Y. Meng, Y. Tian, *Surf. Topogr.: Metrol. Prop.* **2019**, *7*, 023001.
[47] T. G. Chen, A. Cauligi, S. A. Suresh, M. Pavone, M. R. Cutkosky, *IEEE Robot. Autom. Mag.* **2022**, *29*, 24.
[48] T. T. Hoang, J. J. S. Quek, M. T. Thai, P. T. Phan, N. H. Lovell, T. N. Do, *Sens. Actuator A Phys.* **2021**, *323*, 112673.
[49] A. Wang, S. Keten, *Npj. Comput. Mater.* **2019**, *5*, 29.
[50] T. Doi, H. Takagi, N. Shimizu, N. Igarashi, S. Sakurai, *ACS Appl. Polym. Mater.* **2020**, *2*, 4973.
[51] X. Deng, *J. Adhes.* **2018**, *94*, 77.
[52] B. Sharma, A. Sandilya, U. Patel, A. Shukla, S. D. Sadhu, *Int. J. Adhes. Adhes.* **2021**, *110*, 102946.
[53] J. Moon, Y. Huh, J. Park, H. W. Kim, Y. Choe, J. Huh, J. Bang, *ACS Appl. Polym. Mater.* **2020**, *2*, 2444.

Supporting Information

for *Small,* DOI: 10.1002/smll.202206085

Understanding Humidity-Enhanced Adhesion of Geckos: Deep Neural Network-Assisted Multi-Scale Molecular Modeling

Tobias Materzok, Hossein Eslami, Stanislav N. Gorb,*
and Florian Müller-Plathe

SUPPORTING INFORMATION

Understanding Humidity-enhanced Adhesion of Geckos: Deep Neural Network-assisted Multi-scale Molecular Modeling

*Tobias Materzok** *Hossein Eslami* *Stanislav N. Gorb* *Florian Müller-Plathe*

Tobias Materzok, Prof. Dr. Hossein Eslami, Prof. Dr. Florian Müller-Plathe
Email Address: t.materzok@theo.chemie.tu-darmstadt.de
Eduard-Zintl-Institut für Anorganische und Physikalische Chemie and Profile Area Thermofluids and Interfaces
Technische Universität Darmstadt
Alarich-Weiss-Str. 8
D-64287 Darmstadt
Germany
Prof. Dr. Hossein Eslami
Department of Chemistry, Colleges of Sciences
Persian Gulf University
Boushehr 75168
Iran
Prof. Dr. Stanislav N. Gorb
Zoological Institute Functional Morphology and Biomechanics
Kiel University
Am Botanischen Garten 1-9
D-24118 Kiel
Germany

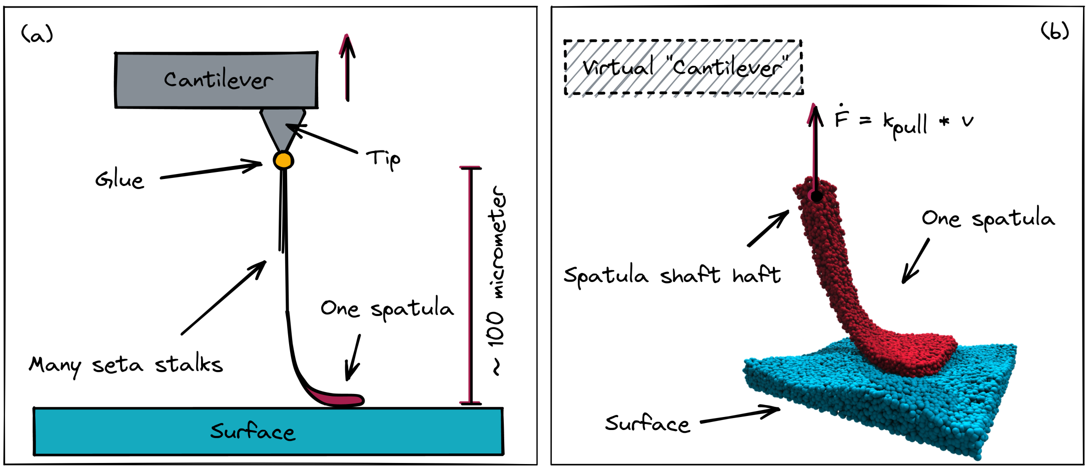

Figure S1: (A) Experimental setup of atomic force microscopy (AFM) experiments that investigate gecko single-spatula adhesion, e.g., by Huber et al.[1][2][3]. A single seta is glued to a cantilever, and then an ion beam is used to cut off everything except isolated single spatulae. Since setae are around 100 μm long, the surface is far away from the AFM tip. (B) The simulation setup used in this work and explained in more detail elsewhere[4]. A virtual "cantilever" (e.g., a non-interacting particle) is linked to the spatula shaft haft with a harmonic spring and pulled vertically upwards.

1 Deep neural network

A deep neural network is a network of nodes. A fully connected layer consists of N hidden layers, and each node of one hidden layer is connected to all nodes of the previous hidden layer, as well as with all nodes of the next hidden layer. Each node is essentially an activation function that computes the output using the sum of the node's inputs that are weighted by their corresponding weight w_{ij}. Linear activation functions like the Rectified Linear Unit (ReLU) or the Scaled Exponential Linear Unit[5] (SELU) are most commonly used for regression problems like ours. The output of one node o_j is the transform of the sum over all inputs $w_{1j} \cdot x_1$ to $w_{nj} \cdot x_n$, essentially $\sum_{i=1}^{n} w_{ij} x_i$ with the activation function ϕ. We use a bias b as well (Equation 1).

$$o_j = \phi(\sum_{i=1}^{n} w_{ij} x_i + b) \tag{1}$$

where

$$\phi(x) = \begin{cases} x, & \text{if } x > 0. \\ \alpha e^x - \alpha, & \text{if } x \leq 0. \end{cases} \tag{2}$$

The networks' weights are tuned such that the input to the network reproduces the output. The backpropagation algorithm computes the gradient of a loss function with respect to the weights that can then be used to update weights to minimize the loss using, e.g., gradient descent. Grid-based hyperparameter search found optimal results for network architecture, activation functions of layers, loss function and optimization method. It resulted in us using the mean squared error as the loss function and Adam[6] for stochastic optimization. In this work, we use the Keras library[7] on top of Tensorflow[8].

Figure 2 illustrates the DNN network architecture. The input vector is connected to a fully connected layer (6x64). We use a Keras Gaussian noise layer with a standard deviation of 0.1 to regularize the inputs (the input ranges from 1 to 3000 kJ mol^{-1} nm^{-2}). To reduce overfitting and improve model generalization, we applied a Keras Gaussian noise layer to the output. The standard deviation of the latter Gaussian is

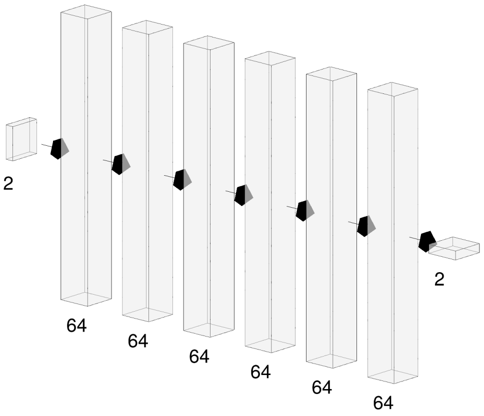

Figure S2: Structure of the deep neural network with two inputs k and k_b and two outputs E and ν.

wt%	RH (%)	E_{meso} (GPa)	v_{meso}	k (kJ mol^{-1} nm^{-2})	k_b (kJ mol^{-1} nm^{-2})
0	0	4.529 ± 0.033	0.409 ± 0.002	198	1282
5	52	4.038 ± 0.045	0.435 ± 0.002	109	1250
10	86	3.838 ± 0.040	0.422 ± 0.002	135	1139
20	100	2.247 ± 0.025	0.496 ± 0.004	3	794

Table S1: The predicted anisotropic force constant coefficients of the mesoscale keratin material and the corresponding Young' moduli and Poisson' ratios.

computed as 10% of the standard deviation of the mean over the whole output data, where the previously computed Young' moduli E and Poisson' ratios ν are used as the output.

We should note here that we scaled the Poisson ratio to be in the same order of magnitude as Young's modulus. Since E of our united-atom gecko keratin ranges from around 2000 MPa to 4500 MPa and Poisson's ratio from 0.4 to 0.5, we multiplied the latter by 10000 to make ν range between 4000 and 5000. Generally, it makes training a neural network easier if all input and outputs are regularized to the same scale.

Except for the output layer, which uses a linear activation function $\phi(x) = x$, all layers use the scaled exponential linear unit[5] (SELU) activation function (Equation 2) with a LeCun[9] kernel initializer and biases are initialized with ones.

2 Computational Details

The united-atom (UA) gecko keratin model uses the GROMOS 54A7 force field[10, 11, 12, 13] for all atoms present in the system, keratin protein and surface.

In an earlier coarse-grained study[14], we found that only the gecko keratin's intrinsically disordered protein regions (IDRs) directly contact the surface and not the beta-folded region of the keratin protein that polymerizes into nanofibrils. Thus, only the IDRs of the gecko keratin protein are responsible for the adhesive energetic interaction between spatula and surface. Therefore, we amorphized a gecko beta-keratin protein (Ge-cprp-9) and only considered the intrinsically disordered parts of the protein.

The exact equilibration protocol, including energy minimization, amorphization at 1300 K with a subsequent cooldown, and multi-step equilibrations in the NPT ensemble with and without soft-core potentials, go beyond this SI.

United-atom keratin simulations are carried out using the GROMACS 2018 software package[15], the GROMOS 54A7 force field[10, 11, 12, 13], and the SPC/E water model[16]. The production runs to calculate Young's modulus are performed in three-dimensional periodic boundary conditions (PBC). The

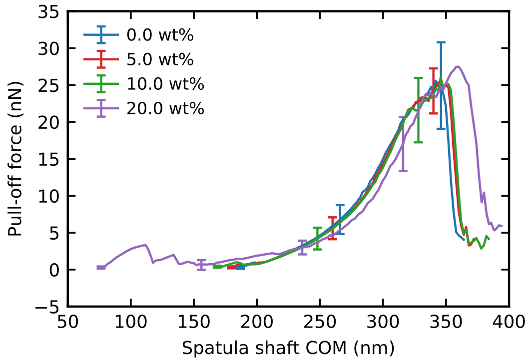

Figure S3: Average force-displacement curves of the mesoscale spatula pull-off at 4 different implicit water contents (legend). The loading rate is $1.66 \cdot 10^{12}$ pN s^{-1}. The average force curve is computed from 10 independent samples, and the standard deviation of the mean is used as the error.

timestep is 2 fs, and a velocity rescale[17] thermostat keeps the temperature at 300 K. A semi-isotropic Berendsen[18] barostat with a compressibility of $4.5 \cdot 10^{-5}$ bar^{-1} in x and y, and a compressibility of 0 bar^{-1} in z, keeps the pressure of the system at 1 bar. Therefore, only size fluctuations in x and y are possible. The system is uniformly strained in the z dimension with a straining rate of 0.00001 nm ps^{-1} = 1.0 mm s^{-1}. Production runs are repeated five times for five independently generated systems ($n = 25$). Young's modulus is computed with a linear fit to the first 1% strain. Poisson's ratio is the average over strain 1% to 5% and calculated using equilibrium runs, i.e., straining the system and running production run at a constant strain.

Mesoscale keratin simulations use the GROMACS 2018 and 2021 software package[15] and are carried out with the force field we derived previously[4], except for the bond force field parameterized in this work using the DNN. The timestep is 20 fs. Van der Waals interactions are modeled using a Lennard-Jones (12-6) potential with a cutoff of 12 nm and the potential-shift-Verlet scheme[19] as a cutoff modifier for a physically[20] smooth transition at the cutoff. A velocity rescale[17] thermostat with a coupling time of $\tau_T = 2$ ps keeps the temperature at 300 K. For simulations in the NPT ensemble used for validating Young's modulus and Poisson's ratio of the DNN predicted anisotropic force constant coefficients k and k_b a Berendsen[18] semi-isotropic barostat is used, as explained above and in more detail in previous work[4].

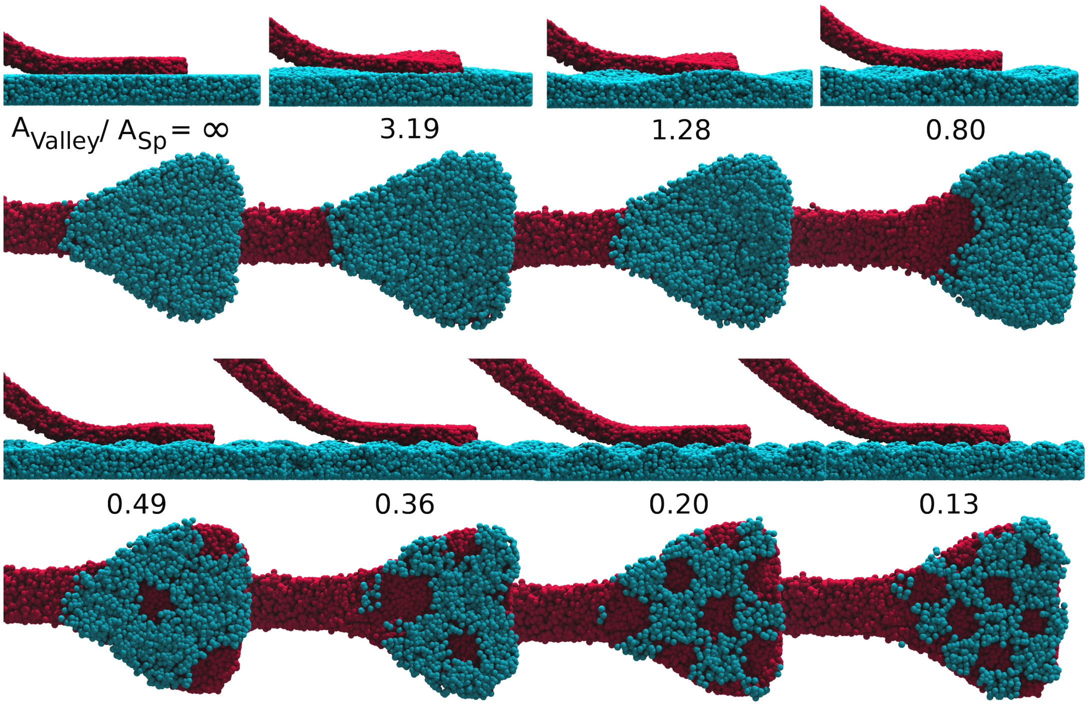

Figure S4: (Top) Spatulae at a material softness corresponding to a low (≈ 0%) humidity (0% water content) attached to rough surfaces of increasing peak density (from top left with $\rho_{\mathrm{Peak}} = 0\ \mu\mathrm{m}^{-2}$ to bottom right with $394.12\ \mu\mathrm{m}^{-2}$). The average height between the peak and valley is 16 nm for all surfaces. (Bottom) View from below the surface, where only surface beads (cyan) that interact with the spatula (red) are shown. The ratio $A_{\mathrm{valley}}/A_{\mathrm{Sp}}$ between the area between peaks and the spatula area is noted underneath each surface.

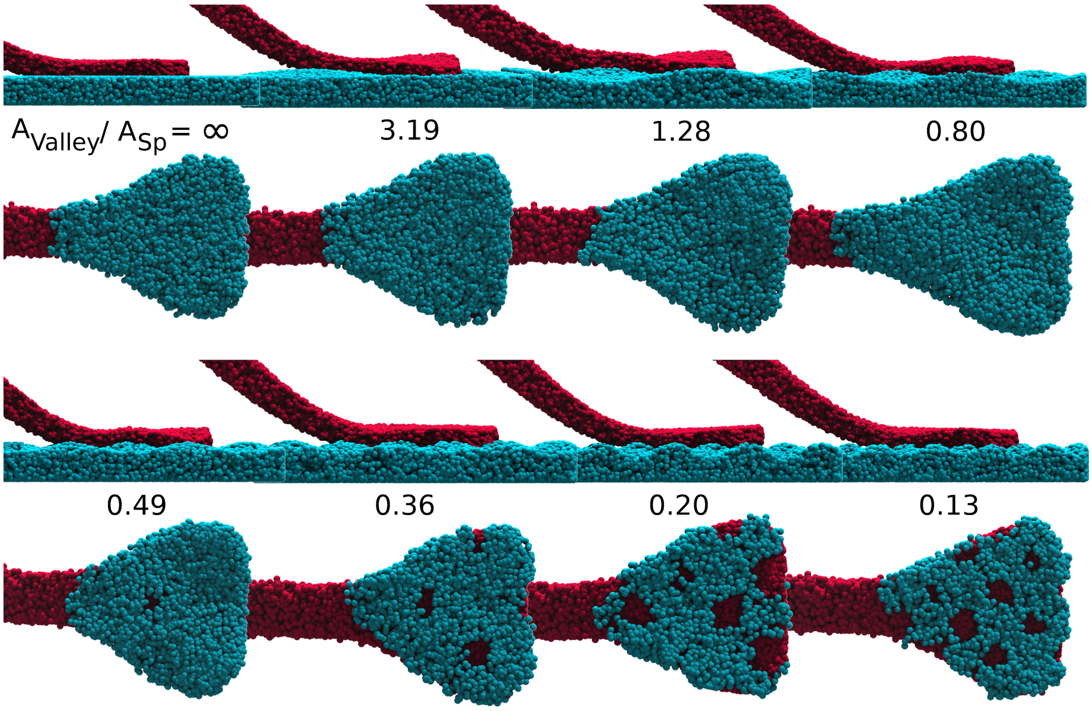

Figure S5: (Top) Spatulae at a material softness corresponding to a high (> 86%) humidity (20% water content) attached to rough surfaces of increasing peak density (from top left with $\rho_{\text{Peak}} = 0\ \mu\text{m}^{-2}$ to bottom right with $394.12\ \mu\text{m}^{-2}$). The average height between the peak and valley is 16 nm for all surfaces. (Bottom) View from below the surface, where only surface beads (cyan) that interact with the spatula (red) are shown. The ratio $A_{\text{valley}}/A_{\text{Sp}}$ between the area between peaks and the spatula area is noted underneath each surface.

References

[1] G. Huber, H. Mantz, R. Spolenak, K. Mecke, K. Jacobs, S. N. Gorb, E. Arzt, *Proc. Natl. Acad. Sci. U.S.A.* **2005**, *102*, 45 16293.

[2] G. Huber, S. N. Gorb, N. Hosoda, R. Spolenak, E. Arzt, *Acta Biomater.* **2007**, *3*, 4 607.

[3] G. Huber, S. N. Gorb, R. Spolenak, E. Arzt, *Biol. Lett.* **2005**, *1*, 1 2.

[4] T. Materzok, D. De Boer, S. N. Gorb, F. Müller-Plathe, *Small* **2022**, *18*, 35 2201674.

[5] G. Klambauer, T. Unterthiner, A. Mayr, S. Hochreiter, *arXiv:1706.02515 [cs, stat]* **2017**, arXiv: 1706.02515.

[6] D. P. Kingma, J. Ba, *arXiv:1412.6980 [cs]* **2017**, arXiv: 1412.6980.

[7] F. Chollet, Keras, **2015**, URL `https://keras.io`.

[8] Martín Abadi, Ashish Agarwal, Paul Barham, Eugene Brevdo, Zhifeng Chen, Craig Citro, Greg S. Corrado, Andy Davis, Jeffrey Dean, Matthieu Devin, Sanjay Ghemawat, Ian Goodfellow, Andrew Harp, Geoffrey Irving, Michael Isard, Y. Jia, Rafal Jozefowicz, Lukasz Kaiser, Manjunath Kudlur, Josh Levenberg, Dandelion Mané, Rajat Monga, Sherry Moore, Derek Murray, Chris Olah, Mike Schuster, Jonathon Shlens, Benoit Steiner, Ilya Sutskever, Kunal Talwar, Paul Tucker, Vincent Vanhoucke, Vijay Vasudevan, Fernanda Viégas, Oriol Vinyals, Pete Warden, Martin Wattenberg, Martin Wicke, Yuan Yu, Xiaoqiang Zheng, TensorFlow: Large-Scale Machine Learning on Heterogeneous Systems, **2015**, URL `https://www.tensorflow.org/`.

[9] Y. Lecun, L. Bottou, Y. Bengio, P. Haffner, *Proc. IEEE* **1998**, *86*, 11 2278.

[10] L. D. Schuler, X. Daura, W. F. v. Gunsteren, *J. Comput. Chem.* **2001**, *22*, 11 1205.

[11] C. Oostenbrink, A. Villa, A. E. Mark, W. F. V. Gunsteren, *J. Comput. Chem.* **2004**, *25*, 13 1656.

[12] N. Schmid, A. P. Eichenberger, A. Choutko, S. Riniker, M. Winger, A. E. Mark, W. F. van Gunsteren, *Eur. Biophys. J.* **2011**, *40*, 7 843.

[13] W. Huang, Z. Lin, W. F. van Gunsteren, *J. Chem. Theory Comput.* **2011**, *7*, 5 1237.

[14] T. Materzok, S. N. Gorb, F. Müller-Plathe, *Soft Matter* **2022**, *18*, 6 1247.

[15] B. Hess, C. Kutzner, D. van der Spoel, E. Lindahl, *J. Chem. Theory Comput.* **2008**, *4*, 3 435.

[16] H. J. C. Berendsen, J. R. Grigera, T. P. Straatsma, *J. Phys. Chem.* **1987**, *91*, 24 6269.

[17] G. Bussi, D. Donadio, M. Parrinello, *J. Chem. Phys.* **2007**, *126*, 1 014101.

[18] H. J. C. Berendsen, J. P. M. Postma, W. F. van Gunsteren, A. DiNola, J. R. Haak, *J. Chem. Phys.* **1984**, *81*, 8 3684.

[19] S. Páll, B. Hess, *Comput. Phys. Commun.* **2013**, *184*, 12 2641.

[20] D. van der Spoel, P. J. van Maaren, *J. Chem. Theory Comput.* **2006**, *2*, 1 1.

Table of Contents

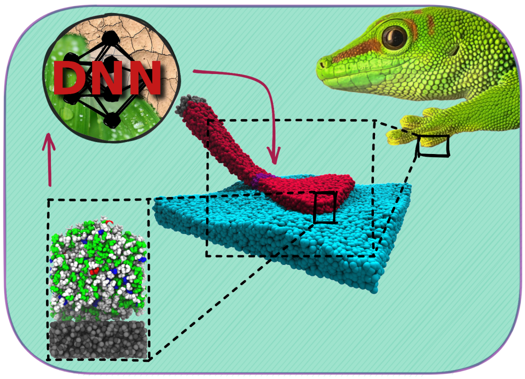

The prominent material-softening hypothesis in humidity-enhanced gecko adhesion is investigated by a bottom-up coarse-grained mesoscale model of an entire gecko spatula designed without explicit water particles present, so that capillary action and water-mediation are excluded. We show that on nanoscopic flat surfaces, the softening of keratin by water uptake cannot nearly account for the experimentally observed increase in gecko sticking power.

3.2 How does Gecko Keratin stick to hydrophilic and hydrophobic surfaces in the presence and absence of water? An atomistic molecular dynamics investigation

Reproduced with permission from Materzok et al. [ACS Nano 2022, **16**, 19261–19270] Copyright 2022 American Chemical Society.

ACS NANO

www.acsnano.org

How Does Gecko Keratin Stick to Hydrophilic and Hydrophobic Surfaces in the Presence and Absence of Water? An Atomistic Molecular Dynamics Investigation

Tobias Materzok,* Annabelle Canestraight,* Stanislav N. Gorb,* and Florian Müller-Plathe*

Cite This: *ACS Nano* 2022, 16, 19261−19270

Read Online

ACCESS | Metrics & More | Article Recommendations | Supporting Information

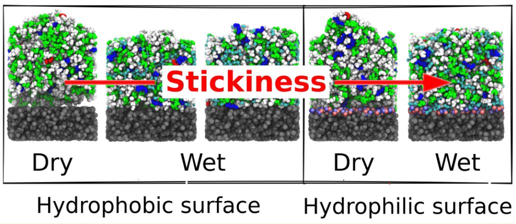

ABSTRACT: **We developed a united-atom model of gecko keratin to investigate the influence of electrostatic and van der Waals contributions to gecko adhesion in scenarios representing gecko's natural habitats. The keratin model assumes that only intrinsically disordered regions directly contact the surface. Contact angles of two generic substrate surfaces that we created match those previously used in AFM experiments on gecko adhesion. Force probe molecular dynamics simulations pulling the keratin from the surface show that the pull-off force increases with increased water content and is inversely related to the water contact angle of the surface. This matches experimental trends. We investigated the number and charge density of keratin and water at the surface, confirming a water-mediating effect and are able to show that keratin folds polar groups to the hydrophilic surface. We decomposed energetic contributions during pull-off, and our computational model shows that in contrast to popular hypotheses, long-range electrostatic interactions determine much of the pull-off process. The contribution of electrostatics to adhesion may be in the order of the van der Waals contributions.**

KEYWORDS: *gecko adhesion, molecular dynamics, pull-off force, humidity-enhanced adhesion, functional material, nanotechnology*

Geckos in humid rain forests, like the genus *Phelsuma* in the family of Gekkonidae, live among a wide variety of plants in their natural habitat. The gold dust day gecko (*Phelsuma laticauda*, Figure 1A,B), living in northern Madagascar, moves on leaves. Hydrophobic epicuticular wax coats plant leaves. A popular hypothesis is that short-ranged van der Waals interactions may dominate adhesion on these nonpolar surfaces, and long-ranged electrostatics may not be essential[1−4] or play a minor role.[5] In contrast, hydrophilic materials like rocks dominate the habitat of geckos in arid climates. The genus *Afroedura* of the Gekkonidae family, also called rock geckos, adapted to a life among rocks and stones (Figure 1C,D). Strong adhesion to hydrophilic surfaces is necessary to move on rocks in dry environments. Rocks commonly comprise oxides,[6,7] and the oxide surface is polar, which results in a hydrophilic surface and a small water contact angle. We hypothesize that electrostatic interactions may determine adhesion on rocks, and that it is modulated by the presence of water.

Our previous work investigated the effect of water on the adhesion and pull-off forces with a coarse-grained gecko keratin model.[8] That model used only dispersion attraction (van der Waals) without long-range electrostatics. The energetic interactions between keratin and surface, which contribute to the force necessary to separate them, depended on only a few parameters. An "average amino acid" of the keratin was represented as a single interaction site,[9] which in turn was parametrized from the MARTINI force field.[10−12] Water and surface elements were both represented by single interaction sites, too. With this model, we were able to show that water fills gaps between spatula and surface and smooths the spatula−surface interface (we called this the water-mediating effect). However, we could not study electrostatic interactions and were limited to a single average amino acid interaction.

Received: August 29, 2022
Accepted: October 14, 2022
Published: October 18, 2022

https://doi.org/10.1021/acsnano.2c08627
ACS Nano 2022, 16, 19261−19270

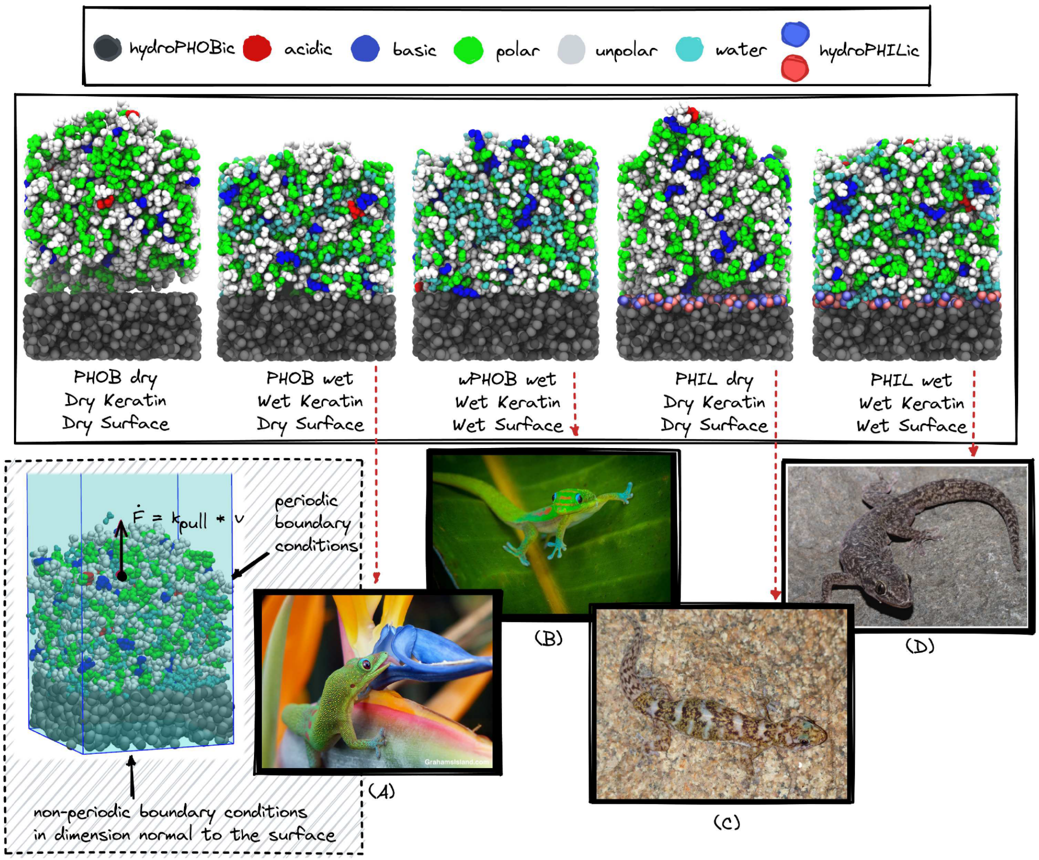

Figure 1. **(Top) Snapshots of systems without and with water (the terminology "dry" and "wet" refers to systems with 0 and 10 wt % water). Surface water contact angle determines hydrophilicity of the surface; our shorthand notation for hydrophobic is "PHOB" and for hydrophilic is "PHIL", with "wPHOB" denoting the case of a small water layer sandwiched between the hydrophobic surface and the wet keratin. The hydrophobic surface beads are in shades of gray. The charged hydrophilic layer are in metallic red and blue. (Bottom left) Periodic boundary conditions parallel to the surface are shown as a transparent blue overlay. (Bottom right) The link between simulation and geckos in different scenarios. Geckos in humid forests, like the genus *Phelsuma*, walk on a wide variety of plants coated with hydrophobic wax (A, B). In contrast, the habitat of geckos living in dry, arid climates, is dominated by hydrophilic inorganic materials like sand, stones, and rocks. They adapted to a life dominated by brown and gray colors, as seen by the color of their camouflage (C, D). Reproduced with permission from (A) Graham Burdekin, (B) Shane Myers, (C) Simon Tonge, and (D) Harith Farooq.**

The current study introduces more chemical detail to the investigation of the humidity effect on gecko adhesion. Instead of having a single interaction site representing the average amino acid, we use a united-atom force field (FF) to represent the amino acids of the Ge-cprp-9 beta keratin. With the detailed atomistic force field, we are able to calculate electrostatic forces, which were not explicitly present in the previous, coarse-grained model. The expectation is that we will be able to clarify how critical the water-mediating effect is that we found with the coarse-grained model and that we will be able to elucidate the molecular mechanisms at the hydrophobic and hydrophilic surface. Since the united-atom force field includes atomic partial charges, we will be able to study how polar amino acids behave at the hydrophobic versus hydrophilic surface, and if and how water bridges form between keratin and the surface.

The present study investigates both hydrophilic and hydrophobic surface conditions without changing the surface topography. The switching allows like-for-like comparisons and isolates the effect of the electrostatic surface interactions present only at hydrophilic surfaces. We abbreviate the scenario with a hydroPHOBic surface as "PHOB" and that with a hydroPHILic surface as "PHIL". Our generic hydrophilic surface has a macroscopic average water contact angle of $\theta_c = 8.2 \pm 5.0°$, and the hydrophobic surface has a contact angle of $\theta_c = 111.3 \pm 1.3°$. Therefore, our two model surfaces are close to the hydrophilicities (read: contact angles) of the experimental work of Huber et al.,[13] whose hydrophilic and hydrophobic surfaces had contact angles of $\approx 10 \pm 14°$ and $\approx 110°$, respectively. We want to stress that our surfaces are constructed to have the same contact angle as in experiment but not the same chemical composition. However, the pull-off force is influenced much more by the water contact angle and less by the chemical composition, as evidenced by many hydrophobic surfaces with different chemistry (like polyethylene or Teflon) showing very

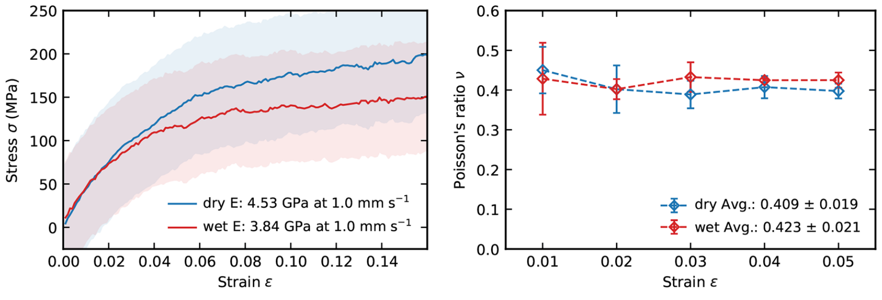

(A) (B)

Figure 2. (A) Stress−strain curves for dry (blue) and wet (red) bulk keratin. Stress σ is plotted against strain ϵ. The strain rate is 1.0 mm s^{-1}. (B) Poisson's ratio over 0 to 5% strain of dry and wet keratin. The standard deviation of the mean is used as the error.

similar pull-off forces. Thus, the exact chemical composition is less relevant than the overall hydrophilicity or hydrophobicity.

The water content of gecko keratin modifies gecko adhesion.[13,14] More water (e.g., due to increasing relative humidity of the environment) leads to an increase of the pull-off forces seen in atomic force microscopy (AFM) experiments[13] and force probe molecular dynamics (FPMD) studies.[8] The molecular mechanisms responsible for the enhanced adhesion are still not fully understood.[13,15−17] One prominent hypothesis is that the change in elasticity (Young's modulus), so-called material softening, is responsible.[15,16,18] The role of capillary forces has also been discussed.[3,13] We recently found evidence that material softening does not explain the humidity-enhanced adhesion but that water acts as a mediator between the spatula and the surface, enhancing adhesion.[8] As a side note, Huber et al.[13] and others found that spatulae exhibit strongly reduced adhesion when completely submerged under water. In this work, we will not investigate underwater adhesion but rather adhesion at ambient relative humidity. To investigate the effect of humidity on the pull-off forces (and in turn on its negative, the adhesion force), we create systems of 0 and 10 wt % water content inside the keratin. The possible range of water content goes from 0 to 30 wt %;[8] therefore, 10 wt % is a value in the middle. We call the scenario "wet" if water is present in the keratin and "dry" if not. Five independently generated systems with different water content and hydrophobic or hydrophilic surfaces are shown in Figure 1 in their equilibrium position with no external pulling or pressing forces acting on the keratin. This figure also illustrates the previously described habitats of the geckos and their relationships to the five different scenarios examined and the setup during FPMD that we will discuss later. Even a single gecko species (e.g., the *Gecko gekko*, whose protein sequence we use in this present work) which lives, among other places, in Indonesia, encounters different weather with dry and wet periods and has different surfaces to climb on. Thus, the different combinations of PHOB vs PHIL and wet versus dry are investigated here.

RESULTS AND DISCUSSION

Linear Elastic Properties of Bulk Gecko Keratin. To validate our model (details can be found in the "Method" section) against real gecko keratin properties, we compute Young's modulus E and Poisson's ratio ν (details in Supporting Information section S6). Figure 2A shows the stress−strain response of the dry (blue) and wet (red) keratin from 0 to 16% strain ϵ_{zz}. The slope of the first 1% strain is used to calculate Young's modulus, similar to Prowse et al.[15] Our dry keratin model, which represents an amorphous and highly cross-linked elastomeric material, has a Young's modulus of 4.53 ± 0.11 GPa at a strain rate of 1.0 mm s^{-1}. The wet gecko keratin has Young's modulus of E = 3.84 ± 0.18 GPa. Both values fall into the experimental range, where 7.3 ± 1.0 GPa[18] is in vacuum and the typically reduced Young's modulus is 3.2 ± 0.2 GPa at 30% relative humidity and 2.2 ± 0.2 GPa at 80% relative humidity.[15]

Stress−strain curves of setae in the literature[15,19] show a decrease in Young's modulus when the relative ambient humidity (RH) increases. Qualitatively, the stress−strain curve flattens, and a plateau forms above 2%. This behavior is reproduced by our united-atom model (Figure 2). However, since the water content of gecko keratin in the experimental studies is not known (only the ambient RH is known), we cannot directly relate our water content of 10% to the relative ambient humidities used in experimental work.

Poisson's ratio ν of our keratin is shown in Figure 2B. The presence of water does not appear to affect it strongly. The dry system has a Poisson's ratio of ν = 0.41 ± 0.02 and wet keratin, being slightly softer, ν = 0.42 ± 0.02 (red). The experimental ν for gecko spatulae and setae is not known. Our result is comparable to previous coarse-grained work[9] with fibrils present, which showed ν being 0.43.

Pull-Off Forces of Keratin on Different Surfaces. We compare pull-off in different scenarios at the same loading rate. The difference in mean pull-off forces F^η between different surface hydrophilicities and water contents (Table 1) shows a clear dependence of the gecko adhesion on the five different scenarios. Figure S5 shows a single force−time curve and a dynamic force spectra. Figure S6 summarizes the forces relative to the dry keratin dry surface (PHOB dry) scenario.

Table 1. Mean Normalized Pull-Off force F^η of Keratin Pull-Off in Different Scenarios and the Standard Deviation of F^{η}[a]

scenario	keratin	surface		F^η (nN)	$\sigma(F^\eta)$ (nN)
PHOB dry	dry	dry	PHOB	1.0	0.4
PHOB wet	wet	dry	PHOB	1.8	0.5
wPHOB wet	wet	wet	PHOB	2.4	0.8
PHIL dry	dry	dry	PHIL	6.6	0.8
PHIL wet	wet	wet	PHIL	8.2	0.3

[a] The theoretical loading rate is $\dot{F}_{\text{theo}} = 1.66 \times 10^{12}$ pN s^{-1}.

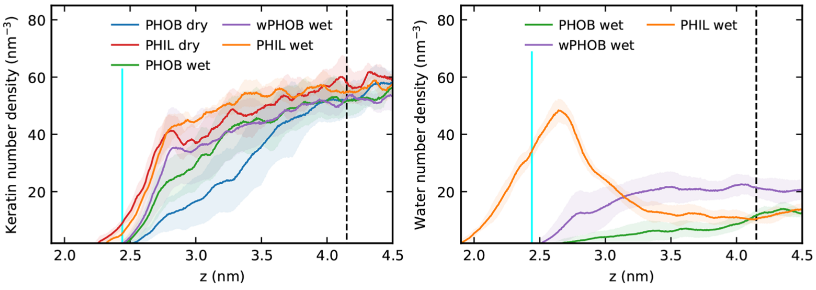

(A) (B)

Figure 3. Number density of keratin (A) and water (B) normal to the surface z in all five scenarios. The vertical cyan line denotes where the surface density is half its bulk value at $z = 2.44$ nm. The range of the Lennard-Jones interaction (1.4 nm) from the surface into the keratin is shown as a vertical dashed black line at $z = 4.15$ nm. Values are averaged over the last 55 ns of the relaxation runs (80 ns long) of five independently generated systems. The standard deviation of the mean is used as the error. The bin width is 0.005 nm.

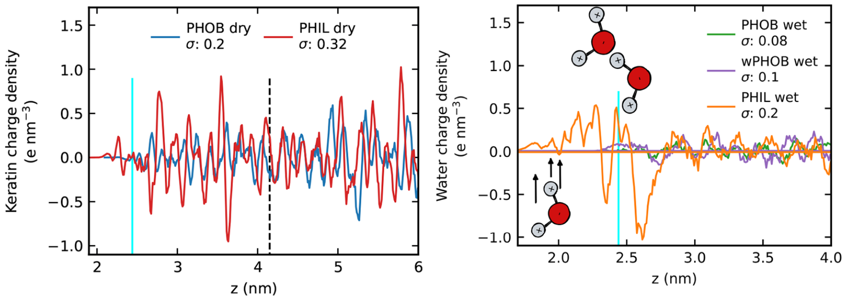

(A) (B)

Figure 4. Charge density of keratin (A) and water (B) in different scenarios normal to the surface z. The standard deviation σ (units: e nm^{-3}) of the charge density, given in the legend, is calculated between 2.44 and 6 nm and is a measure for the amplitude of the charge fluctuations. The vertical cyan line denotes where the surface density is half its bulk value at $z = 2.44$ nm. The range of the Lennard-Jones interaction (1.4 nm) from the surface into the keratin is shown as a vertical dashed black line at $z = 4.15$ nm. Values are averaged over the last 55 ns of the relaxation runs (80 ns long) of five independently generated systems. The bin width is 0.01 nm.

The mean pull-off force F^{η} is larger when the keratin is wet. The largest pull-off force is seen when the surface is hydrophilic (PHIL). The surface hydrophilicity causes a larger increase of the pull-off force than the water content of the keratin. However, a water layer (wPHOB wet) at the surface and water inside the keratin appear to be additive to that of hydrophilicity. The possible reasons are discussed below.

In previous experimental work by Huber et al.,[13] the pull-off force increased by a factor of 2.5 from a hydrophobic surface ($\theta_c \approx 110°$) to a hydrophilic surface ($\theta_c \approx 10 \pm 14°$), similar to the increase by a factor of 3.4 ± 1.2 observed here.

Influence of Water Content and Surface Chemistry on the Keratin Nanostructure and Dynamics Close to the Surface. The number density of keratin as a function of distance normal to the surface (Figure 3A) depends on surface chemistry and water content. Water presence leads to a higher density of keratin near the surface, maximizing the number of short-ranged van der Waals interactions between keratin and the surface. Water accumulates at the hydrophilic surface (Figure 3B) and fills the gaps between the keratin and the surface. Here, up to 10% (400) of the water molecules present are able to penetrate at most 0.6 nm into the hydrophilic slightly porous amorphous surface layer, similar to typical penetration depths of 0.5 nm found in amorphous silicon dioxide.[20,21] In the case of a hydrophobic surface (PHOB wet and wPHOB wet in Figure 3B), the water does not accumulate at the surface but is available to form short-range van der Waals interactions with the surface. As proposed in our previous work,[8] the resulting increase in the total number density of interaction sites (water + keratin) at the keratin−surface interface leads to water mediating the surface−keratin interactions. The atomistic simulations of this work confirm this.

To elucidate the role of electrostatics, we show in Figure 4 the charge density normal to the surface calculated from the atomic partial charges of keratin (Figure 4A) and water (Figure 4B). Recall that MD uses partial charges to account for the asymmetric distribution of electrons in chemical bonds and that we explicitly design our model to be net neutral. Thus, the total charges of the keratin and of the surface are zero. It is possible to discern between charged (polar) atoms at the hydrophilic surface using a bin width of 0.01 nm (compare a typical bond length of 0.1 nm). There is a difference in amplitude between hydrophilic (PHIL) and hydrophobic (PHOB) surfaces.

In Figure 4A, the keratin charge density and its standard deviation σ (computed between $z = 2.44$ and 6 nm) are shown for dry keratin on the hydrophilic and hydrophobic surface. The remaining scenarios are summarized in Figure S7A, and the

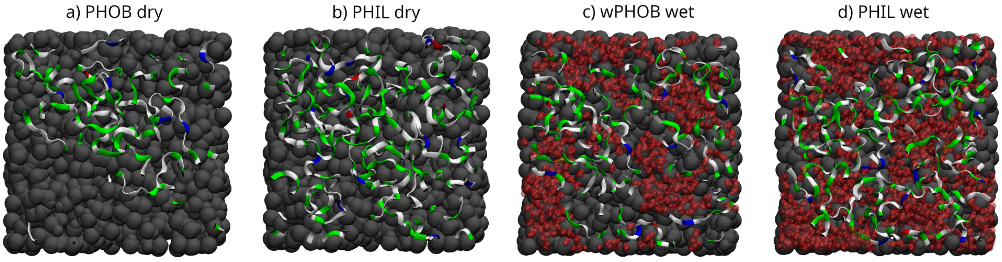

Figure 5. Top viewing snapshots of the keratin in contact with the surface (after 80 ns relaxation run). The keratin material is visualized with ribbons colored by residue types: polar (green), nonpolar (white), acidic (red), and basic (blue). Water is highlighted in red, and the surface is shown in gray. Water fills the gaps between the keratin and the surface. Dry keratin at the dry hydrophobic surface (a), dry keratin at the dry hydrophilic surface (b), water containing keratin at the wet hydrophobic surface (c), and wet keratin at the wet hydrophilic surface (d).

dependence of σ on bin width is shown in Figure S7B. The first two features (positive and negative) inside the hydrophilic top surface layer are positively charged ($z \approx 2.1$ nm) hydrogen-bonded to negatively charged ($z \approx 2.2$ nm) nitrogen and oxygen. Hence, like water, some amino acid atoms can penetrate the hydrophilic, slightly porous amorphous surface layers. Only the hydrophilic surface enhances charge excess at the interface ($z = 2.44$ nm), suggesting that gecko keratin selectively folds more polar amino acid residues toward the hydrophilic surface. Subsequently, at $z > 2.44$ nm, the periodicity of the charge excess suggests a layering (charge alternation) of amino acids throughout the keratin. The relative change in σ compared to the hydrophobic surface of around 60% confirms this (Figure 4A, legend). While surface hydrophilicity influences layering in the keratin, water does not (Figure S7).

The first negative feature of the charge density of water is at around $z = 2$ nm in Figure 4B. This suggests that the oxygen of water is present inside the top surface layer close to the interface, which was observed by previous simulation work on amorphous silica surfaces.[20] The following features are more pronounced than the first and show the hydrogens and oxygens of further layers with more surface-bound water volume available. The reason for hydrogen signals being in front of oxygen is their smaller size; hydrogen can get closer to the surface than oxygen. The absence of pronounced water layers at the dewetted hydrophobic surface (PHOB wet and wPHOB wet) is not surprising.[21] Water charge alternation inside the keratin ($z > 2.44$ nm) is less obvious than for amino acid charges.

Figure 5 views water molecules at the keratin−surface interface in the direction of the surface normal. Water fills the cavities between keratin and the surface. Thus, it smooths the keratin−surface interface and mediates a larger number of energetic interactions between spatula (where water is bound) and surface, confirming what we previously described.[8]

We also measure the flexibility of the keratin by the correlation time for the N to $C_{\alpha i}$ bond vectors of the amino acids closest to the surface. As detailed in Supporting Information section S9 and Figure S8, the influence of the conditions (water content and surface hydrophilicity) is marginal. There is a larger influence of an external force: During preload (external applied pressure of 0.4 pN nm^{-2}), the average power-law exponent that describes the correlation time distribution is 0.81 ± 0.08, whereas during relaxation (no force), it is 1.5 ± 0.19. Thus, the mobility of the amino acid segments is reduced during preload.

Decomposition in Interaction Energy Contributions and Link to Molecular Mechanisms. *Methodology and Theoretical Background.* We study how energy is stored or dissipated during the pull-off process and the influence of different wetting and hydration scenarios. To this end, we calculate the change of individual contributions between the point where keratin is in perfect contact with the surface and to the point of detachment, i.e., when the force is maximum. Elastic energy recovered at a later stage, for example, by the spatula snapping back after detachment, is not considered, as it does not contribute to favor or disfavor the pull-off proper.

The interactions during the pull-off can be separated into the following:

A Keratin−surface interactions (K−S)
    A.1 Lennard-Jones (short-ranged van der Waals ($\sim 1/r^6$))
    A.2 Coulomb (long-ranged electrostatic ($\sim 1/r$))
B Water interactions (W−W, W−K, and W−S)
    B.1 Lennard-Jones (short-ranged van der Waals ($\sim 1/r^6$))
    B.2 Coulomb (long-ranged electrostatic ($\sim 1/r$))
C Elastic interactions inside the keratin (K−K)
    C.1 Network of chemical bonds
    C.2 Lennard-Jones (short-ranged van der Waals ($\sim 1/r^6$))
    C.3 Coulomb (long-ranged electrostatic ($\sim 1/r$))

Only keratin−surface interactions (interactions A) and elastic interactions (interactions C) are experimental observables. In simulations, energies can be further decomposed into contributions by keratin, water and surface. Furthermore, the short-ranged ($\sim 1/r^6$) van der Waals and long-ranged ($\sim 1/r$) electrostatic contributions are separated. This separation is, however, model-dependent.

Keratin Detachment Mechanisms. In Figure 6A, the relative contributions of ΔU_i to the total potential energy, which needs to be overcome for detachment $\sum \Delta U_i$ (the sum of all contributions), are shown. The ratio $\Delta U_i / \sum \Delta U_i$ can be negative if the process is favored and the energy change is negative. Thus, the ratio could also exceed 100% because the sum over all ratios gives $\sum \Delta U_i / \sum \Delta U_i = 1$. Here, we report the changes of interactions A−C, defined in the "Methods" section, upon detachment. Relative contributions further separated into van der Waals and electrostatics are shown in Figure 6B (Table S3 summarizes absolute values).

The two most conspicuous points are as follows: First, energy changes internal to the keratin are at least as important as those of the interactions between keratin and surface (Figure 6A). Second, electrostatic interactions are at least as crucial as van der

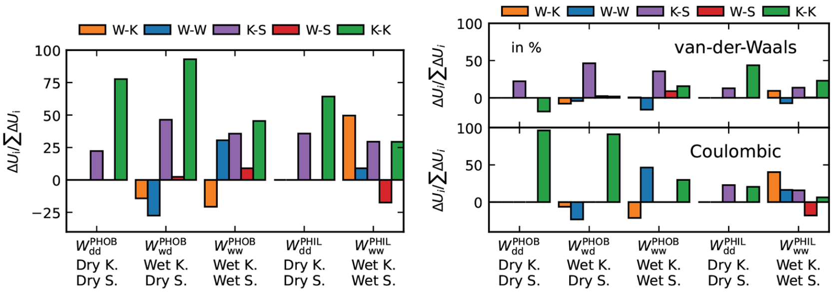

(A) (B)

Figure 6. Relative contributions to the total potential energy change. Percentages are computed as $\Delta U_i / \sum \Delta U_i \times 100$. Thus, a negative energetic change favors the pull-off, a positive change opposes it. (A) Energy contributions according to the interacting components: W: water; K: keratin; S: surface. Interactions are not further separated into their type. (B) Energy contributions of nonbonded interactions according to type: van der Waals interaction modeled by the Lennard-Jones interactions (top), electrostatic interactions (bottom).

Waals interactions (Figure 6B), which to some extent runs against the common folklore.[1−4]

It is not surprising that gecko keratin interacts with a hydrophilic (polar) surface via electrostatics (interaction A.2). However, electrostatic contributions are even present at the hydrophobic (uncharged) surface in the following interactions: keratin−keratin (interaction C.3), keratin−water (interactions B.2 and C.3), and water−water (interaction B.2). Electrostatic keratin−surface (interaction A.2) interactions are not present at hydrophobic surfaces, as seen by the experiment, but electrostatic keratin−keratin (interaction C.3) interactions are still present.

Different scenarios show different energetic mechanisms during the pull-off process. Three influences are most significant: (i) Elastic electrostatic contributions from keratin−keratin interactions (interaction C.3) oppose the pull-off and dominate at hydrophobic surfaces. (ii) The surface chemistry modulates the mediating effect[8] of water: At the hydrophobic surface, water sticks to the keratin and opposes pull-off by short-range van der Waals interactions (interaction B.1) between it and the surface. At a hydrophilic surface, water sticks to the surface and opposes gecko keratin pull-off due to the water−keratin van der Waals (interaction B.1) and electrostatic (interaction B.2) interactions. The presence of water and a hydrophilic surface, thus, lead to a closer attachment of keratin to the surface, resulting in a higher number of energetic interactions, which need to be overcome before the keratin can be detached.

It is also interesting to look at the change of the hydrogen-bonding pattern during pull-off. We define a hydrogen bond to be present when the distance between two heavy atoms is less than 0.35 nm, and the hydrogen donor−acceptor angle is below 30°. In Figure 7, the change of the number of hydrogen bonds is given with respect to the situation at full attachment. The abscissa (L_F) denotes the position of the COM of the top-half of the keratin, with $L_F = 0$ being the point where the keratin detaches, i.e., the point of maximum force.

Hydrogen bonding within the keratin (Figure 7C) shows an increase upon detachment in most environments, possibly with some recovery after detachment ($L_F > 0$). Only for wet keratin on a hydrophilic surface is there a significant reduction. This is more than compensated by newly formed water−keratin hydrogen bonds (Figure 7B) and a concomitant reduction of water−water hydrogen bonds. Another interesting situation is that of a hydrophobic surface with wet keratin and excess water (wPHOB wet): Keratin is forming additional hydrogen bonds to water without giving up existing keratin−keratin hydrogen bonds.

CONCLUSIONS

We present an atomistic gecko keratin model based on the GROMOS 54A7 force field,[22−25] complementing the previous coarse-grained gecko keratin model[8,9] with chemical details and the explicit treatment of long-range electrostatic interactions. We devised hydrophobic and hydrophilic model surfaces by matching the water contact angle of previous experimental work on gecko adhesion. By adding water to the keratin and/or the surface, five scenarios were created for modeling gecko adhesion in different natural environments.

The keratin model assumes that the intrinsically disordered and random-coil domains of the Ge-cprp-9 protein (Figure 8) contact the surface. The fibrils are inside the setae and, therefore, are away from the surface. The keratin has the same cross-linking density as the coarse-grained model by Endoh et al.[9] The elastic characteristics of our keratin model match available experimental data on setae and spatulae (Figure 2).[15,18]

The focus of this work is to investigate gecko adhesion in different environments (Figure 1) via force probe molecular dynamics, simulating the pull-off experiments done using AFM, but on a molecular scale. As experimentally seen by Huber et al.,[13] the pull-off force necessary to detach the keratin increases with the water content of the keratin. It is inversely related to the water contact angle of the surface (Table 1). We calculate that the force needed to detach the keratin from a hydrophilic surface is 3.4 ± 1.2 times larger than from a hydrophobic surface. Our simulation is comparable to the experimental results:[13,26] Huber et al.[13] observe an increase of around 2.5 times between similar hydrophobic and hydrophilic surfaces.

The presence of water and a hydrophilic surface both lead to the keratin attaching more closely to the surface (Table 2). As a result, the first layer of amino acids is less mobile because of the reduction of free volume (Figure S8). The closing of the keratin−surface gap by water increases the number of amino acids near the interface, resulting in more short-range van der Waals keratin−surface interactions. Additionally, we confirm that water mediates keratin−surface interactions.[8] When it

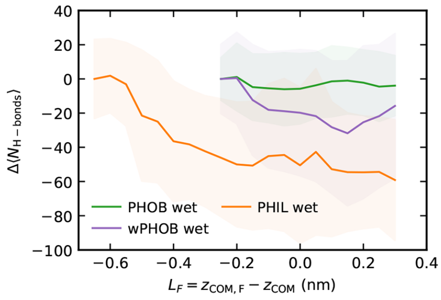

(A) water-water

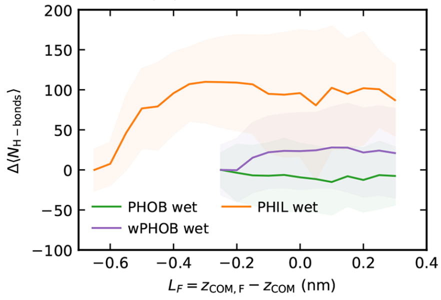

(B) water-keratin

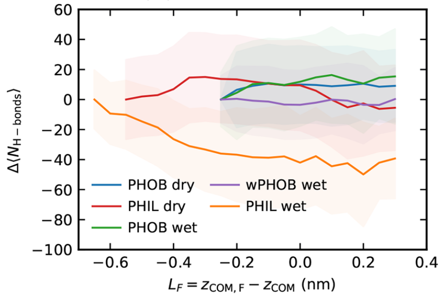

(C) keratin-keratin

Figure 7. Change in the number of hydrogen bonds during pull-off against the distance to the point of detachment ($L_F = z_{\mathrm{COM,F}} - z_{\mathrm{COM}}$ with $z_{\mathrm{COM,F}}$ the top-half keratin COM position at maximum force and z_{COM} the top-half keratin COM position). (A) Changes in water−water hydrogen bonding, (B) water−keratin hydrogen bonding, and (C) keratin−keratin hydrogen bonding. We define a hydrogen bond as the donor−acceptor distance of less than 0.35 nm and an hydrogen donor−acceptor angle of less than 30°. The average number of hydrogen bonds at a distance L_F, and the standard deviation are computed over 50 nonequilibrium pulling simulations at a loading rate of $\dot{F}_{\mathrm{theo}} = 1.66 \times 10^{11}$ pN s^{-1}. We use the standard deviation of the mean as the error.

accumulates at the surface, this leads to an increase in the total number of short-range interactions. The charge density profiles of keratin and water at the surface show that both exhibits enhanced layering (charge alternation) near the hydrophilic surface compared to the hydrophobic surface.

Decomposing energies in short-ranged ($\sim 1/r^6$) van der Waals and long-ranged ($\sim 1/r$) electrostatic interactions by type of interaction gives insight into the molecular interactions governing the pull-off of keratin from a surface (Figure 6). The exact balance between electrostatic and van der Waals contributions may change with the model, but internal comparisons are still possible. The short-ranged van der Waals interactions between keratin and the surface, previously thought to determine the strong adhesion of geckos,[1−4] play a more minor role and are just one of many interaction types in the energy balance during pull-off. The mediating effect of water previously reported[8] is found to vary with surface chemistry. For a hydrophobic surface, the surface water−keratin bridge breaks first between the water and the surface. On a hydrophilic surface, in contrast, the bridge breaks between the water and keratin.

Intrakeratin electrostatic interactions store much of the elastic deformation energy, only recovered after the keratin pull-off. Our computational model shows that intrakeratin electrostatic interactions determine much of the pull-off energy in all scenarios. This result does not conflict with the popular hypotheses that claim that electrostatic interactions play no role[1−4] or just a minor role.[5,27] These refer to electrostatic interactions between a surface and keratin, both of which have net charges since an experiment cannot investigate the intrakeratin electrostatic interactions and is limited to the keratin−surface interactions. In all scenarios, the total electrostatic contributions are of the same magnitude as the van der Waals contributions. They are most important at the hydrophobic surface, where they provide most of the resistance against detachment.

METHODS

United-Atom Model for Gecko Keratin. Immunolocalization by Alibardi[4] examined the location of 16 cysteine-rich beta-proteins of the gecko. The authors showed that especially the Ge-cprp-9 protein is located at the spatula−air interface. It is thought that the beta-sheet region (so-called core-box region) of the Ge-cprp-9 protein[28] polymerizes into nanofibrils and these associate further into fibrils.[9,29,30] The function of these filaments is probably to provide anisotropic elasticity to gecko spatulae and setae.[9]

The Ge-cprp-9 head and tail regions contain large intrinsically disordered regions (Figure 8) that fold into random coils. Intrinsically disordered domains and intrinsically disordered proteins (IDP) have a flat energy landscape in contrast to the typical, strongly funneled energy landscapes of functional proteins.[31] The result of a flat energy landscape in IDPs is that they do not adopt a favored three-dimensional (3D) conformation.

The gecko keratin model assumes that only the head and the tail regions are in contact with the surface and that the core-box region, forming the nanofibrils, is further away from the surface. Thus, we use a truncated Ge-cprp-9 protein and remove the amino acids of the core-box. Therefore, our model does not contain nanofibrils. We exploit that head and tail regions are coil-like and disordered. We create their initial three-dimensional structure using a self-avoiding random walker. A detailed explanation of the random walker is provided in Supporting Information section S1. The interactions are modeled using the united-atom GROMOS 54A7 force field.[22−25] The water model is SPC/E.[35]

Hydrophobic and Hydrophilic Surfaces. The generic hydrophilic and hydrophobic surfaces are a volume of united-atom CH_2 GROMOS 54A7[22−25] beads with number density of $\rho \approx 20$ nm^{-3} and a height of z = 2.475 nm. Beads do not overlap, and with the number density comparable to that of amorphous silicon dioxide, a few water molecules can penetrate up to 0.6 nm into the top surface layer. The top 0.475 nm of the hydrophilic surface include positive and negative charges. The total net charge of the surface is zero. All details can be found in Supporting Information sections S2 and S3.

The macroscopic average contact angle of the hydrophobic surface is θ_c = 111.3 ± 1.3° and of the hydrophilic surface θ_c = 8.2 ± 5.0°, using our SPC/E water model, close to the surfaces studied experimentally by

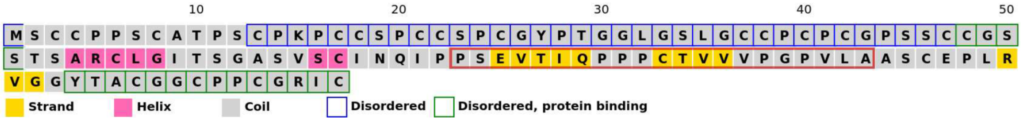

Figure 8. Prediction of the secondary structure of the Ge-cprp-9 protein using PSIPRED4.[32,33] Amino acids that are predicted to fold random coil-like (gray backdrop) and the predicted intrinsically disordered domains (blue enclosure) are in the head and tail regions of the Ge-cprp-9 protein. The core-box region[4] (beta-sheet region) is enclosed in red. Prediction of intrinsically disordered domains is done using DISOPRED3.[34]

Table 2. Average Position of the Top-Half Keratin COM in the Dimension Normal to the Surface z_{COM} after 80 ns Preload Followed by 80 ns Relaxation and the Standard Deviation of the Mean[a]

scenario	z_{COM} (nm)	$\sigma(z_{\mathrm{COM}})$ (nm)
PHOB dry	7.20	0.37
PHIL dry	6.74	0.10
PHOB wet	6.97	0.35
wPHOB wet	6.96	0.33
PHIL wet	6.64	0.08

[a] For both of the hydrophobic and the hydrophilic surfaces, the density is one half of its bulk value at z = 4.4 nm.

Huber et al.[13] More details on the calculation of contact angles are found in Supporting Information section S2, and simulation snapshots are found in Figure S2.

We expect that the surface of an oxide mineral (e.g., the amorphous silica substrate of Huber et al.)[13] is not deformable; at least, it is orders of magnitude stiffer than keratin. We have therefore decided to make our surface completely rigid.

United-Atom Bulk Gecko Keratin Equilibration. All MD simulations are carried out using the GROMACS 2018[36] software package. A barostat and thermostat keep the temperature at 300 K and the pressure at 1 bar. Detailed information is listed in Supporting Information sections S4−S7.

We use only interaction parameters of the GROMOS 54A7 force-field,[22−25] which includes bonded and nonbonded interactions between all atom types. In the united-atom representation, apolar hydrogens are incorporated into their parent carbon atoms. Nonbonded interactions contain van der Waals contributions modeled by Lennard-Jones (12−6) potentials and electrostatic Coulomb interactions due to atomic partial charges to account for the asymmetric distribution of electrons in chemical bonds.

The exact equilibration protocol is detailed in Supporting Information section S5. Gecko keratin contains a large fraction of disulfide bonds.[8,9] We add disulfide bonds to the systems after relaxation in the *NPT* ensemble. One-third of the cysteines (content ≈ 7.5%) are involved in a disulfide bond. Thus, it results in the same cross-linking density as in previous coarse-grained simulations.[9]

The last step of our keratin preparation is to insert water, where necessary, into the system. We create one system with no water (dry) and one with 10 wt % water (wet) for each surface chemistry (PHIL or PHOB). We insert water molecules where they do not overlap with existing atoms. After insertion, they are free to move. Next, we energy-minimize until the maximum force is below 50 kJ mol^{-1} nm^{-1}. Finally, we equilibrate the system in the *NPT* ensemble for 75 ns using a time step of 4 fs. Using a velocity rescale thermostat[37] and a Berendsen barostat,[38] the system is equilibrated at 300 K and 1 bar. The energies and the density converge after around 50 ns. The density of the dry keratin is $\overline{\rho}$ = 1269.6 ± 3.1 kg m^{-3} (a typical experimental keratin density is around 1.3 g cm^{-3}),[39,40] the density of the wet keratin, including the water reaches $\overline{\rho}$ = 1281.8 ± 1.2 kg m^{-3}.

Nonequilibrium Pull-Off Simulations. To measure the pull-off force of the keratin, we use force probe molecular dynamics (FPMD) on periodic semi-infinite keratin attached to a surface (Figure 1) as in our previous work on gecko adhesion.[8] The keratin and surface are periodic in the dimensions parallel to the surface. In the current work, we extended the preload (external force pressing keratin against the surface) and relax (no external force) run times to 80 ns. More details can be found in Supporting Information sections S7 and S8.

In experiment and nature, the spatula is not vertically lifted off the surface but peeled off sideways, like an adhesive tape. Delamination occurs by a proceeding delamination front. The geometry of the delamination front resembles that of a crack propagation zone. Different from a crack inside a polymeric material, however, no chemical bonds are broken (there are none between keratin and surface), and crazes do not precede the delamination front. Our system of (6.8 nm)^2 area is small enough to be regarded as a small part of the much larger (μm^2) delamination zone. Since we cannot simulate (with current computer performance) the full geometry necessary for peel-off, absolute pull-off forces and (pull-off pressures) are not directly comparable to values gathered by AFM experiments. We want to emphasize that the difference between AFM and our pull-off forces is due to different geometries and not the choice of force field.

Results of this work were used as target properties for a multiscale modeling approach to simulate a whole spatula. With the generated mesoscale model we were able to peel-off a whole gecko spatula from a nanoscopic flat hydrophobic surface.[41] As a result, we showed, that pull-off forces extrapolated to loading rates of AFM experiments are comparable to experiments (in the order of 10 nN pull-off force of one spatula) when a peel-off geometry was used. We, therefore, validated the united-atom gecko keratin model developed in this work and believe it is a good candidate to investigate the molecular mechanisms involved in gecko adhesion. In future investigations, we may use both works to investigate contact splitting[42] during gecko adhesion.

ASSOCIATED CONTENT

Supporting Information

The Supporting Information is available free of charge at https://pubs.acs.org/doi/10.1021/acsnano.2c08627.

> How the initial structure is created by the random walker, details about the contact angle calculation, hydrophobic and hydrophilic surface creation, bulk gecko keratin equilibration protocol, computational details in general, computational details about mechanical bulk characterization simulations, nonequilibrium pull-off simulations, equilibration of gecko keratin on the surface, force−time profile and dynamic force spectrum fits, figure about relative pull-off forces, table summarizing fitting procedure used in dynamic force spectrum fits, charge density of keratin in all five scenarios, protein-backbone dynamics near the interface, table summarizing balance of absolute energetic contributions during pull-off (PDF)

AUTHOR INFORMATION

Corresponding Authors

Tobias Materzok − *Eduard-Zintl-Institut für Anorganische und Physikalische Chemie and Profile Area Thermofluids and Interfaces, Technische Universität Darmstadt, D-64287 Darmstadt, Germany;* orcid.org/0000-0002-3576-046X; Email: t.materzok@theo.chemie.tu-darmstadt.de

Annabelle Canestraight − *Department of Chemical Engineering, University of California Santa Barbara, Santa Barbara, California 93106, United States*; Email: acanestraight@ucsb.edu

Stanislav N. Gorb − *Zoological Institute Functional Morphology and Biomechanics, Kiel University, D-24118 Kiel, Germany*; Email: sgorb@zoologie.uni-kiel.de

Florian Müller-Plathe − *Eduard-Zintl-Institut für Anorganische und Physikalische Chemie and Profile Area Thermofluids and Interfaces, Technische Universität Darmstadt, D-64287 Darmstadt, Germany*; orcid.org/0000-0002-9111-7786; Email: f.mueller-plathe@theo.chemie.tu-darmstadt.de

Complete contact information is available at: https://pubs.acs.org/10.1021/acsnano.2c08627

Notes

The authors declare no competing financial interest.

ACKNOWLEDGMENTS

T.M. thanks Hossein Eslami and Eunsang Lee for valuable feedback and Danna de Boer for feedback on the manuscript.

REFERENCES

(1) Dellit, W.-D. *Zur Anatomie und Physiologie der Geckozehe*. Ph.D. Thesis, Universität Jena, Jena, 1934.

(2) Autumn, K.; Liang, Y. A.; Hsieh, S. T.; Zesch, W.; Chan, W. P.; Kenny, T. W.; Fearing, R.; Full, R. J. Adhesive Force of a Single Gecko Foot-Hair. *Nature* **2000**, *405*, 681−685.

(3) Sun, W.; Neuzil, P.; Kustandi, T. S.; Oh, S.; Samper, V. D. The Nature of the Gecko Lizard Adhesive Force. *Biophys. J.* **2005**, *89*, L14−L17.

(4) Alibardi, L. Immunolocalization of Specific Keratin Associated Beta-Proteins (Beta-Keratins) in the Adhesive Setae of Gekko Gecko. *Tissue Cell* **2013**, *45*, 231−240.

(5) Song, Y.; Wang, Z.; Li, Y.; Dai, Z. Electrostatic Attraction Caused by Triboelectrification in Climbing Geckos. *Friction* **2022**, *10*, 44.

(6) Wilson, J. R. A. *Collector's Guide to Rock, Mineral, & Fossil Localities of Utah*; Utah Geological Survey: Salt Lake City, UT, 1995; pp 10−11.

(7) Desire, T.; Dieudonne, B.; Rose, Y.-F. In Situ Genesis of Alumino-Ferruginous Nodules in a Soil Profile Developed on Garnet Rich Micaschist in the High Reliefs of South Cameroon Rainforest Zone (Central Africa). *Open J. Geol.* **2011**, *5*, 56.

(8) Materzok, T.; Gorb, S.; Müller-Plathe, F. Gecko Adhesion: a Molecular-Simulation Perspective on the Effect of Humidity. *Soft Matter* **2022**, *18*, 1247−1263.

(9) Endoh, K. S.; Kawakatsu, T.; Müller-Plathe, F. Coarse-Grained Molecular Simulation Model for Gecko Feet Keratin. *J. Phys. Chem. B* **2018**, *122*, 2203−2212.

(10) Marrink, S. J.; Risselada, H. J.; Yefimov, S.; Tieleman, D. P.; de Vries, A. H. The MARTINI Force Field: Coarse Grained Model for Biomolecular Simulations. *J. Phys. Chem. B* **2007**, *111*, 7812−7824.

(11) Monticelli, L.; Kandasamy, S. K.; Periole, X.; Larson, R. G.; Tieleman, D. P.; Marrink, S.-J. The MARTINI Coarse-Grained Force Field: Extension to Proteins. *J. Chem. Theory Comput.* **2008**, *4*, 819−834.

(12) de Jong, D. H.; Singh, G.; Bennett, W. F. D.; Arnarez, C.; Wassenaar, T. A.; Schäfer, L. V.; Periole, X.; Tieleman, D. P.; Marrink, S. J. Improved Parameters for the Martini Coarse-Grained Protein Force Field. *J. Chem. Theory Comput.* **2013**, *9*, 687−697.

(13) Huber, G.; Mantz, H.; Spolenak, R.; Mecke, K.; Jacobs, K.; Gorb, S. N.; Arzt, E. Evidence for Capillarity Contributions to Gecko Adhesion from Single Spatula Nanomechanical Measurements. *Proc. Natl. Acad. Sci. U.S.A.* **2005**, *102*, 16293−16296.

(14) Stark, A. Y.; Klittich, M. R.; Sitti, M.; Niewiarowski, P. H.; Dhinojwala, A. The Effect of Temperature and Humidity on Adhesion of a Gecko-Inspired Adhesive: Implications for the Natural System. *Sci. Rep.* **2016**, *6*, 30936.

(15) Prowse, M.; Wilkinson, M.; Puthoff, J.; Mayer, G.; Autumn, K. Effects of Humidity on the Mechanical Properties of Gecko Setae. *Acta Biomater* **2011**, *7*, 733−8.

(16) Puthoff, J. B.; Prowse, M. S.; Wilkinson, M.; Autumn, K. Changes in Materials Properties Explain the Effects of Humidity on Gecko Adhesion. *J. Exp. Biol.* **2010**, *213*, 3699−3704.

(17) Stark, A. Y.; Subarajan, S.; Jain, D.; Niewiarowski, P. H.; Dhinojwala, A. Superhydrophobicity of the Gecko Toe Pad: Biological Optimization Versus Laboratory Maximization. *Philos. Trans. Royal Soc.* **2016**, *374*, 20160184.

(18) Huber, G.; Orso, S.; Spolenak, R.; Wegst, U. G. K.; Enders, S.; Gorb, S. N.; Arzt, E. Mechanical Properties of a Single Gecko Seta. *Mater. Res.* **2008**, *99*, 1113−1118.

(19) Taylor, A. M.; Bonser, R. H. C.; Farrent, J. W. The Influence of Hydration on the Tensile and Compressive Properties of Avian Keratinous Tissues. *J. Mater. Sci.* **2004**, *39*, 939−942.

(20) Leroch, S.; Wendland, M. Simulation of Forces between Humid Amorphous Silica Surfaces: A Comparison of Empirical Atomistic Force Fields. *J. Phys. Chem. C* **2012**, *116*, 26247−26261.

(21) Lee, S. H.; Rossky, P. J. A Comparison of the Structure and Dynamics of Liquid Water at Hydrophobic and Hydrophilic Surfaces—a Molecular Dynamics Simulation Study. *J. Chem. Phys.* **1994**, *100*, 3334−3345.

(22) Schuler, L. D.; Daura, X.; van Gunsteren, W. F. An Improved GROMOS96 Force Field for Aliphatic Hydrocarbons in the Condensed Phase. *J. Comput. Chem.* **2001**, *22*, 1205−1218.

(23) Oostenbrink, C.; Villa, A.; Mark, A. E.; van Gunsteren, W. F. A Biomolecular Force Field Based on the Free Enthalpy of Hydration and Solvation: The GROMOS Force-Field Parameter Sets 53A5 and 53A6. *J. Comput. Chem.* **2004**, *25*, 1656−1676.

(24) Schmid, N.; Eichenberger, A. P.; Choutko, A.; Riniker, S.; Winger, M.; Mark, A. E.; van Gunsteren, W. F. Definition and Testing of the GROMOS Force-Field Versions 54A7 and 54B7. *Eur. Biophys. J.* **2011**, *40*, 843.

(25) Huang, W.; Lin, Z.; van Gunsteren, W. F. Validation of the GROMOS 54A7 Force Field with Respect to Beta-Peptide Folding. *J. Chem. Theory Comput* **2011**, *7*, 1237−1243.

(26) Mitchell, C. T.; Dayan, C. B.; Drotlef, D.-M.; Sitti, M.; Stark, A. Y. The Effect of Substrate Wettability and Modulus on Gecko and Gecko-Inspired Synthetic Adhesion in Variable Temperature and Humidity. *Sci. Rep.* **2020**, *10*, 19748.

(27) Izadi, H.; Stewart, K. M. E.; Penlidis, A. Role of Contact Electrification and Electrostatic Interactions in Gecko Adhesion. *J. R. Soc. Interface* **2014**, *11*, 20140371.

(28) Calvaresi, M.; Eckhart, L.; Alibardi, L. The Molecular Organization of the Beta-Sheet Region in Corneous Beta-Proteins (Beta-Keratins) of Sauropsids Explains its Stability and Polymerization into Filaments. *J. Struct. Biol.* **2016**, *194*, 282−291.

(29) Hallahan, D. L.; Keiper-Hrynko, N. M.; Shang, T. Q.; Ganzke, T. S.; Toni, M.; Dalla Valle, L.; Alibardi, L. Analysis of Gene Expression in Gecko Digital Adhesive Pads Indicates Significant Production of Cysteine- and Glycine-Rich Beta-Keratins. *J. Exp. Zool.* **2009**, *312B*, 58−73.

(30) Rizzo, N. W.; Gardner, K. H.; Walls, D. J.; Keiper-Hrynko, N. M.; Ganzke, T. S.; Hallahan, D. L. Characterization of the Structure and Composition of Gecko Adhesive Setae. *J. R. Soc. Interface* **2006**, *3*, 441−451.

(31) Papoian, G. A. Proteins with Weakly Funneled Energy Landscapes Challenge the Classical Structure−Function Paradigm. *Proc. Natl. Acad. Sci. U.S.A.* **2008**, *105*, 14237−14238.

(32) Jones, D. T. Protein Secondary Structure Prediction Based on Position-Specific Scoring Matrices. *J. Mol. Biol.* **1999**, *292*, 195−202.

(33) Buchan, D. W. A.; Jones, D. T. The PSIPRED Protein Analysis Workbench: 20 Years on. *Nucleic Acids Res.* **2019**, *47*, W402−W407.

(34) Jones, D. T.; Cozzetto, D. DISOPRED3: Precise Disordered Region Predictions with Annotated Protein-Binding Activity. *Bioinformatics* **2015**, *31*, 857−863.

(35) Berendsen, H. J. C.; Grigera, J. R.; Straatsma, T. P. The Missing Term in Effective Pair Potentials. *J. Phys. Chem.* **1987**, *91*, 6269−6271.

(36) Hess, B.; Kutzner, C.; van der Spoel, D.; Lindahl, E. GROMACS 4: Algorithms for Highly Efficient, Load-Balanced, and Scalable Molecular Simulation. *J. Chem. Theory Comput.* **2008**, *4*, 435−447.

(37) Bussi, G.; Donadio, D.; Parrinello, M. Canonical Sampling Through Velocity Rescaling. *J. Chem. Phys.* **2007**, *126*, 014101.

(38) Berendsen, H. J. C.; Postma, J. P. M.; van Gunsteren, W. F.; DiNola, A.; Haak, J. R. Molecular Dynamics with Coupling to an External Bath. *J. Chem. Phys.* **1984**, *81*, 3684−3690.

(39) Fraser, R. D. B.; MacRae, T. P.; Parry, D. A. D.; Suzuki, E. The Structure of Feather Keratin. *Polymer* **1971**, *12*, 35−56.

(40) Mason, P. Density and Structure of Alpha-Keratin. *Nature* **1963**, *197*, 179−180.

(41) Materzok, T.; De Boer, D.; Gorb, S.; Müller-Plathe, F. Gecko Adhesion on Flat and Rough Surfaces: Simulations with a Multi-Scale Molecular Model. *Small* **2022**, *18*, 2201674.

(42) Arzt, E.; Gorb, S.; Spolenak, R. From Micro to Nano Contacts in Biological Attachment Devices. *Proc. Natl. Acad. Sci. U.S.A.* **2003**, *100*, 10603−10606.

SUPPORTING INFORMATION

How does Gecko Keratin stick to hydrophilic and hydrophobic surfaces in the presence and absence of water? An atomistic molecular dynamics investigation

Tobias Materzok,*,† Annabelle Canestraight,*,‡ Stanislav N. Gorb,*,¶ and Florian Müller-Plathe*,†

†Eduard-Zintl-Institut für Anorganische und Physikalische Chemie and Profile Area Thermofluids and Interfaces, Technische Universität Darmstadt, Alarich-Weiss-Str. 8, D-64287 Darmstadt, Germany
‡Department of Chemical Engineering, University of California Santa Barbara, 3357 Engrg II UCSB, Santa Barbara, CA, 93106, United States
¶Zoological Institute Functional Morphology and Biomechanics, Kiel University, Am Botanischen Garten 1-9, D-24118 Kiel, Germany

E-mail: t.materzok@theo.chemie.tu-darmstadt.de; acanestraight@ucsb.edu; sgorb@zoologie.uni-kiel.de; f.mueller-plathe@theo.chemie.tu-darmstadt.de

1 Gecko spatula keratin model

A self-avoiding random walker inserts the core-box knockout amino acid sequence into a simulation box of given size under three-dimensional periodic boundary conditions (PBC) until a target density of 1.3 g cm^{-1} is reached. As a basis for our self-avoiding random walker we used the PeptideBuilder library[1] where each added residue (amino acid) is placed by specifying the angles ψ_{i-1}, ω_i and ϕ_i (Figure S1). The coordinates of the alpha carbon at $i-1$ and the aforementioned angles define the position of the new $\mathrm{C}_\alpha i$ and the position of the functional group R_i.

Excluded volume is taken into account for all atoms during the growth of the chain, and moves are only accepted if no overlap occurs. Excluded volume for the C_{i-1} and $\mathrm{C}_{\alpha i-1}$ atoms are not taken into account. We use separate cutoffs for intramolecular excluded volume

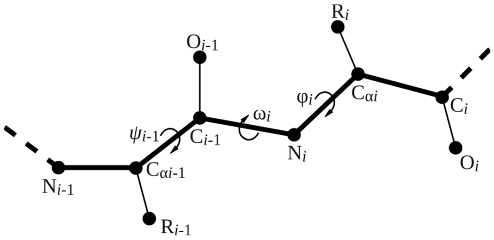

Figure S1: Backbone dihedral angle convention of the PeptideBuilder library[1]. The self-avoiding random walker we developed, places a new residue i by choosing a uniform random number for ψ_{i-1} ω_i and ϕ_i and accepting a move if no overlap occurs.

overlaps $\sigma_{\text{intra}} = 0.185$ nm and for intermolecular overlaps $\sigma_{\text{inter}} = 0.19$ nm.

2 Model hydrophobic and hydrophilic surface

The surface is generated by randomly placing beads inside a target volume until the number density $\rho \approx 20$ nm^{-3} is reached (to compare, silicone density in amorphous silicone dioxide $\rho_{\text{Si}} \approx 20$ nm^{-3}, polyethelyene density $\rho_{\text{CH}_2} \approx 3$ nm^{-3}).The surface slab (periodic in x and y) extends from z=0.1 nm to z=2.475 nm.

All surface beads are treated as atoms of type CH2 of the GROMOS 54A7 FF[2–5]. To create a hydrophilic surface, without changing the surface morphology and roughness, we "switch-on" charges in beads in a thin layer at the surface-air interface. This charged, hydrophilic, layer is made up of the same bead type as the hydrophobic surface (CH2), except that half of the beads have a positive charge (0.5 e) and the other half negative charges (-0.5 e). The ± 0.5 e charge is comparable with partially charged oxygen atoms and their neighboring metal atoms in an oxide mineral. They are included on the beads between z=2.0 and z=2.475 nm. Thus, only the top 0.475 nm of the hydrophilic surface includes positive and negative charges, and we make sure that the total net charge of the surface is zero. Thus the surface is polar and net neutral. For the hydrophobic surface model, all beads are kept uncharged.

The contact angle of the surfaces are computed by the sessile drop method. A cylindrical drop is placed on top of a surface and equilibrated, see Figure S2. We choose a droplet radius of around $R = 4$ nm for the contact angle calculations (see Figure S3). The hydrophobic surface results in an average (N=5, 60 ns equilibration, 20 ns trajectory for analysis) contact angle of 110.8 ± 1.3°, the hydrophilic surface in $\theta_n = 14.7 \pm 3.3°$. The influence of the droplet radius on the liquid-vapor surface tension, and to that extent, the deviation of the calculated contact angle θ_n from the macroscopic contact angle θ_c can be estimated[6] by taking the Tolman length[7] δ (SPC/E water $\delta \approx -0.05$ nm[8]) into account. The increase in the nanoscopic liquid-vapor surface tension compared to the macroscopic surface tension $\gamma_{\text{LV}} = \gamma_{\text{LV}}^{\infty}(1 - 2\delta/R)$ for a SPC/E water drop of 4 nm radius is around 2.5%. The change in contact angle $\Delta\theta$ due to overestimation of the nanoscopic liquid-vapor surface tension can be expressed as

$$\begin{aligned}\Delta\theta &= \cos^{-1}\left(\frac{\gamma_{\text{SL}} - \gamma_{\text{SV}}}{\gamma_{\text{LV}}/1.025}\right) - \cos^{-1}\left(\frac{\gamma_{\text{SL}} - \gamma_{\text{SV}}}{\gamma_{\text{LV}}}\right) \\ &= \theta_n - \theta_c\end{aligned} \tag{1}$$

with γ_{SL} the solid-liquid surface tension, γ_{SV} the solid-vapor surface tension and the SPC/E liquid-vapor surface tension[9,10] $\gamma_{\text{LV}} \approx 62.7$mN m^{-2}. By computing equation S1 we can show that the hydrophobic contact angle is underestimated by 0.55°. By correcting for these finite size effects, the macroscopic average contact angle of the hydrophobic surface is $\theta_c = 111.3 \pm 1.3°$. In contrast, the macroscopic average contact angle of the hydrophilic surface is underestimated, with $\Delta\theta = -6.5 \pm 1.7°$ and the macroscopic average contact angle for the hydrophilic surface is $\theta_c = 8.2 \pm 5.0°$.

3 Surface modelling

We calculate the number of beads given a target number density $\rho_{\text{surface}} = 20$ nm^{-3} and the target surface volume. Then, we insert half of the beads into the volume using uniformly distributed random positions. Next, we move overlapping beads in small, incremental steps, until no overlap $\sigma_{\text{insertion}}$ occurs. Afterwards, we insert the other half of beads at positions surrounding the already inserted beads, since this increases the likelihood of finding empty cavities. We use a slightly modified Boltzmann-inverted Morse-style potential[11] as a probability density function to efficiently sample valid positions surrounding the first half of beads. Similar parameters as the Si-O Morse potential parameters for a amorphous silica surface are used[12] ($R_0 = 0.1628$ nm). We optimized the

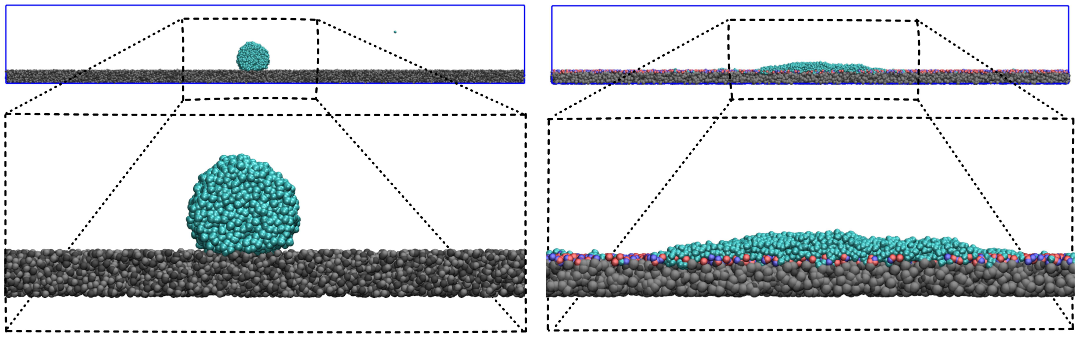

Figure S2: Snapshots of both hydrophobic (left) and hydrophilic (right) surfaces after an 80 ns equilibration run in the NVT ensemble at 300 K. The periodic boundaries are shown as a blue square surrounding the systems.

functional form (Equation S2) and its parameters to make sampling fast and efficient. Internally we use the normalized probability function $P(x) = p(x) / \int_0^\infty p(x)dx$ with $p(x)$ as

$$p(x) = 1 - \exp\left[4\left(e^{30(1-\frac{r}{R_0})} - 2 \cdot e^{\frac{1}{2}30(1-\frac{r}{R_0})}\right)\right] \tag{2}$$

Finally, we correct the positions of beads by moving them in small steps until there is no overlap $\sigma_{\text{insertion}}$.

The overlap cutoffs used in generating the surface are listed in Table S1.

Table S1: Overlap cutoffs used to generate model surface.

Bead-bead distance	$\sigma_{\text{insertion}}$ (nm)
first half-first half	0.27
second half-second half	0.22
first half-second half	0.15

4 Computational details

All bonds are constrained using the LINCS algorithm.[13] Long-range electrostatic interaction are treated by the smooth Particle Mesh Ewald (PME) method[14,15] with a PME order of 4 and a Fourier spacing of 0.12 nm. A real space cutoff of 1.4 nm and a van der Waals interaction cutoff of 1.4 nm is used. We use the Potential-shift-Verlet scheme[16] as a cutoff modifier for a physically[17] smooth transition at the cutoff.

5 Bulk gecko keratin equilibration

To relax and equilibrate the Ge-cprp-9 core-box knockout gecko keratin model the system is energy minimized by slowly switching between a soft-core potential treatment of the interactions and the unmodified interaction potentials, since the extremely dense random walk system has initially strong repulsive forces due to the unspecific treatment of the excluded volume overlap between atoms (as discussed in section S1) during the chain creation.

To solve numerical instabilities in free energy calculations, commonly encountered in e.g thermodynamic integration, realistic soft-core potentials were developed[18,19]. These soft-core potentials are generally used to circumvent the problem of overlapping singularities if the coupling parameter λ is close to the switched-off state. We switch the soft-core potentials from $\lambda = 0.25$ to $\lambda = 1.0$ in steps of $\Delta\lambda = 0.05$ during minimization using steepest descent to energy minimize the very dense system. The modified soft-core interaction potential V_{sc} is coupled to λ as

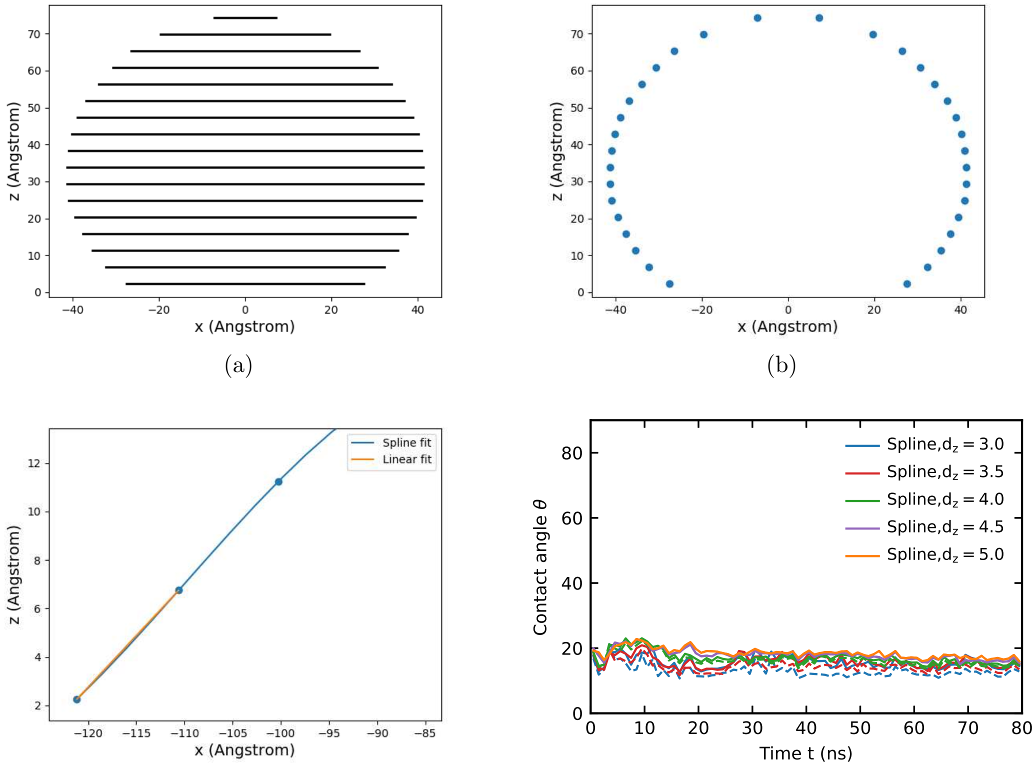

(a) (b)

(c) (d)

Figure S3: The droplet is sliced into layers with a binwidth of $d_z = 0.3$ nm; for illustration purposes, we use a larger d_z for (a). The radial density of each layer is computed with binwidth $r_b = 0.2$ nm. (b) The average number density of water in the center of the droplet is used to find the intersection point between the radial density in each layer, averaged over 1 ns trajectory time, with the position where the density is half the droplets interior. (c) We performed spline and linear fits of the ”edges” of the droplet (here shown for the hydrophilic surface). (d) The calculated contact angle (the arctangent of the slope) is shown against simulation time for the hydrophilic surface. Solid lines are values from spline fits and dashed lines from linear fits. The average calculated contact angle of the last 20 ns is translated to the macroscopic contact angle described in Supplementary Section S2.

$$V_{\mathrm{sc}}(r) = \lambda V(r_\chi) \quad (3)$$

with $r_\chi = (\alpha\sigma^6(1-\lambda)^p + r^6)^{1/6}$ and the soft-core parameter $\alpha = 2$ and soft-core power $p = 2$, which leads to smooth treatment of $r << \sigma$ (Figure S4) and therefore a constant repulsive force at $r = 0$ nm.

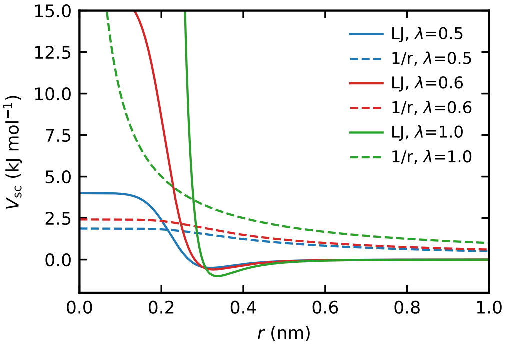

Figure S4: Soft-core potential V_{sc} with increasing coupling parameter λ against distance r, with illustrative Lennard-Jones $\epsilon = 1$ kJ mol^{-1} and $\sigma = 0.3$ nm. Soft-core parameter $\alpha = 2$ and soft-core power $p = 2$ lead to soft-core "singularities" for Lennard-Jones (LJ) and Coulomb (1/r) interactions.

After energy minimization from $\lambda = 0.25$ to 1.0, we further exploit this method to dramatically speed up the high temperature relaxation needed to amorphize the system. Because of the soft-core potentials and the thermal energy at the high annealing temperature of 1300 K ($RT = 11$ kJ mol^{-1}, compare to Figure S4) the decay of the autocorrelation function of the end-to-end vector and of the radius of gyration is reduced down to ≈ 25 ps (from ≈ 2200 ps using hard potentials at 1300 K). We can therefore relax any unrealistic frustrations on the picosecond timescale, *i.e.* the chains loose any correlations to their initial conformations. During the soft-core annealing simulation we run $\lambda = 0.7$ to 1.0 in steps of $\Delta\lambda = 0.1$ totaling four runs of 100 ps with a timestep of 0.4 fs. This "slow push-off" procedure is, for closely related soft-core potentials known to significantly reduce perturbations in local chain conformations.[20] We use a relative dielectric constant of $\epsilon_r = 80$ to simulate the electrostatic screening effect of water the proteins would encounter during their post-translational folding inside the aqueous living cell. A Berendsen thermostat[21], with a coupling time constant of $\tau_T = 0.1$ ps, is used to simulate in the NVT ensemble.

After the high temperature soft-core annealing we cool the system down in steps of 50 K. We step-wise decrease the relative dielectric constant to $\epsilon_r = 1$ with $\epsilon_r(T) = \frac{T}{1\,\mathrm{K}} \cdot 0.08 - 23$. This NVT cool down is performed from 1300 K to 700 K with a timestep of 0.4 fs for 250 ps. To speed up computation times we switch first to 0.6 fs timestep below 800 K, then to 1 fs below 700 K and, finally, to a timestep of 2 fs below 400 K. We further increase the equilibration time from 250 ps to 2.5 ns when the system cooled down to 350 K and to a equilibration time of 5 ns at 300 K. During each cooling step, the potential energies converge and the radius of gyration converged and stays constant at 300 K for 5 ns, however, since our material is made up of a intrinsically disordered protein the radius of gyration differs greatly between chains. At temperatures 350 K and 300 K we transfer the system from the NVT ensemble to the NPT ensemble by using a isotropic Berendsen barostat[21] with a coupling time of $\tau_p = 0.5$ ps and a compressibility of $4.5 \cdot 10^{-5}$ bar^{-1}.

After cool down the density is at $\overline{\rho} = \frac{1268.23+1271.49+1263.09+1271.58}{4} = 1268.6$ kg m^{-3} and we run NPT relaxation for another 5 ns with a velocity rescaling thermostat[22], reaching a density of $\overline{\rho} = \frac{1269.17+1271.63+1265.52+1273.86}{4} = 1270.0$ kg m^{-3} using a timestep of 2 fs.

In the next step we add disulfide bridges to the NPT relaxed systems. Our protocol results in $\approx 1/3$ of cysteins being involved in a disulfide bond, which corresponds to approximately 7.5% cystin content, resulting in the same cross-linking density from previous coarse-grained work.[23] To accomplish 7.5% cross-linking density we systematically grow a cutoff positioned on each cysteine thiol to find neighboring cysteins. We grow these cutoffs in steps of 0.05 nm until the number of possible unique disulfide bridges reaches the target cross-linking density. We make sure that each cysteine can only be cross-linked to one other cysteine. After switching from cysteine's thiol functional groups to a disulfide bridge, the maximum bond length is around 0.6 to 0.8 nm (which means the cut-off grew on average to a radius of 0.6 to 0.8 nm to satisfy our set condition of 7.5% cross-linking density). The cross-linked elastomer-like system is energy minimized with soft-core potentials from $\lambda = 0.25$ to $\lambda = 1.0$ in steps of 0.05. Afterwards we energy minimize without soft-core potentials until the maximum force is below 100 $\mathrm{kJ\,mol^{-1}\,nm^{-1}}$. The maximum bond length after minimization is 0.2049 nm, *i.e.* equal to the equilibrium bond length for disulfide bridges parameterized in the GROMOS FF.

We subsequently run a NPT relaxation of the now cross-linked elastomer-like system. Run time for this step is 10 ns using a timestep of 2 fs, a isotropic Berendsen barostat[21] with a coupling time of $\tau_p = 0.5$ ps and a compressibility of $4.5 \cdot 10^{-5}$ $\mathrm{bar^{-1}}$. Temperature coupling is done with a velocity rescaling thermostat[22]. The density converges after 5 ns to around $\overline{\rho} = \frac{1267.68+1259.67+1264.78+1256.49+1268.46}{5} = 1263.4 \pm 4.6\ \mathrm{kg\,m^{-3}}$.

In the final step of our equilibration protocol for the bulk gecko keratin we insert 0 wt% and 10 wt% SPC/E water under consideration of individual Lennard-Jones σ of the gecko keratin atoms. Next, we perform standard energy minimization until the maximum force is below 50 $\mathrm{kJ\,mol^{-1}\,nm^{-1}}$. Finally, we equilibrate the system in the NPT ensemble for 75 ns using a timestep of 4 fs. The same velocity rescaling thermostat[22] and a Berendsen barostat[21] are used. The energies and the density converge after around 50 ns, the density of the dry gecko keratin converges to a value of $\overline{\rho} = 1269.6 \pm 3.1\ \mathrm{kg\,m^{-3}}$, the density of the wet gecko keratin (plus water) reaches $\overline{\rho} = 1281.8 \pm 1.2\ \mathrm{kg\,m^{-3}}$.

6 Simulations to compute mechanical bulk characteristics

Production runs to calculate the Young's modulus are performed in three-dimensional (3D) periodic boundary conditions (PBC) using a time step of 2 fs. A velocity rescale thermostat[22] is used to keep the systems at 300 K, and a semi-isotropic Berendsen barostat[21] is used to keep the system at 1 bar. The time constant of coupling the temperature is $\tau_T = 0.1$ ps. The barostat coupling time is $\tau_p = 0.5$ ps. We use a compressibility of $4.5 \cdot 10^{-5}$ $\mathrm{bar^{-1}}$ in x and y and a compressibility of 0 $\mathrm{bar^{-1}}$ in z, similar to previous work[23,24]. The barostat therefore only allows size fluctuations in the x and y directions. The system is uniformly scaled in the z direction with a straining rate of $0.00001\ \mathrm{nm\,ps^{-1}} = 1.0\ \mathrm{mm\,s^{-1}}$. For each of the five independently generated systems, five non-equilibrium production runs are simulated, in total 25 stress-strain realizations. The Young's modulus is calculated with a linear fit to the first 1% strain. Poisson's ratio is calculated using equilibrium runs at strains 1% to 5% (*i.e.* scaling the system and subsequent production runs at these strains). The Poisson's ratio we discuss is the average Poisson's ratio over all five strains. Simulations to calculate the Poisson's ratio are done in 3D PBC and are run for 100 ns, properties converge not later than 50 ns and the last 25 ns are used for analysis.

7 Non-equilibrium pull-off simulations

The center of mass of the top half of the keratin z_{COM} is connected to a virtual cantilever *via* a harmonic spring ($k_{\mathrm{pull}} = 500\ \mathrm{kJ\,nm^{-2}}$), mimicking atomic force microscopy (AFM) experiments. During pull-off, the position of the virtual cantilever is moved with constant velocity in the normal direction away from the surface[24]. The force experienced by the top half keratin is $F_{\mathrm{pull}} = k_{\mathrm{pull}}(vt - z(t))$ with v the constant pulling velocity, t the time and $z(t)$ the actual position of the center of mass of the top half keratin.[25] When the pull force gets larger than the force with which the keratin is attached to the surface, the keratin detaches. The maximum force needed to detach the keratin is called pull-off force F, and its negative is the adhesion force. We applied Gaussian smoothing with a kernel width of 0.1 nm to the force profiles, as we have done previously[24], inspired by Sheridan *et al.*[26].

We divide the pull-off force F by the surface area A, which is slightly different between the five independently generated systems after equilibration. The resulting pull-off pressure p is multiplied with the mean surface area ($\langle A \rangle = 45$ nm^2) of all systems to get an averaged pull-off force F^η.

We simulate 10 pull-off runs for seven different loading rates (different pulling velocities v) for all five systems, resulting in 350 pull-off runs for each of the 5 different scenarios, summing up to 1750 non-equilibrium pulling simulations in total. Averages at one loading rate are taken over 50 realizations of the pull-off pathway the gecko keratin takes when it is detached from the surface. The theoretical[25] loading rates $\dot{F}_{\text{theo}} = k_{\text{pull}} v$ range from $1.66 \cdot 10^{11}$ pN s^{-1} to $8.3 \cdot 10^{13}$ pN s^{-1}. To calculate the effective[26] loading rates $\dot{F}$, the Gaussian smoothed force profiles are used to fit a linear function from the beginning $t = 0$ ns until 50% of the time necessary to reach detachment (force maximum).

8 Equilibration of gecko keratin on the surface

The non-equilibrium pull-off simulations are run in two-dimensional (2D) periodic boundary conditions, in contrast to the simulations that are used to calculate the Young's modulus and Poisson's ratio, which need to be performed in 3D PBC to accurately simulate bulk behavior. In 2D PBC, the surface and the keratin are semi-infinite parallel to the surface. They are periodic with a finite volume. All simulations that include the surface are in the NVT ensemble.

Pressure is a thermodynamic equilibrium property, and its instantaneous value fluctuates strongly (Root mean square deviation of the pressure for the dry keratin is at around 300 to 400 bar). Therefore, we should not pick the last step in the NPT equilibration trajectory, but we should carefully choose a configuration where the instantaneous pressure is close to 1 bar. However, since pressure fluctuations are large, the probability of finding configurations in a equilibration trajectory which fulfills two necessities, long enough equilibration time and an instantaneous pressure of 1 bar, is low. Nevertheless, the volume is much less affected by pressure fluctuations since most pressure fluctuations are due to inter-atomic forces. Therefore we are using a configuration where the volume of the trajectory step (frame) is closest to the volume average of the last ≈ 20% of the NPT equilibration.

The x and y box dimensions of the chosen frame are used for generating the generic surface. We insert the generated surface and the chosen keratin equilibration frame into the same simulation box. If water should be present on a "wet surface", we additionally add a layer of water above the surface (a slice of NPT equilibrated bulk water of 0.2 nm thickness). The keratin is inserted with a minimum distance between the surface and the gecko keratin of 1.0 nm. The equation of motion for all surface beads are not computed, therefore the beads do not move during the simulation. They function as a space-fixed external potential in the vapor phase surrounding the keratin, as we have done in previous work.[24]

To forbid water molecules to leave the simulation box, we insert two Lennard-Jones walls at the bottom $z = 0$ nm and top $\max(z)$ of the simulation cell, with a interaction type of CH2. In GROMACS these walls also allow the pull-off in z-direction without being affected by the center-of-mass motion removal. Without walls, the center-of-mass motion removal treatment in GROMACS leads to an effective friction and strongly affects the pull-off force.

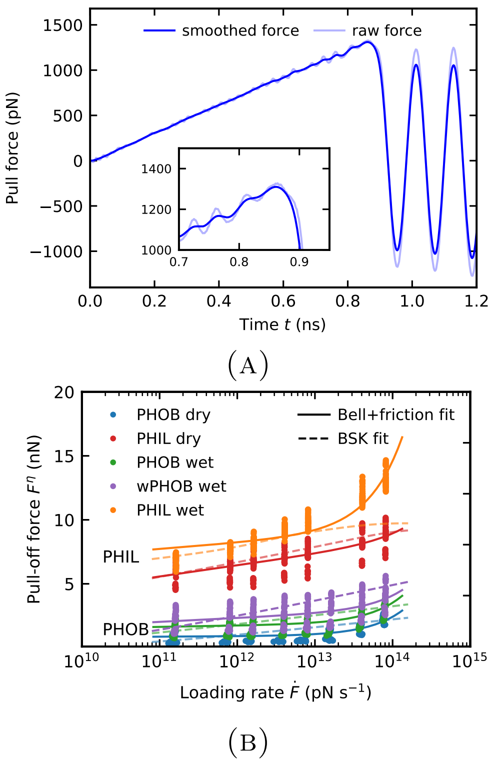

(A)

(B)

Figure S5: (A) Force profile of dry gecko keratin pull-off. At the start of the simulation (after preloading and relaxation runs), the keratin is already attached to the surface. Hence, no jump-in event like in atomic force microscopy occurs. The keratin is then pulled off with a loading rate of $\dot{F}_{\rm theo} = 1.66 \cdot 10^{12}$ pN s^{-1}. The force on the harmonic spring $F_{\rm pull}$ is plotted against the time t. After smoothing the raw force (transparent blue) with a Gaussian kernel with a width respective of 0.1 nm in the position domain, the resulting smoothed force profile (blue) is used to extract the maximum force during pull-off. (B) Dynamic force spectrum for the normalized pull-off force F^η of keratin pull-off from hydrophobic (PHOB) and hydrophilic (PHIL) surfaces against the loading rate $\dot{F}$. For each surface chemistry, dry and wet keratin are first attached and then pulled off, as done previously[24]. Each data point presented is the maximum force extracted from an individual pulling simulation[24], illustrated in (A). Solid lines show the fit to the Bell+friction model, and dashed lines show the mean rupture force predicted by the BSK model. Model parameters are summarized in Supplementary Table S2.

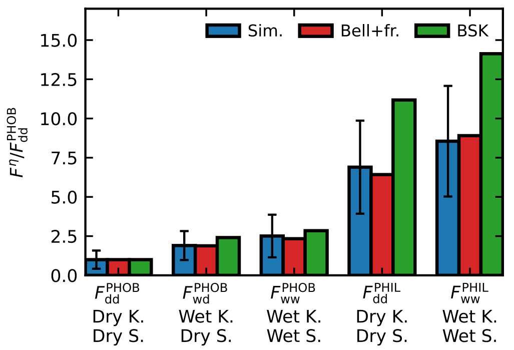

Figure S6: The ratio of pull-off forces to the pull-off force of dry keratin from a dry hydrophobic surface $F^\eta/F^{\rm PHIL}_{\rm dd}$ shows the relative increase due to surface chemistry and water content.

Table S2: Model parameters after performing fits of the Bell+friction model and the BSK model to the dynamic force spectra. The Bell+friction model[25–27], $F = \gamma v + \frac{1}{\beta x_\mathrm{b}} \ln(\frac{\beta k_\mathrm{pull} v \cdot x_\mathrm{b}}{k_0})$, with F being the pull-off force, x_b the distance to the potential barrier and γ the friction coefficient and k_0 the dissociation rate at equilibrium loading rates, was fitted by running a simulated annealing optimization routine (with 1 million steps) parallel 2000 times, randomly selecting 90% of the data points, to operate on. The most frequently found (after rounding to the fourth decimal point) parameter combinations (x_b^Bell, γ^Bell, k_0^Bell) are used as the most probable model parameters. The BSK model[28] with x_b the distance to the transition state, D the diffusivity, and ΔG the activation energy is fitted using global maximum-likelihood estimation. Global means here, that the pull-off force distributions at all 7 loading rates are used simultaneously to fit the BSK distribution. 500 million randomly created model parameter combinations (x_b^BSK, D^BSK, ΔG^BSK) are tested, the parameter combinations with the highest likelihoods are selected and the local space surrounding each parameter combination is tested again one thousand times. We found that this brute force procedure gives higher likelihoods than using more advanced global optimization algorithms, like chained simulated annealing with local optimizers or the more modern, simplicial homology global optimization[29]. Since both models assume a one-dimensional potential barrier during pull-off and we have shown in the main text that many processes take place simultaneously, thus, a more complex energy landscape should be expected, the fits are poor and not used to draw conclusions.

System	x_b^Bell (nm)	γ^Bell ($\mathrm{kJ\,ps\,mol^{-1}\,nm^{-2}}$)	k_0^Bell (ps^{-1})	x_b^BSK (nm)	D^BSK (nm^2)	ΔG^BSK ($k_\mathrm{B}T$)
PHOB dry	0.3494	7367	$1.6 \cdot 10^{-34}$	0.0170	$2.6 \cdot 10^{20}$	43
PHOB wet	0.1028	8055	$6.3 \cdot 10^{-21}$	0.0153	$1.7 \cdot 10^{19}$	44
wPHOB wet	0.0325	5914	$1.0 \cdot 10^{-10}$	0.0086	$1.3 \cdot 10^{21}$	48
PHIL dry	0.0110	3842	$1.0 \cdot 10^{-10}$	0.0102	$8.9 \cdot 10^{13}$	41
PHIL wet	0.0202	27331	$2.0 \cdot 10^{-20}$	0.0423	$3.6 \cdot 10^{5}$	52

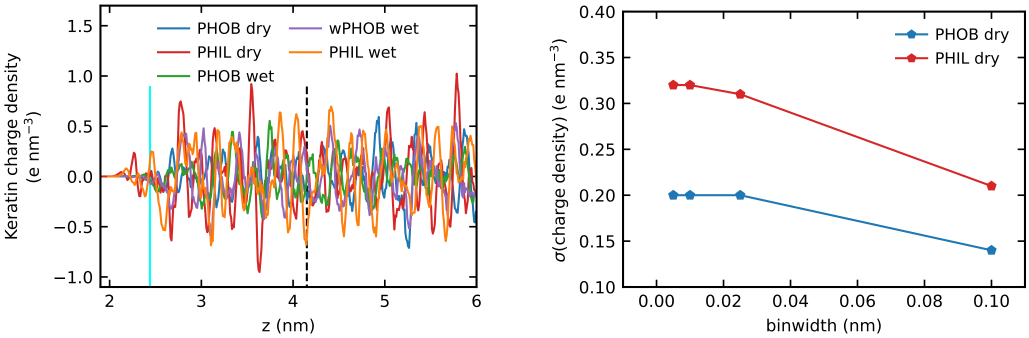

(A) (B)

Figure S7: (A) The charge density of keratin in all five scenarios normal to the surface z. The standard deviation σ of the charge density is calculated between 2.44 nm and 6 nm and is a measure for the amplitude of the charge fluctuations. The standard deviation for the scenarios is as follows: $\sigma(\text{PHOBdry}) = 0.2$ e nm^{-3}, $\sigma(\text{PHOBwet}) = 0.17$ e nm^{-3}, $\sigma(\text{wPHOBwet}) = 0.23$ e nm^{-3}, $\sigma(\text{PHILdry}) = 0.32$ e nm^{-3}, and $\sigma(\text{PHILwet}) = 0.31$ e nm^{-3}. The vertical cyan line denotes where the surface density is half its bulk value at $z = 2.44$ nm. The range of the Lennard-Jones interaction (1.4 nm) from the surface into the keratin is shown as a vertical dashed black line at $z = 4.15$ nm. Values are averaged over the last 55 ns of the relaxation runs (80 ns long) of five independently generated systems. The standard deviation of the mean is used as the error. The binwidth is 0.01 nm. (B) The standard deviation of the charge density calculated between 2.44 nm and 6 nm as a function of binwidth. When the binwidth is smaller than one-fifth of a chemical bond ($<$ 0.1 nm) σ converges.

9 Protein-backbone dynamics near the interface

We define the interface as the first layer of amino acids closest to the surface, *i.e.*, a monolayer of amino acids. Additionally, we define the backbone vector between atom N_i and $C_{\alpha i}$ of an amino acid (Figure S1). We calculate the autocorrelation functions of interface backbone vector orientations. When the autocorrelation function decays to zero, the orientation of the backbone is no longer correlated with its previous orientation. We call this time the decorrelation time τ.

A histogram of decorrelation times τ (Figure S8) reveals that τ follows a power-law distribution. During preload (80 ns long simulation), the mobility of the amino acid segments reduces. Around 20-30% of backbone correlations decay in less than 400 ps (Figure S8 (A), inset). During relaxation (80 ns long), the mobility increases compared to the preload (Figure S8 (B)). The number of very mobile amino acids increases to around 40-60% (inset). Very few backbone orientations are stable, meaning that $p(\tau)$ decays rapidly, and a minimal number of backbone correlations exist longer than 20 ns. During preload, the power-law exponent is much smaller than in the relaxation phase, implying dampened dynamics during preloading of the keratin against a surface.

The mobility of the amino acid segments at the surface-keratin interface monolayer during both preload (with an applied external pressure of 0.4 pN nm^{-2}) and relaxation depends to a small degree on water content and surface chemistry. The hydrophilic surface dampens the keratin-interface mobility, with the power-law exponent decreasing from $\alpha = 1.8$ to 1.6 from PHOB dry to PHIL dry scenarios (Figure S8 (B)). With $\alpha < 1.4$ in wet scenarios, water has an even stronger dampening effect on the mobility of amino acid segments.

Dampened amino acid mobility at the keratin-surface interface may be the reason for the inhibition of fluctuations of the average position above the surface. The reduction in the here discussed power-law exponent also suggests that, in wet and hydrophilic situations, the amino acids form stronger energetic interactions with the surface, which oppose detachment, increasing spatula adhesion.

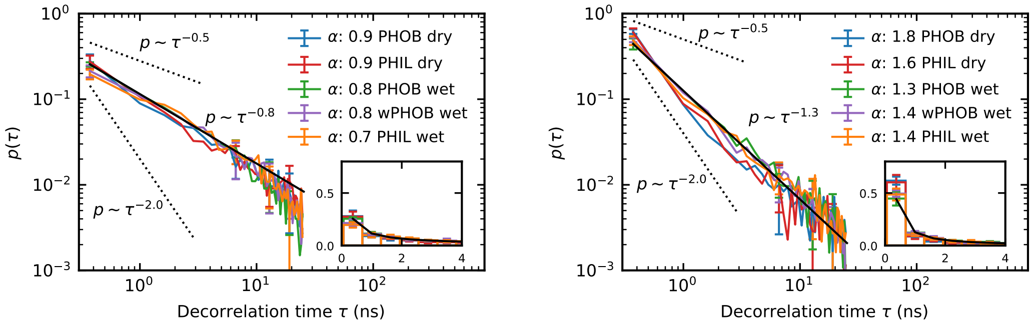

(A) (B)

Figure S8: The probability of amino acid segmental decorrelation times τ during preload (80 ns long) (A) and relaxation (80 ns long) (B). The decorrelation time is defined here as the decay of the autocorrelation function of the vector between atom N_i and $C_{\alpha i}$ of an amino acid (Supplementary Figure S1) at the keratin-surface interface (closest monolayer of amino acids). Shown are the average distributions between all five independent systems for all five scenarios (in total 25 systems), and the standard deviation of the mean is used as the error. We fit with a power-law $p = b \cdot \tau^{\alpha}$. The power-law exponent α is denoted in the legend. The fit for the PHOB wet scenario (green) is shown in black. The inset shows the data with a linear scale between 0 to 4 ns.

Table S3: The work performed on the system until the keratin is pulled off ($L_F = 0$ nm) decomposed into its contributions. The top rows summarize the work related to Lennard-Jones (LJ) type interactions and the bottom rows Coulomb (Cl) type contributions. Thermodynamically, negative energetic contributions favor a process and positive contributions oppose a process. Values are in units of kJ mol^{-1} nm^{-2}.

LJ Type	$W_{\mathrm{dd}}^{\mathrm{PHOB}}$	$W_{\mathrm{wd}}^{\mathrm{PHOB}}$	$W_{\mathrm{ww}}^{\mathrm{PHOB}}$	$W_{\mathrm{dd}}^{\mathrm{PHIL}}$	$W_{\mathrm{ww}}^{\mathrm{PHIL}}$
W-K	0.0	-0.18	0.06	0.0	6.24
W-W	0.0	-0.1	-1.41	0.0	-4.89
K-S	1.24	1.07	3.18	4.93	9.05
W-S	0.0	0.05	0.8	0.0	0.32
K-K	-1.03	0.04	1.39	16.82	15.27
Cl Type	$W_{\mathrm{dd}}^{\mathrm{PHOB}}$	$W_{\mathrm{wd}}^{\mathrm{PHOB}}$	$W_{\mathrm{ww}}^{\mathrm{PHOB}}$	$W_{\mathrm{dd}}^{\mathrm{PHIL}}$	$W_{\mathrm{ww}}^{\mathrm{PHIL}}$
W-K	0.0	-0.14	-1.9	0.0	26.71
W-W	0.0	-0.53	4.14	0.0	10.85
K-S	0.0	0.0	0.0	8.8	10.5
W-S	0.0	0.0	0.0	0.0	-11.89
K-K	5.36	2.09	2.65	7.89	4.22

References

(1) Tien, M. Z.; Sydykova, D. K.; Meyer, A. G.; Wilke, C. O. PeptideBuilder: A simple Python library to generate model peptides. *PeerJ* **2013**, *1*, DOI: `10.7717/peerj.80`.

(2) Schuler, L. D.; Daura, X.; Gunsteren, W. F. v. An improved GROMOS96 force field for aliphatic hydrocarbons in the condensed phase. *J. Comput. Chem.* **2001**, *22*, 1205–1218, DOI: `https://doi.org/10.1002/jcc.1078`.

(3) Oostenbrink, C.; Villa, A.; Mark, A. E.; Gunsteren, W. F. V. A biomolecular force field based on the free enthalpy of hydration and solvation: The GROMOS force-field parameter sets 53A5 and 53A6. *J. Comput. Chem.* **2004**, *25*, 1656–1676, DOI: `https://doi.org/10.1002/jcc.20090`.

(4) Schmid, N.; Eichenberger, A. P.; Choutko, A.; Riniker, S.; Winger, M.; Mark, A. E.; van Gunsteren, W. F. Definition and testing of the GROMOS force-field versions 54A7 and 54B7. *Eur. Biophys. J.* **2011**, *40*, 843, DOI: `10.1007/s00249-011-0700-9`.

(5) Huang, W.; Lin, Z.; van Gunsteren, W. F. Validation of the GROMOS 54A7 Force Field with Respect to beta-Peptide Folding. *J. Chem. Theory Comput.* **2011**, *7*, 1237–1243, DOI: `10.1021/ct100747y`.

(6) Jiang, H.; Patel, A. J. Recent advances in estimating contact angles using molecular simulations and enhanced sampling methods. *Curr. Opin. Chem. Eng.* **2019**, *23*, 130–137, DOI: `10.1016/j.coche.2019.03.012`.

(7) Tolman, R. C. The Effect of Droplet Size on Surface Tension. *J. Chem. Phys.* **1949**, *17*, 333–337, DOI: `10.1063/1.1747247`.

(8) Khalkhali, M.; Kazemi, N.; Zhang, H.; Liu, Q. Wetting at the nanoscale: A molecular dynamics study. *J. Chem. Phys.* **2017**, *146*, 114704, DOI: `10.1063/1.4978497`.

(9) Sakamaki, R.; Sum, A. K.; Narumi, T.; Yasuoka, K. Molecular dynamics simulations of vapor/liquid coexistence using the nonpolarizable water models. *Chem. Phys.* **2011**, *134*, 124708, DOI: `10.1063/1.3574038`.

(10) Vinš, V.; Celný, D.; Planková, B.; Němec, T.; Duška, M.; Hruby, J. Molecular Simulations of the Vapor–Liquid Phase Interfaces of Pure Water Modeled with the SPC/E and the TIP4P/2005 Molecular Models. *EPJ Web Conf.* **2016**, *114*, 02136, DOI: `10.1051/epjconf/201611402136`.

(11) Demiralp, E.; Çağin, T.; Goddard, W. A. Morse Stretch Potential Charge Equilibrium Force Field for Ceramics: Application to the Quartz-Stishovite Phase Transition and to Silica Glass. *Phys. Rev. Lett.* **1999**, *82*, 1708–1711, DOI: `10.1103/PhysRevLett.82.1708`.

(12) Leroch, S.; Wendland, M. Simulation of Forces between Humid Amorphous Silica Surfaces: A Comparison of Empirical Atomistic Force Fields. *J. Phys. Chem. C* **2012**, *116*, 26247–26261, DOI: `10.1021/jp302428b`.

(13) Hess, B.; Bekker, H.; Berendsen, H. J. C.; Fraaije, J. G. E. M. LINCS: A linear constraint solver for molecular simulations. *J. Comput. Chem.* **1997**, *18*, 1463–1472.

(14) Darden, T.; York, D.; Pedersen, L. Particle mesh Ewald: An N log(N) method for Ewald sums in large systems. *J. Chem. Phys.* **1993**, *98*, 10089–10092, DOI: `10.1063/1.464397`.

(15) Essmann, U.; Perera, L.; Berkowitz, M. L.; Darden, T.; Lee, H.; Pedersen, L. G. A smooth particle mesh Ewald method. *J. Chem. Phys.* **1995**, *103*, 8577–8593, DOI: `10.1063/1.470117`.

(16) Páll, S.; Hess, B. A flexible algorithm for calculating pair interactions on SIMD architectures. *Comput. Phys. Commun.* **2013**, *184*, 2641–2650, DOI: `10.1016/j.cpc.2013.06.003`.

(17) van der Spoel, D.; van Maaren, P. J. The Origin of Layer Structure Artifacts in Simulations of Liquid Water. *J. Chem. Theory Comput.* **2006**, *2*, 1–11, DOI: `10.1021/ct0502256`.

(18) Beutler, T. C.; Mark, A. E.; van Schaik, R. C.; Gerber, P. R.; van Gunsteren, W. F. Avoiding singularities and numerical instabilities in free energy calculations based on molecular simulations. *Chem. Phys. Lett.* **1994**, *222*, 529–539, DOI: `10.1016/0009-2614(94)00397-1`.

(19) Zacharias, M.; Straatsma, T. P.; McCammon, J. A. Separation-shifted scaling, a new scaling method for Lennard-Jones interactions in thermodynamic integration. *J. Chem. Phys.* **1994**, *100*, 9025–9031, DOI: `10.1063/1.466707`.

(20) Gartner, T. E.; Jayaraman, A. Modeling and Simulations of Polymers: A Roadmap. *Macromolecules* **2019**, *52*, 755–786, DOI: `10.1021/acs.macromol.8b01836`.

(21) Berendsen, H. J. C.; Postma, J. P. M.; van Gunsteren, W. F.; DiNola, A.; Haak, J. R. Molecular dynamics with coupling to an external bath. *J. Chem. Phys.* **1984**, *81*, 3684–3690, DOI: `10.1063/1.448118`.

(22) Bussi, G.; Donadio, D.; Parrinello, M. Canonical sampling through velocity rescaling. *J. Chem. Phys.* **2007**, *126*, 014101, DOI: `10.1063/1.2408420`.

(23) Endoh, K. S.; Kawakatsu, T.; Müller-Plathe, F. Coarse-Grained Molecular Simulation Model for Gecko Feet Keratin. *J. Phys. Chem. B* **2018**, *122*, 2203–2212, DOI: `10.1021/acs.jpcb.7b10481`.

(24) Materzok, T.; Gorb, S.; Müller-Plathe, F. Gecko adhesion: a molecular-simulation perspective on the effect of humidity. *Soft Matter* **2022**, *18*, 1247–1263, DOI: `10.1039/D1SM01232K`.

(25) Grubmüller, H. Force probe molecular dynamics simulations. *Methods Mol. Biol.* **2005**, *305*, 493–515, DOI: `10.1007/978-1-59259-912-7_23`.

(26) Sheridan, S.; Gräter, F.; Daday, C. How Fast Is Too Fast in Force-Probe Molecular Dynamics Simulations? *J. Phys. Chem. B* **2019**, *123*, 3658–3664, DOI: `10.1021/acs.jpcb.9b01251`.

(27) Bell, G. I. Models for the specific adhesion of cells to cells. *Science* **1978**, *200*, 618–627, DOI: `10.1126/science.347575`.

(28) Bullerjahn, J. T.; Sturm, S.; Kroy, K. Theory of rapid force spectroscopy. *Nat. Commun.* **2014**, *5*, 4463, DOI: `10.1038/ncomms5463`.

(29) Endres, S. C.; Sandrock, C.; Focke, W. W. A simplicial homology algorithm for Lipschitz optimisation. *J. Glob. Optim.* **2018**, *72*, 181–217, DOI: `10.1007/s10898-018-0645-y`.

Graphical TOC Entry

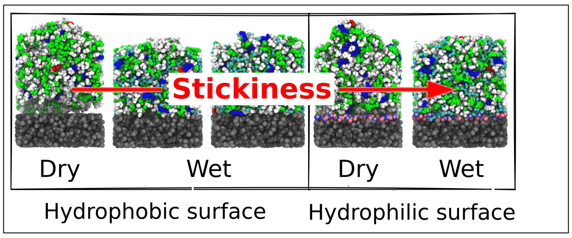

3.3 Gecko Adhesion on Flat and Rough Surfaces: Simulations with a Multi-Scale Molecular Model

Reproduced with permission from Materzok et al. [Small 2022, **18**, 2201674] Copyright 2022 Wiley.

Check for updates

RESEARCH ARTICLE

NANO · MICRO
small

www.small-journal.com

Gecko Adhesion on Flat and Rough Surfaces: Simulations with a Multi-Scale Molecular Model

Tobias Materzok, Danna De Boer, Stanislav Gorb, and Florian Müller-Plathe*

A multiscale modeling approach is used to develop a particle-based mesoscale gecko spatula model that is able to link atomistic simulations and mesoscale (0.44 µm) simulations. It is used to study the detachment of spatulae from flat as well as nanostructured surfaces. The spatula model is based on microscopical information about spatulae structure and on atomistic molecular simulation results. Target properties for the coarse-graining result from a united-atom model of gecko keratin in periodic boundary conditions (PBC), previously developed by the authors. Pull-off forces necessary to detach gecko keratin under 2D PBC parallel to the surface are previously overestimated when only a small region of a spatula is examined. It is shown here that this is due to the restricted geometry (i.e., missing peel-off mode) and not model parameters. The spatula model peels off when pulled away from a surface, both in the molecular picture of the pull-off process and in the force-extension curve of non-equilibrium simulations mimicking single-spatula detachment studied with atomic force microscopy equipment. The force field and spatula model can reproduce experimental pull-off forces. Inspired by experimental results, the underlying mechanism that causes pull-off forces to be at a minimum on surfaces of varying roughnesses is also investigated. A clear sigmoidal increase in the pull-off force of spatulae with surface roughness shows that adhesion is determined by the ratio between spatula pad area and the area between surface peaks. Experiments showed a correlation with root-mean-square roughness of the surface, but the results of this work indicate that this is not a causality but depends on the area accessible.

1. Introduction

The influence of surface roughness on the gecko adhesion has been previously studied on the nanoscale using atomic force microscopy (AFM) and on the macroscale in behavioral experiments with freely moving geckos.[1] Experimental data on the force necessary to pull off single spatulae from hard rough substrates and behavioral observations on living gecko clinging to various surfaces show that the effective adhesion experiences a minimum in root-mean-square roughness (RMS, R_q) from 100 to 300 nm.[1] This means that geckos can perform well on smooth substrates and those containing roughness values higher than the characteristic dimension of the terminal contact elements of the foot (so-called spatulae). Similar results on the geometrical relationships between spatula size, pull-off force and substrate roughness have been previously demonstrated for insects[2] and spiders[3] and supported by a relatively simple but elegant macroscale numerical model.[4]

At the end, gecko feet have thousands of mesoscale (≈0.1–0.5 µm) spatulae that allow geckos to stick to surfaces of varying chemistry, humidity,[5,6] and roughness.[1] Both experimental[1,7–13] and computational[5,6,14,15] researches have attempted to understand gecko adhesion mechanisms. While much remains to be learned, the present article offers a step forward in this field with the first molecular dynamics (MD) simulations of a multiscale model of a whole spatula in contact with surfaces at different roughness.

Our previous investigations of gecko adhesion using MD were done on the coarse-grained (CG) [5] and united-atom (UA)[6] level of molecular resolution. The model with the most detailed level of atomic resolution is UA, where apolar hydrogens are incorporated with their parent carbon atoms into single interaction sites (so-called "UAs"). With that model, we explained gecko adhesion in different scenarios (wet and dry, hydrophobic, and hydrophilic surfaces) on the molecular level. Our CG gecko keratin model treated entire amino acids of the amorphous region[16] as single bead and mapped the entire characteristic beta-sheet folding domain into another, larger single CG bead. With the CG model, we were able to

---

T. Materzok, D. De Boer, F. Müller-Plathe
Eduard-Zintl-Institut für Anorganische und Physikalische Chemie and Profile Area Thermofluids and Interfaces
Technische Universität Darmstadt
Alarich-Weiss-Str. 8, D-64287 Darmstadt, Germany
E-mail: t.materzok@theo.chemie.tu-darmstadt.de
S. Gorb
Zoological Institute Functional Morphology and Biomechanics
Kiel University
Am Botanischen Garten 1-9, D-24118 Kiel, Germany

The ORCID identification number(s) for the author(s) of this article can be found under https://doi.org/10.1002/smll.202201674.

DOI: 10.1002/smll.202201674

understand the effect of water at the hydrophobic surface. Lastly, the mesoscale model of this work uses a coarse-graining procedure to map five whole gecko keratin molecules to a single bead to allow the simulation of a whole spatula. Since, in every coarse-graining step, we pass information from the more-detailed finer-grained model to the coarser model, the current mesoscale model is informed by the deepest level of atomic resolution currently available.

The initial main objective of this work was to investigate the relationship between the pull-off of a semi-infinite (periodic in one or more dimensions) spatula material (gecko keratin) flat-on-flat and the pull-off of a macroscopic spatula. Pull-off forces necessary to detach semi-infinite gecko keratin in 2D periodic boundary conditions (PBC) in MD were orders of magnitude larger than experimental pull-off forces of gecko spatulae when the adhesive spatula pad area is taken into account.[5,6] Our main hypothesis is that this discrepancy is not due to model parameterization. It is rather an artifact, which exists because periodic semi-infinite systems cannot describe the peeling-off process prevalent in the macroscopic detachment of gecko spatulae (and adhesive tapes).

Since MD simulations at the UA or CG scale cannot, with current computational power, simulate a whole gecko spatula, we chose to do a multiscale parameterization of a particle-based mesoscale gecko keratin model that reproduces pull-off pressure, Young's modulus, and Poisson's ratio of the UA reference model (GROMOS 54A7 force field[17–20]). We then applied the resulting force field of the mesoscale keratin material to describe an entire spatula. We use the MD software GROMACS[21] to allow direct comparison of both[5,6] other molecular simulations of gecko adhesion.

Besides the ability to make straightforward comparisons between the mesoscale model and the UA and CG models of gecko keratin, using MD instead of finite element method (FEM), where a meshed representation that follows constitutive laws defines material properties, has multiple advantages: i) the system's behavior comes naturally from particle interactions instead of constitutive laws; thus any process that we may not initially have thought about is allowed to happen naturally by attractive and repulsive forces; ii) constitutive laws do not need to be defined a priori, which could possibly miss critical processes or simplify things too much; iii) a spatula is still small enough to be a statistical-mechanical system and for entropic kinetic energy-related fluctuations to influence the behavior at interfaces. They are absent in FEM but have significant contributions in force probe molecular dynamics.[22]

2. Model Construction and Parameterization

2.1. Bulk Keratin Material Model

Gecko setae and spatulae are primarily made up of beta keratin proteins.[23,24] They form dimers and dimers accumulate to form fibrils.[16,23,25] The fibrils are thought to start at the proximal ends of setae and yield spatula at their distal ends.[25] In the setae, before branching off, the fibril regions are embedded in a soft matrix. After a seta branches into around one thousand individual spatulae, the matrix material decreases and the spatulae are mostly made up of fibrillar regions with anisotropic elasticity.[16,25] We regard the gecko keratin material as a fiber-reinforced elastomer but do not explicitly model fibers and amorphous surroundings.[6] Instead, we use angle-dependent bond potentials between particles to model the anisotropic material characteristics of such a fiber-reinforced elastomer.

The fibrillar structure significantly contributes to mechanical properties, i.e., Young's Modulus E and Poisson's ratio ν.[16] The spatula model must correctly describe the anisotropy arising from it. Our spatula model consists of very coarse-grained beads that incorporate about five keratin molecules. To this end, we introduce bead-bead harmonic bonds $V(r) = K/2 \times (r-b_0)^2$ with an anisotropic bond force constant K and the equilibrium distance b_0. The anisotropic force constant becomes stronger as the direction of a bond aligns to the direction of the fibrils according to the equation:

$$K = k + k_b \times |\cos\theta| \tag{1}$$

where k is the isotropic part of the force constant assigned to every bond, k_b is an additional force constant in the fibril direction, and θ is the angle between the bond vector and the fibril direction. Hence, each bond in our model has an individual anisotropic bond constant depending on its angle towards the fibril direction in the initial structure. For the parameterization of k and k_b, see Section 2.4. Once assigned, the value of K remains unchanged.

To generate the basic periodic keratin model ("bulk keratin"), a box is randomly filled with beads at a number density of 0.012 nm^{-3} such that beads are a minimum of 2.8 nm apart from one another. The typical density of dry keratin ρ = 1.3 g cm^{-3} matches with the UA model of our previous work.[6] Using 1.3 g cm^{-3} as the target mass density, the bead number density of 0.012 nm^{-3} and the volume, the mapping scheme can be estimated: one bead accounts for 65 kD, a gecko keratin dimer for 22 kD; therefore our beads map the mass of five molecules (2.5 dimers). To model a highly cross-linked elastomer-like system similar[6,16] to gecko keratin, each bead is assigned harmonic bonds to its closest 30 neighboring beads. This connectivity is sufficient to make the real-scale spatula stiff enough and stop the system from collapsing. There is no excluded volume in the keratin-keratin interactions. For more than 10 bonds per bead, the system's volume remains essentially constant, with a volume drift of −30 nm^3 in a system of total size 21600 nm^3, see Figure S1A (Supporting Information).

The bond assignment algorithm does mean that some beads will have more than 30 bonds in total, depending on their environment. For each individual bond, we use the initial bead-bead distance as the equilibrium bond length b_0. This maintains the spatula shape when going from a quasi 0 K system to 300 K under the influence of an external potential (e.g., an attractive surface and a force detaching the spatula). The minimum system size required to prevent finite-size effects and to converge Young's modulus is a system of size 60 × 60 × 60 nm^3 (Figure S1B, Supporting Information). For each simulation sample, a different bulk material configuration is generated randomly. Thus, all starting configurations are independent.

2.2. Spatula Model

The spatula model is created the same way as the bulk keratin model. The main difference is that the target volume into which beads are inserted is not a box but rather a realistic spatula shape. We used a scanning electron microscopy image from Xu et al.[26] and transferred the outline of the imaged spatula into a two-dimensional coordinate system. We cleaned up these coordinates since the image was not taken from an orthographic perspective and was not aligned to an optical axis. The resulting polygon is the outline in the x,y plane of a flattened spatula from a top-down perspective. Beads filled into this outline can be seen in **Figure 1** (Top) (the bond network is visible in Figure S2, Supporting Information). The polygon vertices are listed in Table S1 (Supporting Information). To generate different thicknesses in the z direction depending on the distance to the setae proximal end, i.e., distance to the spatula tip, we use two functions to follow the height of the spatula and insert beads only in between these two functions:

$$\begin{aligned} z_{\text{top}} &= \left(\frac{z_h}{2} - r\right) / x_s \times x + r \\ z_{\text{bottom}} &= \left(-\frac{z_h}{2} + r\right) / x_s \times x - r \end{aligned} \tag{2}$$

with $z_h = 20$ nm the height of the spatula pad,[25] x_s the point between the shaft haft and the spatula pad, which is located at 65% the length of the spatula in x direction $l_x \times 0.65$ and $x = 0$ being located at the spatula haft face (extent and naming of different regions of the spatula can be found in Table S2, Supporting Information). The shaft haft side length in z and y is $r = 50$ nm (see Figure 1), a value comparable to the radius used in FEM models.[15,26] The (virtual) fibril direction goes from the shaft haft to the spatula pad tip, which is in the x direction in the initial setup. After bending (as described later), we generate the (virtual) fibrils again following the curvature, going from spatula haft to spatula pad tip by using a local orientation field instead of the x direction. For each simulation sample, a new system is generated from scratch. In total, we simulate 10 spatulae, each having an independent starting configuration.

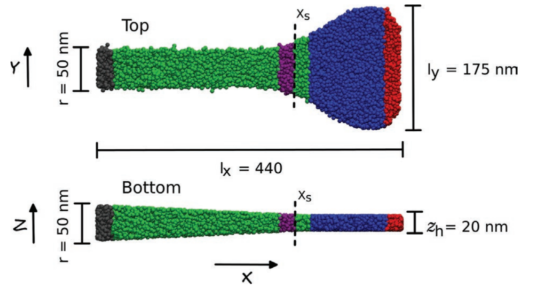

Figure 1. (Top) The top-viewing perspective of the spatula. The area of the spatula pad is $A_{\text{Sp}} = 19880$ nm^2. (Bottom) The shape of the spatula from its side is inspired by the finite element model of Sauer et al.[15] and the finite element calculations of Xu et al.[26] Keratin beads are colored in green, and we superimpose the green colored beads with named areas used throughout this work. Colors are illustrative and do not mean that properties differ between them. From left to right: spatula shaft haft (grey), joint (purple), and spatula pad (blue), which in this representation is overlaid by spatula tip (red). Table S2 (Supporting Information) summarizes these areas with the exact numerical values.

2.3. Surface Model

The surface is generated much like the bulk keratin model (Section 2.1). It has the same random arrangement of beads and the same bead density. For details, see Section S1 (Supporting Information). In total, we investigate eight peak densities ρ_{Peak} in which the total number of peaks per surface area ranges from 15.76 to 394.12 µm^{-2} (in addition to the perfectly flat surface with $\rho_{\text{Peak}} = 0$ µm^{-2}). In **Figure 2**, two such surfaces are shown.

We expect a surface representing an oxide mineral (e.g., the amorphous silica substrate of Huber et al.[8] that is used in the UA model of gecko keratin[6]) to not be able to deform. Such a surface is orders of magnitude stiffer than keratin, so we decided to make our surface completely rigid. Hence, we do not calculate interactions between surface beads and do not integrate the equation of motion for surface beads, effectively creating a space-fixed attractive external potential.

2.4. Parameterization of the Anisotropic Bonded Interactions of the Mesoscale Keratin Force Field

Experimental results have reported Young's moduli at a low of 1.2 GPa from nanoindentation tests and a high of 7.3 ± 1.0 GPa from in situ tensile tests.[27] Humidity also affects the elasticity of setal keratin, as 30% relative humidity produces $E = 3.2 \pm 0.2$ GPa and 80% relative humidity 2.2 ± 0.2 GPa.[28] A previous computational model found absolutely dry seta keratin to have a $E = 9.2$ GPa.[16] The target Young's modulus of 4.5 GPa for our spatula model is, thus, well within the range of experimental values and was set to reproduce the

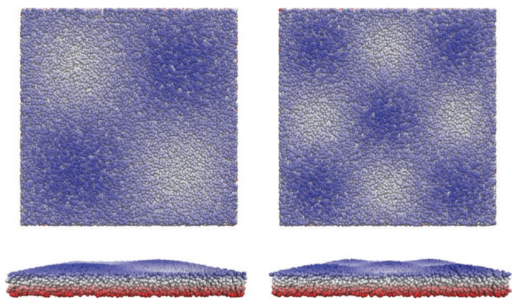

Figure 2. Two different surfaces are shown with increasing peak density (left $\rho_{\text{Peak}} = 15.76$ µm^{-2} and right $\rho_{\text{Peak}} = 39.41$ µm^{-2}). Beads are colored according to their height. For easier comprehension, the surfaces are not phase-shifted. In reality, depending on phase shift, the center of the surface (where the spatula attaches), could present anything between a valley and a peak. The height between the peak and valley is 16 nm for all surfaces, resulting in a root-mean-squared roughness of $R_q = \sqrt{\frac{1}{n}\sum (z_m - \langle z_m \rangle)} = 4$ nm with z_m the surface profile.

UA model of gecko keratin.[6] Existing literature on setae/spatulae keratin simply assumes a Poisson's ratio of $\nu = 0.2$,[15] 0.4,[16] or 0.5.[29] With our UA keratin model,[6] we calculated the Poisson's ratio to be $\nu = 0.4$ in the absolute dry state. Here, bond coefficients were tuned to yield $E = 4.5$ GPa and $\nu = 0.4$. The result of a wide range of combinations of k and k_b (Equation (2)) is shown in Figure S3 (Supporting Information), and details about the method are summarized in Section S2 (Supporting Information). The best fit to our UA target properties of $E = 4.5$ GPa and $\nu = 0.4$ is accomplished by $k_b = 1220$ kJ mol^{-1} nm^{-2} and $k = 226$ kJ mol^{-1} nm^{-2} (green symbol in Figure S3, Supporting Information), which results in $E = 4.518 \pm 0.036$ GPa and $\nu = 0.401 \pm 0.002$. Therefore, the mechanical properties of our model agree well with the above discussed experimental measurements.

2.5. Parameterization of the Nonbonded Interactions of the Mesoscale Keratin Force Field

We use force probe molecular dynamics (FPMD), as we have done in previous work.[5,6] We use FPMD to find the necessary size of the bulk keratin material for pull-off simulations and then to parameterize the nonbonded force field parameters for spatula-surface interactions. Details can be found in Section 3. The maximum force necessary to separate the bulk keratin system from the surface, called the pull-off force F_{pull}, is averaged over ten independently generated systems. To make the pull-off force intensive, we normalize it with the surface contact area, thereby calculating the pull-off pressures p.

With a mesoscale keratin material of height 20 and 90 nm box dimensions, the dimensions parallel to the surface (in Section S3 (Supporting information), we explain how we chose the box dimensions), the ε and σ values for a 12-6 Lennard–Jones (LJ) potential are parameterized against UA pulling results.[6] The UA model was, like the mesoscale keratin material used for the nonbonded parameterization, periodic in the directions parallel to the surface. For details about the UA model, see Section S4 (Supporting Information). Its force field was the GROMOS 54A7 FF.[17–20] It was made up of an amorphized gecko beta-keratin protein Ge-cprp-9, from which only the intrinsically disordered parts of the protein were considered. It was assumed that the disordered section of the protein is the part that is in contact with the surface and responsible for the adhesive interaction between spatula and surface.[6] The virtual cantilever is linked to the top half of the keratin in both the UA model and in the bulk keratin mesoscale model of this work, see **Figure 4** (red). We will come back to this in the computational details (Section 3).

At a loading rate of $\dot{F} = 1.66 \times 10^{12}$ pN s^{-1}, the average pull-off pressure of the UA model on top of a flat hydrophobic surface was $p = 12.92 \pm 5.3$ kJ mol^{-1} nm^{-3} (21.45 ± 8.85 pN nm^{-2}). Comparable pull-off pressures were found in previous coarse-grained work.[5] The hydrophobic surface model was a space-fixed flat surface of ≈3 nm height made up of GROMOS CH2 beads at a density of 20 nm^{-3}, which had a water contact angle of $\theta_c = 111.3°$.

This UA pulling pressure is the target against which we optimize the keratin-surface LJ parameters of the mesoscale model of this work, running pulling simulations for each parameter combination. The coarse-grained pull-off pressure are shown in **Figure 3**. For the production calculations, we use $\sigma = 4.0$ nm and $\varepsilon = 610$ kJ mol^{-1} for nonbonded interactions, which give the ratio of mesoscale and atomistic pull-off pressures $p/p^{\text{ua}} = 1.004$. Finally, we recall that nonbonded interactions exist only between the keratin and the surface. Interactions within the keratin are exclusively modeled as a network of harmonic bonds.

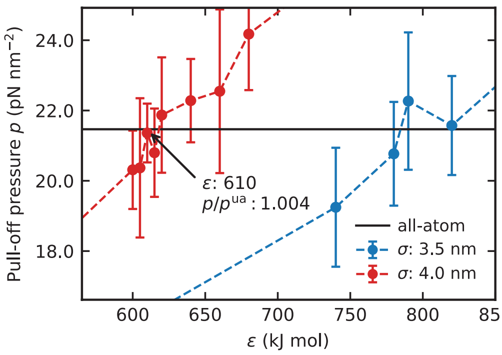

Figure 3. Pull-off pressure as a function of Lennard–Jones (LJ) ε for the bulk keratin systems pulled off a hydrophobic surface with nonbonded LJ parameters σ at 3.5 nm (blue) or 4.0 nm (red). The periodic box dimensions are 90 nm × 90 nm and the force field parameters used for this validation are $k = 226$ kJ mol^{-1} nm^{-2} and $k_b = 1220$ kJ mol^{-1} nm^{-2}. The average is computed from 10 independent samples, and the standard deviation of the mean is used as the error.

3. Computational Details

General simulation details can be found in Section S5 (Supporting Information), those concerning the mesoscale keratin material simulations (with PBC) are summarized in Section S5.1 and Section S5.2 (Supporting Information).

The mesoscale spatula is prepared in six steps; for details, see Section S6 (Supporting Information). After the first 4 steps, the final preparation, which involves pulling, is broken into two parts, as was done[15] by Sauer et al. The spatula shaft is first

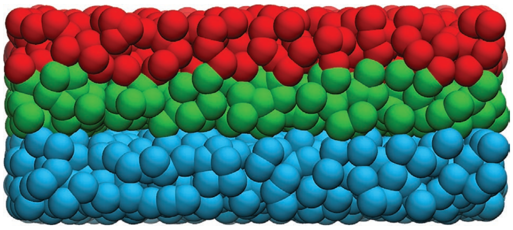

Figure 4. The mesoscale keratin material (green) used in the nonbonded parameterization on top of a flat surface (cyan) of dimensions 90 nm × 90 nm. The system is periodic in the two dimensions parallel to the surface. The surface height is 13 nm and the bulk material is 20 nm thick. Highlighted in red is the top-half of the bulk keratin. The center-of-mass of the top-half is connected to a virtual cantilever.

bent upwards so that it has an inclination of some degree to the surface (step 5), equilibrated at this point. Then the equilibrated spatula configuration is pulled vertically at the shaft haft off the surface (step 6).

Equilibrium configurations are extracted from the trajectory at spatula inclinations of θ_S = 45, 60, and 75°, as shown in **Figure 5**, which are the same configurations as examined by Sauer et al.[15] The spatula inclination θ_S is the angle between the vector pointing from the joint to the shaft haft and the vector parallel to the surface, with the joint being at $l_x \times 0.35$ to $l_x \times 0.4$, as shown in Figure 1B in purple.

Although it is unknown what exact spatula inclination exists in nature, some inclination can be assumed from experimental imaging,[35–37] so we reset the bond network of the extracted configurations and regenerate all anisotropic bonds using the local fibril direction. The local fibril direction is calculated with a spline fit through the averaged positions of beads in the plane dissecting the spatula and normal to the surface. In essence, a local orientation field is used to calculate the bond angle, with the center between two connected beads as the bond position. Reapplying the bond assignment algorithm changes the equilibrium shape of the spatula to that of the target inclination. These shapes at $\theta_S = 45°$, 60°, and 75° are the final equilibrium configurations of the spatulae that are used in the pull-off simulations, similar to the previous investigation by Sauer et al.[15]

For calculations involving a rough surface, the inclined spatulae (only $\theta_S = 45°$ is used) are placed on top of a surface with different peak densities. In the preload step (an applied external pressure of 0.2553 kJ mol^{-1} nm^{-3} or 0.4 pN nm^{-2}, corresponding to a force of 5076 kJ mol^{-1} nm^{-1} in case of the full-size spatula, we remember the spatula pad area is $A_{\mathrm{Sp}} = 19880$ nm^2) is applied for 600 ns. Subsequently, the system is relaxed for 500 ns with no applied force. These are times sufficient to converge the distance between spatula and surface completely.

In the final pull-off simulation, the spatula is pulled away from the surface by linking the center of mass of the spatula shaft haft (Figure 1, grey) to a virtual cantilever (with the harmonic force constant $k_{\mathrm{pull}} = 1000$ kJ mol^{-1} nm^{-2}) and moving the virtual cantilever at a constant pulling velocity away from the surface. The pulling velocities of the cantilever result in loading rates $\dot{F} = 16.6 \times 10^{12}$ pN s^{-1}, 1.66×10^{12} pN s^{-1}, 0.83×10^{12} pN s^{-1} and 0.332×10^{12} pN s^{-1}.

To summarize all steps of the entire spatula pull-off process and simulation: i) generate the spatula and create bonds; ii) preload the spatula pad against the flat surface; iii) relax the system; iv) move the spatula shaft haft COM 20 nm upwards; v) bend the spatula upwards by applying force normal to the shaft; vi) extract configurations with defined spatula inclinations and recreate the bond network; vii) pull the spatula vertically off the surface by the shaft haft COM.

Additionally, we simulate spatula detachment from rough surfaces using the resulting spatula configuration from step (vi). To summarize the simulations involving a rough surface: (viii) preload the spatula for 600 ns against the rough surface; (ix) relax the system; (x) pull the spatula off the rough surface.

There are effectively no periodic boundary conditions. The static surface has an area of 356 × 356 nm^2. The surface and spatula are surrounded by vacuum. All spatula detachment simulations are done in the NVT ensemble with a thermostat keeping the temperature constant at 300 K. As for the detachment simulation of periodic mesoscale keratin material, the preload step uses a SD thermostat[34] with $\tau_T = 1$ ps; the relaxation step uses SD with $\tau_T = 10$ ps; and all other steps use a velocity rescaling thermostat[33] with $\tau_T = 1$ ps.

4. Results and Discussion

4.1. Spatula Detachment with Varying Loading Rates at 45° Inclination

By comparing the pull force against the time of periodic mesoscale keratin material in **Figure 6**A to the spatula pull-off (Figure 6B) (with milestones denoted by vertical lines and the corresponding times), it is clear that the pull-off proceeds differently. In the case of the periodic material, the force (here shown as pressure) increases linearly with time until a maximum is reached. This pull-off force (also called critical force or rupture force) is then overcome, and the material detaches quickly, as can be seen in the displacement of the center of mass of the top-half of the keratin-sheet (red). For the spatula (Figure 6B), the force does not increase linearly but changes in slope. At the peak of the force curve (139–156 ns for a loading rate of 1.66×10^{12} pN s^{-1}), the maximum is not sharply defined but stretches over a time period (and displacement range). This behavior is only seen with the spatula shape because the spatula pad is peeled-off by delamination (see **Figure 7** 139–156 ns). After reaching the critical force needed to detach the spatula from the surface, the force oscillates around zero (at $t > 160$ ns). However, the oscillation is less distinctly harmonic

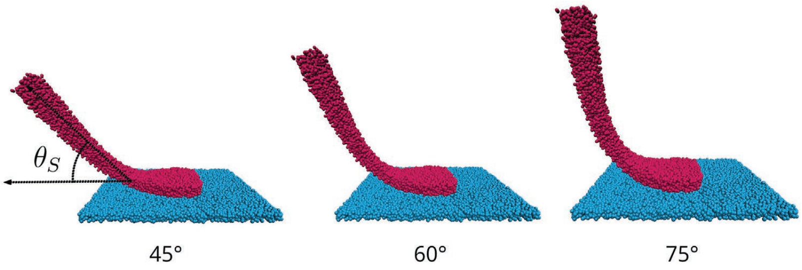

Figure 5. Equilibrium configurations of spatulae at different inclinations. The spatula inclination θ_S is defined as the angle between spatula shaft haft, joint and surface, as illustrated in the figure with black vectors.

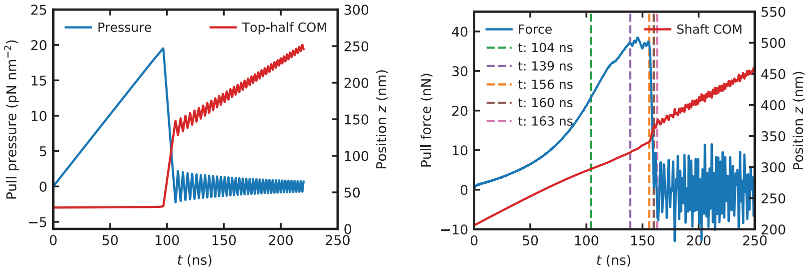

(A) (B)

Figure 6. A) Pull-off of the bulk keratin material from a flat surface at a loading rate of $\dot{F} = 1.66 \times 10^{12}$ pN s^{-1}. The pull-off pressure is shown in blue, and the displacement of the shaft position is shown in red, with "Top-half COM" denoting the center of mass (COM) of the top half of the bulk keratin and "Shaft COM" the COM of the shaft haft. After detachment (around $t = 100$ ns), the material is quickly pulled up (red) away from the surface and oscillates around the virtual cantilever (red line oscillations at $t > 100$ ns), resulting in oscillations in the force. B) Pull-off force of a spatula (inclination $\theta_S = 45°$) from a fixed flat surface at a loading rate of 1.66×10^{12} pN s^{-1}. For illustrative purposes, one single trajectory is shown ($n = 1$).

compared to the periodic mesoscale keratin material since the spatula geometry allows other motions (e.g., wiggling) in addition to vertical oscillations of its center of mass (See Movie S1, Supporting Information).

The pull-off force and pull-off pressure (i.e., their respective maximum values) have been observed to be proportional to the logarithm of the loading rate,[38] as $F_{\text{pull}} \sim \log(\dot{F})$. To investigate this dependence in more detail in our work, **Figure 8**A shows the dynamic force spectrum where each data point is the average over 10 independent spatula systems. At the lowest loading rate, the pull-off force needed to detach the spatula from the surface is ≈35 nN. This value increases with the loading rate. At $\dot{F} = 16.6 \times 10^{12}$ pN s^{-1}, it reaches 60 nN. Loading rates in the order of 10^{12} pN s^{-1} are not accessible by experiments, with the fastest atomic force microscopy (AFM) experimental loading rates[39] only reaching orders of 10^8 pN s^{-1}.

With a smaller spatula that consists of fewer beads, lower loading rates are computationally accessible. We, therefore, scale down the mesoscale spatula to 70% of its original size to reduce the number of particles and allow longer simulation times. To give an idea about trends at lower loading rates, in Figure 8B, the pull-off pressure p of our full-size spatula model is displayed together with that for a smaller spatula. It shows a systematic difference between different sized spatulae. This difference exists not only for the pull-off pressure p (round markers) but also in the position of the maximum force as a function of the loading rate (triangle markers). It may be a result of the fact that the amount of material involved in bending is smaller with a smaller spatula, and the curvature to accomplish the same inclination, larger, thereby creating a stiffer spatula. This stiffer spatula has a smaller change in the position of the maximum force. Smaller spatulae also have the additional benefit of allowing more adhesive contacts by setal area,[40] which was clearly exploited by evolution since animal groups with heavier representatives (lizards) use more but smaller pads.[36]

Both pull-off pressure and the change in the position of maximum force show that there are two regimes: one at lower loading rates that seems to be scaling linearly with $\log(\dot{F})$, and a change in the slope with the highest loading rate. If we assume the linear-log law for pull-off force against loading rate to continue down to experimental loading rates, we can extrapolate the pull-off force F (Figure 8B). The extrapolated pull-off force $F_{\text{predicted}} = \log(\dot{F} \times m) \times F_0$ for a spatula in the AFM-accessible regime is 25 nN for $\dot{F} = 10^8$ pN s^{-1} and 12 nN for $\dot{F} = 10^4$ pN s^{-1}. These pull-off forces match very well with pull-off forces of spatulae from experiments, which were found to be in the range of 8–20 nN.[1,8,9] It should be noted, however, that loading rates are not given in the literature, so we can only presume that they are somewhere between 10^1 and 10^8 pN s^{-1}.

Since the pull-off forces match well with experiments, this validates the spatula model created in this work. This validation, in itself, is a major result of the current work, as there is no other work that reproduces experimental gecko spatula pull-off forces in a bottom-up fashion.

4.2. Energy Contributions to Spatula Detachment

The rupture of the adhesive interactions between the spatula and the surfaces during pull-off involves the dissipation of adhesive and bending energy, with the dissipated adhesive energy

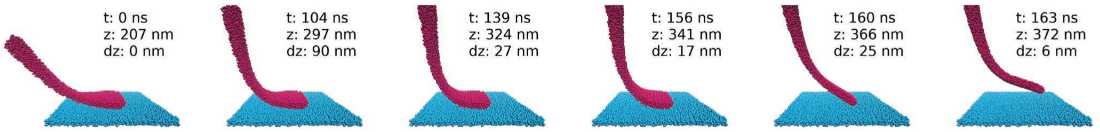

Figure 7. Process of pulling of a spatula ($\theta_S = 45°$) from a flat surface. In the first few hundred nanoseconds, the spatula bends as the spatula shaft is pulled upwards, normal to the surface. Between 140 ns and 160 ns, the spatula pad is peeled off the surface. As the crack moves from the spatula joint to the spatula tip, the adhesion energy is overcome and the detachment of the spatula pad occurs quickly in under 3 ns. After detachment, the energy stored in the spatula material from bending is released into a wiggling motion that may lead to short re-attachments of the spatula.

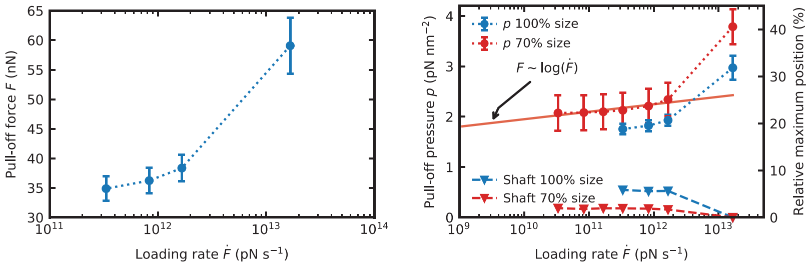

(A) (B)

Figure 8. A) Dynamic force spectrum of spatula ($\theta_S = 45°$) pull-off against loading rate at a flat surface. B) Dynamic pressure spectrum shows the pull-off forces normalized with the area under the spatula pad. Here, the differently sized spatulae are compared. Since the smaller spatula includes fewer beads, lower loading rates are computationally more accessible. The pull-off pressure p (left axis) and the percentage change of the position of maximum force z^f_{COM} of the spatula shaft compared to a reference position at fastest pulling $z^f_{\mathrm{COM}}(\dot F = 16.6 \times 10^{12}$ pN s$^{-1})$ (right axis) are shown against the loading rate. Round markers denote the pull-off pressure and triangle markers are used for the change in maximum position due to loading rate. The relative maximum position is defined as the shift of the position of the force maximum at the given loading rate $z^f_{\mathrm{COM}}(\dot F)$ with respect to that at the maximum loading rate 16.6×10^{12} pN s^{-1} in percent. The average is computed from 10 independent samples, and the standard deviation of the mean is used as the error.

$|\Delta U_{\mathrm{LJ}}|$ being generally smaller than the work required to break adhesive interactions.[41] We calculate $|\Delta U_{\mathrm{LJ}}|$ as the sum of the change of the nonbonded interactions between spatula and surface. We calculate the pull-off work as $\Delta W_P = -\int F_{\mathrm{pull}}\, dz_{\mathrm{COM}}$, with z_{COM} denoting the position of the shaft haft COM (see Figure 1). We compute the ratio $|\Delta U_{\mathrm{LJ}}|/\Delta W_P$ for four different loading rates averaged over 10 independent simulations as a function of z_{COM} (In Figure S5A (Supporting Information), the ratios at the position of maximum force are highlighted in red; in Figure S5B (Supporting Information), the properties are shown side-by-side) and summarized in **Figure 9** for all contributions. Depending on the loading rate, ≈54–66% of the pull-off work is the cost of overcoming the adhesive interactions between spatula and surface. Only in the case of a very high loading rate of 16.61×10^{12} pN s^{-1} (blue) is the cost of overcoming adhesive interactions significantly lower at ≈30%. A related computational investigation of the adhesive behavior of amyloid nanofibers showed a cost of 80% in a pure peeling situation and ≈50–60% for a situation where a joint, or hinge, was present.[42]

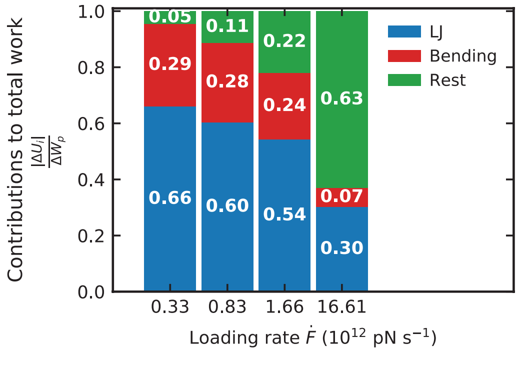

Figure 9. The ratio of overcome adhesive energy (blue) at the position of the maximum force is compared to overcome contributions from bending (red) and dissipated rest (green) energies to work of pull-off for different loading rates (for $\theta_S = 45°$). The ratios are annotated at the stacked bars. The average is computed from 10 independent samples.

The ratio between bending energy $|\Delta U_{\mathrm{Bond}}|$ and pull-off work W_p (Figure 9 and as a function of distance shown in Figure S5C and the underlying energies in Figure S5D, Supporting Information) shows a smaller contribution of ≈7–29%. In the case of the fast pull-off, the bending energy accounts only for 7% of the work needed to overcome attachment. At the slowest loading rate, the work needed to overcome the bending of the spatula is 29% of the total work needed.

At high loading rates, energy is dissipated as heat ("Rest"). This rest is dissipated into kinetic energy and can be measured as a temperature increase of the spatula in the NVE ensemble (when no thermostat regulates the temperature).

Until the position of maximum force, the bending energy $|\Delta U_{\mathrm{Bond}}|$ increases and opposes the process as the spatula stretches and bends upwards out of its equilibrium inclination.

Force response on loading rate has been investigated on various levels,[38,43,44] and it is known that pulling too quickly leads to biased attached-to-detached pathways.[44] We show here that this trend is also true for pulling a spatula off a surface.

4.3. Spatula Detachment for Different Spatula Inclinations

A highly curved spatula has a higher pull-off force (**Figure 10**) than a less curved spatula. Our results show the opposite trend of what Sauer et al. produced with their FEM model.[15] They showed that as the spatula curvature increased, the pull-off force decreased. They assume that spatulae are straight, whereas we assume that spatulae have some inherent curvature. These authors' assumption implies that bending energy favors the detachment because the straight spatula is bent upward during pull-off, and the potential energy increases with the upward bending of the spatula. The contribution of the bending energy $|\Delta U_{\mathrm{Bond}}|$ to the work of pull-off $W_p = \Delta U_{\mathrm{LJ}} + \Delta U_{\mathrm{Bond}} + \Delta U_{\mathrm{rest}}$ would be negative and would compensate, in part, the spatula pad adhesion. Thus, the more the spatula is curved, the

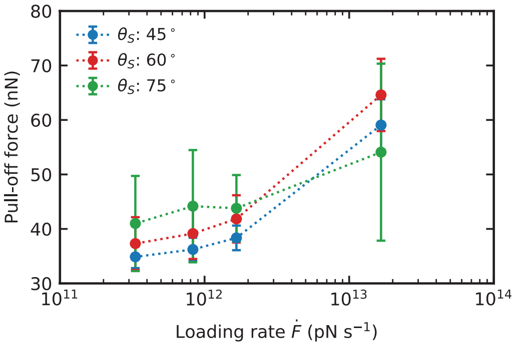

Figure 10. Dynamic force spectrum of spatula pull-off against loading rate depends on spatula inclination θ_S. Shown is the force spectrum for a perfectly flat surface. We assume that the average pull-off force for $\theta_S = 75°$ at the highest loading rate (green) is influenced by the large error, and its position below the two other θ_S pull-off force should not be taken as a true trend. The average is computed from 10 independent samples, and the standard deviation of the mean is used as the error.

stronger the pad adhesion would be compensated, resulting in smaller pull-off forces for highly curved spatulae. However, we observe something different, a highly curved spatula has a higher pull-off force (Figure 10) as the bending energy is smaller (Figure S6, Supporting Information), and the compensation is, thus, necessarily smaller in these geometries. This observation is confirmed by the contributions from the adhesive and bending, and dissipated energies overcome (Figure S6, Supporting Information).

With increasing spatula inclination θ_S, the error in the pull-off force F increases at all loading rates (Figure 10). A spatula inclination of 45° has the lowest pull-off force and the most minor error. As the curvature of the equilibrium spatula shape increases, the pull-off force and standard deviation increase, too.

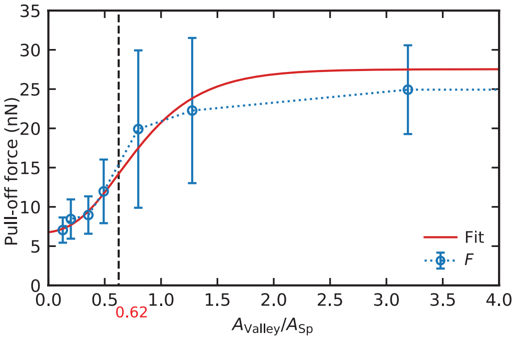

Figure 11. Pull-off force as a function of $A_{\mathrm{valley}}/A_{\mathrm{Sp}}$. The pull-off forces averaged over 10 independent simulations (blue) are used to fit a sigmoidal (Richards[45]) curve (red) that is used to compute the second derivative of this fit (not shown). The intersection of the second derivative of the sigmoidal curve with zero at $A_{\mathrm{valley}}/A_{\mathrm{Sp}} = 0.62$ is marked with a vertical black line. The average is computed from 10 independent samples, and the standard deviation of the mean is used as the error.

This last point is essential since different AFM-based studies of gecko adhesion may differ in the angle of connecting the spatula to the cantilever. There could be further implications if different geckos have different spatula inclinations or if variability in spatula inclinations between spatulae of the same seta exist.

Returning to Sauer et al., the contrast between our and their results might also stem from the differences in their FEM treatment compared to our MD treatment of the pull-off. In non-equilibrium MD, we simulate an AFM-like pull-off. However, the FEM study does not consider dynamics, loading rates or any lost dissipated "rest" energy and essentially treats pull-off at equilibrium.

4.4. Influence of Surface Roughness on Spatula Adhesion

Spatula adhesion has been observed to depend on surface RMS roughness, R_q[1,35] (the RMS distance between the surface profile and its average height). Huber et al.[1] demonstrated that as a surface changes from low R_q to high R_q, the pull-off force passes through a wide minimum between R_q = 100 nm and 300 nm. The authors hypothesized that when R_q is on the scale of spatula sizes, it allows only partial contact between the spatula and the surface because the asperities (the peaks and valley) would be too small for the spatula to attach to.

In **Figure 11**, the spatula pull-off force against the area per valley ratio $A_{\mathrm{valley}} = 1/\rho_{\mathrm{peak}}$ to spatula area A_{Sp} (top) at constant R_q = 4 nm, is shown (Figure S7 (Supporting Information) shows the pull-off force against the peak density)and summarized, as the peak density decreases, the pull-off force increases. The ratio $A_{\mathrm{valley}}/A_{\mathrm{Sp}}$ is well fitted by a sigmoidal (Richards[45]) curve fit (red). When the spatula area exceeds the area of surface asperities ($A_{\mathrm{valley}}/A_{\mathrm{Sp}} < 1$), the spatula is unable to form close contact with the surface (**Figure 12**). The assumption of Huber et al.[1] that spatulae cannot adhere to asperities of similar but smaller dimensions is confirmed here. However, this is not necessarily a function of the RMS roughness. Their surfaces were fortuitously crafted with different roughness wavelengths that also resulted in different RMS roughnesses. Our results indicate a primary dependence on roughness wavelength rather than RMS roughness R_q.

Movie S2 (Supporting Information) shows the pull-off at $A_{\mathrm{valley}}/A_{\mathrm{Sp}} = 3.19$. At $A_{\mathrm{valley}}/A_{\mathrm{Sp}} < 1$; the pull-off force declines rapidly until the spatula cannot follow the surface topography anymore and simply attaches to the peaks of the surface, as seen in Figure 12 at $A_{\mathrm{valley}}/A_{\mathrm{Sp}} < 0.49$. A critical trend change can be observed when the area per valley reaches a value of ≈60% (Figure 11) of the spatula pad. Asperities with smaller sizes prohibit the spatula from completely attaching to the surface (Figure 12).

There is a small apparent discrepancy between the pull-off force for the flat surface in Figure 11 (28 nN) and that of the loading rate investigations (Figure 8, 37 nN). This is due to the different preparation of the systems (no preloading in Figure 8). The minimum pull-off force ≈7 nN, is seen at a peak density of $A_{\mathrm{valley}}/A_{\mathrm{Sp}} = 0.13$. Movies S3, S4, and S5 (Supporting Information) display multiple starting configurations where the spatula is attached to surfaces of $A_{\mathrm{valley}}/A_{\mathrm{Sp}} = 3.19$, 1.28, and 0.49.

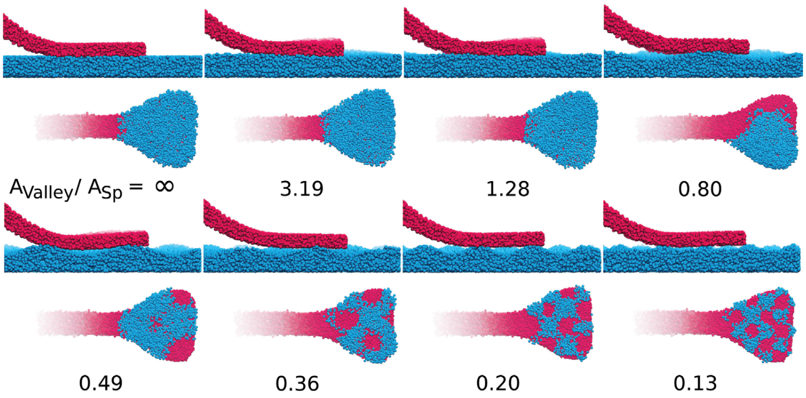

Figure 12. (Top) Sections of spatula attached to rough surfaces shown with increasing peak density (from top left with $\rho_{\text{Peak}} = 0\ \mu\text{m}^{-2}$ to bottom right with 394.12 μm^{-2}). The average height between the peak and valley is 16 nm for all surfaces, resulting in a root-mean-squared roughness of $R_q = 4$ nm. (Bottom) Viewed from underneath the surface, the only part of the spatula displayed are surface beads (cyan), which are inside the interaction cutoff of the spatula beads (red). The ratio $A_{\text{valley}}/A_{\text{Sp}}$ between the area between peaks and the spatula area is noted underneath each surface.

5. Conclusion

We developed a mesoscale particle model for a gecko spatula to study the effect of sub-micron surface roughness on the spatula adhesion. The model whose building blocks have the size of 65 kDa or 83 nm^3 has been constructed using the results from finer-grained molecular models, namely atomistic and coarse-grained (one bead per amino acid).

We thus bridge the nanoscale atomistic molecular simulations of keratin-surface interaction to mesoscale simulations of whole spatulae. Using a hybrid bottom-up-top-down coarse-graining protocol, we showed successfully that the UA model of gecko keratin[6] provides the correct adhesive interactions with the surface. Naive extrapolation of vertical pull-off simulations in 2D PBC of gecko keratin to sizes of real spatula pads greatly overestimated the force necessary to detach the spatula since pull-off forces would be hundreds of times larger than what AFM experiments showed. Here we showed that the CG force field parameterized in 2D PBC, which reproduces the UA keratin properties, matches with AFM studies if the same force field is used for a mesoscale spatula with its true shape and size. Using a simple extrapolation from fast MD loading rates to likely AFM loading rates, we observe typical pull-off forces for single spatulae of ≈12 nN (exp. 8 to 20 nN[1,8,9]). The necessary ingredient is to use the actual shape of a spatula and allow peel-off, rather than vertical detachment, to happen.

Spatulae of various sizes show systematic differences in pull-off. Per contact area, the pull-off force of a smaller spatula is larger. Using the same amount of material, more and smaller spatulae are therefore more “efficient”. We find that it is the higher stiffness of smaller spatulae that oppose the peel-off.

Analysis of the energy contributions to spatula pull-off showed that around two-thirds of the pulling work is expended to overcome the adhesive nonbonded interactions, around one-third is the energy to bend the spatula, and only ≈5% is lost through dissipation (at the lowest loading rate). The partitioning of energies is, of course, model-dependent. It is, however, unlikely that the contributions of the adhesive interactions will change much since our mesoscale coarse-graining is based on the result of UA adhesive interactions. When the maximum force is reached, and the spatula is about to be detached, the force is essentially only determined by adhesive nonbonded interactions.

Care should be taken in AFM experiments to correctly characterize the spatula since the adhesion also depends on the inclination of the spatula θ_S, and as inclination increases, its error increases too. High inclinations increase the pull-off force due to smaller compensation of the pad adhesion during bending. Large scatter of pull-off forces due to high inclinations of $\theta > 60°$ may also lead to premature detachments of spatulae or parts of synthetic gecko adhesives, which would decrease the product’s overall reliability.

The spatula pull-off force shows a strong dependence on the characteristic wavelength of the surface roughness, i.e., the lateral extent of depressions and protrusions. The pull-off force follows a sigmoidal increase. At short wavelengths, the spatula cannot follow the terrain and, in turn, can only attach to the peaks of the rough surface. The most significant increase of pull-off force happens where the area per surface feature reaches about 60% of the area of the spatula pad. From this point on, the spatula can closely attach to the surface topography.

Supporting Information

Supporting Information is available from the Wiley Online Library or from the author.

Acknowledgements

The authors would like to thank the German Academic Exchange Service (DAAD) for bringing together T.M. and D.B. in a summer internship at TU Darmstadt. D.D. would like to thank the 2021 ACS IRES program, which was made possible by the generous support of the U.S. National Science Foundation, under grant OISE-1854174.

Open access funding enabled and organized by Projekt DEAL.

Conflict of Interest

The authors declare no conflict of interest.

Data Availability Statement

The data that support the findings of this study are available from the corresponding author upon reasonable request.

Keywords

gecko adhesion, molecular dynamics, multiscale molecular model, pull-off force, roughness, spatula

Received: March 16, 2022
Revised: July 7, 2022

---

[1] G. Huber, S. N. Gorb, N. Hosoda, R. Spolenak, E. Arzt, *Acta Biomater.* **2007**, *3*, 607.
[2] D. Voigt, J. M. Schuppert, S. Dattinger, S. N. Gorb, *J. Insect Physiol.* **2008**, *54*, 765.
[3] J. O. Wolff, S. N. Gorb, *J. Exp. Biol.* **2012**, *215*, 179.
[4] A. Kovalev, A. E. Filippov, S. N. Gorb, *Bioinspir. Biomim.* **2018**, *13*, 066004.
[5] T. Materzok, S. Gorb, F. Müller-Plathe, *Soft Matter* **2022**, *18*, 1247.
[6] T. Materzok, A. Canestraight, S. N. Gorb, F. Müller-Plathe, **2022**, in preparation.
[7] K. Autumn, Y. A. Liang, S. T. Hsieh, W. Zesch, W. P. Chan, T. W. Kenny, R. Fearing, R. J. Full, *Nature* **2000**, *405*, 681.
[8] G. Huber, H. Mantz, R. Spolenak, K. Mecke, K. Jacobs, S. N. Gorb, E. Arzt, *Proc. Natl. Acad. Sci. U.S.A.* **2005**, *102*, 16293.
[9] W. Sun, P. Neuzil, T. S. Kustandi, S. Oh, V. D. Samper, *Biophys. J.* **2005**, *89*, L14.
[10] K. Autumn, S. T. Hsieh, D. M. Dudek, J. Chen, C. Chitaphan, R. J. Full, *J. Exp. Biol.* **2006**, *209*, 260.
[11] H. Izadi, K. M. E. Stewart, A. Penlidis, *J. R. Soc. Interface* **2014**, *11*, 20140371.
[12] A. Y. Stark, M. R. Klittich, M. Sitti, P. H. Niewiarowski, A. Dhinojwala, *Sci. Rep.* **2016**, *6*, 30936.
[13] A. Y. Stark, S. Subarajan, D. Jain, P. H. Niewiarowski, A. Dhinojwala, *Philos. Trans. Royal Soc.* **2016**, *374*, 20160184.
[14] R. A. Sauer, *Comput. Methods Biomech. Biomed. Eng.* **2009**, *12*, 627.
[15] R. A. Sauer, M. Holl, *Comput. Methods Biomech. Biomed. Eng.* **2013**, *16*, 577.
[16] K. S. Endoh, T. Kawakatsu, F. Müller-Plathe, *J. Phys. Chem. B* **2018**, *122*, 2203.
[17] L. D. Schuler, X. Daura, W. F. V. Gunsteren, *J. Comput. Chem.* **2001**, *22*, 1205.
[18] C. Oostenbrink, A. Villa, A. E. Mark, W. F. V. Gunsteren, *J. Comput. Chem.* **2004**, *25*, 1656.
[19] N. Schmid, A. P. Eichenberger, A. Choutko, S. Riniker, M. Winger, A. E. Mark, W. F. van Gunsteren, *Eur. Biophys. J.* **2011**, *40*, 843.
[20] W. Huang, Z. Lin, W. F. van Gunsteren, *J. Chem. Theory Comput.* **2011**, *7*, 1237.
[21] B. Hess, C. Kutzner, D. van der Spoel, E. Lindahl, *J. Chem. Theory Comput.* **2008**, *4*, 435.
[22] B. Heymann, H. Grubmüller, *Biophys. J.* **2001**, *81*, 1295.
[23] D. L. Hallahan, N. M. Keiper-Hrynko, T. Q. Shang, T. S. Ganzke, M. Toni, L. D. Valle, L. Alibardi, *J. Exp. Zool. B: Mol. Dev. Evol.* **2009**, *312B*, 58.
[24] L. Alibardi, *Tissue Cell* **2013**, *45*, 231.
[25] N. W. Rizzo, K. H. Gardner, D. J. Walls, N. M. Keiper-Hrynko, T. S. Ganzke, D. L. Hallahan, *J. R. Soc. Interface* **2006**, *3*, 441.
[26] Q. Xu, Y. Wan, T. S. Hu, T. X. Liu, D. Tao, P. H. Niewiarowski, Y. Tian, Y. Liu, L. Dai, Y. Yang, Z. Xia, *Nat. Commun.* **2015**, *6*, 8949.
[27] G. Huber, S. Orso, R. Spolenak, U. G. K. Wegst, S. Enders, S. N. Gorb, E. Arzt, *Mater. Res.* **2008**, *99*, 1113.
[28] M. Prowse, M. Wilkinson, J. Puthoff, G. Mayer, K. Autumn, *Acta Biomater.* **2010**, *7*, 733.
[29] X. Dong, R. Zhang, Y. Tian, M. A. Ramos, T. S. Hu, Z. Wang, H. Zhao, L. Zhang, Y. Wan, Z. Xia, Q. Xu, *ACS Appl. Polym. Mater.* **2020**, *2*, 2658.
[30] S. Páll, B. Hess, *Comput. Phys. Commun.* **2013**, *184*, 2641.
[31] D. van der Spoel, P. J. van Maaren, *J. Chem. Theory Comput.* **2006**, *2*, 1.
[32] H. J. C. Berendsen, J. P. M. Postma, W. F. van Gunsteren, A. DiNola, J. R. Haak, *J. Chem. Phys.* **1984**, *81*, 3684.
[33] G. Bussi, D. Donadio, M. Parrinello, *J. Chem. Phys.* **2007**, *126*, 014101.
[34] N. Goga, A. J. Rzepiela, A. H. de Vries, S. J. Marrink, H. J. C. Berendsen, *J. Chem. Theory Comput.* **2012**, *8*, 3637.
[35] B. N. J. Persson, S. Gorb, *J. Chem. Phys.* **2003**, *119*, 11437.
[36] E. Arzt, S. Gorb, R. Spolenak, *Proc. Natl. Acad. Sci. U.S.A.* **2003**, *100*, 10603.
[37] G. Huber, S. N. Gorb, R. Spolenak, E. Arzt, *Biol. Lett.* **2005**, *1*, 2.
[38] H. Grubmüller, *Methods Mol. Biol.* **2005**, *305*, 493.
[39] F. Rico, A. Russek, L. González, H. Grubmüller, S. Scheuring, *Proc. Natl. Acad. Sci. U.S.A.* **2019**, *116*, 6594.
[40] M. Varenberg, N. M. Pugno, S. N. Gorb, *Soft. Matter.* **2010**, *6*, 3269.
[41] A. R. C. Baljon, M. O. Robbins, *Science* **1996**, *271*, 482.
[42] A. Wang, S. Keten, *Npj. Comput. Mater.* **2019**, *5*, 1.
[43] G. Hummer, A. Szabo, *Proc. Natl. Acad. Sci. U.S.A.* **2001**, *98*, 3658.
[44] S. Sheridan, F. Gräter, C. Daday, *J. Phys. Chem. B* **2019**, *123*, 3658.
[45] F. J. Richards, *J. Exp. Bot.* **1959**, *10*, 290.

NANO small MICRO

Supporting Information

for *Small,* DOI: 10.1002/smll.202201674

Gecko Adhesion on Flat and Rough Surfaces: Simulations with a Multi-Scale Molecular Model

Tobias Materzok, Danna De Boer, Stanislav Gorb, and Florian Müller-Plathe*

SUPPORTING INFORMATION

Gecko Adhesion on Flat and Rough Surfaces: Simulations with a Multi-scale Molecular Model

Tobias Materzok Danna De Boer Stanislav Gorb* Florian Müller-Plathe**

Tobias Materzok, Danna De Boer, Prof. Dr. Florian Müller-Plathe
Email Addresses: t.materzok@theo.chemie.tu-darmstadt.de, f.mueller-plathe@theo.chemie.tu-darmstadt.de
Eduard-Zintl-Institut für Anorganische und Physikalische Chemie and Profile Area Thermofluids and Interfaces
Technische Universität Darmstadt
Alarich-Weiss-Str. 8
D-64287 Darmstadt
Germany
Prof. Dr. Stanislav Gorb
Email Address: sgorb@zoologie.uni-kiel.de
Zoological Institute Functional Morphology and Biomechanics
Kiel University
Am Botanischen Garten 1-9
D-24118 Kiel
Germany

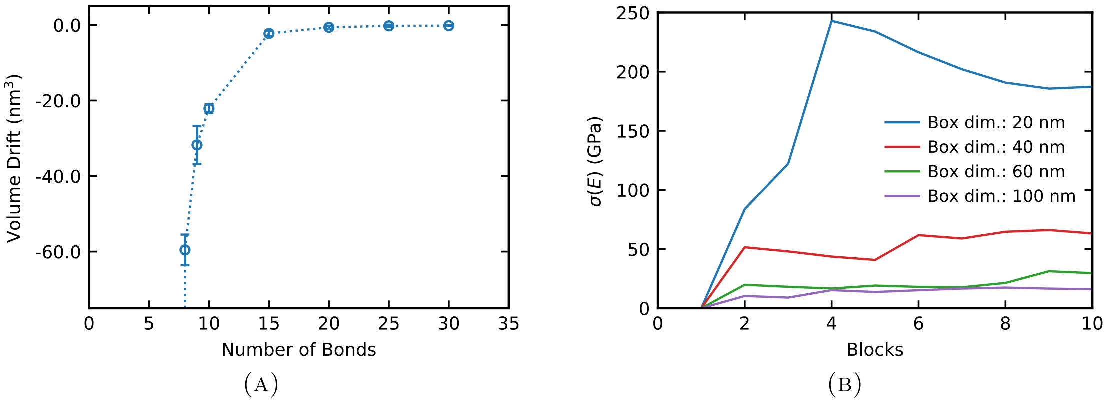

Figure S1: (A) Volume drift (or change) of keratin bulk material in the NPT ensemble (1 bar, 300 K) over 200 ns simulation time against the bond number with an initial system size of $60 \cdot 60 \cdot 60$ nm. The average is computed from 10 independent samples and the standard deviation of the mean is used as the error. (B) Convergence of the standard deviation of the Young's modulus $\sigma(E)$ against the number of independent simulations used for averaging and, in different colors, the system sizes that were tested. 30 bond neighbors are used for these simulations. A system size of $60 \cdot 60 \cdot 60$ nm with 30 bonds neighbors is sufficiently large.

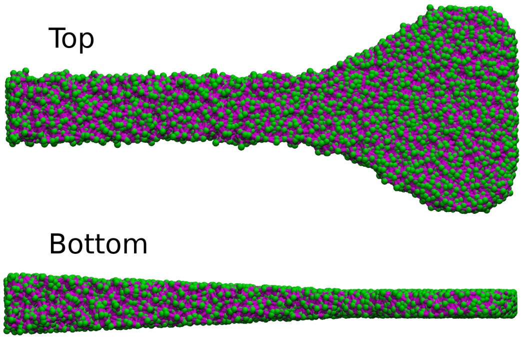

Figure S2: (Top) The top-viewing perspective of the spatula. Spatula beads are shown in green and a visual representation of the bond network is shown in purple. (Bottom) The shape of the spatula from its side is inspired by the finite element model of Sauer et al.[1] and the finite element calculations of Xu et al.[2]

Vertex	x (nm)	y (nm)	Vertex	x (nm)	y (nm)
1	0.000	82.780	62	0.000	92.780
2	0.000	60.900	61	0.000	114.660
3	22.680	61.330	60	22.680	114.230
4	44.160	61.080	59	44.160	114.480
5	66.780	61.310	58	66.780	114.250
6	89.140	61.550	57	89.140	114.010
7	113.090	61.540	56	113.090	114.020
8	138.600	62.230	55	138.600	113.330
9	163.710	62.470	54	163.710	113.090
10	188.760	62.100	53	188.760	113.460
11	213.790	62.450	52	213.790	113.110
12	237.290	62.260	51	237.290	113.300
13	256.460	59.770	50	256.460	115.790
14	273.290	55.720	49	273.290	119.840
15	287.650	50.800	48	287.650	124.760
16	302.490	45.000	47	302.490	130.560
17	317.480	37.370	46	317.480	138.190
18	332.730	26.260	45	332.730	149.300
19	347.200	17.070	44	347.200	158.490
20	362.240	8.890	43	362.240	166.670
21	376.230	2.460	42	376.230	173.100
22	390.260	0.360	41	390.260	175.200
23	402.970	0.000	40	402.970	175.560
24	415.000	2.270	39	415.000	173.290
25	423.820	6.910	38	423.820	168.650
26	430.010	13.090	37	430.010	162.470
27	434.190	20.690	36	434.190	154.870
28	437.410	30.860	35	437.410	144.700
29	438.180	44.000	34	438.180	131.560
30	438.960	61.000	33	438.960	114.560
31	439.730	81.800	32	439.730	93.760

Table S1: All 62 vertices of our mesoscale spatula model.

Name	Extent (relative to l_x of spatula)	Color in Figure 1
Spatula pad	70% to 100%	blue
Shaft haft	0% to 5%	grey
Spatula tip	95% to 100%	red
Spatula joint	60% to 65%	purple
x_s	65%	-

Table S2: Names, colors and the position of different areas of the mesoscale spatula model. The extent is relative to the spatula length in the x direction l_x.

1 Surface model details

The surface is generated much like the bulk keratin model, it has the same random arrangement of beads and the same bead density. We use the same minimum distance between beads and the same target density to fill the simulation box up to a maximum height z_m with beads. The minimum height of the surface is always 13 nm. In the case of rough surfaces, we insert beads underneath a three-dimensional landscape defined by $z_m = 13\text{ nm} + \lambda \sin(x \cdot \pi n_p / l_x^s + \pi X_x) \cdot \sin(y \cdot \pi n_p / l_y^s + \pi X_y)$ with the peak height $\lambda = 8$ nm, the number of peaks in x and y direction n_p, and the length of the surface in x and y: l_x^s and l_y^s. We apply a random phase shift using a uniformly distributed random number $X \sim U([0, 2])$ in the x and y directions to simulate random placements of the spatula on top of a surface.

2 Details about the parameterization of the anisotropic bonded interactions of the mesoscale keratin force field

Before parameterizing the bond coefficients k and k_b, the ideal bulk keratin system size is determined by applying strain of 0, 1, and 2% in the (virtual) fibril direction for ten independently created bulk keratin systems of different sizes. For each system, Young's modulus is calculated. This is done by increasing box lengths, as shown in Figure S1 (B). By ideal bulk system size, we mean here that computation is expeditious and that the average and standard deviation of Young's modulus E are converged. No finite-size effects affect our force field parameterization, and statistics are distinct enough to distinguish between fitting or unfitting parameters. For each system size, Young's modulus along the (virtual) fibril direction E is calculated for all ten systems, and the smallest system size at which the standard deviation of Young's modulus is converged is chosen. As seen in Figure S1 (B), a system size of $(60)^3$ nm is sufficiently large and is used from here on out for all simulations of Young's modulus and Poisson's ratio.

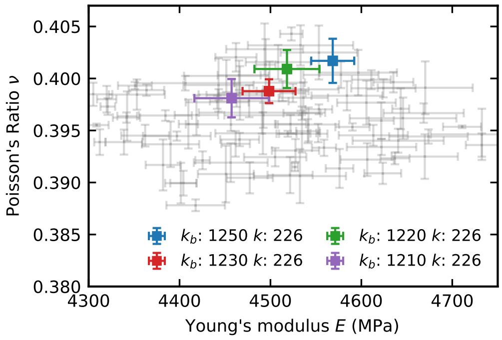

Figure S3: Resulting Poisson's ratios ν and Young's moduli E of the bulk keratin material system of the combination of k and k_b values (listed in Table S3). The standard deviation using three samples for averaging (grey) and 10 samples (colored) are used as the error. The bond coefficients labeled in the legend are in units of kJ mol^{-1} nm^{-2}. Grey data points are listed in Table S3. The average is computed from 10 independent samples and the standard deviation of the mean is used as the error.

k (kJ mol^{-1} nm^{-2})	k_b (kJ mol^{-1} nm^{-2})	E (MPa)	$\sigma(E)$ (MPa)	ν	$\sigma(\nu)$
220	1150	4229.89	11.34	0.399	0.001
220	1250	4523.01	12.37	0.404	0.001
230	1150	4308.66	13.32	0.396	0.000
230	1250	4596.50	42.65	0.401	0.002
235	1150	4312.27	6.13	0.394	0.001
235	1250	4584.15	38.98	0.398	0.001
240	1150	4338.86	20.17	0.394	0.001
240	1250	4645.88	58.69	0.396	0.002
245	1150	4401.44	17.26	0.390	0.002
245	1250	4643.31	9.31	0.397	0.002
255	1150	4404.21	14.41	0.390	0.001
255	1250	4673.84	43.26	0.394	0.001
260	1150	4417.73	32.20	0.388	0.001
260	1250	4732.51	17.59	0.394	0.001
223	1250	4553.27	42.13	0.402	0.003
223	1230	4508.45	35.65	0.402	0.002
223	1220	4451.48	46.55	0.400	0.002
223	1210	4442.88	38.58	0.399	0.003
229	1250	4577.57	41.32	0.400	0.001
229	1230	4499.05	38.81	0.400	0.002
229	1220	4513.33	28.54	0.399	0.001
229	1210	4476.64	43.26	0.398	0.002

Table S3: A small selection of results of the bulk keratin material parametrization of the anisotropic bond coefficients k and k_b. The Young's modulus E is calculated between 0% and 2% strain in the direction of the (virtual) fibrils, and the Poisson's ratio ν is the average between 1% and 2% strain orthogonal to the fibril direction. The values are averages over 3 independently generated systems.

3 Details about the parameterization of the nonbonded interactions of the mesoscale keratin force field

We compare different system sizes to ensure that finite-size effects are negligible. Figure S4 shows that p converges slowly with increasing system size. For the smallest system of $30 \cdot 30$ nm (blue), each bead is bonded to $N_{\text{bonds}}/N = 8.6\%$ of all beads, leading to finite-size effects. For a system of size $90 \cdot 90$ nm, the ratio of bonds to the number of beads is only 0.9%. We continue with this size since it is a good compromise of the value of p with computational efficiency.

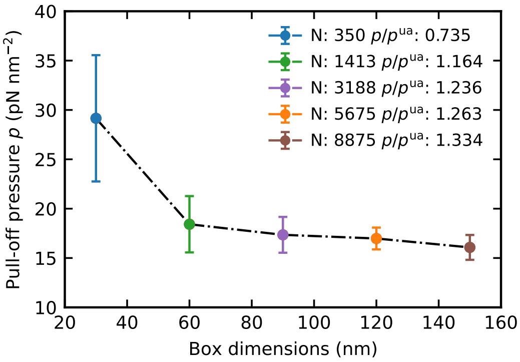

Figure S4: Pull-off pressure of different sized bulk keratin systems ranging from 30 nm box length (total number of beads $N = 350$) to 150 nm ($N = 8875$). With an increasing number of beads, the average and the standard deviation of the pull-off pressure converges. The ratio of the bulk keratin pull-off pressure to the all-atom pull-off pressure p/p^{ua} is shown in the legend. The force field parameters used for this validation are $k = 226$ kJ mol^{-1} nm^{-2}, $k_b = 1220$ kJ mol^{-1} nm^{-2}, $\sigma = 2.8$ nm, and $\epsilon = 1000$ kJ mol^{-1}. The average is computed from 10 independent samples and the standard deviation of the mean is used as the error.

4 United-atom gecko keratin model

The united-atom (UA) gecko keratin model uses the GROMOS 54A7 force field for all atoms present in the system, keratin protein and surface[3, 4, 5, 6].

In earlier coarse-grained work[7] we discovered that only the intrinsically disordered protein regions (IDRs) of the gecko keratin directly contact the surface and not the beta-folded region of the keratin protein that polymerizes into nanofibrils. Thus only the IDRs of the gecko keratin protein are responsible for the adhesive energetic interaction between spatula and surface. Therefore we amorphized a gecko beta-keratin protein (Ge-cprp-9), where only the intrinsically disordered parts of the protein are considered.

The exact equilibration protocol, including energy minimization, amorphization at 2000 K with subsequent cool down, and multi-step equilibrations in the NPT ensemble with and without soft-core potentials, would go beyond the scope of this SI.

Additionally, gecko keratin contains a large fraction of disulfide bonds.[8, 7] We cross-link one-third of the cysteines ($\approx 7.5\%$ of the amino acids in the protein). Therefore, achieving the same cross-link density as in a previous coarse-grained work.[8]

The united-atom keratin simulations of the previous work were carried out using the GROMACS 2018 software package[9]. The production runs to calculate Young's modulus were performed in three-dimensional periodic boundary conditions (PBC). The timestep was 2 fs, and a velocity rescale[10] thermostat kept the temperature at 300 K. A semi-isotropic Berendsen[11] barostat with a compressibility of $4.5 \cdot 10^{-5}$ bar^{-1} in x and y, and a compressibility of 0 bar^{-1} in z, kept the pressure of the system at 1 bar. Production runs were repeated five times for five independently generated systems ($n = 25$). Young's modulus was computed with a linear fit to the first 1% strain. Poisson's ratio was computed as the average over strain 1% to 5%.

5 Simulation details

All simulations are carried out using the GROMACS 2018 and 2021 software packages[9]. The van der Waals interaction cutoff is 12 nm, and van der Waals interactions are modeled using the 12-6 Lennard-Jones potential. We use the potential-shift-Verlet scheme[12] as a cutoff modifier for a physically[13] smooth transition at the cutoff. We simulate state points in NVT and NPT with a temperature of 300 K and a pressure of 1 bar, respectively. Different thermostats and barostats are used at different stages; see the following subsections. The timestep is 20 fs.

5.1 Mechanical property calculations with the mesoscale keratin material

Young's modulus and Poisson's ratio are calculated for the three-dimensionally periodic mesoscale keratin material by scaling the initial system configuration in (virtual) fibril direction to give strains of 0 to 2%.

A semi-isotropic Berendsen barostat[11] with a compressibility of 0 bar^{-1} in the fibril direction keeps the pressure at 1 bar using a coupling time of $\tau_p = 100$ ps and allows the perpendicular dimensions to adjust. A velocity rescale thermostat[10] is used with a coupling time of $\tau_T = 2$ ps. The systems are simulated for 200 ns. Pressure, density, and bond energies converge during the first nanosecond of the simulation. The last 180 ns are assumed to be in equilibrium and are used for the analysis of mechanical properties.

5.2 Mesoscale keratin material detachment simulations

To perform mesoscale keratin material detachment simulations, the material with the optimized parameters (Section 3) is placed on top of a surface of height 13 nm with a minimum distance between surface and bulk of $\sigma = 4.0$ nm. The fibril direction is parallel to the surface. The PBC in directions parallel to the surface makes the mesoscale keratin material and surface semi-infinite, i.e., two infinite plates in adhesive contact. The surface beads are fixed in place. The center of mass (COM) of the beads of the top half of the bulk keratin is connected by a harmonic bond to a virtual particle, which can be moved at will and which mimics the action of a cantilever.

The pulling simulations of the mesoscale keratin material periodic parallel to the surface are performed in three consecutive steps. First, the keratin material is preloaded (i.e., pressed against the surface) with a constant pressure of 0.2553 kJ mol^{-1} nm^{-3} (corresponding to a constant force of 2068 kJ mol^{-1} nm^{-1} in the $90 \cdot 90$ nm system) acting on the top half of the material for 100 ns (red particles in Figure 5). Next, the system is allowed to relax for 100 ns with no external force applied. Finally, the keratin material is pulled away from the surface in the direction normal to the surface. To this end, the virtual cantilever is moved away from the surface with constant velocity $v = 0.001$ nm ps^{-1} (with the harmonic force constant $k_{\text{pull}} = 1000$ kJ mol^{-1} nm^{-2} or $k_{\text{pull}} = 1660$ pN nm^{-1}), with the virtual particle located initially at the COM of the top half of the keratin. The resulting loading rate, $\dot{F} = k_{\text{pull}} v = 1.66 \cdot 10^{12}$ pN s^{-1}, is equal to the loading rate of the united-atom reference simulations[14].

The preload and relax phases use a stochastic dynamics (SD) thermostat[15] with a coupling time of $\tau_T = 1$ ps to inhibit any possibility of the harmonic keratin network to periodically oscillate without being able to dissipate the energy. The final pulling simulation, when the virtual cantilever moves away from the surface to pull off the bulk keratin material, uses a velocity rescale thermostat[10] with $\tau_T = 1$ ps, because the friction of the SD thermostat would bias the measured pull-off force. All simulations take place in the NVT ensemble with a large vacuum volume above the keratin to allow the pull-off.

6 Spatula detachment simulations

Initially, the spatula is generated as described in Section 2.2. Then we push the spatula pad beads (Figure 1 blue and Table S3) for 100 ns with a constant pressure of 0.2553 kJ mol^{-1} nm^{-3} against the surface. The surface beads are fixed in space. The center of mass (COM) of the shaft haft, designated as the first five percent (in x dimension, with the shaft haft coming before the spatula pad) of the spatula length ($l_x \cdot 0-5\%$), as seen in Figure 1 (grey) and described in Table S3, is kept from rotating around the axis normal to the surface by a flat-bottom[16, 17] potential (as implemented in GROMACS[9]) with $k_{\text{flat-bottom}} = 2 \cdot 10^4$ kJ mol^{-1} nm^{-2}, the distance where the potential starts is $r_0 = 2$ nm. After this preload step, the system is allowed to relax with no applied forces for another 100 ns. A flat-bottom[16, 17] potential is, however, still used to restrict the spatula from rotating around the axis normal to the surface.

In the fourth step, the spatula is prepared to be bent upwards. Therefore, we move the shaft haft COM away from the surface for 300 ps with $k_{\text{pull}} = 1 \cdot 10^5$ kJ mol^{-1} nm^{-2} and a velocity of 0.1 nm ps^{-1}. Simultaneously, the shaft haft is kept from rotating as described above. This step is done to correct a GROMACS specific error that arises when the spatula initially bends opposite of the set bending direction (due to thermal fluctuations).

As done by Sauer et al.[1], the main pulling mechanism is broken into two parts: bending the shaft so that it has an inclination of some degree to the surface (step 5), and then pulling the spatula vertically off that surface (step 6). The bending is carried out by applying an umbrella potential ($V(\theta) = k/2\,(\theta - \theta_0)^2$ with $k = 5 \cdot 10^9$ kJ mol^{-1} rad^{-2}) on the COM of the spatula shaft haft using an "angle-axis" geometry. This is GROMACS terminology for an angle-dependent harmonic potential between two vectors. Here, one vector is defined between two COMs, and the second vector is defined by an axis. The angle-axis is defined between the shaft haft COM and the spatula tip COM (Table S3) and the vector parallel to the surface $\{-1, 0, 0\}$. We rotate with 0.001 deg ps^{-1} upwards (Note that the angle-force constant is in units of radians, while the unit for the rate of bending is expressed in degree, as used in GROMACS). This pulling results in a force normal (upwards) to the shaft bending the spatula along the way.

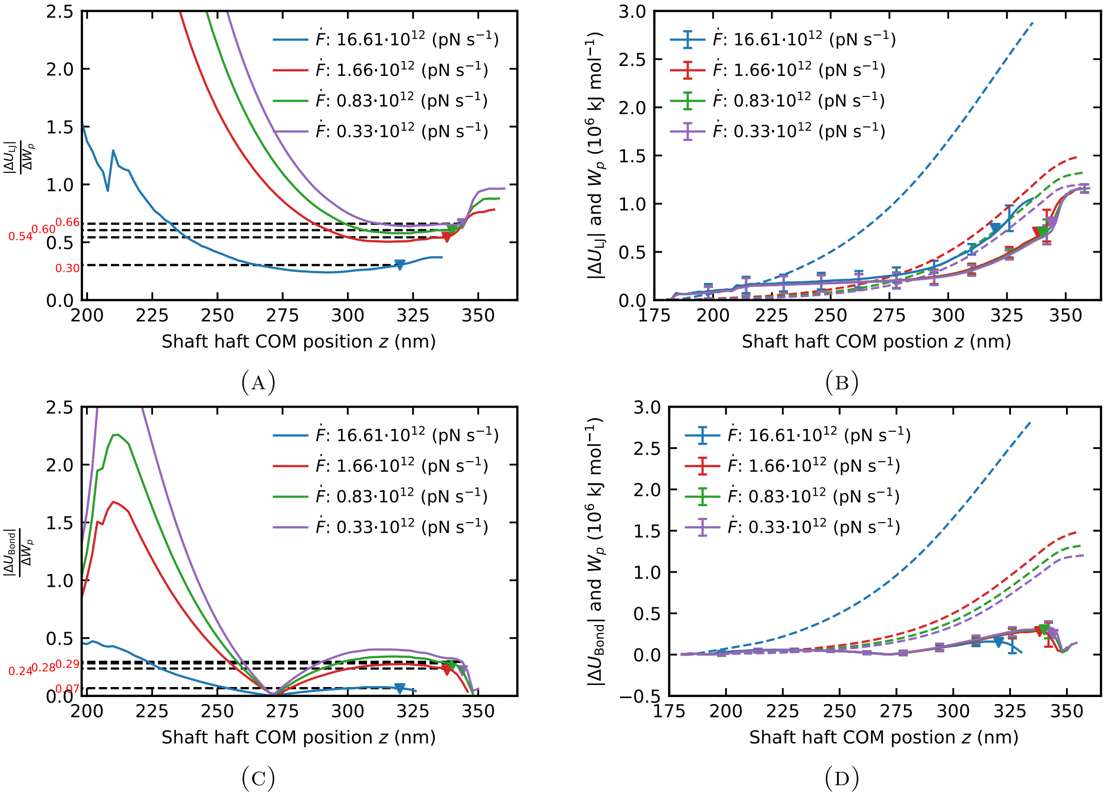

(A)

(B)

(C)

(D)

Figure S5: (A) Ratio of adhesive energy overcome during detachment to work of pull-off for different loading rates. The position of the shaft haft when the force is at its maximum (pull-off) is marked with a triangle. Red values at the beginning of black dashed lines note the ratio at the position of pull-off. (B,D) Energies (solid lines) and work (dashed lines) shown side-by-side for the varying loading rates. (C) Ratio of bending energy to work of pull-off. Data shown is the average computed from 10 independent samples.

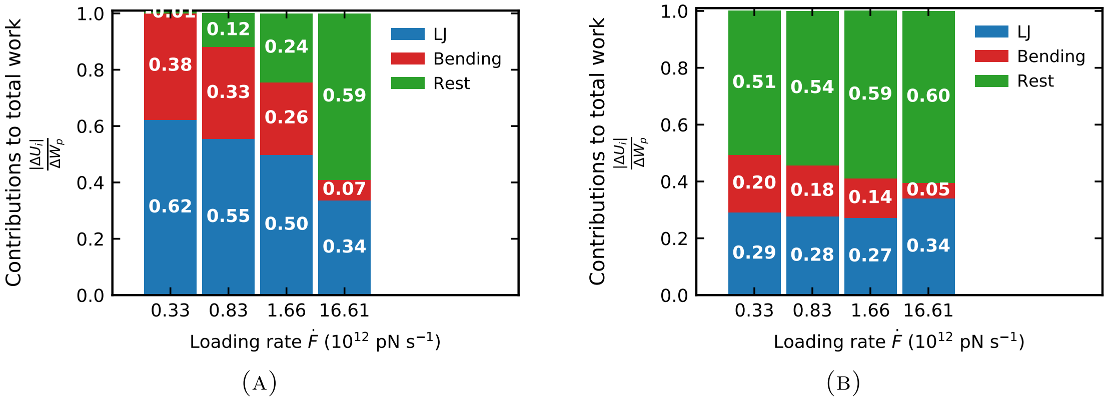

(A) (B)

Figure S6: The ratio of overcome adhesive energy (blue) at the position of the maximum force is compared to contributions overcome from bending (red) and dissipated rest (green) energies to work of pull-off for different loading rates. The ratios are annotated in the stacked bars. The spatula equilibrium inclination is $\theta_S = 60°$ (A) and (B) $\theta_S = 75°$. The average is computed from 10 independent samples.

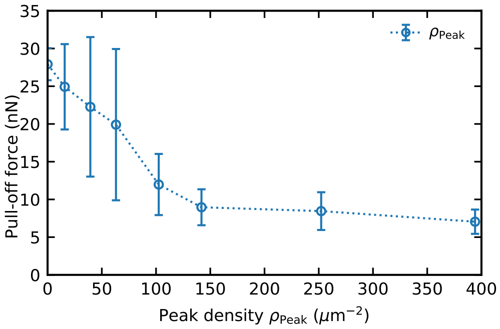

Figure S7: The pull-off force is shown against the peak (or valley) density. The data points are the average computed from 10 independent samples and the standard deviation of the mean is used as the error.

References

[1] R. A. Sauer, M. Holl, *Comput. Methods Biomech. Biomed. Eng.* **2013**, *16*, 6 577.

[2] Q. Xu, Y. Wan, T. S. Hu, T. X. Liu, D. Tao, P. H. Niewiarowski, Y. Tian, Y. Liu, L. Dai, Y. Yang, Z. Xia, *Nat. Commun.* **2015**, *6*, 1 8949.

[3] L. D. Schuler, X. Daura, W. F. v. Gunsteren, *J. Comput. Chem.* **2001**, *22*, 11 1205.

[4] C. Oostenbrink, A. Villa, A. E. Mark, W. F. V. Gunsteren, *J. Comput. Chem.* **2004**, *25*, 13 1656.

[5] N. Schmid, A. P. Eichenberger, A. Choutko, S. Riniker, M. Winger, A. E. Mark, W. F. van Gunsteren, *Eur. Biophys. J.* **2011**, *40*, 7 843.

[6] W. Huang, Z. Lin, W. F. van Gunsteren, *J. Chem. Theory Comput.* **2011**, *7*, 5 1237.

[7] T. Materzok, S. Gorb, F. Müller-Plathe, *Soft Matter* **2022**, *18*, 6 1247.

[8] K. S. Endoh, T. Kawakatsu, F. Müller-Plathe, *J. Phys. Chem. B* **2018**, *122*, 8 2203.

[9] B. Hess, C. Kutzner, D. van der Spoel, E. Lindahl, *J. Chem. Theory Comput.* **2008**, *4*, 3 435.

[10] G. Bussi, D. Donadio, M. Parrinello, *J. Chem. Phys.* **2007**, *126*, 1 014101.

[11] H. J. C. Berendsen, J. P. M. Postma, W. F. van Gunsteren, A. DiNola, J. R. Haak, *J. Chem. Phys.* **1984**, *81*, 8 3684.

[12] S. Páll, B. Hess, *Comput. Phys. Commun.* **2013**, *184*, 12 2641.

[13] D. van der Spoel, P. J. van Maaren, *J. Chem. Theory Comput.* **2006**, *2*, 1 1.

[14] T. Materzok, A. Canestraight, S. N. Gorb, F. Müller-Plathe, *Nat. Commun.* **2022**, under review.

[15] N. Goga, A. J. Rzepiela, A. H. de Vries, S. J. Marrink, H. J. C. Berendsen, *J. Chem. Theory Comput.* **2012**, *8*, 10 3637.

[16] G. M. Clore, M. Nilges, D. K. Sukumaran, A. T. Brünger, M. Karplus, A. M. Gronenborn, *EMBO Rep.* **1986**, *5*, 10 2729.

[17] H. Ryu, T.-R. Kim, S. Ahn, S. Ji, J. Lee, *PLOS ONE* **2014**, *9*, 10 e108888.

Table of Contents

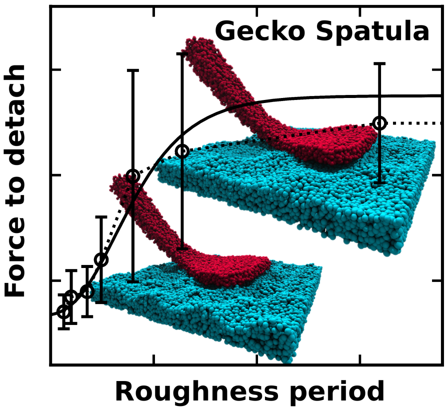

A multiscale modeling approach derives a particle-based mesoscale gecko spatula model that is able to link atomistic and mesoscale simulations and yield pull-off forces similar to experimental work. A root-mean-square roughness causality is disproven and a roughness wavelength-dependent sigmoidal trend is revealed, instead. We confirm an experimental hypothesis.

3.4 Gecko adhesion: a molecular-simulation perspective on the effect of humidity

Reproduced with permission from Materzok et al. [Soft Matter 2022, **18**, 1247-1263] Copyright 2022 The Royal Society of Chemistry.

Soft Matter

ROYAL SOCIETY
OF CHEMISTRY

PAPER

View Article Online
View Journal | View Issue

Check for updates

Cite this: *Soft Matter*, 2022, **18**, 1247

Gecko adhesion: a molecular-simulation perspective on the effect of humidity†

Tobias Materzok, *[a] Stanislav Gorb*[b] and Florian Müller-Plathe*[a]

Received 23rd August 2021,
Accepted 29th December 2021

DOI: 10.1039/d1sm01232k

rsc.li/soft-matter-journal

Gecko adhesion is investigated by molecular dynamics simulations. It is known, that the gecko adhesion system shows increased pull-off forces in humid environments. A coarse-grained model of gecko beta keratin, previously developed in our group, is extended and used to elucidate the molecular mechanisms involved in this humidity effect on adhesion. We show that neither the change of the elastic properties of gecko keratin, nor capillary forces, can solely explain the increased pull-off forces of wet gecko keratin. Instead, we establish a molecular picture of gecko adhesion where the interplay between capillary bridges and a mediator effect of water, enhances pull-off forces, consistent with observations in AFM experiments at high humidities. We find that water density is raised locally, in molecular scale asperities of the gecko keratin and that this increase in local water density smoothes the surface-spatula interface. Water, which is absorbed into the keratin, acts as a mediator, and leads during pull-off to the dominant contribution in the van der Waals energy, because the dispersion interactions between water and surface are primarily opposing the pull-off.

1 Introduction

Geckos owe their incredible ability to run on walls[1] and even on ceilings due to billions of spatulae at the end of millions of setae on their toes. The spatulae are in molecular close contact with the surface. The mechanisms behind this remarkable adhesive ability have been investigated for decades[2–4] and shown to be, among others, van der Waals interactions. Additionally, gecko adhesion is typically enhanced by increased relative ambient humidity, however, the mechanism behind this humidity effect is still intensively debated.[4–7] The dominant hypothesis is the change in the Young modulus of setae upon swelling.[5,6,8] The potential role of humidity-enhanced capillary forces has also been discussed.[4,9] The special case of a water layer present on all kinds of surfaces[4,6,10] at high humidity has been investigated, and the enhanced adhesion has been explained by either capillary forces or material softening. Mitchell *et al.*[11] recently came to the conclusion, that the two mechanisms are not mutually exclusive, but that capillary forces increase pull-off forces at hydrophilic surfaces and that material softening is responsible for the increased adhesion at hydrophobic surfaces. A molecular perspective on the humidity effect is, to our knowledge, non existent, but of great importance for understanding gecko adhesion and for the design of biologically-inspired synthetic gecko adhesives.

The multi-level hierarchical structure of the gecko adhesion systems begins at the millimeter scale, where millions of setae (around one hundred micrometers long) are situated on lamellae, found on each gecko's toe pad. Fibrillar structures inside the setae containing beta keratin filaments[12,13] split at the end of each seta into hundreds to thousands of spatulae (around one hundred nanometers long).[14,15] This milli- to nanoscale structure gives the gecko the ability to attach its spatulae to a wide range of surface roughnesses.[16,17]

As the gecko walks on a substrate the amino acids of the keratin on the spatula surface are in close contact with the surface atoms. We hypothesize that the main driving force of

---

[a] *Eduard-Zintl-Institut für Anorganische und Physikalische Chemie and Profile Area Thermofluids and Interfaces, Technische Universität Darmstadt, Alarich-Weiss-Str. 8, D-64287 Darmstadt, Germany. E-mail: t.materzok@theo.chemie.tu-darmstadt.de, f.mueller-plathe@theo.chemie.tu-darmstadt.de*

[b] *Zoological Institute Functional Morphology and Biomechanics, Kiel University, Am Botanischen Garten 1-9, D-24118 Kiel, Germany. E-mail: sgorb@zoologie.uni-kiel.de*

† Electronic supplementary information (ESI) available: Section S1: Gecko keratin model creation procedure; Section S2: insertion of water into gecko keratin; Section S3: dry gecko keratin equilibration; Section S4: wet gecko keratin equilibration; Table S1: pulling velocities and loading rates used; Table S2: table of force probe molecular dynamics simulation results; Fig. S1: smoothed force profiles as function of pulling velocity; Fig. S2: pull-off pressures of wet keratin on a dry surface; Fig. S3: pull-off pressures of wet keratin as a function of Young modulus; Fig. S4: density profile of weakly hydrophilic keratin during pull-off; Fig. S5: density profile of weakly hydrophilic keratin during pull-off; Movie S1: pull-off: weakly hydrophilic keratin from wet surface; Movie S2: pull-off: strongly hydrophilic keratin from wet surface; Movie S2b: pull-off: strongly hydrophilic keratin from wet surface (transparent keratin); Movie S3: pull-off: weakly hydrophilic keratin from dry surface; Movie S3b: pull-off: weakly hydrophilic keratin from dry surface (transparent keratin); Movie S4: pull-off: strongly hydrophilic keratin from dry surface; Movie S4b: pull-off: strongly hydrophilic keratin from dry surface (transparent keratin). See DOI: 10.1039/d1sm01232k

humidity-enhanced adhesion can be explained by van der Waals interactions. To verify the hypothesis we extend a purely Lennard-Jones based coarse-grained model of dry gecko keratin, previously developed in our group,[13] which was validated against mechanical properties of setae and spatula with the Young modulus and Poisson's ratio, but did not yet encompass adhesion to a surface, by implementing a water and a surface model. The extension of the coarse-grained model allows us to attach the gecko keratin model to a surface and study the effect of water upon pull-off.

To investigate the humidity effect and the role of water on the ability to increase adhesion, this study uses as a first force probe molecular dynamics (FPMD) simulations – to compute pull-off forces of the keratin from a hydrophobic surface with a contact angle of greater than 110°. The primary target of our model is to achieve a balance between realistic, experimental systems and computational efficiency, allowing us to reach the time and length scales necessary to make reasonable comparisons against experimental pull-off forces and pulling velocities. Since our aim is to elucidate molecular mechanisms of the enhanced pull-off force in humid environments on hydrophobic surfaces, we are particularly interested in the experimental conditions of Huber *et al.*[4] Their work showed increased pull-off forces of a single spatula with increasing ambient humidity on a hydrophobic octadecyltrichlorosilane self-assembled monolayer (OTS-SAM) surface. Since the water content and hydrophilicity of gecko keratin at given humidities is not known, we use one water content (10 wt%). We also experimentally investigate the upper boundary of water content at very high ambient humidities for gecko keratin-like materials, and show that the water content in our models are within the experimental range of possible water contents.

We use the term hydrophilicity as a way to relate between the experimentally-observed phenomenon which influences the contact angle of water on flat surfaces and our molecular perspective, where the strength of water–keratin energetic interactions and water–water interactions result in a macroscopic experimentally-observable contact angle. Huber *et al.*[4] calculated the contact angle of gecko claw keratin and estimated the contact angle for spatula keratin. The gecko claw keratin had a contact angle of around 128°. We show, however, that gecko claw keratin can absorb up to 30% of water content at high humidities. Due to this discrepancy, on one side a super-hydrophobic contact angle and on the other side a major absorption of water, we are skeptical of the contact angle estimated by Huber *et al.*[4] for gecko spatula keratin. We expect that there is a correlation between contact angle and water content. The contact angle of water on polyamide surfaces immersed in water shows a decrease in contact angle with exposure time to water[18] and a correlation between water content increase and contact angle decrease is established for increasing hydrophilicity of aliphatic polyamides.[19] Because we do not know the real experimental hydrophilicity of spatula keratin, we create different gecko keratin models with different hydrophilicities. Higher hydrophilicity would result in a smaller contact angle with water, lower hydrophilicity would lead to a larger contact angle. Due to our multiple keratin models-approach, we can study the effect of possible hydrophilicities of adhesive materials on the pull-off force in ambient humidity. This insight into the effect of hydrophilicity of the adhesive material may drive the design of better biologically-inspired synthetic gecko adhesives.

We conduct simulations of bulk keratin, without a surface present, in order to extract mechanical properties. They are validated against experimental results and the effect of water is discussed. We conduct non-equilibrium simulations in which dry or wet keratin is pulled off the surface by an external force, which we call pulling simulations, for short, from here on. We will show an additional effect of water besides the effective reduction of the Young modulus and the capillary forces. In the hypothetical case of a strongly hydrophilic keratin (same applies to synthetic adhesive materials), which may readily absorb water into its interface region between surface and spatula, water acts as a mediator for keratin to surface interactions. Water also smoothes the molecular scale roughness of gecko keratin and allows it to form additional molecular contacts with the underlying surface. This smoothing of the molecular scale roughness due to water may also be a important factor in case of surfaces which are rougher than our OTS-SAM, where water would fill into surface cavities.

There are three main results from this study. First, depending on keratin hydrophilicity, either capillary bridges or a water mediating effect enhances adhesion in scenarios where water is present, which we show by correlating the change in van der Waals interaction with density profiles (Section 3.3.3). Second, we demonstrate that water fills the molecular asperities between the spatula and surface, effectively smoothing the spatula-surface interface. This smoothing is evident in the two-dimensional density profiles and trajectory movies (ESI†), both of which show that water fills into the gaps between keratin and the surface and smoothens the interface (Section 3.3.3). Lastly, because spatula softening cannot explain the enhanced pull-off forces, we challenge the popular hypothesis in gecko adhesion research that water making the keratin soft is solely responsible for the enhanced pull-off forces (Sections 3.1 and 3.3.2). In Section 3.1, we also validate our model against experimental material characteristics.

2 Models and computational details

2.1 Force probe molecular dynamics: pulling simulations

We use FPMD to compute pull-off forces of gecko keratin from a space-fixed surface in presence of different water contents (0 or 10% water content in keratin and/or a water layer between the surface and the keratin or a dry hydrophobic surface). In resemblance to atomic force microscopy (AFM) experiments with gecko setae and spatulae,[20] a virtual cantilever is linked to the keratin and the cantilever is moved vertically, away from the surface, until the keratin detaches. To accomplish this setup, the keratin model is placed into contact with a surface, which then strongly adheres to that surface. By moving the virtual cantilever (modelled as a virtual particle) away from its initial position, perpendicular to the surface, a force opposed to the adhesion force is introduced. When the pull-off force exceeds the adhesion force, the gecko keratin adhesive material is lifted from the surface. When in FPMD the adhesion force is larger than the friction forces opposing the pull-off, *i.e.* internal friction or a water phase in ligand-unbinding experiments, the unbinding process is rapid and is also called rupture event. FPMD is a non-equilibrium molecular dynamics (MD) method which is typically used to gain insight into unfolding pathways[21] or receptor–ligand unbinding.[22]

In our model the virtual particle is linked by a harmonic spring to the center of mass (COM) of the top layer nanofibrils of our gecko keratin model, which reduces the bias on the interface region. We initially position the virtual particle $z(t = 0)$ at the COM of the top layer nanofibrils $z = z_{\mathrm{COM,EQ}} := 0$ and move it vertically, in z-direction, away from the surface, at different constant pulling velocities. We define z the position of the virtual particle and z_{COM} the position of the COM of the top layer nanofibrils. The pulling direction of the keratin on the surface is indicated by the arrow in z-direction alongside the typical system size in Fig. 1. Details of the models and computational details follow below.

Moving the virtual particle away from the surface at constant velocity leads to a linear increase in force $F_{\mathrm{pull}} = k_{\mathrm{pull}}(vt)$ with v being the pulling velocity and t the time. Molecular unbinding events lead to an increase of the distance between the keratin and the surface. The force experienced by the keratin is therefore $F_{\mathrm{pull}} = k_{\mathrm{pull}}(vt - z(t))$, where $z(t)$ denotes the position of the virtual particle in pulling direction.

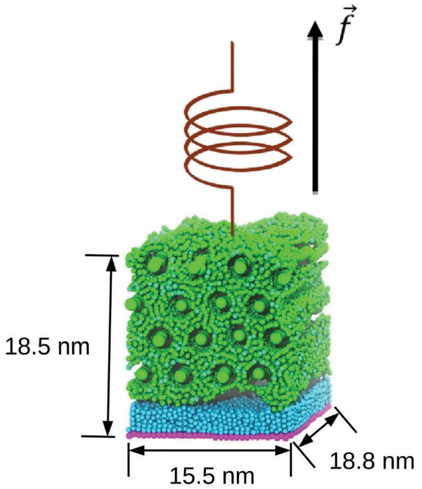

Fig. 1 Pulling simulation setup. The gecko keratin is shown in green on top of the octadecyltrichlorosilane self-assembled monolayer (cyan) which is linked to the constrained SiO_2 surface (purple). Four layers of nanofibrils are stacked on top of each other, each parallel to the surface. The center of mass of the keratin's top nanofibrils is linked to a virtual particle with an harmonic spring. The virtual particle is moved at constant pulling velocity away from the surface, pulling the keratin off the space-fixed surface.

We use FPMD simulations to investigate the effect of humidity on the pull-off force of gecko keratin. For each set of conditions (pulling velocity, water presence, hydrophilicity), 30 independent runs are performed and averaged.

2.2 Models

2.2.1 Dry gecko keratin model. We extend the biologically inspired coarse-grained two-bead model of gecko setae/spatulae beta keratin developed previously in our group by Endoh *et al.*[13] This coarse-grained model for gecko setae/spatulae keratin was targeted at the mechanical characteristics of the Young modulus and Poisson's ratioand is able to reproduce these mechanical properties. It was inspired top-down, by experimental insights, and bottom-up by reparameterizations of the MARTINI force field[23–25] (MARTINI FF). As a reference structure, avian feather beta keratin was used, which is assumed to be close to gecko setae keratin in its nanoscale structure, since the amino acid sequences are very similar between both species.[13,26] The avian feather keratin reference established: (1) the beta-sheet region (Core-box region[12,26]) of the peptide folds in similar fashion and forms dimers. (2) The dimers associate to nanofibrils,[27] which associate further to a more mesoscale fibrillar structure, also visible in scanning electron microscopy (SEM) cross-sections of gecko setae.[15] (3) The distance between dimers, in the fibril direction and, assuming hexagonal packing, the distance orthogonal to the fibril direction. A more detailed description can be found in the original work.[13] Endoh *et al.* mapped the entire sequence of dimer amino acids into a single coarse-grained bead, which was called "Core" bead, or CR bead in short, for its representation of the Core-box region. The keratin amino acid sequence is, however, not only composed of beta-sheet regions forming Core (CR) beads, but surrounded by regions which are predicted to fold in a random-coil like structure, which are known as the head and tail region.[12,28] The average amino acid of the gecko keratin head- and tail sequence, analyzed by Endoh *et al.*, is mapped into a single coarse-grained bead, representing this random-coil region, and are called "Amorphous" (AM) beads. The average[13] head region is made up of 64 amino acids and the tail region of 23 amino acids, which translates to 87 AM beads in total. The MARTINI FF was used as a start in the parameterization process of this coarse-grained keratin model. The energetic terms overestimate the interactions, and should be viewed as the ideal upper boundary.[13]

The Lennard-Jones parameters of the coarse-grained keratin model are shown in Table 2. The interaction between the CR and the AM beads is $\varepsilon_{\mathrm{CR-AM}} = 28.6\ \mathrm{kJ\ mol^{-1}}$ and, given the large size difference between CR and AM beads we shift the potential by a distance $r_0^{\mathrm{CR-AM}}$. The potential in eqn (1) shifts the position of the singularity to $r = r_0^{\mathrm{CR-AM}}$.

$$U_{\mathrm{LJ}}(r) = 4\varepsilon\left[\left(\frac{\sigma^{\mathrm{AM}}}{r - r_0^{\mathrm{CR-AM}}}\right)^{12} - \left(\frac{\sigma^{\mathrm{AM}}}{r - r_0^{\mathrm{CR-AM}}}\right)^{6}\right] \quad (1)$$

Like Endoh *et al.*, we use 16 CR beads in the nanofibrillar direction of the simulation box. For the initial configuration a total of 16 nanofibrils are fitted into the initial simulation box of dimensions 15.485 nm, 13.411 nm, and 18.92 nm, with hexagonal packing. We use the same system size as the previous work,[13] which is in the order of the thickness of a spatula (having a thickness of about 20 nm). More details about the procedure to generate the initial structure can be found in Section S1 (ESI†). A bulk simulation of the dry keratin is used to calculate mechanical properties, in three-dimensional periodic boundary conditions (3D PBC). Dry keratin is placed on top of a hydrophobic surface under 2D PBC, and is used for the pull-off simulations.

2.2.2 Dry gecko setae keratin model on a dry hydrophobic surface. We extend this gecko keratin model with parameters for a hydrophobic surface and for water, and hence, call the old model without water, the dry gecko keratin model. The hydrophobic surface is inspired by work of Huber *et al.*[4] (a illustration of the gecko – setae – spatula – molecular level can be found in the work of Sauer *et al.*[29] SEM images of the Spatula attached to a surface in Verenberg *et al.*[30]) in which gecko spatulae were pulled-off a octadecyltrichlorosilane self-assembled monolayer (OTS-SAM) covalently bonded to a SiO_2 substrate, as was done by Huber *et al.* in their experimental study. The SiO_2 substrate is constrained, and does not move, functioning as a space-fixed external potential in the vapor phase surrounding the keratin. We integrate the OTS with the SiO_2 substrate into single coarse-grained molecules made up of two different MARTINI bead types. Five MARTINI C1 type beads are connected in series and the end of this alkane chain is connected to one MARTINI Qa bead. C1 type beads represent the apolar alkane chain and the Qa bead the first layer of the SiO_2 surface, respectively. Huber *et al.*[4] measured the height of the monolayer to be 2.4 nm thick; the MARTINI FF maps four heavy atoms to one coarse-grained bead. Our mapping was chosen such, that this thickness is reasonably reproduced by the combined Lennard-Jones radii, leading to the five C1 beads described. The tails of the OTS-SAM are free to move in this model. We freeze, however, the position of the Qa beads after we performed an energy minimization, to obtain a fixed surface. This fixed surface allows the keratin to be pushed against and subsequently pulled-off from. The packing behavior of OTS on a silicon dioxide substrate and the resulting tilt angle of the alkane chain, is well understood.[31–34] Since we include the covalently bonded SiO_2 surface as a bead, it allows straight forward implementation of the equilibrium tilt angle $\theta_0^{\mathrm{Qa-C1-C1}}$. We use a common packing density of 1 molecule per 0.22 nm, which leads to a tilt angle of $\theta_0^{\mathrm{Qa-C1-C1}} = 173.0°$.[33] The distance between the Qa bead, representing the SiO_2 layer, and the keratin is large enough, that the Lennard-Jones interactions are beyond their cutoff or very rarely sampled during pull-off. A full representation of the SiO_2 layer, including beads which do not carry a C_{18} alkane, was therefore not used. Table 1 lists the bonded parameters for the OTS-SAM surface molecules.

Lennard-Jones interaction parameters between the alkane chains (C1 beads) and the keratin are computed by the geometric mixing rule. As mentioned earlier, the interaction parameters in the dry keratin model are overestimated. Additionally, recent studies showed that the MARTINI FF generally overestimates protein aggregation.[35] There are many different combination rules to compute nonbonded interaction parameters of the Lennard-Jones potential for unlike interactions. To compute nonbonded interaction parameters between the overestimated interactions from Endoh *et al.* and the interaction parameters of the MARTINI FF we use scaled geometric mixing. To that effect, we scale the geometric mean of $\varepsilon_{\mathrm{C1-CR}}$ and $\varepsilon_{\mathrm{C1-AM}}$ by a factor of 0.1. As previously mentioned, we will publish results soon, showing that the pull-off forces of our keratin are comparable with experiment, if the whole spatula is simulated and peel-off is possible. Interactions between the silica Qa beads and the keratin are not computed. Table 2 summarizes the Lennard-Jones interaction parameters of the dry keratin model and the hydrophobic surface.

Table 1 Interaction parameters of one octadecyltrichlorosilane self-assembled monolayer coarse-grained molecule. The equilibrium bond length r_0 and the spring constant k_b are taken from the MARTINI force field. The equilibrium angle $\theta_0^{\mathrm{Qa-C1-C1}}$ is chosen in accordance to Barriga *et al.*[33] The force constant of the harmonic angle potential k_a is taken from the MARTINI force field

Type	r_b (nm)	k_b (kJ mol^{-1} nm^{-1})	Bond angles	θ_0 (deg)	k_a (kJ mol^{-1})
C1–C1	0.47	1250	C1–C1–C1	180.0	25.0
Qa–C1	0.47	1250	Qa–C1–C1	173.0	25.0

Since we equilibrate the bulk keratin with different water contents and varying interactions under *NPT* conditions, the size of the keratin patch varies slighty in each of the equilibrations, which means there is not one surface fitting all. Instead, we create the surface automatically for each set of water content and interaction parameters. One of the resulting gecko keratin patches pressed against the hydrophobic surface is shown in Fig. 2 with the nanofibrils placed parallel to the surface. Here the surface has the dimensions 15.4156 nm and 18.7958 nm. In contrast to the wet gecko keratin model, no water is included yet. In the systems containing water two 12-6 Lennard-Jones walls, at $z = 0$ nm and $z = 40$ nm with interaction parameters of C1, are keeping the water beads from leaving the simulation box. We assume that these walls will not alter our results, since the total energetic interaction of the wall at $z = 0$ nm with the rest of

Table 2 Lennard-Jones interaction parameters of the coarse-grained gecko keratin model and the coarse-grained octadecyltrichlorosilane self-assembled monolayer with itself, and with the dry keratin model. With σ the Lennard-Jones radius, the shift of the Lennard-Jones singularity r_0 and the interaction energy ε

Type	σ (nm)	r_0 (nm)	ε (kJ mol^{-1})
AM–AM	0.59	0.0	8.0
CR–AM	0.59	0.8327	28.6
C1–C1	0.47	0.0	3.5
Qa–C1	0.62	0.0	2.0
C1–CR	0.5266	0.8327	1.8917
C1–AM	0.5266	0.0	0.5292
P4–CR	0.5266	0.8327	22.6
BP4–CR	0.5266	0.8327	22.6
P4–AM	0.5266	0.0	6.3
BP4–AM	0.5266	0.0	6.3
P4–C1	0.47	0.0	2.1
BP4–C1	0.47	0.0	2.1

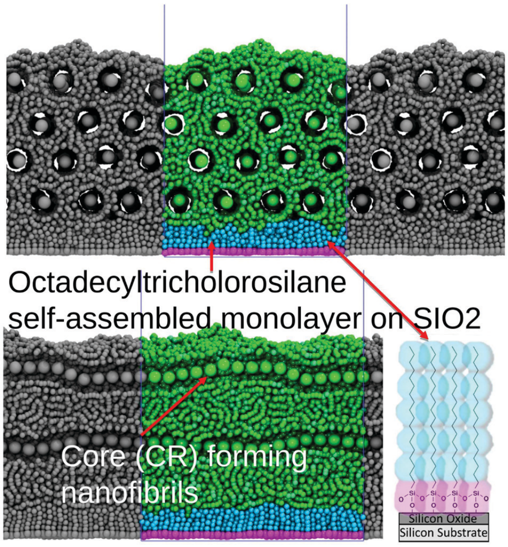

Fig. 2 Top: Front view (*xz*-plane) of the dry gecko keratin. The gecko keratin in green is pushed against the hydrophobic octadecyltrichlorosilane self-assembled monolayer (cyan) during the preloading phase. The fixed SiO_2 beads (purple) do not move throughout the simulation and serve as anchor points in the vacuum. Periodic images are displayed in *x* and *y* (grey), in *z*-direction we do not use periodic images. Bottom: Side view (*yz*-plane) of the gecko keratin model.

the system is negligible small (the wall–AM interaction is less then 0.001% of the total Surface–AM interaction energy, or 3.6×10^{-5}% of the total interaction energy of the system). And the wall at $z = 40$ nm is more than a dozen cutoff lengths away from the keratin throughout our simulations.

2.2.3 Wet gecko setae keratin model on a hydrophobic surface. The water model employed in our system consists of MARTINI water and antifreeze water (which we will collectively refer to as just water), where we replaced, as is done in the literature,[36] 10% of the water beads of type P4 with antifreeze beads of type BP4. This mixture prevents freezing and clustering at 300 K.[36] BP4 behaves as P4 with the system, except in its interaction with water itself.[36] Each MARTINI water bead maps onto 4 water molecules. In Table 2 the Lennard-Jones parameters for the interaction between water with the keratin and the surface are shown.

Reptilian keratin can take up to 30 wt% (see Section 2.5). We expect a lower water content at typical ambient relative humidity and have, therefore, decided to use 10 wt% throughout this work. Since our water model is a purely Lennard-Jones solvent, we may be able to make generalizations about the influence of solvophobicity of keratin. One of these solvents would be methanol, for example. We will come back to that idea in the conclusion. Fig. 3 shows the bulk wet keratin after water insertion.

To generate a system with 10% water content, we use a *NPT* equilibrated dry gecko keratin system. Then, we step-wise insert water beads as described in Section S2 (ESI†). After the last insertion step we perform an additional *NPT* equilibration of 50 ns. Fig. 3 shows the wet keratin system after insertion of the water. A bulk simulation of the wet keratin is used to calculate mechanical properties using 3D PBC. A placement of the resulting wet keratin system on top of a hydrophobic surface under 2D slab PBC is used for the pull-off simulations.

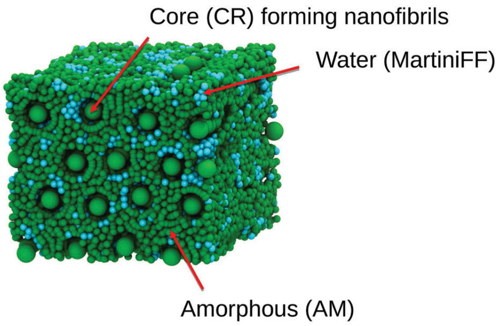

Fig. 3 Wet gecko keratin after inserting water under three-dimensional periodic boundary conditions, used later for the calculation of mechanical properties. The keratin in (green) is swollen with water (cyan). Snapshot at 1 bar after 1 μs *NPT* equilibration.

In addition to the water inside the wet keratin system, we also place a monolayer of MARTINI water (10% anti-freeze water) between the hydrophobic surface and the keratin, just before the keratin model is pushed against the surface. We call these setups, which represent the case if setae press against hydrophobic surfaces coated in dew drops, wet surface or wet hydrophobic surface. The initial configuration of the monolayer above the hydrophobic surface is at $z_{\text{waterlayer}} = \max X(C1;z) + \sigma_{P4} + 0.5$ nm, with $X(C1;z)$ the coordinates of the alkane chain beads in *z*-dimension and σ_{P4} the Lennard-Jones radius of the water beads. As an example, one of the wet keratin systems on a wet hydrophobic surface of size 16.3318 nm and 18.4326 nm contain 1071 P4 water beads and 119 BP4 antifreeze beads in the monolayer above the surface, in comparison, the wet keratin contains 4123 water beads.

2.3 Parameter variation

To test how robust our choice of interaction parameters is on the properties we want to investigate, we perform parameter variation of the dry gecko keratin model, the wet gecko keratin model as well as their interactions with the hydrophobic surface. The interaction strengths of unlike interactions between the keratin beads and MARTINI water beads are calculated as $\varepsilon_{ij} = \lambda\sqrt{\varepsilon_{ii}\varepsilon_{jj}}$ where as the Lennard-Jones σ were kept. To explore the robustness of our model, we scale the Lennard-Jones potential. In case of the dry keratin this effectively means scaling the well-depth of the Lennard-Jones potential ε of the AM–AM and CR–AM interactions. In case of the wet keratin, the water–amorphous (W–AM) and water–core (W–CR) interactions are scaled (The P4 and BP4 beads of the MARTINI force field, both have the same interactions with keratin and surface). In total,

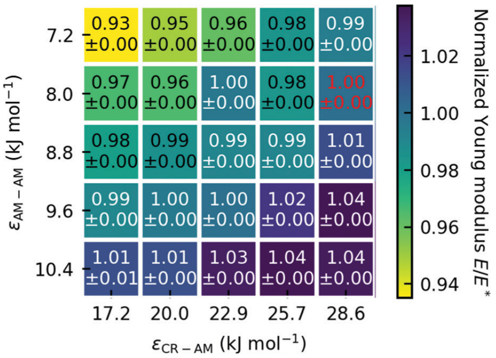

Fig. 4 Normalized Young modulus E/E^*, with the Young modulus E relative to the Young modulus of the original parameters of Endoh *et al.* E^*. The red text highlights the Young modulus of the original model at 12.56 GPa. The Young modulus is robust against variation of ε. We use the standard deviation of the mean as the error.

25 dry keratin systems with different interaction energies ε are equilibrated. We then calculate the mechanical properties, Young modulus and Poisson's ratio, and the pull-off force for all 25 systems. Fig. 4 shows the Young modulus as a function of the parameter variation and Fig. 9 shows five pull-off spectra for five variations of ε_{AM-AM} at constant ε_{CR-AM} = 28.6 kJ mol^{-1}. We concluded, that the trends are robust against parameter variation of the dry keratin and choose the original parameter set for the dry gecko keratin model (ε_{AM-AM} = 8.0 kJ mol^{-1} and ε_{CR-AM} = 28.6 kJ mol^{-1}) for the following parameter variation of the wet gecko keratin model. Here, the W–AM and W–CR interactions are scaled, resulting in an additional 9 wet keratin systems with different hydrophilicities of the keratin. We call the wet keratin model with the smallest scaling factor λ = 0.5, for both W–AM and W–CR interactions, the weakly hydrophilic gecko keratin. The system with λ = 1.0, for W–AM and W–CR, the strongly hydrophilic gecko keratin. Fig. 5 shows the weakly and strongly hydrophilic keratin systems resting above the wet hydrophobic surface.

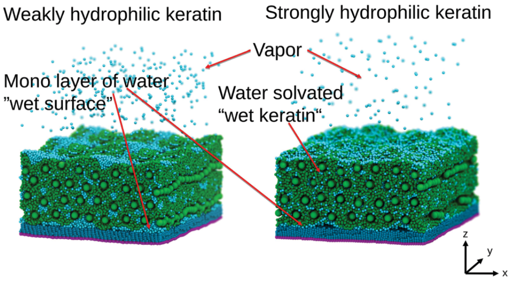

Fig. 5 Wet gecko keratin systems. The keratin in green is swollen with water (cyan). On the left the weakly hydrophilic keratin shows clustering of water beads and more water in the vapor phase compared to the strongly hydrophilic keratin on the right. The strongly hydrophilic keratin on the right leads to a more uniform distribution of the water beads, especially in the interface region between surface and keratin. In both cases a water vapor above the keratin is visible.

2.4 Computational details

All simulations are carried out using the GROMACS 2018[37] software package. The Lennard-Jones cutoff is 2.1 nm. All intermolecular forces are parameterized into our force field, including electrostatics and dispersion interactions, therefore we have no explicit charges present in the system.

The Equilibration procedure for the dry gecko keratin and the wet gecko keratin can be found in the Sections S3 and S4 (ESI†).

2.4.1 Bulk calculations. Production runs to calculate the mechanical bulk properties, Young modulus and Poisson's ratio, are performed under three-dimensional PBC using a time step of 10 fs. A Berendsen thermostat and a semi-isotropic Berendsen barostat[38] are used to keep the system at 300 K and 1 bar. The time constant of coupling the temperature is τ_T = 2 ps. The barostat uses a coupling time of τ_p = 5 ps and a compressibility of 4.5×10^{-5} bar^{-1} in *xy*, but a compressibility of 0 bar^{-1} in *z*, as was done in the previous work.[13] Thus, no size fluctuations are allowed in the direction parallel to the nanofibrils. The systems are stretched, *i.e.* uniformly scaled, in the direction of the nanofibrils, in steps of 1%, ranging from 0% to 5% strain. Simulation times are 100 nm at each strain. After testing for convergence we use the last 70 nm for the computation of the Young modulus and Poisson's ratio. We perform 6 production runs and use the standard deviation of the mean as the error estimate.

2.4.2 Hydrophobic surface equilibration. For the pull-off simulations, we transfer the equilibrated bulk gecko keratin systems into 2D PBC above a hydrophobic surface. The system is only periodic in the coordinates parallel to the surface (*x*,*y*). From the bulk keratin *NPT* equilibrations, we choose a configuration closest to 1 bar pressure, since our pulling simulations are run in *NVT* conditions. To accomplish that, we choose the latest frame in the trajectory where the squared deviation in the instantaneous pressure is $(1\ \text{bar} - p_{\text{inst.}})^2 \leq 0.03\ \text{bar}^2$. In our model the keratin fibrils are parallel to the surface (*y*-direction). The *x* and *y* simulation box lengths are used to generate the hydrophobic surface (Section 2.2.2). After inserting the OTS-covered hydrophobic surface into an otherwise empty box of the correct dimensions, it is energy minimized using steepest descent until the maximum force is below 0.1 kJ mol^{-1} nm^{-1}. For the wet surface systems, we then add a water layer above the hydrophobic surface and perform an energy minimization of the surface and the water together. The keratin systems are inserted, such, that the minimum distance between the surface beads and the keratin beads is 2.0 nm.

2.4.3 Gecko keratin pull-off simulations. The gecko keratin pulling simulations are performed in the *NVT* ensemble after the hydrophobic surface equilibration (Section 2.4.2). After transferring the dry or wet keratin system above the energy minimized dry or wet hydrophobic surface, the keratin is placed near to the surface. We quickly move the keratin in 7700 simulation steps with a time step of 1 fs and a Berendsen thermostat with a time constant of coupling the temperature of τ_T = 2 ps, closer to the surface. The COM of the top layer of the CR beads z_{COM} is moved with a harmonic spring,

k_{push} = 3000 kJ mol^{-1} nm^{-2} and a velocity of 10 × 10^{8} μm s^{-1} (or 10^{3} nm ns^{-1}), very shortly towards the surface. We then pick a configuration from the resulting trajectory where the minimum distance between any surface bead and any keratin bead is ≈0.3 nm.

We mimic the experimental preloading force for the spatula described by Xu *et al.*[20] over a simulation time of 100 nm. We choose a long equilibration time of 100 nm, but z_{COM} already converges in around 25 nm. Xu *et al.*[20] used a preload of 10 nm on the spatula that, according to the authors SEM image, had an elliptic area of roughly $A = \pi \cdot 2a \cdot 2b = \pi \cdot \frac{200\ \text{nm}}{2} \cdot \frac{150\ \text{nm}}{2} = 23\,560\ \text{nm}^2$, with $2a$ the width and $2b$ the height of the ellipse. This amounts to a pressure of p = 4.24 bar. We translate this experimental preloading to a pushing in the direction towards the surface using a constant force. We want to mention here, that the size of the spatula can be used to calculate the corresponding preloading force, but a comparison of the force needed to pull-off the keratin is not possible. This is because the pull-off force is smaller when an adhesive is peeled off compared to the flat-on-flat pull-off we simulate. This peel-off is not possible to simulate with periodic boundary conditions, which are necessary for our system size. However, we will publish results of a full mesoscale spatula soon, showing that our pull-off forces are comparable to experimental studies if peel-off is taken into account. Instead of simulating the complete peel-off of the spatula, flat-on-flat pull-off simulates just a small section of a spatula, small enough that flat-on-flat pull-off is justified. We calculate the preloading force for all 25 dry keratin and 9 wet keratin systems, given their varying sizes, after equilibration using different interaction parameters and different water contents. As an example, in one of the systems this results in a constant-force preload of F_{preload} = 73.97 kJ mol^{-1} nm^{-1}. A Nosé–Hoover thermostat[39,40] is used to keep the systems at 300 K. The time constant of coupling the temperature is τ_{T} = 2 ps.

Afterwards, we let the system relax to mimic the time when the experimental setup is switched from preloading to pulling. The time this takes in experiments is not mentioned in the literature for gecko spatula pull-off. We give the system 100 nm to relax.

The pull-off runs are simulated with a harmonic spring constant linked to the COM of the top layer nanofibrils which is pulled away from the surface. We varied the harmonic spring constant between 3000 and 7000 kJ mol^{-1} nm^{-2}, together with the corresponding pulling velocity to maintain a constant loading rate $\dot{F} = k_{\text{pull}} \cdot v$. We did not see a difference in maximum force, therefore we decide to proceed with a value of k_{pull} = 5000 kJ mol^{-1} nm^{-2}. We discuss the loading rate dependence (changing $\dot{F} = k_{\text{pull}} \cdot v$) below in Fig. 9. Since at this point in our protocol we start from a structure where the keratin is attached to the surface, a jump-in, typically observed in AFM force curves, can not be observed. Every 100 steps we gather the force on the harmonic spring, by which we get a raw force profile over the pulling simulation. Fluctuations in the raw force profile due to the resonance frequency of the harmonic spring and due to thermal fluctuations of the particles linked to this harmonic spring, are artifacts which are smoothed by a Gaussian function (Fig. 6) with a kernel width respective of 0.1 nm, as was done by Sheridan *et al.*[21] The pull-off force is the maximum force during the pulling run. It is the force needed to separate the keratin from the surface. This force is obtained by taking the highest value of the smoothed force profiles.

To test the dependence of the pull-off force on the pulling velocity v (which is proportional to the loading rate), we use different pulling velocities ranging from 3 × 10^{5} μm s^{-1} to 3 × 10^{7} μm s^{-1} (or 0.3 to 30 nm ns^{-1}). The pulling velocities used in this work are summarized in Table S1 (ESI†) with their corresponding loading rates $\dot{F} = k_{\text{pull}} \cdot v$. For the range of pulling velocities we perform 30 pull-off runs from the same relaxed structure.

By using kernel density estimation[41] on the maximum pull-off forces extracted from the smoothed force profiles (Fig. 6), the most probable pull-off force is accessible.

To estimate the error in the pull-off forces we perform an additional set of simulations for the weakly hydrophilic wet gecko keratin system. After the wet keratin equilibration (Section 4) we start five pull-off simulations (Section 2.4.3) with different initial velocities. These five blocks repeat the 100 ns preload step and the 100 ns relaxation. For the range of pulling velocities from 3 × 10^{-4} μm s^{-1} to 1 × 10^{-2} μm s^{-1} we perform 30 pull-off runs each. This results in 150 pull-off runs for each pulling velocity or a total of 1050 pull-off runs, used in the estimation of the error. The resulting maximum pull-off forces are accumulated, and, using kernel density estimation we extract the most probable pull-off force for each velocity. From the most probable pull-off forces at each pulling velocity, we calculate the standard deviation between the five blocks.

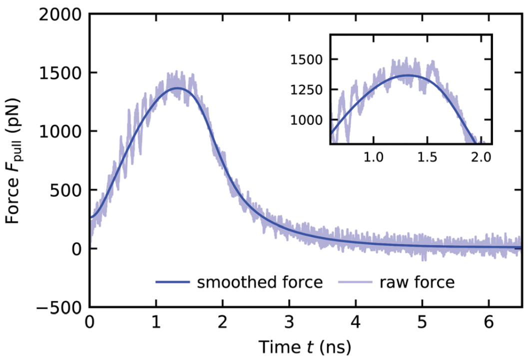

Fig. 6 Force profile of a wet gecko keratin pull-off from a dry hydrophobic octadecyltrichlorosilane self-assembled monolayer with a pulling velocity of v = 3 × 10^{5} μm s^{-1}. The force on the harmonic spring F_{pull} is plotted against the time t. After smoothing the raw force (transparent blue) with a Gaussian kernel with a width respective of 0.1 nm in the position domain, the resulting smoothed force profile (blue) is used to extract the maximum force during pull-off. The force starts at zero but rises sharply. The Gaussian smoothing leads to non-zero force at t = 0 nm, but this behavior does not influence the smoothed profile afterwards and we only use the maximum force in the smoothed force profile in our investigation.

This standard deviation is used as the error estimate in the pull-off forces.

2.5 Experimental assessment of the water content in reptile keratin

Dry shed skin samples (dorsal and ventral scales) of the snake Naja nigricollis and dry pieces of claw tips of the Gekko gecko toes were used in this experiment. Initially, individual samples were weighted at 24 °C and 23% relative humidity using Cubis II Ultra-Micro Balance (Sartorius) with the resolution of 0.1 µg. Then the samples were kept for 48 h at 24 °C and 90% relative humidity and weighted again. Finally, the samples were kept for 48 h at 24 °C and 23% relative humidity and weighted again. The mass loss in % due to the water evaporation was calculated.

3 Results and discussion

3.1 Elastic properties of wet and dry bulk gecko keratin: water-moderated softening of keratin depends on its hydrophilicity

The attachment of spatulae depends on the elastic properties of the keratin in two ways: (1) a flexible spatula is able to follow the surface topography and allows for more contact. (2) The pull-off force, the force needed to separate the spatula from the surface is directly proportional to the Young modulus. To validate the elastic properties of our keratin models, we calculate the Young modulus and Poisson's ratio and validate against experimental results. Fig. 7 shows the stress–strain behavior from 0% to 5% strain ε_{zz}, of the dry Endoh *et al.*[13] model in black, after parameter variation of the dry gecko keratin model in grey and alongside a strongly and weakly hydrophilic gecko keratin in blue and cyan. The parameter variations (grey) (also Fig. 4) show that the dry keratin is robust against variations in the nonbonded interaction parameters, a reason being that most load is taken by the bonds between CR beads, which are largely unaffected by the nonbonded interactions.

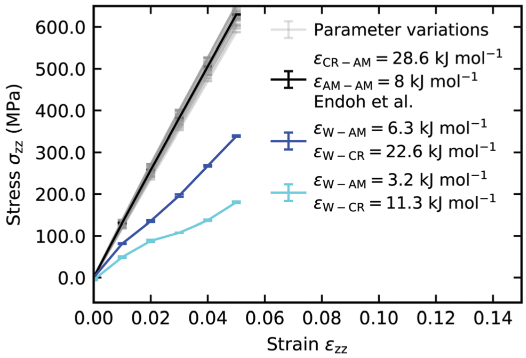

Fig. 7 Tensile stress–strain curves for bulk dry gecko keratin (black) at small variations from the original Lennard-Jones interactions energies ε (grey) and wet keratin (10 wt% water). The stress σ_{zz} is plotted against the strain ε_{zz} along the fibrillar direction. Strongly hydrophilic keratin (blue) and weakly hydrophilic keratin (cyan) show similar qualitative trend change compared to the dry keratin, as is seen with the trend change in experimental studies on dry *versus* wet keratin,[5] as the Young modulus is decreased and the stress–strain curve becomes flatter at strains over 1% to 2%. We use the standard deviation of the mean as the error.

The slope of the first 1% of the stress–strain curve is used to calculate the Young modulus. The calculated Young moduli for all parameter variations of the dry keratin are shown in Fig. 4. The Young modulus of the dry keratin using the original model parameters E^* is highlighted in red. The highlighted Young modulus of E^* = 12.56 GPa is around 5% less than the result of Endoh *et al.*[13] (13.2 GPa). A possible explanation may be the much longer *NPT* equilibration of 100 nm compared to 7.5 nm and the longer trajectory used for analysis (30 nm *versus* 7.5 nm). The resulting Young modulus of our models is robust against variation of ε_{AM-AM} and ε_{CR-AM}. Decreasing the CR–AM interaction energy from the original ε_{CR-AM} = 28.6 kJ mol^{-1} by 40% to ε_{CR-AM} = 17.2 kJ mol^{-1} only decreases the elastic modulus to 97% of its original value. Modifying the AM–AM interactions influences the elastic modulus only slightly more.

The hydrophilicity of the gecko keratin, modeled by the interaction between the keratin and the water (ε_{W-CR} and ε_{W-AM}) has, however, significantly greater effect on the Young modulus. In experimental stress-strain studies[5,42] the effect of changing the relative ambient humidity (RH) is to flatten the stress–strain curve, leading to a beginning plateau formation above 1% to 2% strain. Increasing RH leads to a greater uptake of water into the keratin, which increases the water content of the material and leads to a reduction of the Young modulus. Qualitatively, in Fig. 7, the flattening of the stress–strain curve is comparable to the behavior of experimentally[5,42] observed deviations due to RH. Since the water content of gecko keratin at these relative ambient humidities is not known, we can take no conclusion of whether the weakly hydrophilic or strongly hydrophilic keratin is closer to experiment, both having a water content of 10%.

We may want to make a very careful observation of the effects of keratin hydrophilicity on the elastic properties, resembling the change in elastic properties due to changing RH. It is however important to keep in mind that changing the hydrophilicity does not entail a change in water content of the keratin and no resulting swelling effects. In experimental work[43] the elastic modulus of dry biological materials (*e.g.* insect exoskeletons) was found to be about five times higher than for the same material affected by ambient humidity. For experimental specimens, typically only the ambient relative humidity (RH) is reported, whereas the corresponding water content appears to be unknown. Also, in the case of avian feathers,[42] going from 0% RH to 50% RH decreased the Young modulus from 3.66 GPa to 2.58 GPa, which translates to 30%. The change between 50% RH and 100% RH was even more pronounced, with an additional decrease by 43%. This experimentally[42] found decrease in the elastic modulus with increasing RH in beta keratin materials can be compared with changes we observe (Fig. 8(A)). The Young modulus of our strongly hydrophilic keratin E^0 (red in Fig. 8), of E^0 = 6.78 ± 0.31 GPa is 54% of the elastic modulus of the dry keratin, *i.e.* a decrease of 47%. The weakly hydrophilic keratin, with a Young modulus of 4.75 ± 0.21 GPa is 38% of the dry elastic modulus.

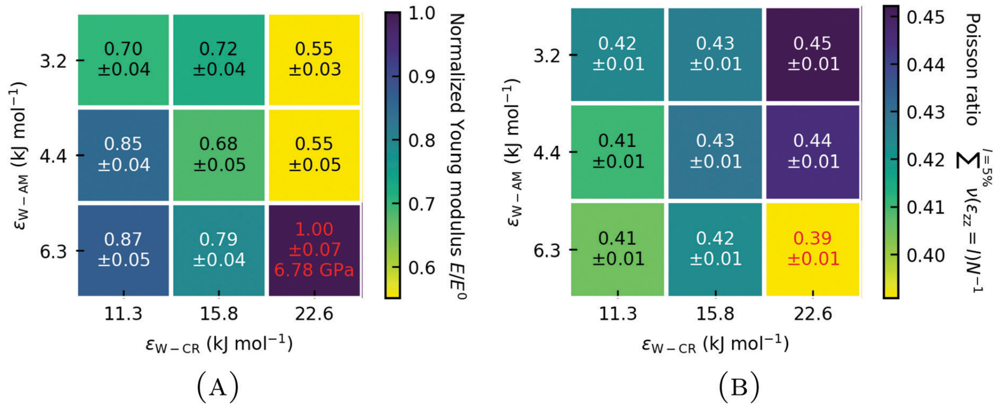

(A) (B)

Fig. 8 (A) Normalized Young modulus E/E^0 of wet gecko keratin as a function of W–AM and W–CR Lennard-Jones interaction energy ε. The Young modulus E is normalized with the Young modulus of the unscaled Berthelot combination E^0 for the Lennard-Jones interaction parameter ε between MARTINI force field water and the coarse-grained parameters of the keratin model, representing the strongly hydrophilic keratin. (B) Mean Poisson ratio $\frac{1}{N}\sum^{l=5\%} \nu(\varepsilon_{zz}=l)$ over 0% to 5% strain of the wet keratin as a function of the Lennard-Jones interaction energies ε. Results from strongly hydrophilic wet gecko keratin (red). We use the standard deviation of the mean as the error and error propagation where two values are compared.

Or, as Fig. 8 shows, 70% of the strongly hydrophilic keratin, resulting in a decrease of 30%. This reduction in the elastic modulus from the dry keratin model to the strongly hydrophilic keratin model to the weakly hydrophilic keratin model matches the reduction in Young modulus seen by Taylor *et al.*[42] in avian feather keratin. In this careful observation, it would suggest that our strongly hydrophilic gecko keratin model may have the elastic properties of keratin at 50% RH and our weakly hydrophilic keratin model may have the elastic properties at 100% RH. Again, comparison of our computational models to experiments is difficult, since in the literature detailed specifications are often missing.

The hydrophilicity of the amorphous phase (W–AM interaction energy) has a stronger effect on the Young modulus than the hydrophilicity of the nanofibrils (W–CR interaction energy). But as a general trend, lowering the hydrophilicity of keratin leads to a decreased Young modulus, independent of whether the amorphous phase or the nanofibrils are less hydrophilic. This general trend can also be seen with Poisson's ratio (Fig. 8(B)). The Eisenberg hydrophobicity scale[44] of the gecko keratin protein sequences[12,26] shows them on average to be on the more hydrophobic end ($\langle H \rangle > 0.2$). Our result indicate that this leads to a more flexible spatula, compared to protein sequences which would be more hydrophilic in nature. One may speculate that there is a evolutionary trend towards a more weakly hydrophilic keratin, making the keratin more flexible in humid environments, which would increase the pull-off force needed to separate the spatula from the surface, as we will see later on. A completely hydrophobic spatula material would, however, not allow the uptake of water and increased RH in humid environments would no longer be beneficial for attachment.

3.2 Assessment of the water content in reptile keratin

We used Gekko gecko (Tokay gecko) as a model system (like most other studies) and, to generalize, these results, we also tested water uptake in a snake. For the snake skin samples the water uptake capacity was 20.16% (SD = 3.97, n = 12), whereas for claw tip of the gecko it was 30.62% (SD = 4.08, n = 4). The obtained results were well repeatable also in several hydration/dehydration cycles. Lower water uptake capacity of the snake skin may be potentially explained by possibly higher lipid content in the skin of this snake species often occupying rather arid regions in comparison to the Tokay geckos living under rather humid ambient conditions.

3.3 Adhesion of gecko keratin to the hydrophobic surface

3.3.1 Pull-off force dependence on the pulling velocity. As the virtual particle is moved vertically away from the surface, the force on the COM of the top layer nanofibrils due to the harmonic potential connecting it to the virtual particle, increases linearly at all pulling velocities until the keratin detaches from the surface. For all fast pulling velocities, periodic oscillations after detachment are observed, which are due to the keratin swinging around the virtual particle, to which it is harmonically bonded (Fig. S1, ESI†). The slow pulling velocities result in a smaller force on the harmonic spring after detachment (the position of the virtual particle is closer to the COM of the top layer nanofibrils during pull-off), and consequently the smaller force in the harmonic spring can be dissipated internally. As expected, the maximum force at the detachment event decreases with decreasing pulling velocities. The computed most probable pull-off forces yield a dynamic force spectrum, the pull-off force F as a function of the pulling velocity v (Fig. 9).

We fit the dynamic force spectrum to the Bell + friction model,[21,45,46] $F = \gamma v + \frac{1}{\beta x_b}\ln\left(\frac{\beta k_{\text{pull}} v \cdot x_b}{k_0}\right)$, with F the pull-off force, γ the friction coefficient, x_b the distance to the potential

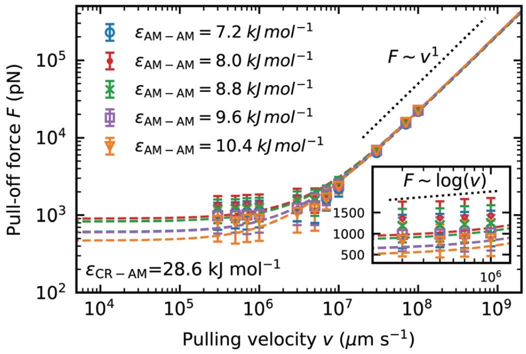

Fig. 9 Dynamic force spectrum for the maximum pull-off force F of dry keratin detachment from a dry hydrophobic surface against pulling velocity v. For five different Lennard-Jones interaction energies ε_{AM-AM}. Each data point is computed from the most probable pull-off force from a sample of 30 simulations. The standard deviation of the mean of five independently equilibrated force probe molecular dynamics simulations at their corresponding velocities are used as the error estimate. Dashed lines represent the fits to the Bell + friction model.

barrier and k_0 the dissociation rate at equilibrium loading rates. We compare the pull-off force at a pulling velocity of $v = 3 \times 10^5$ µm s^{-1} predicted by the Bell + friction fit, to incorporate the information from the faster pulling velocities. The fit to the Bell + friction model shows for our lowest pulling velocities a deviation from the theoretically predicted scaling of $F \sim \log(v)$ for the limit of very low loading rates (Fig. 9 inset). It should be noted here again, that our low pulling velocities correspond to loading rates in the order of 10^{12} pN s^{-1}, which is outside the accessible range of AFM-experiments (the fastest experimental setups[22] to date have loading rates reaching 10^8 pN s^{-1}), hence the limit of low loading rates predicted by theory is not accessible to our molecular dynamics simulations. The theoretically predicted scaling in the limit of high loading rates $F \sim v^1$ is clearly visible at pulling velocities $v > 10^8$ µm s^{-1}. The largest pull-off force in dry keratin on a dry surface is seen in the model using the original Lennard-Jones interaction energy $\varepsilon_{AM-AM} = 8$ kJ mol^{-1} with 932 ± 456 pN. If the original AM–AM interaction is increased or decreased a decrease in pull-off force can be observed. In the most extreme case of $\varepsilon_{AM-AM} = 10.4$ kJ mol^{-1} the Young modulus increases by 4% and the pull-off force decreases by ≈50% to 501 ± 45 pN.

3.3.2 Effect of humidity on gecko keratin adhesion: effect of keratin softening not solely responsible for enhanced adhesion.

Water content has a reliable effect on the pull-off force of keratin detachment from a hydrophobic surface. If the keratin is swollen with 10% water, the pull-off force is increased, independent on the exact hydrophilicity of the keratin material and independent of the pre-existence of a water layer between the surface and the keratin ("wet surface") (Fig. 10 and Table S2, ESI†). The increase in the mean pull-off force from the dry keratin on a dry surface F_{dd} = 932 pN (using ε_{AM-AM} = 8 kJ mol^{-1} and ε_{CR-AM} = 28.6 kJ mol^{-1}) to wet keratin on a dry surface F_{wd} = 1317 pN is of 41%. Even greater is the effect of a surface water layer on the pull-off force. Here, the mean pull-off force of wet keratin on a wet surface F_{ww} is nine times larger than F_{dd} with F_{ww} = 8440 pN. The pull-off force needed to detach dry weakly hydrophilic keratin from a wet surface F^1_{dw} clearly shows, that a water layer is a strong modifier of the pull-off force, as dry keratin sticking to a wet surface F^1_{dw} = 7821 pN is six times stronger than wet keratin to a dry surface (F_{wd}).

Fig. 10 would suggest, that the effect of a water layer and the effect of wet keratin are additive rather than multiplicative/synergetic. The gap-filling capability of the water layer is high, since it is sandwiched between a hydrophobic surface and the keratin, modeling setae flattening water layers on hydrophobic surfaces (Section 2.2.3). Our findings predict that geckos on hydrophobic surfaces in environments with 100% RH, such as on plant leaves in rain forests, can effectively use water layers to enhance their attachment.

For a better comparison between weakly and strongly hydrophilic gecko keratin, the change in pull-off force between a wet keratin on a dry hydrophobic surface F_{wd} relative to a dry keratin on a dry surface F_{dd} and a wet keratin on a wet surface F_{ww} relative to a dry keratin on a wet surface F^1_{dw} (with superscript 1 for the single, weakly hydrophilic, system), is shown in Fig. 11 and Fig. S2 (ESI†). The effect of wet keratin on the pull-off force on a hydrophobic dry surface (Fig. 11(A)) is best compared to the increase in pull-off force of a single spatula on the octadecyltrichlorosilane self-assembled monolayer of Huber *et al.*,[4] with humidity, which ranged from ≈6 nm at 0% RH to ≈9 nm at 60% RH (the size of the spatula was not described in their work, a comparison of absolute pull-off pressures $p = F/A$ may also be misplaced, since experimentally spatulae are pulled off in a way which leads to crack formation, which is absent in our periodic model, essentially a infinite

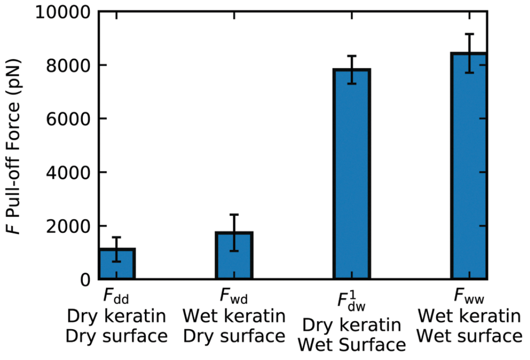

Fig. 10 Mean pull-off forces of four different systems including wet keratin on a dry hydrophobic surface, wet keratin on a wet hydrophobic surface (a layer of water between gecko keratin and the hydrophobic surface during the pushing step, modeling setae flattening water layers on a hydrophobic surface). To establish the pull-off force of dry keratin on a wet surface, pulling simulations with the weakly hydrophilic keratin are used, to compute the pull-off force F^1_{dw}. Here the error of wet weakly hydrophilic keratin on a wet surface is used. Comparing the mean pull-off forces shows a robust trend of increasing force with increasing amount of water (dry keratin on a dry surface to wet keratin on a wet surface).

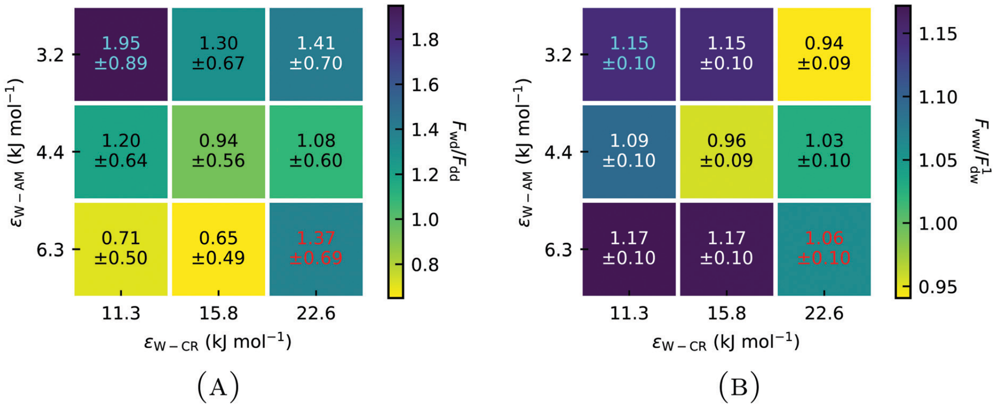

Fig. 11 (A) Pull-off forces of wet keratin attached to a dry surface F_{wd} relative to the pull-off force of dry keratin on a dry surface F_{dd} at different Lennard-Jones interaction energies ε for Water–Core (W–CR) and Water–Amorph (W–AM) interactions. (B) Pull-off force of wet keratin on a wet surface F_{ww} relative to the pull-off force of dry weakly hydrophilic keratin on a wet surface F^1_{dw} shows the influence of wet keratin on the pull-off force in the context of a wet surface. Wet keratin on both a dry and a wet surface leads to increased pull-off forces compared to dry keratin. (Red) increased pull-off force for the strongly hydrophilic keratin. (Cyan) increases of the weakly hydrophilic keratin.

large plate made out of gecko keratin with finite volume. Nonetheless, we included pull-off pressures in Fig. S2 for completeness, ESI†). This increase by 50% is in agreement with our wet keratin model (Fig. 11(A)). Here we see an increase in pull-off force of the strongly hydrophilic wet keratin on a dry surface by ≈50% relative to pull-off force needed to detach the dry keratin. This compares well with our above discussion of the modulus, which suggested that the strongly hydrophilic keratin behaves as if the keratin is at around 50% RH. Weakly hydrophilic wet keratin leads to a pull-off force increase to ≈180%, comparing well with the increased pull-off forces at 100% RH. To repeat, we do not change the water contents and there is no experimental data which would allow us to know how much water content is in gecko keratin at a given RH.

The effect of swelling the keratin which sits on the top of a surface water layer (going from a dry keratin on a wet surface to a wet keratin on a wet surface) on the pull-off force (Fig. 11(B)) shows a moderate average increase of ≈8% relative to a weakly hydrophilic dry keratin attached to a wet surface. Clearly, the hydrophilicity of the keratin affects the resulting pull-off force, the strongly hydrophilic keratin increases the pull-off force, when wet, by ≈37% (Fig. 11(A)). In contrast, a weakly hydrophilic keratin increases the pull-off force by ≈95% when wet.

The increase in pull-off force can not simply be explained by the change in the elastic modulus (Fig. 8), which would predict the highest pull-off forces for the keratins using the parameter sets $\varepsilon_{CR-W} = 22.6$ kJ mol^{-1} and either $\varepsilon_{W-AM} = 3.2$ kJ mol^{-1} or $\varepsilon_{W-AM} = 4.4$ kJ mol^{-1}. Instead the highest pull-off force is observed with the weakly hydrophilic gecko keratin ($\varepsilon_{CR-W} = 11.3$ kJ mol^{-1} and $\varepsilon_{W-AM} = 3.2$ kJ mol^{-1}). Fig. S3 (ESI†) shows minimal to no correlation between increasing Young modulus by hydrophilicity of the wet keratin and increasing pull-off pressures. The minimal trend observable may show increasing pull-off pressures with increasing Young modulus on a dry surface which is contrasted by decreasing pull-off pressures on a wet surface by increasing Young modulus. Additionally, if a water layer is present, the pull-off force of the keratin is not as significantly modified by the hydrophilicity of the keratin, and, therefore not by the change in Young modulus. Which means that the decreased Young modulus at higher humidity can not be solely responsible for the enhanced pull-off forces, putting into question the dominant hypothesis[5,6,17] discussed in the literature.

To understand the effect of water on the pull-off force, the location of the water is important. Fig. 12 and 13 show the density maps of keratin and water for the weakly and strongly hydrophilic keratin with a layer of water between the keratin and the surface (in case of the wet surface systems). Comparing the first 1 nm of the preloading step of the weakly hydrophilic keratin, seen on the very left of Fig. 12, to the densities of the last configurations at 50 nm at the very right, it is clearly visible that the water starts to accumulate and is filling the free volume between surface and keratin. This gap-filling and clustering is not as clearly visible in the strongly hydrophilic keratin (Fig. 13). It may be a reasonable assumption that keratin outside computer simulation will encounter a similar free volume between the surface and the material of the spatula. These asperities (roughnesses) between the keratin interface and the surface, may be filled by water, making the keratin interface smooth, which increases the number of attractive interactions between spatula and surface. There is however, to the best of our knowledge, no literature on the nanometer scale roughness of gecko spatulae. There are however images[30,47] on the hundreds of nanometers scale, from which we assume a roughness in the single digits.

3.3.3 Humidity-induced enhancement of keratin-surface adhesion: two molecular mechanisms for two hydration scenarios. To further explore the differences of our models in regard to the strongly (Movies S2 and S2b, ESI†) and weakly (Movie S1, ESI†)

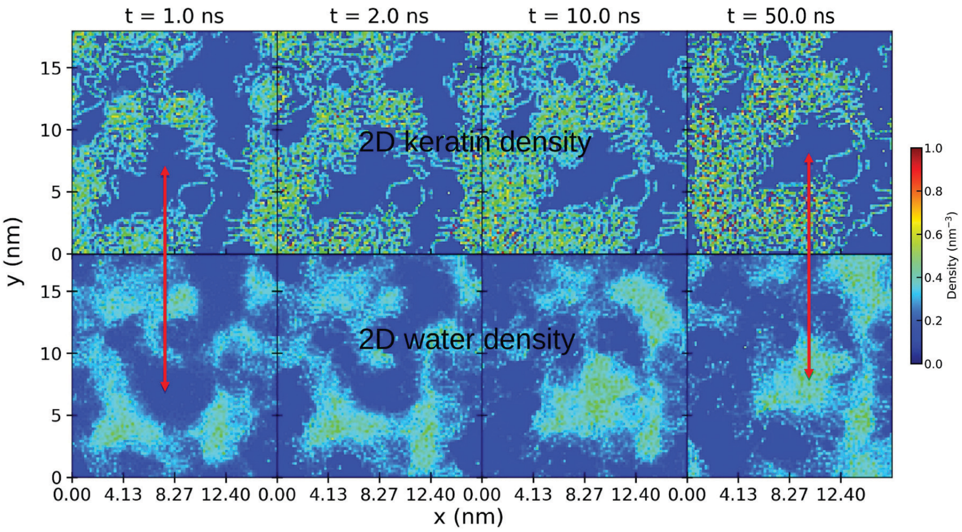

Fig. 12 Density profile in the first 0.7 nm layer above the wet surface during preloading of the weakly hydrophilic keratin. The 2D density profile of the gecko keratin is shown at the top and the water density profile is shown at the bottom. Going from left to right, the density plots were calculated at different times during the preload. At *t* = 0 nm the smallest distance between keratin and the surface is 2.0 nm.

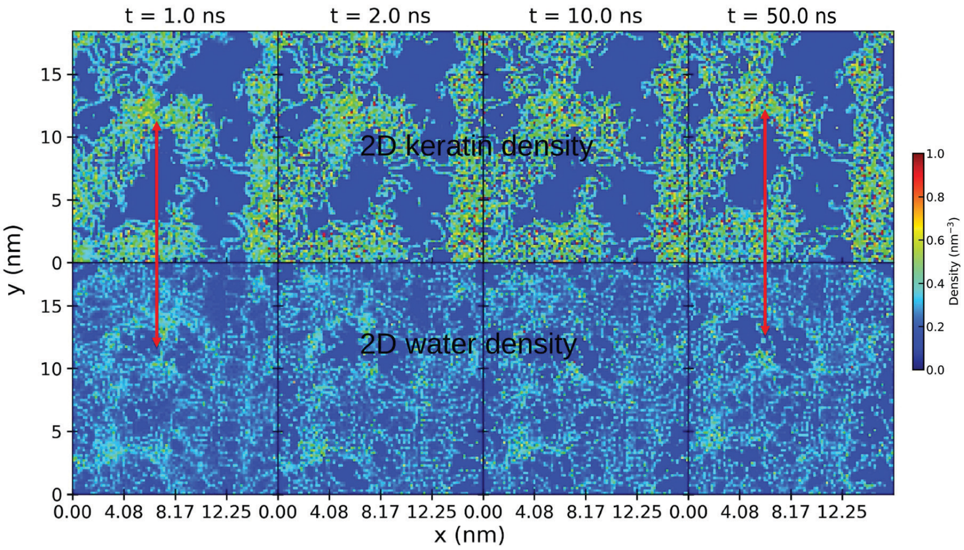

Fig. 13 Density profile in the first 0.7 nm layer above the surface during preloading for the strongly hydrophilic keratin. The 2D density profile of the gecko keratin is shown at the top and the water density profile is shown at the bottom. Going from left to right, the density plots were calculated at different times during the preload. At *t* = 0 nm the smallest distance between keratin and the surface is 2.0 nm.

hydrophilic keratin, Fig. S4 and S5 (ESI†) show the densities of keratin and water during pull-off from a wet surface. Initially, the water is filling the gaps between the surface and the weakly hydrophilic keratin, but this gap-filling is not seen in case of the strongly hydrophilic keratin (ESI,† Movies S3 and S3b show the weakly hydrophilic gecko keratin pull-off from a dry surface, and ESI,† Movies S4 and S4b show the pull-off of strongly hydrophilic keratin from a dry surface). Thus, in case of the weakly hydrophilic keratin, the higher gap-filling ability may explain the main contribution to the increased pull-off force seen in

Table 3 Geometries of water during pull-off of the wet gecko keratin systems. The weakly hydrophilic keratin ($\varepsilon_{\mathrm{W-AM}}$ = 3.2 kJ mol^{-1} and $\varepsilon_{\mathrm{W-CR}}$ = 11.3 kJ mol^{-1}) at the top and the strongly hydrophilic keratin at the bottom ($\varepsilon_{\mathrm{W-AM}}$ = 6.3 kJ mol^{-1} and $\varepsilon_{\mathrm{W-CR}}$ = 22.6 kJ mol^{-1})

$\varepsilon_{\mathrm{W-CR}}$ (kJ mol^{-1})	$\varepsilon_{\mathrm{W-AM}}$ (kJ mol^{-1})	Geometry
11.3	3.2	Capillary bridge
15.8	3.2	Capillary bridge
22.6	3.2	Capillary bridge
11.3	4.4	Capillary bridge
15.8	4.4	—
22.6	4.4	No bridge
11.3	6.3	No bridge
15.8	6.3	No bridge
22.6	6.3	No bridge

Fig. 11(A). The formation of water bridges at the contacting asperities lead to a capillary force and subsequently increases the pull-off force.

In contrast, a strongly hydrophilic keratin absorbs the water into the interface region (and probably, on longer time scales, into its volume) which inhibits the formation of capillary bridges (Fig. S5, ESI†). The strongly hydrophilic keratin therefore shows only small capillary bridges, containing a small number of water beads. The water absorbs into the strongly hydrophilic keratin interface and acts as a mediator for keratin–surface interactions. Water beads interact simultaneously with the keratin and with the surface and this molecular bridge acts a proxy for stronger keratin attachment. This mediating effect of water is different from capillary forces in that a volume of water is missing and, therefore, the surface tension of that water volume is not existent. The molecular water bridges enhance attachment by increased dispersion attraction between spatulae and surface. This explains the increased pull-off forces in case of the wet strongly hydrophilic keratin on a dry surface. The keratin interacts with the water and the water, with the surface.

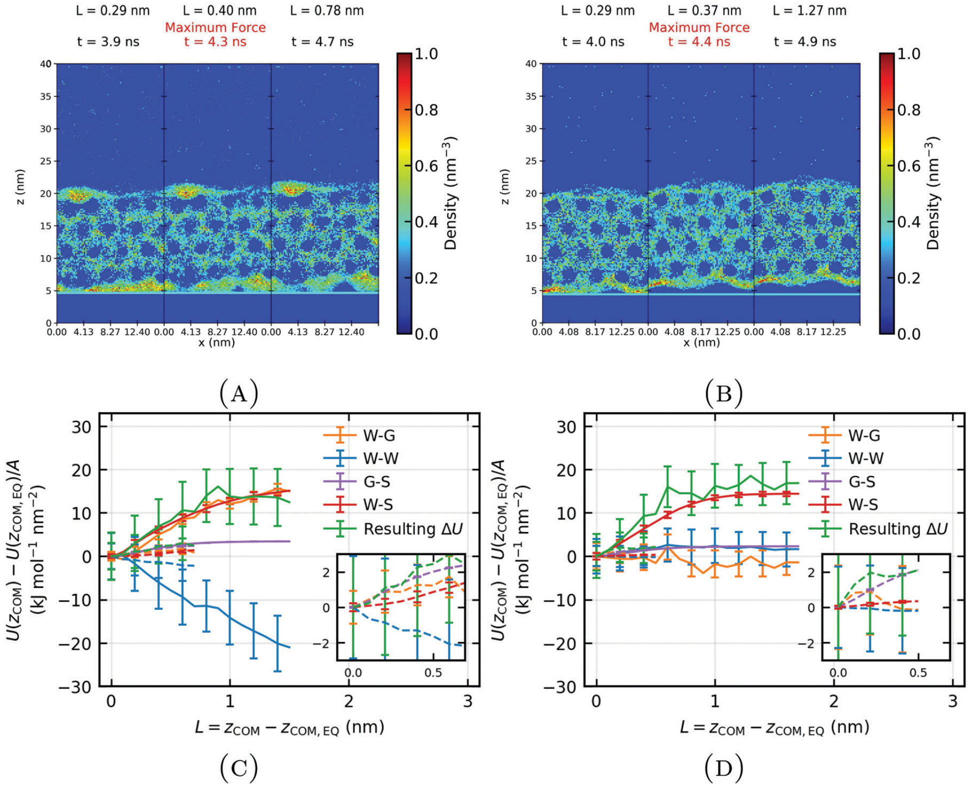

Fig. 14 Density profiles of the weakly (A) and strongly (B) hydrophilic gecko keratin on a wet surface during pull-off. Contributions to the van der Waals energy, modeled by the Lennard-Jones interaction energies, of the weakly (C) and strongly (D) hydrophilic keratin. The water–keratin (W–K), water–water (W–W), keratin–surface (K–S) and water–surface (W–S) potential energies are shown as a function of the displacement of the center of mass of the top nanofibril layer from its equilibrium position $L = z_{\mathrm{COM}} - z_{\mathrm{COM,EQ}}$, normalized with the area A of the systems. Dashed lines represent the energies of the wet keratin on a dry surface (also shown in the insets), solid lines the energies of wet keratin on a wet surface. The decomposed Lennard-Jones energies of 30 force probe molecular dynamics runs are binned according to the instantaneous position z_{COM} (binwidth of 0.1 nm). The average energy at displacement z_{COM} and the standard deviation can thus be calculated. Energies are computed at our slowest pulling velocity of 3×10^4 µm s^{-1}. The energies are set to zero at the initial equilibrium configuration, after the relaxation step, when the keratin is attached to the surface. (A and C) represents the weakly hydrophilic keratin ($\varepsilon_{\mathrm{W-AM}}$ = 3.2 kJ mol^{-1} and $\varepsilon_{\mathrm{W-CR}}$ = 11.3 kJ mol^{-1}). (B and D) shows the strongly hydrophilic keratin ($\varepsilon_{\mathrm{W-AM}}$ = 6.3 kJ mol^{-1} and $\varepsilon_{\mathrm{W-CR}}$ = 22.6 kJ mol^{-1}). We use the standard deviation of the mean as the error.

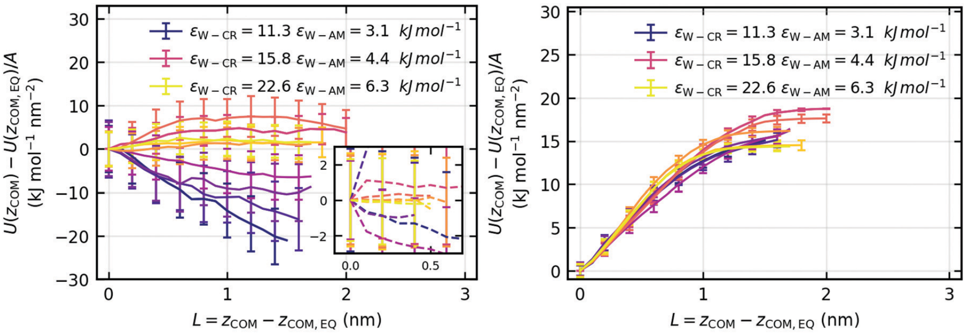

(A) (B)

Fig. 15 Water–water Lennard-Jones interaction energies (A) and water–surface energies (B) are shown as a function of the displacement of the center of mass of the top layer nanofibrils from its equilibrium position $L = z_{COM} - z_{COM,EQ}$, normalized with the area A of the systems. Dashed lines represent the energies of the wet keratin on a dry surface (shown in the inset), solid lines represent the energies of wet gecko keratin on a wet surface. The decomposed Lennard-Jones energies of 30 force probe molecular dynamics runs are binned according to the instantaneous position z_{COM} (binwidth of 0.1 nm). The average energy at displacement z_{COM} and the standard deviation can thus be calculated. Energies are computed at our slowest pulling velocity of 3×10^4 µm s^{-1}. The energies are set to zero at the initial equilibrium configuration, after the relaxation step, when the keratin is attached to the surface. With increasing hydrophilicity (deep purple to bright yellow) favorable water–water interactions (A) turn unfavorable, as the pull-off no longer shows miniscus bridges. This clear trend which separates weakly and strongly hydrophilic keratin is only seen in case of the pull-off from a wet surface, at a dry surface (inset) this trend is not as clearly observable. The opposing water–surface (B) interactions do not directly converge after pull-off in case of a weakly hydrophilic keratin (deep purple), but show convergence for a strongly hydrophilic keratin (bright yellow). We use the standard deviation of the mean as the error.

Thus, depending on the hydrophilicity of the keratin, water can form capillary bridges or absorb into the interface and acts as a mediator for enhanced attractive interactions. Table 3 summarizes the resulting water geometries for our wet keratin systems. The capillary bridges seen in Fig. S4 and in ESI,† Movie S1 are of convex shape, because the surface is hydrophobic (the C1 type beads, making up the hydrophobic surface, lead to a contact angle of larger than 110° for the MARTINI water[48]). The capillary force of a convex capillary bridge is much less than that of a capillary bridge of concave shape, which would be present on hydrophilic surfaces.[49,50]

Since gecko spatula protein sequences[12] are not extremely hydrophilic (Eisenberg *et al.*[44] hydrophobicity scale $\langle H \rangle > 0.2$), and since we observe higher gap-filling capability of water at the weakly hydrophilic keratin interface, we assume that capillary forces will play a pronounced role for gecko adhesion on wet surfaces. But we have also shown (Fig. 11(A)) that no such wet surface is necessary for enhanced pull-off forces of wet keratin. Therefore capillary forces can not be solely responsible for the humidity effect, leaving the decreased Young modulus and the mediator effect of water to be significant contributions to the effect of humidity on these surfaces.

To elucidate the underlying molecular mechanism resulting in the attachment differences with different hydrophilic keratins in more detail, the potential energy over the course of 30 pulling runs is decomposed into its different van der Waals contributions. Because fluctuations in the raw force profile (Fig. 6) are due to fluctuations in z_{COM}, we histogram the van der Waals energetic contributions to their respective positions $z_{COM,i}$ (binwidth of 0.1 nm). The average and standard deviation of the decomposed energy are calculated for each bin independently. The standard deviation of each bin is used as the error in the energy decomposition plots.

Energy changes as a function of the displacement of wet keratin from the wet and dry surface $L = z_{COM} - z_{COM,EQ}$, are shown in Fig. 14, as $\Delta U = U(z_{COM}) - U(z_{COM,EQ})$, normalized with the area A of the systems. The displacement at maximum force ($L = 0.40$ nm) of the weakly hydrophilic keratin (Fig. 14(A and C)) corresponds roughly to a COM position of $z_{COM} \approx 18.0$ nm. The maximum force (at $L = 0.37$ nm) during the pull-off of the strongly hydrophilic keratin (Fig. 14(B and D)) corresponds roughly to a COM position of $z_{COM} \approx 17.9$ nm.

As the weakly hydrophilic keratin is pulled off from the wet surface, unfavorable water–keratin (W–K, orange), water–surface (W–S, red) and keratin–surface (K–S, purple) oppose the detachment (Fig. 14(C)). However, as the weakly hydrophilic wet keratin detaches from the surface, favorable water–water interactions are created, favoring the detachment process. The pull-off is not dominated by keratin–surface (K–S) van der Waals interactions but by water–keratin (W–K) and water–surface (W–S) interactions. Since the main opposition to detachment is due the loss of favorable water–keratin and water–surface interactions and, additionally, a increase in favorable water–water interactions is observable, the pull-off of weakly hydrophilic keratin from a wet surface is dominated by capillary forces.

In contrast to the opposing capillary forces of the weakly hydrophilic keratin on a wet surface, the pull-off of the strongly hydrophilic keratin from a wet surface seems to be only primarily opposed by the loss of favorable water–surface (W–S, red) interactions (Fig. 14(D)). The water functioned as a mediator for enhanced interactions with the surface. Since the water is absorbed into the interface of the strongly hydrophilic keratin, the pull-off and subsequent loss in water–surface contacts, leads to a increase of favorable interactions between water and keratin (W–K, orange). As the water is removed from the surface during pull-off, it is able to form new, more favorable, water–keratin (W–K) interactions, which aids detachment.

Favorable water–water interactions during pull-off (Fig. 15(A)) of the wet keratin from a wet surface are correlated with the observation of capillary bridges, described in Table 3. When water coalescence into a capillary bridge, water–water energies decrease favorably for pull-off and the change in water–surface energy does not converge directly after the maximum force (Fig. 15(B)). In case of strongly hydrophilic keratin, after the detachment event at $L \approx 0.4$ nm, the water–surface interaction energy converges to a plateau at larger separation (Fig. 15(B) yellow). This mechanism is only seen with the more strongly hydrophilic keratin, where the water becomes an extension of the keratin and functions as a mediator for enhanced van der Waals interactions while additionally smoothing its roughnesses. This leads to stronger attachment due to increased opposition against pull-off, by water–surface interactions, when compared to the weakly hydrophilic keratin. Quantitatively this amounts to a difference in water–surface interactions between weakly and strongly hydrophilic keratin, at $L = 0.4$ nm of $U^{\text{weakly}}(L = 0.4\text{ nm}) - U^{\text{strongly}}(L = 0.4\text{ nm}) = -2.1\text{ kJ mol}^{-1}\text{ nm}^{-2}$, *i.e.* the mediator effect in the pull-off of strongly hydrophilic keratin is clearly stronger.

Even though the capillary mechanism leads to a strong opposition by water–keratin energy (Fig. 14(C), orange), it is compensated on the hydrophobic surface to a large degree by creation of favorable water–water interactions. Therefore, in the case of weakly hydrophilic keratin, adhesion may not completely make use of this strong water–keratin interaction. This may explain the apparent independence of the hydrophilicity of wet gecko keratin on a wet surface, as seen in Fig. 11(B).

4 Conclusion

We investigated the effect of humidity on the pull-off forces of gecko keratin from surfaces by means of force probe molecular dynamics simulations using a coarse-grained model for keratin, water and a silica surface covered by an alkyl monolayer. To the extend of our knowledge, these are the first non-equilibrium molecular dynamics simulations studying the pull-off of gecko keratin. Since it is not known how much water content is present in gecko keratin at a given humidity, we used an intermediate water content of 10%. What is not known either is the hydrophilicity of gecko keratin. We have, therefore, explored a wide range of different hydrophilicities of our gecko keratin model. Therefore, this work showed robustly the larger pull-off forces needed to detach wet gecko keratin compared to dry gecko keratin. More importantly different molecular mechanisms were detected, how water increases the pull-off forces at high humidities. Our main findings can be summarized as follows: (i) capillary forces dominate the adhesion for weakly hydrophilic gecko keratin on a wet surface; (ii) but capillary forces play no role if gecko keratin is hydrophilic enough, for water to readily absorb from the layer on the surface into the gecko keratin; (iii) water on the surface acts as a mediator for keratin-surface interactions, as it interacts strongly with the gecko keratin, and opposes the pull-off as water–surface interactions are lost; (iv) water smoothes out nanoscale roughnesses in the gecko keratin interface by filling gaps between it and the surface (v) on dry hydrophobic surfaces, capillary forces are far less important; they are completely absent for strongly hydrophilic keratin, and increase moderately in relevance with increasing keratin hydrophobicity; (vi) the mediator effect of water plays a role in the pull-off from dry hydrophobic surfaces, the dominant contributions arise, however, from the reduction in favorable keratin-surface interactions.

Our wet keratin systems showed decreases in the Young moduli with water content comparable to experiment,[5] especially the qualitative flattening of the stress–strain curve and the starting of a plateau formation above 1% to 2% strain. We have also shown that the dominant hypothesis[5,6,8] of the decreased Young modulus explaining the better adhesion at high humidity, can not be confirmed. The weakly hydrophilic keratin had by a clear margin, not the lowest Young modulus, but showed the highest pull-off forces.

Since our water model is that of the MARTINI force field,[23–25] which is a fairly generic solvent particle without a dipole moment, the mechanisms found here may also be relevant for the influence of solvophobicity of keratin for other solvents, for example, methanol. Previous work[51] found in the chloroform-derived gecko's toe pad extract, NMR peaks at 0.8 ppm (ωCH_3) and 1.1 ppm ($(CH_2)_n$), classified as non polar lipids. The chloroform extraction reduced the mass of the sample by 8–10 wt%, comparable to our water content. It may be the case, that the effect we observe, may also have some bearing on these lipids. Previous work indeed suggests that, by removing lipids, the maximum shear adhesion of gecko's toe pad shads on hydrophobic surfaces is decreased.[7]

Conflicts of interest

The authors declare no competing financial interest.

Acknowledgements

T. M. would like to thank Hossein Eslami, Donatas Surblys and Jeffrey M. Young for fruitful discussions. Some simulations for this work were performed on the Lichtenberg-Hochleistungsrechner at Technische Universität Darmstadt.

References

1 Q. Jiang, Z. Wang, J. Zhou, W. Chen and Z. Dai, Analysis of Reaction Force and Locomotor Behavior on Geckos in Time- and Frequency-domain during Climbing on Vertical

Substrates, *J. Bionic Eng.*, 2019, **16**, 115–129, DOI: 10.1007/s42235-019-0011-x.

2 B. C. Mahendra, Contributions to the bionomics, anatomy, reproduction and development of the Indian house-gecko, Hemidactylus flaviviridis Rüppel, *Proc. Indian Acad. Sci.*, 1941, **13**, 288–306.

3 E. Arzt, S. Gorb and R. Spolenak, From micro to nano contacts in biological attachment devices, *Proc. Natl. Acad. Sci. U. S. A.*, 2003, **100**, 10603–10606, DOI: 10.1073/pnas.1534701100.

4 G. Huber, H. Mantz, R. Spolenak, K. Mecke, K. Jacobs, S. N. Gorb and E. Arzt, Evidence for capillarity contributions to gecko adhesion from single spatula nanomechanical measurements, *Proc. Natl. Acad. Sci. U. S. A.*, 2005, **102**, 16293–16296, DOI: 10.1073/pnas.0506328102.

5 M. Prowse, M. Wilkinson, J. Puthoff, G. Mayer and K. Autumn, Effects of humidity on the mechanical properties of gecko setae, *Acta Biomater.*, 2010, **7**, 733–738, DOI: 10.1016/j.actbio.2010.09.036.

6 J. B. Puthoff, M. S. Prowse, M. Wilkinson and K. Autumn, Changes in materials properties explain the effects of humidity on gecko adhesion, *J. Exp. Biol.*, 2010, **213**, 3699–3704, DOI: 10.1242/jeb.047654.

7 A. Y. Stark, S. Subarajan, D. Jain, P. H. Niewiarowski and A. Dhinojwala, Superhydrophobicity of the gecko toe pad: biological optimization versus laboratory maximization, *Philos. Trans. Royal Soc.*, 2016, **374**, 20160184, DOI: 10.1098/rsta.2016.0184.41.

8 G. Huber, S. Orso, R. Spolenak, U. G. K. Wegst, S. Enders, S. N. Gorb and E. Arzt, Mechanical properties of a single gecko seta, *Mater. Res.*, 2008, **99**, 1113–1118, DOI: 10.3139/146.101750.

9 W. Sun, P. Neuzil, T. S. Kustandi, S. Oh and V. D. Samper, The Nature of the Gecko Lizard Adhesive Force, *Biophys. J.*, 2005, **89**, L14–L17, DOI: 10.1529/biophysj.105.065268.

10 Z. Peng, Y. Yang and S. Chen, Coupled effects of the temperature and the relative humidity on gecko adhesion, *J. Phys. D: Appl. Phys.*, 2017, **50**, 315402, DOI: 10.1088/1361-6463/aa7a97.

11 C. T. Mitchell, C. B. Dayan, D.-M. Drotlef, M. Sitti and A. Y. Stark, The effect of substrate wettability and modulus on gecko and gecko-inspired synthetic adhesion in variable temperature and humidity, *Sci. Rep.*, 2020, **10**, 19748, DOI: 10.1038/s41598-020-76484-6.

12 L. Alibardi, Immunolocalization of specific keratin associated beta-proteins (betakeratins) in the adhesive setae of Gekko gecko, *Tissue Cell*, 2013, **45**, 231–240, DOI: 10.1016/j.tice.2013.01.002.

13 K. S. Endoh, T. Kawakatsu and F. Müller-Plathe, Coarse-Grained Molecular Simulation Model for Gecko Feet Keratin, *J. Phys. Chem. B*, 2018, **122**, 2203–2212, DOI: 10.1021/acs.jpcb.7b10481.

14 R. Ruibal and V. Ernst, The structure of the digital setae of lizards, *J. Morphol.*, 1965, **117**, 271–293, DOI: 10.1002/jmor.1051170302.

15 N. W. Rizzo, K. H. Gardner, D. J. Walls, N. M. Keiper-Hrynko, T. S. Ganzke and D. L. Hallahan, Characterization of the structure and composition of gecko adhesive setae, *J. R. Soc., Interface*, 2006, **3**, 441–451, DOI: 10.1098/rsif.2005.0097.42.

16 T. W. Kim and B. Bhushan, Effect of stiffness of multi-level hierarchical attachment system on adhesion enhancement, *Ultramicroscopy*, 2007, **107**, 902–912, DOI: 10.1016/j.ultramic.2006.11.008.

17 G. Huber, S. N. Gorb, N. Hosoda, R. Spolenak and E. Arzt, Influence of surface roughness on gecko adhesion, *Acta Biomater.*, 2007, **3**, 607–610, DOI: 10.1016/j.actbio.2007.01.007.

18 C. Canal, R. Molina, E. Bertran and P. Erra, Wettability, ageing and recovery process of plasma-treated polyamide 6, *J. Adhes. Sci. Technol.*, 2004, **18**, 1077–1089, DOI: 10.1163/1568561041257487.

19 C. W. Extrand, Water Contact Angles and Hysteresis of Polyamide Surfaces, *J. Colloid Interface Sci.*, 2002, **248**, 136–142, DOI: 10.1006/jcis.2001.8172.

20 Q. Xu, Y. Wan, T. S. Hu, T. X. Liu, D. Tao, P. H. Niewiarowski, Y. Tian, Y. Liu, L. Dai, Y. Yang and Z. Xia, Robust self-cleaning and micromanipulation capabilities of gecko spatulae and their bio-mimics, *Nat. Commun.*, 2015, **6**, 8949, DOI: 10.1038/ncomms9949.

21 S. Sheridan, F. Gräter and C. Daday, How Fast Is Too Fast in Force-Probe Molecular Dynamics Simulations?, *J. Phys. Chem. B*, 2019, **123**, 3658–3664, DOI: 10.1021/acs.jpcb.9b01251.

22 F. Rico, A. Russek, L. González, H. Grubmüller and S. Scheuring, Heterogeneous and rate-dependent streptavidin–biotin unbinding revealed by high-speed force spectroscopy and atomistic simulations, *Proc. Natl. Acad. Sci. U. S. A.*, 2019, **116**, 6594–6601, DOI: 10.1073/pnas.1816909116.

23 S. J. Marrink, H. J. Risselada, S. Yefimov, D. P. Tieleman and A. H. de Vries, The MARTINI force field: coarse grained model for biomolecular simulations, *J. Phys. Chem. B*, 2007, **111**, 7812–7824, DOI: 10.1021/jp071097f.43.

24 L. Monticelli, S. K. Kandasamy, X. Periole, R. G. Larson, D. P. Tieleman and S.-J. Marrink, The MARTINI Coarse-Grained Force Field: Extension to Proteins, *J. Chem. Theory Comput.*, 2008, **4**, 819–834, DOI: 10.1021/ct700324x.

25 D. H. de Jong, G. Singh, W. F. D. Bennett, C. Arnarez, T. A. Wassenaar, L. V. Schäfer, X. Periole, D. P. Tieleman and S. J. Marrink, Improved Parameters for the Martini Coarse-Grained Protein Force Field, *J. Chem. Theory Comput.*, 2013, **9**, 687–697, DOI: 10.1021/ct300646g.

26 D. L. Hallahan, N. M. Keiper-Hrynko, T. Q. Shang, T. S. Ganzke, M. Toni, L. D. Valle and L. Alibardi, Analysis of gene expression in gecko digital adhesive pads indicates significant production of cysteine- and glycine-rich beta-keratins, *J. Exp. Zool. B: Mol. Dev. Evol.*, 2009, **312B**, 58–73, DOI: 10.1002/jez.b.21242.

27 M. Calvaresi, L. Eckhart and L. Alibardi, The molecular organization of the betasheet region in Corneous beta-proteins (beta-keratins) of sauropsids explains its stability and polymerization into filaments, *J. Struct. Biol.*, 2016, **194**, 282–291, DOI: 10.1016/j.jsb.2016.03.004.

28 R. D. B. Fraser and D. A. D. Parry, The role of β-sheets in the structure and assembly of keratins, *Biophys. Rev.*, 2009, **1**, 27, DOI: 10.1007/s12551-008-0005-0.

29 R. A. Sauer, Multiscale modelling and simulation of the deformation and adhesion of a single gecko seta, *Comput. Methods Biomech. Biomed. Eng.*, 2009, **12**, 627–640, DOI: 10.1080/10255840902802917Publisher: Taylor & Francis eprint.

30 M. Varenberg, N. M. Pugno and S. N. Gorb, Spatulate structures in biological fibrillary adhesion, *Soft Matter*, 2010, **6**, 3269–3272, DOI: 10.1039/C003207G.

31 S. R. Wasserman, Y. T. Tao and G. M. Whitesides, Structure and reactivity of alkyl- 44 siloxane monolayers formed by reaction of alkyltrichlorosilanes on silicon substrates, *Langmuir*, 1989, **5**, 1074–1087, DOI: 10.1021/la00088a035.

32 I. M. Tidswell, B. M. Ocko, P. S. Pershan, S. R. Wasserman, G. M. Whitesides and J. D. Axe, X-ray specular reflection studies of silicon coated by organic monolayers (alkylsiloxanes), *Phys. Rev. B: Condens. Matter Mater. Phys.*, 1990, **41**, 1111–1128, DOI: 10.1103/PhysRevB.41.1111.

33 J. Barriga, B. Coto and B. Fernandez, Molecular dynamics study of optimal packing structure of OTS self-assembled monolayers on SiO_2 surfaces, *Tribol. Int.*, 2007, **40**, 960–966, DOI: 10.1016/j.triboint.2006.02.030.

34 E. E. Flater, W. R. Ashurst and R. W. Carpick, Nanotribology of octadecyltrichlorosilane monolayers and silicon: self-mated versus unmated interfaces and local packing density effects, *Langmuir*, 2007, **23**, 9242–9252, DOI: 10.1021/la063644e.

35 M. Javanainen, H. Martinez-Seara and I. Vattulainen, Excessive aggregation of membrane proteins in the Martini model, *PLoS One*, 2017, 12, DOI: 10.1371/journal.pone.0187936.

36 P. S. Schmalhorst, F. Deluweit, R. Scherrers, C.-P. Heisenberg and M. Sikora, Overcoming the Limitations of the MARTINI Force Field in Simulations of Polysaccharides, *J. Chem. Theory Comput.*, 2017, **13**, 5039–5053, DOI: 10.1021/acs.jctc.7b00374.

37 B. Hess, C. Kutzner, D. van der Spoel and E. Lindahl, GROMACS 4: Algorithms for Highly Efficient, Load-Balanced, and Scalable Molecular Simulation, *J. Chem. Theory Comput.*, 2008, **4**, 435–447, DOI: 10.1021/ct700301q.

38 H. J. C. Berendsen, J. P. M. Postma, W. F. van Gunsteren, A. DiNola and J. R. Haak, Molecular dynamics with coupling to an external bath, *J. Chem. Phys.*, 1984, **81**, 3684–3690, DOI: 10.1063/1.448118.45.

39 S. Nosé, A unified formulation of the constant temperature molecular dynamics methods, *J. Chem. Phys.*, 1984, **81**, 511–519, DOI: 10.1063/1.447334.

40 W. G. Hoover, Canonical dynamics: Equilibrium phase-space distributions, *Phys. Rev. A: At., Mol., Opt. Phys.*, 1985, **31**, 1695–1697, DOI: 10.1103/PhysRevA.31.1695.

41 M. Rosenblatt, Remarks on Some Nonparametric Estimates of a Density Function, *Ann. Math. Stat.*, 1956, **27**, 832–837, DOI: 10.1214/aoms/1177728190.

42 A. M. Taylor, R. H. C. Bonser and J. W. Farrent, The influence of hydration on the tensile and compressive properties of avian keratinous tissues, *J. Mater. Sci.*, 2004, **39**, 939–942, DOI: 10.1023/B:JMSC.0000012925.92504.08.

43 N. Barbakadze, S. Enders, S. Gorb and E. Arzt, Local mechanical properties of the head articulation cuticle in the beetle Pachnoda marginata (Coleoptera, Scarabaeidae), *J. Exp. Biol.*, 2006, **209**, 722–730, DOI: 10.1242/jeb.02065.

44 D. Eisenberg, E. Schwarz, M. Komaromy and R. Wall, Analysis of membrane and surface protein sequences with the hydrophobic moment plot, *J. Mol. Biol.*, 1984, **179**, 125–142, DOI: 10.1016/0022-2836(84)90309-7.

45 G. I. Bell, Models for the specific adhesion of cells to cells, *Science*, 1978, **200**, 618–627, DOI: 10.1126/science.347575.

46 H. Grubmüller, Force probe molecular dynamics simulations, *Methods Mol. Biol.*, 2005, **305**, 493–515, DOI: 10.1007/978-1-59259-912-7_23.

47 B. N. J. Persson and S. Gorb, The effect of surface roughness on the adhesion of elastic plates with application to biological systems, *J. Chem. Phys.*, 2003, **119**, 11437–11444, DOI: 10.1063/1.1621854.

48 A. Ramazani, T. Mandal and R. G. Larson, Modeling the Hydrophobicity of Nanoparticles 46 and Their Interaction with Lipids and Proteins, *Langmuir*, 2016, **32**, 13084–13094, DOI: 10.1021/acs.langmuir.6b01963.

49 M. Dörmann and H.-J. Schmid, Simulation of Capillary Bridges between Particles, *Proc. Eng.*, 2015, **102**, 14–23, DOI: 10.1016/j.proeng.2015.01.102.

50 P. A. Kralchevsky and K. Nagayama, Particles at Fluids Interfaces and Membranes, in *Studies in Interface Science*, ed. P. A. Kralchevsky and K. Nagayama, Elsevier, 2001, vol. 10, pp. 469–502.

51 D. Jain, A. Y. Stark, P. H. Niewiarowski, T. Miyoshi and A. Dhinojwala, NMR spectroscopy reveals the presence and association of lipids and keratin in adhesive gecko setae, *Sci. Rep.*, 2015, **5**, 9594, DOI: 10.1038/srep09594.

Electronic Supplementary Material (ESI) for Soft Matter.

Gecko adhesion: a molecular-simulation perspective on the effect of humidity

Tobias Materzok,*,† Stanislav Gorb,*,‡ and Florian Müller-Plathe*,†

†*Eduard-Zintl-Institut für Anorganische und Physikalische Chemie and Profile Area Thermofluids and Interfaces, Technische Universität Darmstadt, Alarich-Weiss-Str. 8, D-64287 Darmstadt, Germany*

‡*Zoological Institute Functional Morphology and Biomechanics, Kiel University, Am Botanischen Garten 1-9, D-24118 Kiel, Germany*

E-mail: t.materzok@theo.chemie.tu-darmstadt.de; sgorb@zoologie.uni-kiel.de; f.mueller-plathe@theo.chemie.tu-darmstadt.de

1 Gecko Keratin Model Creation Procedure

Since one CR bead represents one dimer, each CR bead is covalently bonded to two head regions and two tail regions. The first AM bead in the squence of either the head or tail region is placed orthogonal to the direction of the nanofibrils with a 90 degrees angle between each sequence. The initially placed AM beads are extended by a self-avoiding random walker until all AM beads are fitted into the simulation box. The resulting structure may contain hotspots which are relaxed in the equilibration protocol for the dry gecko keratin (Section S3).

2 Insertion of Water into Gecko Keratin

We step-wise insert water beads such that the resulting interaction with the whole system is favorable $\Delta E_{\text{insertion}} \leq 0$. Thus we only insert beads beyond the Lennard-Jones radius σ of both, the keratin model (CR and AM) and the water beads inserted in previous steps. We use a slightly modified Boltzmann-inverted Lennard-Jones potential (Equation S1) of the Water-Amorphous (W-AM) interaction as a probability density function to efficiently find low energy positions inside the keratin close to AM beads. Then we check if these insertion points would result in favorable interactions $\Delta E_{\text{insertion}}$.

$$P(x) = 1 - \exp\left[12\left(\left(\frac{\sigma_{\mathrm{W-AM}}}{x}\right)^{12} - \left(\frac{\sigma_{\mathrm{W-AM}}}{x}\right)^{6}\right)\right] \tag{1}$$

The amount of water beads inserted at each step, depends on the free volume inside the keratin. After each insertion step we subsequently perform NPT equilibration runs for 0.25 ns each (computational details are described below). Then we repeat the insertion of water beads in this NPT equilibrated wet keratin model. We repeat these two steps (insertion of water beads and subsequent NPT equilibration) until the desired water content is reached.

3 Dry Gecko Keratin Equilibration

In the first step, the AM beads of the initial dry gecko keratin configuration (three-dimensional orthorhombic boundary conditions) are energy minimized using steepest descent until the maximum force is below 100 $\mathrm{kJ\,mol^{-1}\,nm^{-1}}$. The resulting structure is quickly relaxed at 0 K in the microcanoncial ensemble with a small time step of 1 fs for 1 ns while keeping the CR beads fixed.

After scaling the Lennard-Jones interaction parameters (Section 2.3) the equilibration protocol of Endoh et al.[1] is used, with a longer equilibration, by using smaller time steps in the beginning (5 fs instead of 15 fs) and increasing the last NPT equilibration from 7.5 ns to 100 ns. A Berendsen thermostat[2] with a time constant for coupling the temperature of $\tau_T = 1$ ps and a simulation time step of 5 fs is employed to simulate the system at 2000 K for 150 ns in the NVT ensemble. This is done to relax unphysical frustrations[1]. Following the NVT relaxation, the system is cooled down to 300 K in steps of 50 K with a time step of 10 fs. Each cooling step is performed over 3 ns and the final step at 300 K is run for 7.5 ns. Next, a semi-isotropic Berendsen barostat[2] with a coupling time of $\tau_p = 5$ ps and a compressibility of $4.5 \cdot 10^{-5}$ $\mathrm{bar^{-1}}$ is used to equilibrate the system in NPT over 100 ns at 1 bar. The density converges after 30 to 40 ns to 1274 $\mathrm{kg\,m^{-3}}$, similarly, Lennard-Jones interactions converge also after 30 to 40 ns.

4 Wet Gecko Keratin Equilibration

To swell the dry keratin model with water, we insert water beads into the NPT equilibrated dry keratin system, under 3D PBC. With our target of 10% water content we need to add 4123 water beads, in total, into the model. However, in the first step we only insert on average 351 water beads into the dry keratin system (in the fifth step we insert on average 246 beads and in the twentieth step just 143 beads in the wet keratin), because we only insert water beads such that the systems energy is favorable upon insertion. After each insertion step we run a NPT equilibration for 0.25 ns. By adding just a small number of water beads, at one time, into a system of 22528 keratin beads, under the restrictions described above, the pressure, volume, density and all energetic terms converge in just under 100 ps. The short NPT equilibrations are performed with a time step of 5 fs. A Berendsen thermostat and a semi-isotropic Berendsen barostat[2] are used to keep the system at 300 K and 1 bar. A time constant for coupling the temperature of $\tau_T = 1$ ps and coupling time of the barostat of $\tau_p = 1$ ps with a compressibility of $4.5 \cdot 10^{-5}$ bar^{-1} is adopted. After the last insertion step, we extend the NPT equilibration of the wet keratin by simulating the system for an additional 50 ns with a time step of 10 fs.

Table S1: Range of pulling velocities used in the force probe molecular dynamics simulations and the corresponding loading rates, given the spring constant $k_{\mathrm{pull}} = 5000\ \mathrm{kJ\,mol^{-1}\,nm^{-2}}$. The pulling velocity is the velocity with which the virtual particle is moved away from the surface. This virtual particle is linked with a harmonic spring to the center of mass of the top layer of the nanofibrils.

Pulling velocity v ($\mu\mathrm{m\,s^{-1}}$)	Loading rate $\dot{F}$ (pN s^{-1})
$3 \cdot 10^5$	$2.5 \cdot 10^{12}$
$5 \cdot 10^5$	$4.5 \cdot 10^{12}$
$7 \cdot 10^5$	$5.8 \cdot 10^{12}$
$1 \cdot 10^6$	$8.3 \cdot 10^{12}$
$3 \cdot 10^6$	$2.5 \cdot 10^{13}$
$5 \cdot 10^6$	$4.2 \cdot 10^{13}$
$7 \cdot 10^6$	$5.8 \cdot 10^{13}$
$1 \cdot 10^7$	$8.3 \cdot 10^{13}$
$3 \cdot 10^7$	$2.5 \cdot 10^{14}$

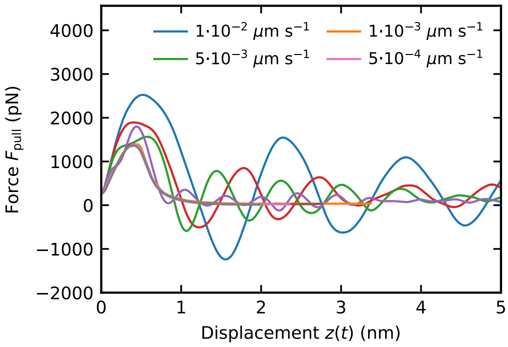

Figure S1: Smoothed force profiles as a function of virtual particle displacement $z(t)$ at different pulling velocities. The maximum at the beginning of each curve corresponds to the unbinding event of the gecko keratin from the hydrophobic octadecyltrichlorosilane self-assembled monolayer. The fast pulling velocities show periodic oscillations after the maximum force, due to keratin oscillating in the harmonic potential around the linked virtual particle. The slowest pulling velocities converge almost immediately to zero after the maximum, by quickly dissipating the forces internally. All forces eventually decay to zero after detachment.

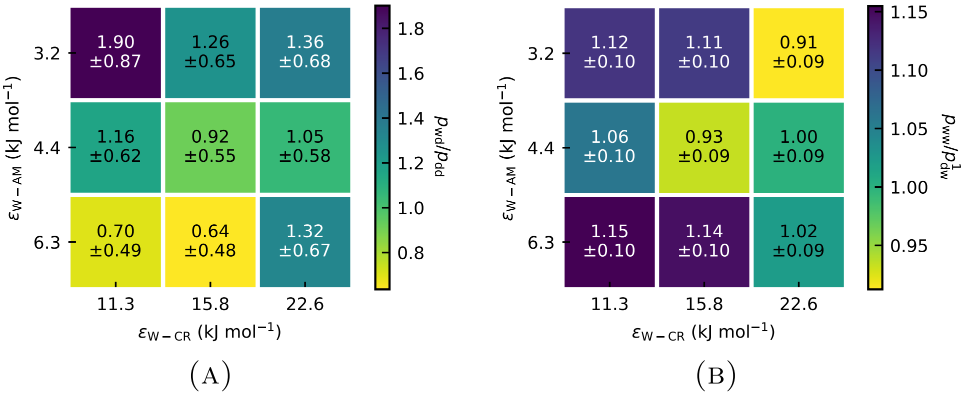

(A) (B)

Figure S2: (A) Pull-off pressures of wet keratin attached to a dry surface p_{wd} relative to the pull-off pressure of dry keratin on a dry surface p_{dd} at different Lennard-Jones interaction energies ϵ for Water-Core (W-CR) and Amorph-Water (W-AM) interactions. (B) Pull-off pressures of wet keratin on a wet surface p_{ww} relative to the pull-off force of dry weakly hydrophilic keratin on a wet surface p^1_{dw} shows the influence of wet keratin on the pull-off force in the context of a wet surface. Wet gecko keratin on both a dry and a wet surface leads to increased pull-off pressures compared to dry gecko keratin.

Table S2: Results of the force probe molecular dynamics simulations of the wet and dry models. Nomenclature for the type works as follows, the first index classifies if the keratin itself is dry (d) or wet (w), the second index classifies the surface as dry (d) or wet (w). Lennard-Jones interaction parameters of the dry gecko keratin model AM-AM interaction and the interactions of MARTINI water with the gecko keratin model. The Lennard-Jones interaction energies ϵ are in units kJ mol^{-}1. The pull-off force F (in pN) computed for a loading rate of $2.5 \cdot 10^{12}$ pN s^{-1} predicted by Bell+friction fits. Each Bell+friction model was fitted to the most probable pull-off forces of loading rates spanning three orders of magnitude. The standard deviation $\bar{\sigma}$ is computed from five different equilibrations. By using the surface area of the simulation box A, the pull-off forces can be compared between systems as pull-off pressures $p = F/A$, which shows that the change in surface area due to the swelling of the keratin is not large enough to change any trends if one only compares pull-off forces, instead of pull-off pressures.

Type	$\epsilon_{\mathrm{AM-AM}}$	$\epsilon_{\mathrm{W-CR}}$	$\epsilon_{\mathrm{W-AM}}$	F (10^3 pN)	$\bar{\sigma}$ (pN)	A (nm^3)	p (pN nm^{-3})
dd	7.2	-	-	6	456	290.4	2.2
dd	8	-	-	9	456	289.7	3.2
dd	8.8	-	-	9	456	289.2	3.0
dd	9.6	-	-	6	456	288.7	2.2
dd	10.4	-	-	5	456	288.1	1.7
wd	8	11.3	6.3	16	456	298.7	5.3
wd	8	11.3	3.2	22	456	297.1	7.3
wd	8	11.3	4.4	15	456	299.1	4.9
wd	8	15.8	6.3	12	456	298.2	4.0
wd	8	15.8	3.2	13	456	298.8	4.5
wd	8	15.8	4.4	11	456	296.6	3.5
wd	8	22.6	6.3	15	456	301.0	5.1
wd	8	22.6	3.2	8	456	294.0	2.7
wd	8	22.6	4.4	7	456	295.9	2.5
ww	8	11.3	6.3	74	520	298.7	24.6
ww	8	11.3	3.2	90	520	297.1	30.2
ww	8	11.3	4.4	90	520	299.1	30.0
ww	8	15.8	6.3	80	520	298.2	27.0
ww	8	15.8	3.2	85	520	298.8	28.6
ww	8	15.8	4.4	75	520	296.6	25.2
ww	8	22.6	6.3	83	520	301.0	27.6
ww	8	22.6	3.2	92	520	294.0	31.2
ww	8	22.6	4.4	91	520	295.9	30.9
dw	8	11.3	3.2	78	520	289.8	27.0

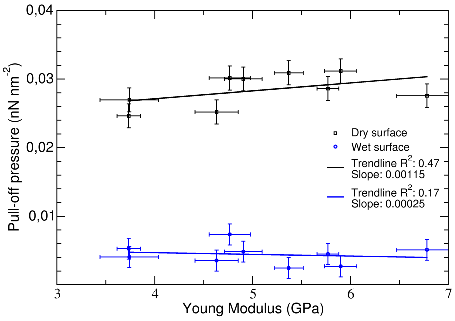

Figure S3: Pull-off pressures of wet gecko keratin as a function of Young modulus from the dry (black) and wet (blue) hydrophobic surface. Difference in the elastic modulus are due to different hydrophilicities of our wet gecko keratin model.

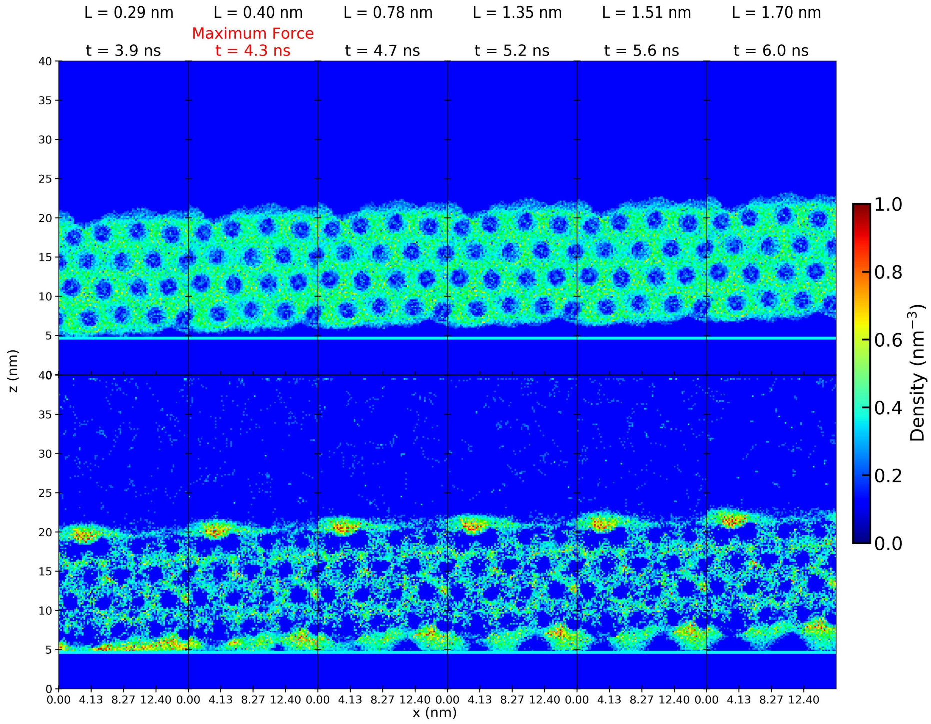

Figure S4: Density profiles of the weakly hydrophilic gecko keratin on the wet surface during pull-off. The 2D density profile of the keratin is shown on the top and the water density profile is shown at the bottom. Going from left to right density plots were calculated at different times during the pull-off. The unbinding event, the moment of maximum pull-off force, is marked in red on the top at a displacement of $L = z_{\text{COM}}(t) - z_{\text{COM,EQ}} = 0.4$ nm, with z_{COM} the position of the center of mass of the top layer nanofibrils. The Gibbs dividing surface of the alkane tails is shown as a horizontal cyan line. Convex capillary bridges can be seen in the bottom density profile of water, between the Gibbs dividing surface of the alkanes and the keratin.

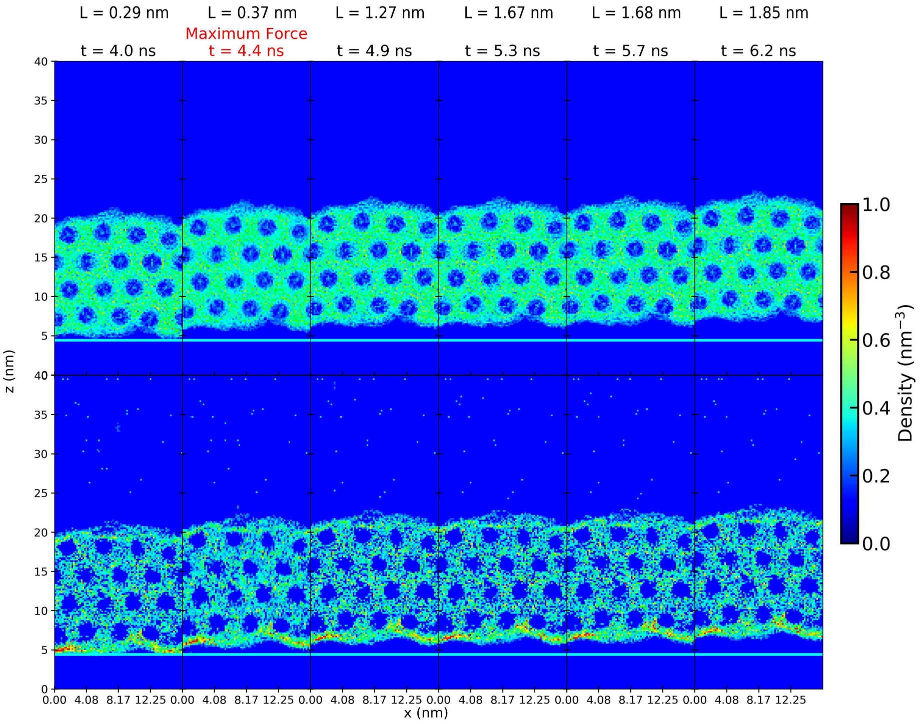

Figure S5: Density profiles of the strongly hydrophilic gecko keratin on the wet surface during pull-off. The 2D density profile of the keratin is shown on the top and the water density profile is shown at the bottom. Going from left to right density plots were calculated at different times during the pull-off. The unbinding event, the moment of maximum pull-off force, is marked in red on the top at a displacement of $L = z_{\mathrm{COM}}(t) - z_{\mathrm{COM,EQ}} = 0.37$ nm, with z_{COM} the position of the center of mass of the top layer nanofibrils. The Gibbs dividing surface of the alkane tails is shown as a horizontal cyan line. The keratin is pulled straight of the surface, without the formation of capillary bridges.

References

(1) Endoh, K. S.; Kawakatsu, T.; Müller-Plathe, F. Coarse-Grained Molecular Simulation Model for Gecko Feet Keratin. *J. Phys. Chem. B* **2018**, *122*, 2203–2212, DOI: `10.1021/acs.jpcb.7b10481`.

(2) Berendsen, H. J. C.; Postma, J. P. M.; van Gunsteren, W. F.; DiNola, A.; Haak, J. R. Molecular dynamics with coupling to an external bath. *J. Chem. Phys.* **1984**, *81*, 3684–3690, DOI: `10.1063/1.448118`.

4 Conclusions

From Nano to Micro: A Multiscale Journey. This work contributes to the understanding of gecko adhesive mechanisms and, consequently, may be useful in informing gecko-inspired synthetic designs with a true multiscale simulation procedure. The most significant contribution to the literature is a newly found molecular picture enabled by this work's multiscale simulations. With the molecular simulations performed during this work, we cover length scales ranging from atomistic (1 bead = 1 atom) over coarse-grained (1 bead = 1 amino acid) to mesoscale (1 bead = 1 protein aggregate). The new models and procedures designed and validated by us will not only allow rapid investigations of new questions concerning gecko adhesion but the here developed framework for the investigation of adhesion mechanisms can be adapted to study other dry adhesives.

Challenging Established Ideas: The Discovery of Water-Mediated Adhesion. It is long established that an increase in relative humidity of the environment leads to enhanced stickiness of gecko spatulae. Several mechanisms have been put forward to describe this characteristic. We challenge the established ideas that capillary forces (i) or material softening (ii) are primarily responsible for humidity-enhanced adhesion. Instead, this work discovered with coarse-grained and confirmed with atomistic simulations that water molecules fill into molecular gaps between surface and spatula and mediate (iii) an increase in the strength and number of attractive interactions between keratin and surface. Water absorbs partially into the spatula interface and leads to an increase in local density, thus increasing the effective surface energy of the spatula. Filling molecular gaps (~ 2 nm) smooths the spatula-surface interface and increases the interfacial contact area. While the simulation setup of the atomistic (UA) and coarse-grained (CG) simulations ruled out capillary forces (i), it demonstrated the same relative increase in stickiness observed during AFM investigations using single spatulae. Still, since we used explicit water molecules in these simulations, we were not able to rule out the keratin softening hypothesis (iii) at this point of the work.

From Naive Extrapolation to Mesoscale Validation. The UA and CG models were used to simulate the detachment of the keratin protein from an infinite (periodic) surface in vertical direction. This work developed pull-off procedures for the UA and CG models using 2D periodic boundary conditions (PBC) parallel to the surface. As simulations are only as good as their experimental validity, we naively extrapolated these pull-off forces to typical spatula contact areas to yield the corresponding stickiness of whole spatulae and discovered a systematic overestimation of the adhesion. The extrapolation would conclude that pull-off forces are hundreds of times larger than what AFM single-spatula experiments have observed. We then developed a mesoscale model of gecko keratin to test whether simple extrapolation was the correct pathway for a validity check. Using a hybrid bottom-up-top-down coarse-graining protocol, we used UA-model results as targets for the coarse-graining. With the developed mesoscale spatula model, we showed that restricting the allowed motions (i.e., the missing peel-off) and not the model parameters are responsible for overestimating the pull-off forces in 2D PBC. We extracted expected pull-off forces for single spatulae of around 12 nN (AFM experiments demonstrated a range of 8 to 20 nN). Thus, the necessary element to validate the pull-off simulations against the experiment is to use the true shape of a spatula and allow peel-off rather than vertical detachment and extrapolation. To our knowledge, no other model has been able to bottom-up reproduce experimental gecko spatula pull-off forces, making the experimental validity of the UA and mesoscale models a major achievement of this work.

Rapid Model Adaptation Enabled by Machine Learning. To isolate the three primarily discussed mechanisms underlying humidity-enhanced adhesion, we adjusted the coarse-grained harmonic interactions within the spatula model to reproduce the elasticity of water-swollen gecko keratin. Thus, the adapted spatula did not contain explicit water molecules, rigorously ruling out capillary forces (i) and water-mediation (ii). The elastic constants of water-swollen gecko keratin were determined by UA simulations in turn. The equilibrium water content at a given relative humidity was calculated by atomistic grand-canonical molecular dynamics. This work developed a deep neural network to infer bonded force field parameters that produce the exact target material properties at specific water contents (and relative humidities). While we only adjusted the bonded force field, which affect the elasticity of the keratin, the interactions with the surface were kept to rule out indirect contributions of water particles from the underlying UA simulations.

The Role of Water Mediation in Geckos' Adhesion on Flat Surfaces. We attached the previously discussed softened mesoscale spatula model to surfaces with bi-sinusoidal undulation of 16 nm height and periodicities ranging from infinity to feature sizes smaller than 13% of the spatula pad area. While AFM experiments reported an increase in adhesion on the hydrophobic flat surface due to humidity by around 200 to 300%, the implicitly fully „water-soaked“ spatula attaches better by just 10%. As a result, we can rule out material softening (iii) as the mechanism underlying humidity-enhanced adhesion in single-spatula AFM experiments on flat surfaces. Water-mediation (ii) dominates the humidity-enhanced adhesion of single spatulae at the flat hydrophobic surface over the entire relative humidity range. Additionally, when the keratin is dry, and the relative humidity is at 0%, the elasticity particularly contributes to the stickiness. But as the relative humidity increases and is greater than 0%, water molecules start to appear between spatula and surface and begin to mediate interactions between them. Thus, as the relative humidity increases and the water starts to absorb into the spatula-surface interface, water-mediation (ii) becomes dominant.

The Role of Material Softening in Humidity-Enhanced Adhesion on Nanostructured Surfaces. While material softening (iii) is not responsible for humidity-enhanced spatula stickiness on flat surfaces, it increases adhesion by up to 120% under very humid conditions (when the relative humidity is above 86%) if the characteristic feature length of the surface is smaller than the spatula. Here, the material softening effect (iii) may be responsible for 1/3 to 1/2 of the increased single-spatula stickiness compared to the dry condition. The higher flexibility of spatula keratin allows it to follow surface features smaller than itself. Finally, capillary bridges are either nonexistent on hydrophobic surfaces at relative humidities smaller than the supersaturation limit or they are of convex geometry. Depending on curvature, convex capillary bridges can even be repulsive.[44, 45]

Reconsidering Electrostatic Interactions in Gecko Adhesion. Since experimental investigations cannot study intra-keratin electrostatic interactions, the prevalent hypothesis claims that electrostatic interactions play no role in gecko adhesion. Clearly, and supported by our simulations, electrostatic interactions are relevant at hydrophilic surfaces. Furthermore, we showed that intra-keratin electrostatic interactions store elastic energy during the pull-off process. This energy is only recovered after detachment. Independent of water content and surface chemistry, the total electrostatic contributions are of the same magnitude as the van-der-Waals contributions. However, they specifically contribute to the stickiness of dry gecko keratin at the hydrophobic surface.

The Role of Intra-keratin Electrostatic Interactions in Geckos' Adhesive Mechanisms. Our simulations showed that intra-keratin electrostatic interactions are relevant at hydrophobic surfaces and store elastic energy during the pull-off process, which is only recovered after detachment. During the peel-off and pull-off process of a gecko spatula from a surface, the keratin undergoes elastic deformations. These deformations result from the stretching and bending of the keratin fibers and amino acid chains as the spatula is peeled or pulled away from the surface. The energy stored in these elastic deformations is recovered only after detachment is completed. Therefore the elastic energy contributes to the work of detachment (opposing it), while the recovery energy does not. These intra-keratin electrostatic interactions, which occur, in part, between charged and polar amino acid residues within the keratin protein, contribute to the overall stickiness of the spatula and are essential for its ability to adhere to surfaces. The contributions were found to be of the same magnitude as the van-der-Waals contributions, and are particular relevant at the hydrophobic surface.

Water-Mediated Adhesion and the Crucial Role of Electrostatic Interactions at Hydrophilic Surfaces In addition to the intra-keratin electrostatic interactions, our simulations also showed that keratin-surface electrostatic interactions are at least as crucial as keratin-surface van-der-Waals interactions at hydrophilic surfaces. Moreover, a remarkable observation is the modulation of the water-mediation effect. Water sticks to the keratin at hydrophobic surfaces and opposes detachment through short-range van-der-Waals interactions between water and the surface. Conversely, water adheres to hydrophilic surfaces and resists gecko keratin pull-off through van-der-Waals and electrostatic interactions between it and the keratin. Thus, the water-mediation effect is modulated by the surface's hydrophilicity, resulting in different electrostatic interactions between water, keratin and the surface.

5 Outlook

In this work, we used multiscale molecular dynamics (MD) simulations to investigate the adhesion mechanisms of geckos, with a particular focus on the role of water-mediated adhesion. To accomplish this, we created a united-atom (UA) gecko keratin model and developed a novel multiscale method that combined bottom-up and top-down approaches. This method allowed us to use data from the UA model to inform a mesoscale coarse-grained gecko spatula model. This method demonstrated good accuracy in predicting stickiness and reproducing experimental atomic force microscopy (AFM) results of single spatulae. Our findings challenge the established ideas on humidity-enhanced adhesion and the relevance of electrostatics. In particular, our simulations demonstrate the effect of water-mediated adhesion, the relevance of intra-keratin electrostatic interactions, the modulation of the water-mediated effect at hydrophilic surfaces, and their contribution to the overall stickiness of the spatula.

This outlook will discuss the potentials of this work, possible avenues for research in gecko-inspired adhesives, including further studies on gecko adhesion mechanisms, open-questions and a call to further collaborate across disciplines.

The general potentials of this work in the future are:

- Extending our understanding of adhesion mechanisms: By using multiscale MD simulations to investigate the adhesion mechanisms of geckos, this thesis may contribute to the broader field of biological dry adhesion science. Some of our findings may help inform future research on dry adhesion, including developing new theories and models, especially considering humidity-enhanced adhesion and intra-keratin elasticities.
- Improving the accuracy of adhesive simulation methods: Our multiscale method demonstrated a way to incorporate data from different modeling scales in a straightforward manner for investigating gecko adhesion using molecular dynamics. This method could be adapted and applied to other dry adhesives to model their stickiness, for example, plant-based pectin, by considering their unique properties and characteristics. Combining bottom-up and top-down approaches could prove to be a valuable strategy to simulate and understand the adhesive properties of other mesoscale or microscale adhesive systems, as they are present in spiders, insects, plant seeds or even synthetic gecko-inspired adhesives. Moreover, we developed a procedure that enables the extrapolation of pull-off pressures obtained from nanoscale two-dimensional periodic boundary condition simulations to larger-scale mesoscopic and microscopic adhesive systems.

- Inspiring interdisciplinary research: This study combines knowledge and techniques from various disciplines, including materials science, biology, biophysics, and computational chemistry. As such, it may inspire interdisciplinary collaborations between researchers in these fields.

Despite our advances in this field, many unanswered questions regarding gecko adhesion still need to be answered. This section will first focus on the more pressing questions and provide possible avenues to address them. We will then list the remaining questions that still require further investigation.

Validation and Verification. While the simulations presented in this work demonstrate good accuracy, more work should be done to verify the results against more complex experimental setups. We propose to use high-speed AFM to verify the extrapolation regime of our mesoscale spatula work, in essence, we propose to compute the pull-off forces at near-MD loading rates using single-spatula AFM. Moreover, comparing results from single-spatula AFM at ultra-flat hydrophobic surfaces at extremely low humidities against simulations with the same humidities could clarify the scaling law of the water-mediation effect on adhesion.

Investigating the Stickiness of other Gecko Keratin Proteins. This works multiscale pipeline generates amorphized amino acid sequence-based adhesives on top of hydrophilic and hydrophobic surfaces. We focused on the Ge-cprp-9 protein that is located at the spatula-air interface. Further studies should be conducted on the other 15 cysteine-rich gecko proteins using our multiscale method to explore their adhesion potential. Suppose we would know the stickiness of all the gecko keratin proteins. In that case, analyses can correlate their stickiness with their amino acid sequence properties, including the distribution of hydrophobic and hydrophilic amino acids and charged and uncharged residues, and determine the key factors contributing to their adhesion. This information may provide usefulness to further elucidate the evolution of gecko adhesion and may be useful in the development of gecko-inspired adhesives through the development of a strong understanding of the correlation between sequence chemistry and stickiness.

Can the United-Atom Keratin and Mesoscale Spatula Models be Combined using an Adaptive Resolution Coarse-Graining Approach? One avenue worth pursuing would be to combine the different model resolutions, which would enable to investigate peel-off at a united-atom resolution. The united-atom gecko keratin model could be bottom-up coarse-grained using methods like adaptive resolution coarse-graining. The UA model would be coarse-grained with decreasing mapping resolution as a function of distance to the surface. The united-atom region directly in contact with the surface would be unchanged. Since the change in resolution would create discontinuities if the differently resolved regions were directly interfaced, transition regions would be needed. There are two main challenges: 1) What bottom-up coarse-graining method would be best utilized for a non-equilibrium simulation of, effectively, a highly cross-linked elastomer? 2) How should the parameters of the transition regions, which need to be small enough to provide a smooth transition but large enough to avoid a sudden discontinuity, be defined? Two ways to approach these problems would be to rely on a trial-and-error approach or optimization methods, like the cost-effective Bayesian optimization, which is particularly suited for optimizing high-cost functions like MD simulations, to find the best setup.

Manufacturing of Copolymers for Gecko-Inspired Synthetic Adhesives. Gecko-inspired adhesives have shown promise in the laboratory, and further research may reveal their potential in various applications. Novel gecko-keratin-inspired copolymers could potentially be developed. Currently, it is thought that gecko-inspired adhesives may be useful in a range of applications, including medical devices and robotics. Less apparent applications may include products for home decor or reversible mounting solutions. Our discovery of the water-mediation effect and intra-keratin electrostatics has shown that these are key driving forces of gecko spatula stickiness. However, developing gecko-keratin-inspired copolymers requires careful design to achieve these properties. A multiscale simulation strategy may be able to optimize the design of these copolymers with tailored monomer sequences that accomplish water-mediated adhesion and intra-polymer electrostatics to a similar extent as in gecko keratin. To achieve this, our united-atom pipeline must first be adapted such that the automated model creation pipeline creates monomer sequences instead of amino acid sequences. Furthermore, the mesoscale model is currently modelling the shape of a gecko spatula. This shape needs to be adapted to shapes that can be achieved experimentally (i.e., angled mushrooms tips, pillars, microwedges, nanoforests).

Other Species with Dry Adhesion: Exploring Differences and Similarities in their Adhesion Mechanisms. Exploring the adhesion mechanisms of other species that exhibit dry adhesion can provide valuable insight into other working strategies. Comparative studies can examine and contrast the adhesion mechanisms of different species, elucidating differences and similarities and identifying the factors that impact their adhesion. While our multiscale pipeline may be a useful approach in investigating the adhesion mechanisms of other species, it is important to note that the multiscale approach needs to be customized for each adhesive system with a new united-atom model. If the adhesive system comprises an amorphous protein-based material, then our amorphization and multiscale protocol can be directly applied. This protocol involves using a self-avoiding random walker to place amino acid chains inside a simulation box, followed by an amorphization process to equilibrate the system. However, our amorphization protocol is not suitable for systems that feature a specific, well-defined three-dimensional structure.

Further, exciting but unanswered questions related to our work are:

- How can surfaces be modified to prevent spiders and other insects from climbing walls and stairs in residential environments?
- Can the simulations be extended to consider the behavior of gecko-inspired synthetic adhesives in real-world conditions?
- How can the results of the simulations be validated against more complex experimental setups, such as actual gecko movement?
- How does the molecular structure of gecko keratin change over time, for example, due to wear and tear or changes in the environment?
- Is it possible to integrate finite element simulations and molecular dynamics in order to simulate the complete setae, including the spatula?

- Can X-ray photoelectron spectroscopy (XPS), single-spatula AFM, and scanning tunneling microscopy (STM) improve MD simulations and enable the investigation of the impact of surface chemistry and water on stickiness using more realistic surfaces?
- How does temperature affect the water-mediation effect?
- Does the dampening of the gecko keratin chain mobility suggest the involvement of entropy-based adhesion mechanisms?
- Utilizing multiple different force fields, what is the extent of uncertainty in the balance between the various energetic interactions at the spatula-surface interface?
- What is the role of capillary forces at hydrophilic surfaces in very humid environments?

In summary, the outlook for future research in gecko adhesion and gecko-inspired adhesives is broad and promising. From investigating gecko adhesion mechanisms at different scales to developing new materials and designs inspired by gecko stickiness, the potential for invention in this field is extensive. As we move forward, it will be essential to continue acknowledging the current research's limits and challenges while working to overcome them through interdisciplinary cooperation.

In closing, this thesis represents a substantial step forward in understanding gecko adhesion mechanisms. It has the potential to inspire further research that focuses on the water-mediation effect and the usage of multiscale simulation approaches for mesoscale to microscale adhesion systems. One crucial element of success is that we collaborate across disciplines to apply our knowledge and models together, as we have demonstrated in this work.

Literatur

(1) Jiang, Q.; Wang, Z.; Zhou, J.; Chen, W.; Dai, Z. Analysis of Reaction Force and Locomotor Behavior on Geckos in Time- and Frequency-domain during Climbing on Vertical Substrates. *J. Bionic Eng.* **2019**, *16*, 115–129.

(2) Alibardi, L. Immunolocalization of specific keratin associated beta-proteins (beta-keratins) in the adhesive setae of Gekko gecko. *Tissue Cell* **2013**, *45*, 231–240.

(3) Endoh, K. S.; Kawakatsu, T.; Müller-Plathe, F. Coarse-Grained Molecular Simulation Model for Gecko Feet Keratin. *J. Phys. Chem. B* **2018**, *122*, 2203–2212.

(4) Ruibal, R.; Ernst, V. The structure of the digital setae of lizards. *J. Morphol.* **1965**, *117*, 271–293.

(5) Rizzo, N. W.; Gardner, K. H.; Walls, D. J.; Keiper-Hrynko, N. M.; Ganzke, T. S.; Hallahan, D. L. Characterization of the structure and composition of gecko adhesive setae. *J. R. Soc. Interface* **2006**, *3*, 441–451.

(6) Calvaresi, M.; Eckhart, L.; Alibardi, L. The molecular organization of the beta-sheet region in Corneous beta-proteins (beta-keratins) of sauropsids explains its stability and polymerization into filaments. *J. Struct. Biol.* **2016**, *194*, 282–291.

(7) Hallahan, D. L.; Keiper-Hrynko, N. M.; Shang, T. Q.; Ganzke, T. S.; Toni, M.; Valle, L. D.; Alibardi, L. Analysis of gene expression in gecko digital adhesive pads indicates significant production of cysteine- and glycine-rich beta-keratins. *J. Exp. Zool. B: Mol. Dev. Evol.* **2009**, *312B*, 58–73.

(8) Materzok, T.; Canestraight, A.; Gorb, S. N.; Müller-Plathe, F. How does Gecko Keratin stick to hydrophilic and hydrophobic surfaces in the presence and absence of water? An atomistic molecular dynamics investigation. *ACS Nano* **2022**, accepted.

(9) Kim, T. W.; Bhushan, B. Effect of stiffness of multi-level hierarchical attachment system on adhesion enhancement. *Ultramicroscopy* **2007**, *107*, 902–912.

(10) Huber, G.; Gorb, S. N.; Hosoda, N.; Spolenak, R.; Arzt, E. Influence of surface roughness on gecko adhesion. *Acta Biomater.* **2007**, *3*, 607–610.

(11) Mahendra, B. C. Contributions to the bionomics, anatomy, reproduction and development of the Indian house-gecko, Hemidactylus flaviviridis Rüppel. *Proc. Indian Acad. Sci.* **1941**, *13*, 288–306.

(12) Autumn, K.; Liang, Y. A.; Hsieh, S. T.; Zesch, W.; Chan, W. P.; Kenny, T. W.; Fearing, R.; Full, R. J. Adhesive force of a single gecko foot-hair. *Nature* **2000**, *405*, 681–685.

(13) Israelachvili, J. N., *Intermolecular and Surface Forces*; Academic Press: 2011.

(14) Wilson, J. R., *A Collector's Guide to Rock, Mineral, & Fossil Localities of Utah*; Utah Geological Survey: 1995.

(15) Desire, T.; Dieudonne, B.; Rose, Y.-F. In Situ Genesis of Alumino-Ferruginous Nodules in a Soil Profile Developed on Garnet Rich Micaschist in the High Reliefs of South Cameroon Rainforest Zone (Central Africa). *Open J. Geol* **2011**, *5*.

(16) Dellit, W.-D. Zur anatomie und physiologie der Geckozehe, PhD Thesis, 1934.

(17) Sun, W.; Neuzil, P.; Kustandi, T. S.; Oh, S.; Samper, V. D. The Nature of the Gecko Lizard Adhesive Force. *Biophys. J.* **2005**, *89*, L14–L17.

(18) Song, Y.; Wang, Z.; Li, Y.; Dai, Z. Electrostatic attraction caused by triboelectrification in climbing geckos. *Friction* **2020**, DOI: `10.1007/s40544-020-0387-3`.

(19) Huber, G.; Mantz, H.; Spolenak, R.; Mecke, K.; Jacobs, K.; Gorb, S. N.; Arzt, E. Evidence for capillarity contributions to gecko adhesion from single spatula nanomechanical measurements. *Proc. Natl. Acad. Sci. U.S.A.* **2005**, *102*, 16293–16296.

(20) Stark, A. Y.; Klittich, M. R.; Sitti, M.; Niewiarowski, P. H.; Dhinojwala, A. The effect of temperature and humidity on adhesion of a gecko-inspired adhesive: implications for the natural system. *Sci. Rep.* **2016**, *6*, 30936.

(21) Mitchell, C. T.; Dayan, C. B.; Drotlef, D.-M.; Sitti, M.; Stark, A. Y. The effect of substrate wettability and modulus on gecko and gecko-inspired synthetic adhesion in variable temperature and humidity. *Sci. Rep.* **2020**, *10*, 19748.

(22) Materzok, T.; Gorb, S. N.; Müller-Plathe, F. Gecko adhesion: a molecular-simulation perspective on the effect of humidity. *Soft Matter* **2022**, *18*, 1247–1263.

(23) Materzok, T.; Eslami, H.; Gorb, S. N.; Müller-Plathe, F. Understanding Humidity-enhanced Adhesion of Geckos: Deep Neural Network-assisted Multi-scale Molecular Modeling. *Small* **2022**, under review.

(24) Prowse, M.; Wilkinson, M.; Puthoff, J.; Mayer, G.; Autumn, K. Effects of humidity on the mechanical properties of gecko setae. *Acta Biomater.* **2010**, *7*, 733–8.

(25) Puthoff, J. B.; Prowse, M. S.; Wilkinson, M.; Autumn, K. Changes in materials properties explain the effects of humidity on gecko adhesion. *J. Exp. Biol.* **2010**, *213*, 3699–3704.

(26) Stark, A. Y.; Subarajan, S.; Jain, D.; Niewiarowski, P. H.; Dhinojwala, A. Superhydrophobicity of the gecko toe pad: biological optimization versus laboratory maximization. *Philos. Trans. Royal Soc.* **2016**, *374*, 20160184.

(27) Huber, G.; Orso, S.; Spolenak, R.; Wegst, U. G. K.; Enders, S.; Gorb, S. N.; Arzt, E. Mechanical properties of a single gecko seta. *Mater. Res.* **2008**, *99*, 1113–1118.

(28) Persson, B. N. J.; Gorb, S. The effect of surface roughness on the adhesion of elastic plates with application to biological systems. *J. Chem. Phys.* **2003**, *119*, 11437–11444.

(29) Filippov, A.; Popov, V. L.; Gorb, S. N. Shear induced adhesion: Contact mechanics of biological spatula-like attachment devices. *J. Theor. Biol.* **2011**, *276*, 126–131.

(30) Sauer, R. A.; Holl, M. A detailed 3D finite element analysis of the peeling behaviour of a gecko spatula. *Comput. Methods Biomech. Biomed. Eng.* **2013**, *16*, 577–591.

(31) Burdekin, G. Gold dust day gecko drinks from bird of paradise flower, With permission by the photographer, 2017.

(32) Myers, S. Gold dust day gecko I, With permission by the photographer.

(33) Tonge, S. Afroedura transvaalica, With permission by the photographer, 2017.

(34) Farooq, H. Afroedura gorongosa, With permission by the photographer, 2017.

(35) Marrink, S. J.; Risselada, H. J.; Yefimov, S.; Tieleman, D. P.; de Vries, A. H. The MARTINI force field: coarse grained model for biomolecular simulations. *J. Phys. Chem. B* **2007**, *111*, 7812–7824.

(36) Monticelli, L.; Kandasamy, S. K.; Periole, X.; Larson, R. G.; Tieleman, D. P.; Marrink, S.-J. The MARTINI Coarse-Grained Force Field: Extension to Proteins. *J. Chem. Theory Comput.* **2008**, *4*, 819–834.

(37) De Jong, D. H.; Singh, G.; Bennett, W. F. D.; Arnarez, C.; Wassenaar, T. A.; Schäfer, L. V.; Periole, X.; Tieleman, D. P.; Marrink, S. J. Improved Parameters for the Martini Coarse-Grained Protein Force Field. *J. Chem. Theory Comput.* **2013**, *9*, 687–697.

(38) Alder, B. J.; Wainwright, T. E. Studies in Molecular Dynamics. I. General Method. *J. Chem. Phys.* **1959**, *31*, 459–466.

(39) Frenkel, D.; Smit, B., *Understanding Molecular Simulation: From Algorithms to Applications*, Google-Books-ID: 5qTzldS9ROIC; Elsevier: 2001.

(40) Xu, Q.; Wan, Y.; Hu, T. S.; Liu, T. X.; Tao, D.; Niewiarowski, P. H.; Tian, Y.; Liu, Y.; Dai, L.; Yang, Y.; Xia, Z. Robust self-cleaning and micromanipulation capabilities of gecko spatulae and their bio-mimics. *Nat. Commun.* **2015**, *6*, 8949.

(41) Grubmüller, H. Force probe molecular dynamics simulations. *Methods Mol. Biol.* **2005**, *305*, 493–515.

(42) Sheridan, S.; Gräter, F.; Daday, C. How Fast Is Too Fast in Force-Probe Molecular Dynamics Simulations? *J. Phys. Chem. B* **2019**, *123*, 3658–3664.

(43) Rico, F.; Russek, A.; González, L.; Grubmüller, H.; Scheuring, S. Heterogeneous and rate-dependent streptavidin–biotin unbinding revealed by high-speed force spectroscopy and atomistic simulations. *Proc. Natl. Acad. Sci. U.S.A.* **2019**, *116*, 6594–6601.

(44) Dörmann, M.; Schmid, H.-J. Simulation of Capillary Bridges between Particles. *Procedia Eng.* **2015**, *102*, 14–23.

(45) Kralchevsky, P. A.; Nagayama, K. in *Studies in Interface Science*, Kralchevsky, P. A., Nagayama, K., Hrsg.; Particles at Fluids Interfaces and Membranes, Bd. 10; Elsevier: 2001, S. 469–502.

Erklärung zum Eigenanteil an den Veröffentlichungen

Die vorliegende Dissertation wurde unter der Leitung von Herrn Prof. Dr. Florian Müller-Plathe in der Zeit vom 01. Februar 2019 bis zum 24. April 2022 im Fachbereich Chemie der Technischen Universität Darmstadt durchgeführt. Im Folgenden ist aufgelistet, mit welchem Anteil ich an der Veröffentlichung beteiligt war.

Teile dieser Arbeit sind bereits veröffentlicht:

1. Mein Anteil an der folgenden Veröffentlichung beträgt 90%:
   T. Materzok, S. N. Gorb, F. Müller-Plathe, *Gecko adhesion: a molecular-simulation perspective on the effect of humidity*, Soft Matter, **18**, 1247-1263, DOI: 10.1039/D1SM01232K (2022)
2. Mein Anteil an der folgenden Veröffentlichung beträgt 85%:
   T. Materzok, A. Canestraight, S. N. Gorb, F. Müller-Plathe, *How Does Gecko Keratin Stick to Hydrophilic and Hydrophobic Surfaces in the Presence and Absence of Water? An Atomistic Molecular Dynamics Investigation*, ACS Nano, **16**, 19261–19270,
   DOI: 10.1021/acsnano.2c08627 (2022)
3. Mein Anteil an der folgenden Veröffentlichung beträgt 85%:
   T. Materzok, D. de Boer, S. N. Gorb, F. Müller-Plathe, *Gecko Adhesion on Flat and Rough Surfaces: Simulations with a Multi-Scale Molecular Model*, Small, **18**, 2201674,
   DOI: 10.1002/smll.202201674 (2022)
4. Mein Anteil an der folgenden Veröffentlichung beträgt 85%:
   T. Materzok, H. Eslami, S. N. Gorb, F. Müller-Plathe, *Understanding Humidity-Enhanced Adhesion of Geckos: Deep Neural Network-Assisted Multi-Scale Molecular Modeling*, Small,
   DOI: 10.1002/smll.202206085 (2023)

Datum

Tobias Materzok

Erklärung zur Begutachtung der Veröffentlichungen

Weder Referent Prof. Dr. Florian Müller-Plathe noch Koreferent Prof. Dr. Stanislav N. Gorb der vorliegenden kumulativen Doktorarbeit waren an der Begutachtung nachstehender Veröffentlichungen beteiligt.

1. T. Materzok, S. N. Gorb, F. Müller-Plathe, *Gecko adhesion: a molecular-simulation perspective on the effect of humidity*, Soft Matter, **18**, 1247-1263, DOI: 10.1039/D1SM01232K (2022)
2. T. Materzok, A. Canestraight, S. N. Gorb, F. Müller-Plathe, *How Does Gecko Keratin Stick to Hydrophilic and Hydrophobic Surfaces in the Presence and Absence of Water? An Atomistic Molecular Dynamics Investigation*, ACS Nano, **16**, 19261–19270, DOI: 10.1021/acsnano.2c08627 (2022)
3. T. Materzok, D. de Boer, S. N. Gorb, F. Müller-Plathe, *Gecko Adhesion on Flat and Rough Surfaces: Simulations with a Multi-Scale Molecular Model*, Small, **18**, 2201674, DOI: 10.1002/smll.202201674 (2022)
4. T. Materzok, H. Eslami, S. N. Gorb, F. Müller-Plathe, *Understanding Humidity-Enhanced Adhesion of Geckos: Deep Neural Network-Assisted Multi-Scale Molecular Modeling*, Small, DOI: 10.1002/smll.202206085 (2023)

Datum

Referent
Prof. Dr. Florian Müller-Plathe

Koreferent
Prof. Dr. Stanislav N. Gorb